Mécanique de la banquise Arctique et des matériaux granulaires : deux milieux, deux approches

Florent Gimbert

UNIVERSITÉ DE GRENOBLE

Thèse

Pour obtenir le grade de

Docteur de l'Université de Grenoble

Spécialité : **Sciences de la Terre et de l'Environnement**

Arrêté ministériel : 7 août 2006

Présentée par

Florent GIMBERT

Thèse dirigée par **David AMITRANO et Jérôme WEISS**

préparée au sein de l' **Institut des Sciences de la Terre**
et de **Terre, Univers, Environnement**

Mécanique de la banquise Arctique et des matériaux granulaires : deux milieux, deux approches

Mechanics of Arctic sea ice and granular materials : two media, two approaches

Soutenue publiquement le **7 Novembre 2012**,
devant le jury composé de :

M. Daniel FELTHAM
Professeur, University College of London, Rapporteur

M. Farhang RADJAI
Directeur de Recherche au CNRS, LMGC Montpellier, Rapporteur

M. Stéphane SANTUCCI
Chargé de Recherche au CNRS, ENS Lyon, Examinateur

M. Yves GUÉGUEN
Professeur à l'ENS-Paris, Dpt TAO, Examinateur

M. David MARSAN
Professeur à l'UdS, ISTerre Chambéry, Examinateur

M. David AMITRANO
Maître de Conférence à l'IUT1, ISTerre Grenoble, Directeur de thèse

M. Jérôme WEISS
Directeur de Recherche au CNRS, LGGE Grenoble, Directeur de thèse

Abstract

Two approaches to study the mechanical behaviour of Arctic sea ice in one hand, and of granular media on the other hand, are presented in this thesis.

First, a continuum mechanics analysis is conducted on sea ice in order to extract the relevant physics that, to the first order, explains the observed recent acceleration of sea ice drift and deformation. An original method to determine the mechanical properties of the sea ice cover at large time and spatial scales, i.e. over the whole Arctic basin and over 40 years of record, is proposed by quantifying the amplitude of inertial motion of ice drifters. This method allows to estimate an average ice cover friction, that is currently not accessible through other means at those large spatio-temporal scales. We show that a genuine mechanical weakening of the Arctic sea ice, associated to changes in the degree of fragmentation of the ice cover, comes into play to explain the observed changes in terms of sea ice kinematics and dynamics. This underlines the necessity to take into account this component in modelling studies, as well as to develop specific tools to measure an internal friction at local scales.

Second, a statistical mechanics analysis is adopted in order to characterize the mechanical heterogeneities associated to the macroscopic behaviour of frictional granular materials submitted to compressive loading. From numerical modeling and experimental studies, quantitative estimates of heterogeneities that develop in the shear stress and strain fields are provided. At short timescales, intense stress and strain localization is reported, associated at the macroscopic instability to specific multi-scale properties. Thus, at this flow instability, these strain field properties significantly differ from the shear band formation observed after the instability when considering large time scales. The connection between these two characteristic features remains to be understood.

Résumé

Dans cette thèse, deux approches de caractérisation d'un comportement mécanique sont présentées, l'une sur la banquise Arctique, l'autre sur les milieux granulaires.

Premièrement, une analyse de type mécanique des milieux continus est réalisée sur la banquise de manière à extraire la physique qui, au premier ordre, explique l'augmentation récente des vitesses de dérive et de déformation. Une méthode originale pour accèder aux propriétés mécaniques de la couverture de glace aux grandes échelles de temps et d'espace, i.e. sur tout le bassin Arctique et au cours de ces 40 dernières années, est proposée en quantifiant l'amplitude de la composante inertielle du mouvement des bouées enchâssées dans la glace. Le point fort de cette méthode réside dans le fait qu'elle apporte des informations sur la friction moyenne de la couverture de glace qui, jusqu'à maintenant, n'étaient pas disponible à ces échelles spatio-temporelles. A partir d'un modèle simple, nous montrons qu'un affaiblissement mécanique de la banquise, se traduisant par des changements dans le degré de fracturation de la couverture de glace, intervient au premier ordre dans la cinématique et la dynamique des glaces de mer. Cette observation souligne la nécessité de prendre en compte cette composante de manière appropriée dans les modèles ainsi que de développer des outils spécifiques pour accèder à cette quantité à l'échelle locale.

Deuxièmement, une analyse de type mécanique statistique est adoptée dans l'étude numérique et expérimentale des milieux granulaires frottants sous compression. L'étude des hétérogénéités associées aux champs de contrainte et de déformation ainsi que leur lien avec le comportement mécanique macroscopique de ce matériau est réalisée. Aux petites échelles de temps, de fortes concentrations de contrainte et de déformation sont mises en évidence. De plus, des propriétés multi-échelles spécifiques caractérisent ces champs à l'instabilité macroscopique. Ainsi, à ce point d'instabilité, ces champs de déformation observés aux petites échelles de temps présentent des propriétés trés différentes de celles présentées par la bande de cisaillement, habituellement caractérisée aux grandes échelles de temps. Le lien entre ces deux comportements caractéristiques reste à élucider.

Remerciements

Je voudrais tout d'abord remercier les membres de mon jury de thèse Farhang Radjai, Daniel Feltham, Stéphane Santucci et Yves Guéguen pour avoir rapporté et examiné mon travail. Je les remercie tout particulièrement pour l'intérêt qu'ils ont indifféremment porté à mon travail sur la banquise et les milieux granulaires, quelqu'en aient été leurs spécialités respectives.

Je tiens ensuite à remercier les personnes m'ayant encadré dans cette aventure scientifique qu'est la thèse, mes directeurs officiels Jérôme Weiss et David Amitrano et coencadrants David Marsan et Gaël Combe. La partie "navigation" parfois tortueuse de cette aventure, je l'ai principalement vécu avec Jérôme, avec qui j'ai constamment exploré les frontières entre glaciologie et sciences des matériaux, une approche que j'ai particulièrement appréciée. Par tous les vents et quelque soit la problématique, Jérôme a toujours fait preuve d'un fort interêt et soutien à l'égard de mon travail, ce qui a été pour moi une grande source de motivation pour mener à bien ce que j'entreprenais. Je remercie David (A) d'une part pour m'avoir laissé la liberté de continuer ma navigation à travers les floes de la banquise durant ma thèse, un milieu d'exploration qui devait initialement se limiter à mon stage de M2R, et d'autre part pour m'avoir encouragé et soutenu dans mon travail sur les milieux granulaires. Je remercie David (M), l'"aiguilleur" de la navigation sur la partie banquise qui, ne s'etant presque jamais fait surprendre par Coriolis !, a formalisé et apporté des réponses concrètes aux questionnements que j'ai pu avoir. Enfin, je remercie Gaël pour m'avoir initié à la modélisation numérique rigoureuse des milieux granulaires et avisé des secrets et comportements parfois peu intuitifs qu'ils détiennent.

Je tiens aussi à remercier tout particulièrement Nicolas Jourdain qui, de par sa vision d'océanographe et ses idées salvatrices de modèle analytique, a beaucoup apporté à mon travail sur la banquise. Dans le même registre, je remercie aussi Bernard Barnier et Jean Marc Molines pour m'avoir permis d'obtenir différents jeux de données caractérisant la dynamique de l'océan et de l'atmosphère à l'issue de discussions motivantes.

Côté Terre solide, je tiens à remercier les chercheurs de l'équipe mécanique des failles qui m'ont accueilli à ISTerre, François Renard, Anne-Marie Boullier, Michel Bouchon, Jean-Pierre Gratier, Mai-Linh Doan... J'ai beaucoup aimé les discussions mensuelles instructives et variées sur les séismes et autres observations des failles de la Terre, depuis la faille de Belledonne jusqu'à la San Andreas, que je côtoie aujourd'hui de très (trop ?) près... Je les remercie aussi pour leur soutien logistique, notamment pour m'avoir permis de partir en conférences à plusieurs reprises, m'avoir laissé remplir une bonne partie des espaces disques de l'équipe avec mes simulations granulaires.

Enfin, je tiens à remercier proches et amis qui m'ont apporté un soutien sans "failles" (François, la transition est pour toi...) ainsi que beaucoup de bonheur durant ces années de thèse. Avec vous tous l'aventure ne s'est pas limitée à la thèse (a parfois empiété dessus ? non...) et j'entends bien à ce que celà dure...

Tout d'abord, je remercie les membres proclamés ou d'adoption de la team "Alti-Ligérienne", aujourd'hui Rhône-Alpins pas vraiment malgrès eux, amis et compagnons de toujours : Gasp, Adri, Alex, Cam, Cap, Lois (même si encore jamais vraiment vu...), Jo, Dav, Sim. Merci pour vôtre présence, jovialité et "gratinage" de tous les instants ! Je pense aussi, en vrac, aux virées avec Luc-Luc, Soph', Bapt, Pierre (Lainé), Cécile (Arcis)...

Je remercie les thésards et compagnons de galère ISTerriens : Thomas, Pierre (Bou), Guénolé, Pierre (Bot), Jean, Rachelle, Gabi, Anne, Benjamin, Aurélien, Diane, Dimitri, Aurore, Mathieu (s), Cécile, Mathilde, Amir, Vincent, Isabella... J'ai passé de très bons moments à l'intérieur et en dehors des murs d'ISTerre avec vous, depuis les fameux canyons signés Planès "à prendre au sérieux" jusqu'aux "à plats" intenables dont seul Pierre en détient les secrets, en passant bien sûr par la case Nespresso ou les bières à EVE, qui sont définitivement restées les plus populaires... surtout vers la fin !

Je remercie aussi les thésards et chercheurs du LGGE : Marion, Xav, Vincent (Pel), Vincent (Pey), Antoine, Martin, Cécile, Joseph... pour les sorties et moments partagés au pan, sur les skis ou autour d'une bonne tablée...

Je remercie la team TAO : Juju, J-A, Kelly, Dublanch', Darrioul', Benjamin, Lola, Le ptit Gaspard, Le tout petit Zéphir, les chats... (j'arrête là car je m'emporte !) pour tous ces moments, missions et visites parfois (très) inattendus.

Je souhaite enfin remercier ma famille. Je remercie ma mère qui, de part son optimisme sur la vie et son humanité profonde, m'apporte une grande confiance en l'avenir. Je remercie mon père qui, en plus de me rappeler régulièrement d'où je viens, nous a fournis en bons légumes du jardin ces trois dernières années... leur absence se fait d'ailleurs lourdement sentir aujourd'hui ! Je remercie mes chères et tendres grandes soeurs pour avoir continué de bichonner le petit dernier, jusque dans la relecture de ce manuscrit ou encore le concoctage de bonnes petites patisseries pour son pot de thèse... Vous êtes au top ! Je remercie aussi Christian, mes beaux frères et ma belle famille pour tous ces moments conviviaux passés ensemble, sources d'oxygène et tant appréciables !

Enfin je te remercie Anne So, pour me rendre heureux en ayant partagé au quotidien tous ces moments avec moi, et pour continuer de les faire vivre aujourd'hui...

Table des matières

Table des figures

Avant propos

Dans cette thèse, on s'attache à caractériser les comportements mécaniques de deux milieux géophysiques distincts, à savoir la banquise Arctique et les milieux granulaires. La banquise est une fine pellicule de glace de quelques mètres d'épaisseur se formant à la surface des océans polaires. Un matériau granulaire peut être, dans sa globalité, défini comme un milieu discret, constitué de particules individualisées interagissant mécaniquement les unes avec les autres.

Ces deux matériaux comportent un point commun majeur : ce sont des matériaux constitués de particules solides frottantes pour lesquelles on observe un comportement mécanique de déformations irréversibles très riche. Nous verrons notamment que le comportement mécanique de ces matériaux varie entre un comportement fragile fortement intermittent, associé à une déformation qui se concentre le long de zones de cisaillement très marquées, et un comportement fluide, où le comportement moyen peut être assimilé à un écoulement visqueux.

Nous verrons aussi que ces contrastes de comportement dépendent fortement des échelles de temps et d'espace considérées, ce qui conditionne directement le cadre d'analyse adopté pour comprendre et décrire le comportement mécanique de ces objets géophysiques complexes. De ce fait, dans la littérature, deux approches distinctes sont communément adoptées pour l'étude des déformations irréversibles.

D'une part, un formalisme mathématique peut être développé en utilisant une approche continue de manière à rendre compte des différents processus de déformation. Généralement, les échelles d'analyse en temps et en espace adoptées dans ce cas sont supérieures aux échelles caractéristiques des hétérogénéités du milieu, de manière à permettre l'homogénéisation de son comportement. Ce cadre d'analyse sera adopté dans la première partie de cette thèse pour l'étude de la banquise Arctique. Une analyse spectrale focalisée sur la réponse de la banquise au forçage de Coriolis ainsi que le développement d'un modèle mécanique analytique continu nous permettra d'accéder et de quantifier, à partir de données cinématiques, la résistance mécanique interne de la banquise, et donc de caractériser sa rhéologie.

D'autre part, une approche alternative physique statistique vise à considérer la multiplicité des échelles de temps et d'espace en étudiant comment les marqueurs de rupture tels que les glissements inter grains dans les milieux granulaires ou la formation de "linear kinematic features" observés dans la banquise résultent de l'interaction d'événements plastiques "locaux" observés à diverses échelles. Nous adopterons ce formalisme en seconde partie de cette thèse pour l'étude de la "rupture" ou localisation de la déformation dans les milieux granulaires frottants sous compression. L'analyse de la réponse cinématique de ces matériaux modèles nous permettra de mieux comprendre les liens qui unissent les propriétés microscopiques au comportement mécanique macroscopique de ces assemblages. Nous verrons que l'on est capable de déterminer à

l'aide d'outils statistiques les échelles de temps et d'espace des hétérogénéités qui se développent dans la dynamique d'un assemblage granulaire soumis à chargement mécanique, ainsi que le rôle de ces dernières dans le comportement mécanique global, i.e. macroscopique, de l'assemblage.

Ce manuscrit est donc l'illustration de l'élaboration de deux approches distinctes, l'une mécanique des milieux continus, l'autre physique statistique, pour une meilleur compréhension du comportement mécanique des matériaux complexes tels que la banquise Arctique et les milieux granulaires. Nous verrons, en discutant l'approche alternative dans les introductions respectives de ces deux parties indépendantes, comment celles-ci sont complémentaires.

Première partie

L'amplitude des oscillations inertielles de banquise dans le bassin Arctique comme rhéomètre de la couverture de glace

Magnitude of sea ice inertial oscillations in the Arctic basin as a proxy of the mechanical strength of the ice cover

Chapitre 1

Introduction

Au regard de son rôle important dans le changement climatique, la banquise fait partie intégrante des modèles climatiques actuels. Une composante mécanique de cette dernière est intégrée de manière à reproduire sa cinématique (vitesse de dérive) et sa dynamique (accélération). Cependant, ces mêmes modèles climatiques sous estiment largement le déclin actuellement observé de la banquise, que ce soit à travers son extension spatiale (*Stroeve et al.*, 2007) ou bien ses propriétés cinématiques et dynamiques (*Rampal et al.*, 2011).

Parce que la banquise se comporte comme un milieu fragile, qui se déforme par un processus de fracturation, la relation entre variation globale de la masse de la couverture de glace et sa dynamique n'est pas triviale. Nous exposons dans cette introduction les différentes composantes et caractéristiques pouvant influencer la dynamique de la banquise de manière à introduire l'approche adoptée dans cette thèse, visant à identifier et quantifier les processus physiques qui, au premier ordre, sont à la source des changements observés dans la dynamique de la banquise. Nous proposerons ensuite, dans les deux chapitres de cette partie dédiée à la banquise, un cadre d'analyse de la réponse de la banquise Arctique au forçage de Coriolis. Nous verrons que l'on est capable, à travers cette analyse, de capturer les paramètres qui au premier ordre interviennent dans les changements dynamiques de la banquise observés actuellement aux grandes échelles de temps et d'espace. Le modèle analytique simple que nous proposons nous permettra notamment de conclure que des changements purement rhéologiques dans la couverture de glace sont necessaires pour expliquer les changements dynamiques observés actuellement.

1.1 Le déclin de la banquise observé à travers son comportement cinématique

Les changements dans la cinématique et la dynamique de la banquise à l'échelle pluriannuelle, i.e. de l'ordre de la trentaine d'années, ont pu être mis en évidence dans le cadre de la thèse de Pierre Rampal (*Rampal*, 2009) à partir du jeu de données IABP. Ce jeux de données consiste en des bouées dérivantes enchassées chaque année dans la banquise depuis 1979 jusqu'à nos jours. La Figure 1.1 montre les vitesses mensuelles moyennes de la banquise enregistrées par les bouées IABP de Janvier 1979 à Décembre 2007. Une augmentation significative des vitesses de glace est reportée sur les trente dernières années, correspondant en moyenne à 12% d'augmentation par décennie. Ce déclin ne se limite pas aux vitesses de dérive de la banquise, mais est aussi observé dans ses vitesses de déformation. La Figure 1.2 montre, sur

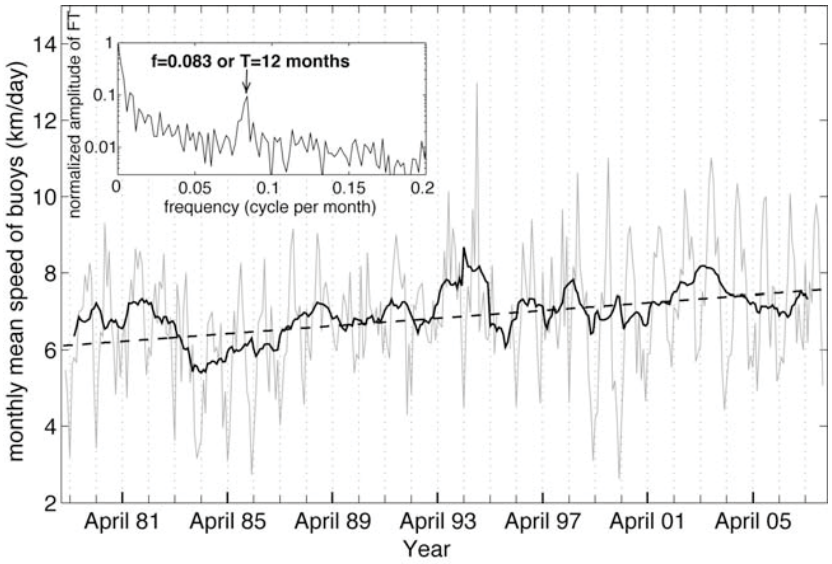

FIGURE 1.1 – Vitesses mensuelles moyennes de la banquise enregistrées par les bouées IABP de Janvier 1979 à Décembre 2007 (*Rampal et al.*, 2009a). Les vitesses sont calculées à partir d'un échantillonnage des positions de bouées réalisé à 12 heures et sont moyennées par mois (courbe grise). La courbe noire représente une moyenne glissante du signal réalisée sur 12 mois. La droite en pointillés montre une interpolation linéaire du signal, mettant en évidence une augmentation moyenne des vitesses de 12% par décennie au cours des 30 dernières années. L'encadré montre la transformation de Fourier du signal, mettant en évidence le cycle annuel des vitesses matérialisé par un pic à 12 mois.

la même période de temps, l'évolution pluri-annuelle d'un proxy de la vitesse de déformation $\sigma_{\dot{D}}$, calculé entre les déplacements relatifs de couples de bouées (*Rampal et al.*, 2009a). Une augmentation drastique d'environ 50% par décennie en hiver comme en été est observée sur $\sigma_{\dot{D}}$ durant la période 1979-2007. Lorsque la banquise se déplace et se déforme plus facilement au gré des vents et des courants océaniques, celle-ci va être expulsée en plus grande quantité vers l'extérieur du bassin Arctique à travers les détroits périphériques, majoritairement à travers le détroit du Fram (voir la Figure 2.1 pour la situation géographique). Ainsi, on s'attend à ce que l'augmentation des vitesses de dérive et des taux de déformation entraine une perte de masse globale de la banquise (*Rampal et al.*, 2011), et donc son déclin progressif.

La question posée suite à ces observations est la suivante : quels sont les facteurs et processus à l'origine de ces changements cinématiques observés ?

1.2 Les causes probables de ce déclin

Dans le contexte d'une hausse des températures atmosphériques liée au changement climatique, deux composantes distinctes du "système mécanique banquise" peuvent être à la source

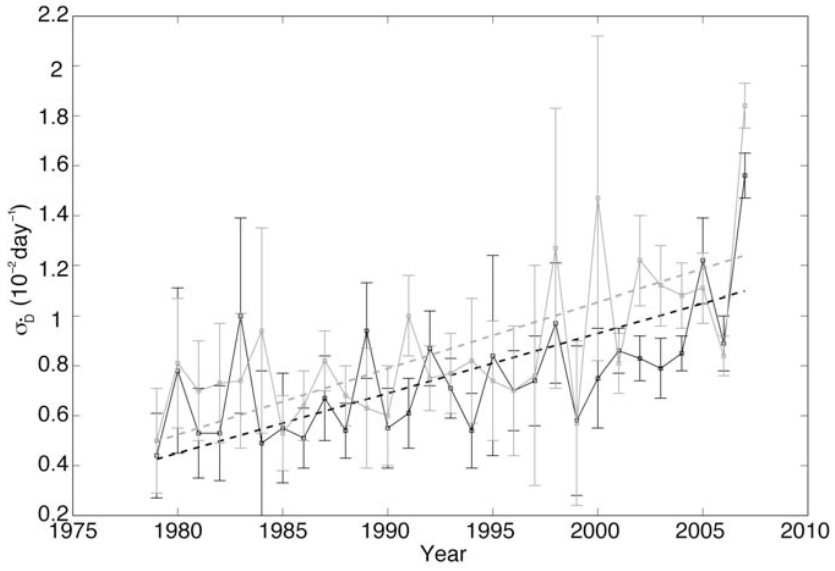

FIGURE 1.2 – Proxy de la vitesse de déformation moyenne de la banquise enregistrée par les bouées IABP en hiver et en été de Janvier 1979 à Décembre 2007 (*Rampal et al.*, 2009a). Ce proxy est calculé pour des échelles de temps inférieures à 1 jour et des échelles spatiales de l'ordre de 50 km à 500 km. La variation hivernale est mise en évidence par la courbe noire et la variation estivale par la courbe grise. Les barres d'erreur sont estimées à partir d'une méthode de bootstrap. Les fits linéaires montrent une augmentation par décennie de 51% en hiver et 52% en été.

des changements dans le comportement dynamique de la banquise observés précèdemment :

- soit le forçage mécanique extérieur appliqué à la banquise a subi des modifications au cours de ces dernières années, entrainant une modification de la réponse mécanique de cette dernière,
- soit les propriétés physiques intrinsèques à la banquise, intervenant dans sa résistance mécanique, ont subi des changements notables ces dernières années, induisant des changements dans sa réponse dynamique.

Les objectifs de notre étude sont donc, dans ce contexte, d'identifier les paramètres physiques pertinents pour caractériser la dynamique de la banquise, et surtout de déterminer quels paramètres doivent avoir varié et dans quelle mesure.

Les vents, et dans une moindre mesure les courants océaniques, sont considérés comme les deux forçages principaux agissant sur la dérive et la déformation de la banquise. Le couplage entre les interfaces océan/glace et atmosphère/glace est complexe et, jusqu'alors, seule la paramétrisation du frottement à ces interfaces permet de rendre compte du forçage extérieur appliqué à la couverture de glace. L'intensité du forçage océanique est très difficile à évaluer, du fait des observations très éparses dont on dispose sur les courants océaniques dans le bassin

Arctique. L'océan joue principalement le rôle d'amortisseur visqueux dans le déplacement de la banquise. Ainsi, les modifications pouvant affecter la cinématique du système banquise sont essentiellement des changements dans le frottement à l'interface océan-glace ou dans la résistance mécanique de la couche superficielle de l'océan. Il est par exemple connu qu'une augmentation de la fonte de glace peut affecter la stratification de la surface des océans, principalement en modifiant l'épaisseur de la couche de mélange (couche d'Ekman (*Ekman*, 1905)). Par conséquent, les flux de surface de l'océan et donc la dynamique de la glace peuvent en être affectés.

Le forçage atmosphérique, quant à lui, joue majoritairement le rôle de forçage mécanique vis à vis de la banquise, i.e. est responsable de la majeure partie de son advection. Nous disposons, principalement grâce aux bouées du programme IABP et aux réanalyses réalisées dans les modèles atmosphériques, d'observations beaucoup plus abondantes à son égard. L'index d'Oscillation Arctique (AO) donne une indication sur la force de la circulation au dessus de l'Arctique : durant les régimes de circulation anticycloniques (AO négative), la pression atmosphérique est plus importante, les vitesses de vent sont faibles, et la banquise est supposée être plus épaisse et avoir une plus grande extension spatiale. Durant les AO positives, les vitesses de vent sont plus importantes, ce qui produit des ouvertures de glaces, et donc un export facilité du bassin.

Concernant les propriétés physiques intrinsèques à la couverture de glace, on observe, ces dernières années :

- Une diminution des concentrations de glace. On définit la concentration de glace α comme la proportion, par unité de surface considérée, de surface occupée par la glace. Pour une surface totale S_T considérée, on a donc $\alpha = S_{glace}/S_T$, où S_{glace} est la surface occupée par la glace. La Figure 1.3 montre les concentrations (en %) de glace enregistrées au milieu de l'hiver 2011-2012 (Janvier 2012) et à la fin de l'été austral 2011 (Septembre 2011). La variation saisonnière dans les valeurs de concentration est évidente sur ces représentations. En hiver, le bassin est entièrement recouvert de glace (les concentrations sont proches de 1 partout dans le bassin) alors qu'en été, toute la zone périphérique du bassin, i.e. le long des côtes de la Russie et de l'Alaska, est pratiquement dépourvue de glace. Ainsi, l'essentiel de la glace pluri-annuelle, i.e. pérenne d'une année sur l'autre, se trouve dans la zone que l'on appelera la zone centrale, au Nord des côtes du Groenland. On distingue clairement, dans cette zone et en été, des variations spatiales de concentration, avec des zones bleues foncées à l'intérieur du pack. La Figure 1.4 représente la variation pluri-annuelle de l'étendue spatiale de la couverture de glace dans le bassin Arctique, sur la période Mai 1979 à Mai 2012. On observe une décroissance de 2.3% par décennie sur cette période de temps.
- Une diminution des épaisseurs de glace. La Figure 1.5 montre les variations spatio-temporelles des épaisseurs de glace observées par croisières sous marines et par le satellite ICEsat. On identifie clairement (Figure 1.5(c) et (f)) une répartition spatiale des épaisseurs similaire à la répartition spatiale des concentrations observée précèdemment. De fortes épaisseurs sont observées au large des côtes de Groenland et sont progressivement décroissantes

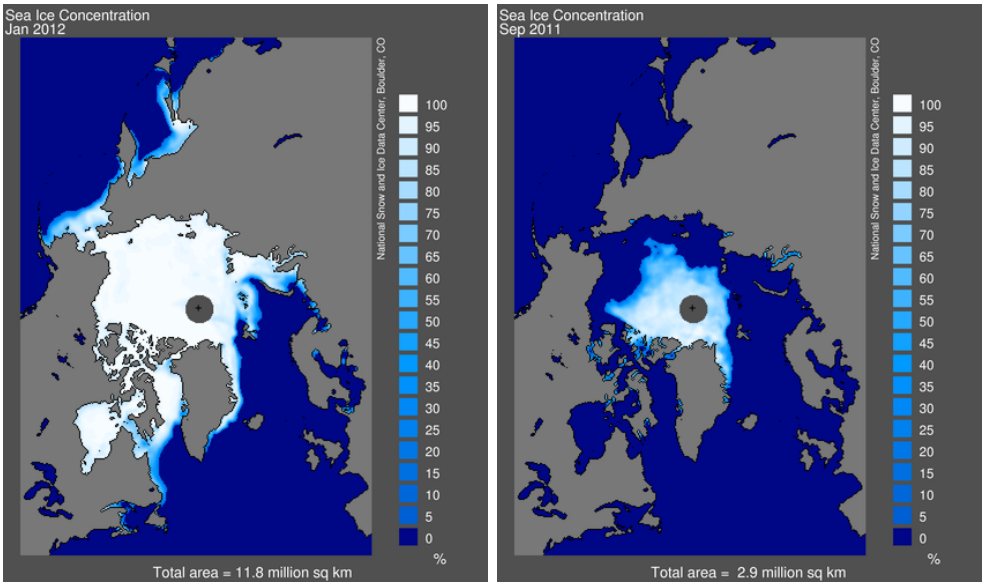

(a) (b)

FIGURE 1.3 – Observations satellites des concentrations de glace dans le bassin Arctique en (a) Janvier 2012 et (b) Septembre 2011. Source NSIDC : *http* : *//nsidc.org/cgi − bin/bist/bist.pl?config = seaice_index*

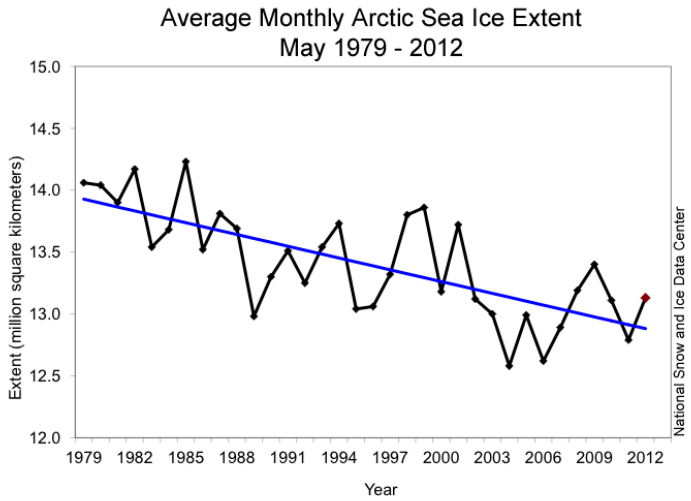

FIGURE 1.4 – Moyenne mensuelle de l'étendue spatiale, en millions de kilomètres carrés, de la banquise Arctique sur la période Mai 1979 à Mai 2012. Une interpolation linéaire (courbe bleu) montre une décroissance de 2.3% par décennie. Source NSIDC : *http* : *//nsidc.org/arcticseaicenews/*

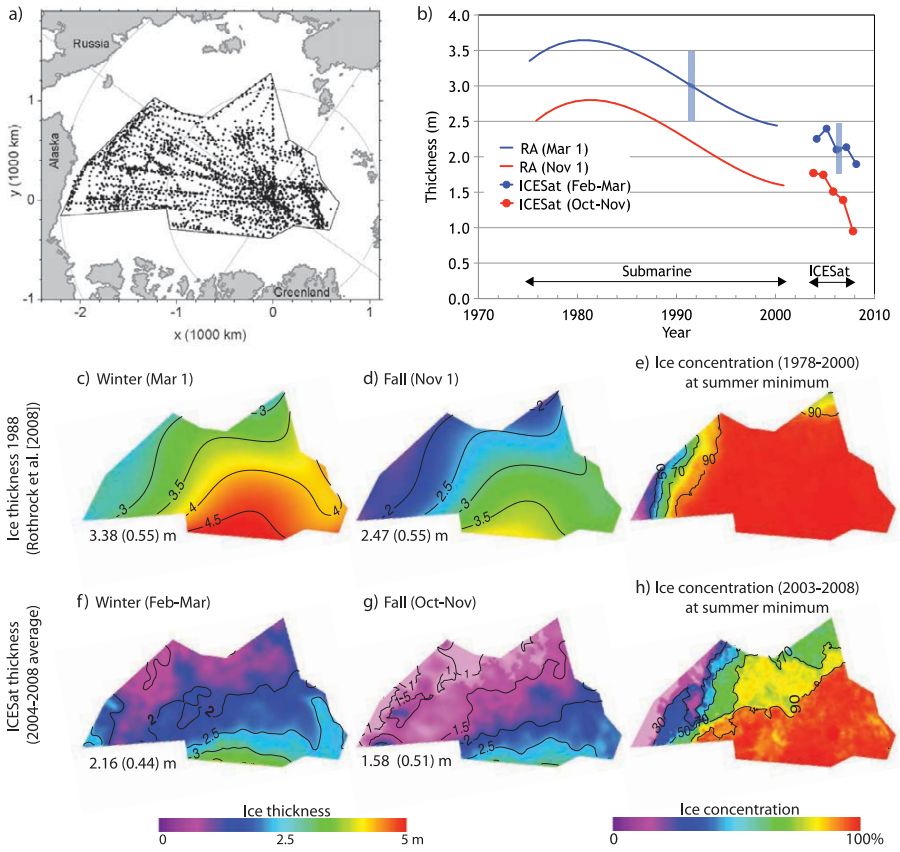

FIGURE 1.5 – Variation spatiale et temporelle des épaisseurs de glace observées par croisières sous marines et par le satellite ICEsat (*Kwok and Rothrock*, 2009). (a) Tracé des profils réalisés par les croisières sous marines. (b) Epaisseurs de glaces enregistrées en hiver (bleu) et en été (rouge) de 1975 à 2008. On remarque une variation annuelle et pluri-annuelle des épaisseurs de glace. (c,d) Variation spatiale des épaisseurs en hiver et au printemps 1988. (e) Valeur moyenne de la concentration au minimum d'été (1978-2000). (f,g) Variation spatiale moyenne des épaisseurs en hiver (Fev-Mar) et au printemps (Oct-Dec) depuis ICEsat (2003-2008). (h) Valeur moyenne de concentration au minimum d'été (2003-2008).

lorsque l'on se rapproche des côtes Canadiennes. De plus, la décroissance pluri-annuelle des épaisseurs est évidente sur la Figure 1.5(b) : les auteurs reportent une épaisseur moyenne mesurée de 3.64 m durant la saison d'hiver 1980 contre 1.89 durant la saison d'hiver 2009, c'est à dire une diminution d'épaisseur d'environ un facteur 2 entre 1980 et aujourd'hui.

1.3 La déformation de la banquise : un processus de fracturation

La Figure 1.6 montre une image satellite de la banquise Arctique prise le 6 Avril 1996, donc à la fin de l'hiver Arctique. Comme vu précédemment, à cette période de l'année, la couverture de glace est caractérisée par de fortes concentrations (proches de 1) et épaisseurs. Il est clair sur cette image que la couverture de glace n'est pas assimilable à une plaque uniforme et continue.

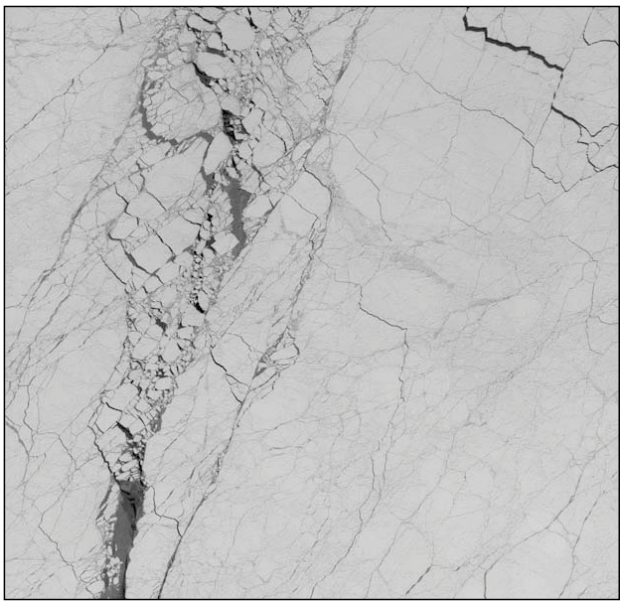

FIGURE 1.6 – Image satellite SPOT de la banquise Arctique en niveaux de gris prise le 6 Avril 1996, centrée autour de N 80°11' , W 108°33' et couvrant 59×59 km^2 (*Weiss and Marsan*, 2004).

On voit très distinctement, grâce aux différences d'albedo entre la glace épaisse et l'eau libre, des zones sombres matérialisant des fractures récemment ouvertes. Ces fractures forment des ensembles de chenaux pouvant atteindre plusieurs centaines de kilomètres. En regardant l'image plus en détails, on distingue, dans les zones de fracturation intense, des particules individualisées, appelées "floes" dans le jargon de la communauté banquise. A l'inverse, dans les zones de fracturation moindre, la banquise s'apparente plutôt à un milieu continu traversé par un réseau de fractures d'extension variable. En été et dans la zone marginale, bien que non montré ici, la fragmentation de la banquise Arctique en floes est plus fréquente. Dans ces conditions, le "milieu" banquise s'apparente à des particules flottantes individualisées interagissant les unes avec les autres à travers une dynamique de contacts, donc à un milieu granulaire. Ainsi, lorsque l'on étudie la banquise, on étudie un milieu dont les propriétés statiques sont en changement permanent, variant entre les deux cas extrêmes d'un milieu purement continu, de concentration égale à 1 et d'épaisseur importante, et un milieu totalement discontinu, dans lequel les floes dérivent librement (en 'free drift' en anglais) au gré des courants atmosphériques et marins.

Pour aller plus loin dans la nature des interactions glace-glace rencontrées dans la couverture de glace, la Figure 1.7 représente les états de contraintes enregistrés par un capteur de contraintes entre mi-Octobre 1997 et la fin Juin 1998, i.e. lors de l'hiver Arctique. Le capteur de contrainte détermine la contrainte agissant sur un point dans le plan horizontal de la couverture de glace en mesurant les changements de déformation radiale d'un anneau cylindrique. Ainsi, les contraintes principales σ_1 et σ_2 peuvent être calculées. Dans le diagramme des invariants de contrainte

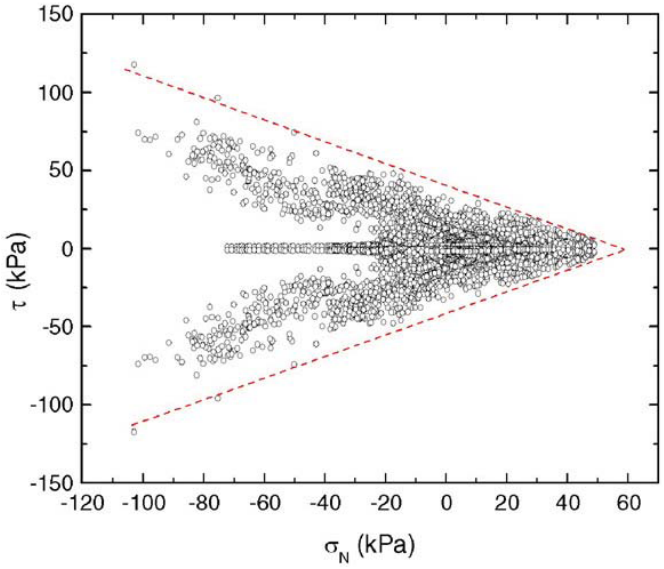

FIGURE 1.7 – Etats de contrainte, mesurés par capteur de contraintes in-situ, recensés dans la banquise. Ces états de contrainte sont ici répertoriés dans un graphique contrainte déviatorique τ en fonction de la contrainte normale σ_N. Ces données ont été enregistrées toutes les heures au capteur "Baltimore" de mi-Octobre 1997 à fin Juin 1998, i.e. lors de l'hiver Arctique (*Weiss et al.*, 2007).

τ versus σ_N, où τ est le cisaillement et σ_N la pression moyenne, on peut voir que les états de contraintes résident dans une enveloppe pouvant être délimitée par la limite de Coulomb $|\tau| = |\tau_0| - \mu\sigma_N$, avec $|\tau_0| = 40$ kPa et $\mu = 0.7$, $|\tau_0|$ étant la valeur de la cohésion et μ étant le coefficient de friction interne de la banquise. A partir de ces observations, on peut considérer que la banquise s'apparente à un milieu solide frottant où la fracturation au sens de Coulomb est le mécanisme majeur de déformation.

Par conséquent, les changements de concentration et d'épaisseur de la couverture de glace dûs à la fonte vont avoir des effets multiples sur le comportement mécanique de la banquise. Premièrement, de manière directe, on s'attend à ce qu'une glace en moyenne plus fine et plus faiblement concentrée se déplace plus librement aux gré des vents et courants marins. Cependant, parce que le processus de fracturation est un processus de déformation fortement non linéaire, l'influence des changements de concentration et d'épaisseur sur la dynamique de la banquise n'est pas triviale. En effet, on s'attend à ce que la résistance mécanique de la banquise puisse être conditionnée par la structure du réseau de fractures traversant le milieu en hiver ou encore par l'arrangement spatial entre les floes individualisés en été.

Pour illustrer ce propos, on peut considérer l'exemple simple d'un assemblage granulaire modèle, que l'on considère dans la deuxième partie de cette thèse. Le cas de figure imagé et très idéalisé ici, représente donc une banquise consistant en un assemblage de floes (i.e. parti-

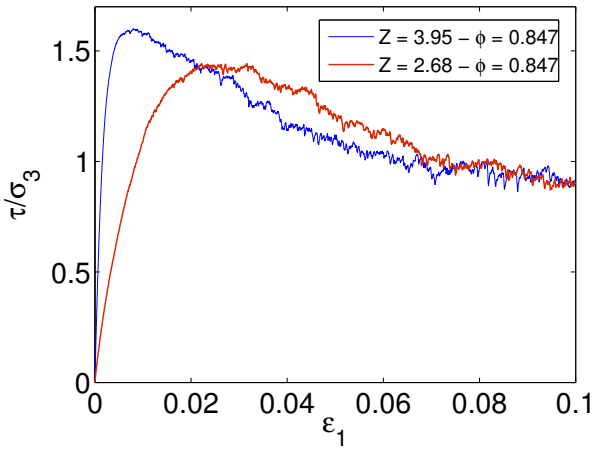

FIGURE 1.8 – Réponse macroscopique contrainte déviatorique τ/σ_3 versus déformation axiale ϵ_1 de deux échantillons granulaires de même densité d'empilement $\phi = 0.847$ initiale pésentant des nombres de coordination initiaux Z différents, égaux à 3.95 pour la courbe bleue et 2.68 pour la courbe rouge.

cules de glace individualisées) interagissant avec une limite en frottement bornée par le critère de Coulomb, ce qui, au premier ordre, correspond à l'essentiel de la physique de la banquise décrite précèdemment. On considère deux échantillons identiques du point de vue du nombre de grains (10000 grains), de la distribution de tailles de grains (uniforme d'un ratio 3 entre la surface de la plus grande particule et celle de la plus petite), de la densité ϕ (jouant le rôle de la concentration α pour faire le parallèle avec la banquise, ici $\phi = 0.847$) et de la rigidité des grains ($\kappa = 1000$, voir deuxième partie). La valeur de friction considérée est fixée à $\mu = 0.5$. Aucune cohésion n'est considérée ici. La seule différence entre ces échantillons initiaux est le nombre de coordination Z, i.e. le nombre de contacts moyen par grains, égal à 3.95 dans un cas (proche du cas isostatique pour des assemblages de grains circulaires 2D sans frottement) et 2.68 dans l'autre cas, donc très inférieur. Les méthodes de préparation de ces échantillons ainsi que les détails du code utilisé et de la configuration de chargement sont explicités dans la deuxième partie de cette thèse. La Figure 1.8 montre la courbe de chargement que l'on obtient lorsque l'on réalise un essai de compression sur ces échantillons. On voit clairement que la rigidité initiale macroscopique de l'assemblage de ces particules, donnée par la pente de la courbe contrainte déformation observée avant le pic de contrainte, est différente. Ainsi, à porosité identique, plus le nombre de coordination entre les grains est faible, plus les réarrangements entre les grains sont facilités dans la phase initiale du chargement et donc plus la rigidité initale de l'assemblage est faible. Ainsi, pour un même forçage extérieur, i.e. ici une même valeur de contrainte appliquée, la déformation de l'ensemble est plus importante pour l'échantillon à faible nombre de coordination. Autrement dit, pour une même valeur de densité, la rigidité macroscopique équivalente d'un assemblage granulaire est largement supérieure pour un échantillon fortement coordonné que pour un échantillon faiblement coordonné. Ce point est spécifiquement traité et discuté dans

l'étude menée par *Agnolin and J.N. Roux* (2007).

Cet exemple simple illustre un effet indirect potentiel de la diminution d'épaisseur et de concentration de la couverture de glace. On peut en effet imaginer que, dans la banquise, la disposition spatiale des chenaux, l'arrangement spatial des floes, le nombre de contacts par floes, etc... soient drastiquement conditionnés par le mécanisme de fracturation, engendrant ainsi des modifications considérables et non linéaires de la rhéologie de la banquise. C'est donc précisemment le rôle des changements dans les propriétés intrinsèques de la banquise, où l'importance relative des effets directs et indirects des variations d'épaisseur et de concentration sur la rhéologie de la banquise sont potentiellement à considérer, ainsi que les changements dans les différents forçages extérieurs (vents, courants océaniques, friction aux limites) sur les changements dynamiques de la banquise, que nous nous proposons de quantifier dans cette première partie de thèse.

Dans le contexte plus global du déclin de la banquise, les changements de rhéologie de la banquise renforcent la boucle de rétroaction thermodynamique liée aux variations d'albedo (Figure 1.9) : une couverture de glace qui s'affaiblit mécaniquement se fracture plus facilement, augmentant ainsi sa proportion d'eau libre, donc l'absorption d'énergie solaire par la banquise

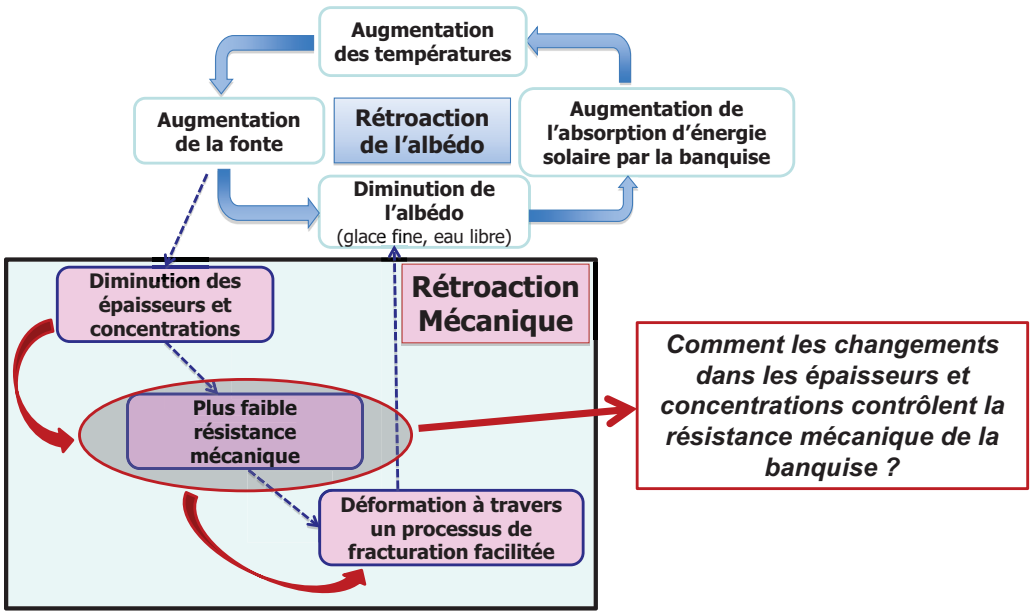

FIGURE 1.9 – Boucle de rétroaction de l'albédo modifiée, montrant l'interaction possible entre les processus thermodynamiques (en bleu) et mécaniques (en rouge) (*Rampal*, 2009).

et donc sa fonte.

Ainsi, nous nous proposons de développer une méthode visant à étudier comment la résistance mécanique de la banquise varie dans l'espace et dans le temps, connaissant ses variations d'épaisseur, de concentration et sa dynamique. Comme dans tout travail de caractérisation d'une rhéologie, il est nécessaire, dans la mise en place du problème, de définir les échelles caractéristiques du comportement mécanique de la banquise à partir desquelles une moyennisation peut être réalisée.

1.4 Identification des échelles caractéristiques pertinentes de temps et d'espace

Comme vu précèdemment, la fracturation au sens de Coulomb est le mécanisme majeur de déformation dans la couverture de glace Arctique. Ainsi, c'est une déformation à seuil, donc fortement non linéaire, qui prend place dans un milieu élastique très hétérogène. La dissipation locale d'énergie mécanique par un processus de friction solide (cf Figure 1.7) génère des redistributions de contraintes à grande distance, associée à une fracturation multi-échelles, une localisation forte de la déformation et une intermittence spatiale et temporelle. Cette physique sous jacente présente donc les mêmes ingrédients que celle que l'on étudiera dans la deuxième partie de cette thèse, dans le cas des milieux granulaires frottants. Le problème majeur lorsque l'on veut caractériser la rhéologie de ce type de milieu est l'identification des échelles caractéristiques de temps et d'espace.

La Figure 1.10(a) montre un champ de déformation cisaillante de la banquise Arctique à l'échelle du bassin obtenu sur une période d'observation de 3 jours. Ce champ de déformation est calculé à partir du système "RADARSAT Geophysical Processor System" (RGPS) ($www-radar.jpl.nasa.gov/rgps/radarsat.html$), qui identifie et suit, à partir d'images satellites, environ 40000 points à la surface de la banquise en utilisant la correlation d'images. Partant d'une grille régulière initiale de 10 km de résolution, la déformation de cette grille permet d'obtenir les vitesses des noeuds et donc les gradients de vitesse spatiaux. Qualitativement, les caractéristiques d'une déformation fragile sont évidentes sur cette figure : on identifie des zones de localisation intense de la déformation qui se traduisent par des fractures materialisées par de fortes valeurs de déformation cisaillante, associées, bien que non montré ici, à de la dilatation. Ces zones qui concentrent la déformation sont, dans la communauté banquise, appelées "linear kinematic features", et pourraient être plus généralement dénommées failles.

L'étude réalisée par *Marsan et al.* (2004) a consisté à évaluer de manière quantitative la structure spatiale de ce champ de déformation. Par une analyse de décimation réalisée sur la déformation totale, que l'on utilisera et détaillera dans la deuxième partie de cette thèse, *Mar-*

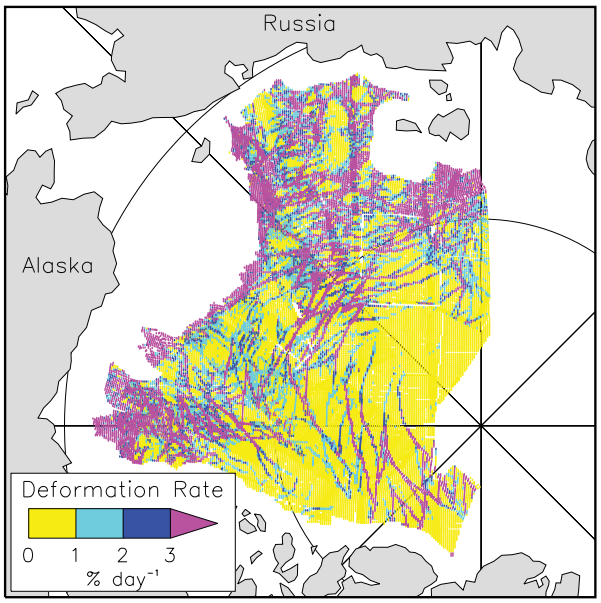

(a)

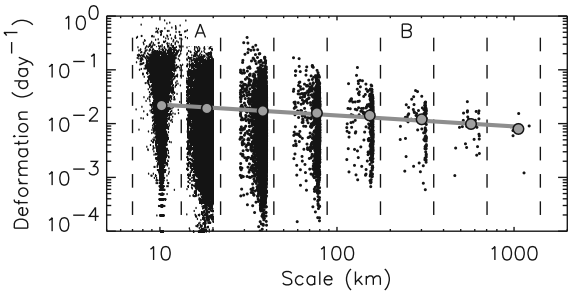

(b)

FIGURE 1.10 – Analyse multi-échelles du champ de déformation totale de la banquise Arctique calculé sur un intervalle de temps de 3 jours (*Marsan et al.*, 2004). (a) Champs de taux déformation totale enregistré par le RGPS le 6 Novembre 1997 à partir de 42571 cellules RGPS. (b) Dependance spatiale du taux de déformation totale.

san et al. (2004) montrent que la valeur moyenne de l'invariant de déformation dépend, en loi de puissance, de l'échelle considérée pour la calculer (Figure 1.10(b)). Cette observation montre qu'il n'y a pas, à cette échelle de temps de 3 jours, d'échelle caractéristique associée au champ de déformation observé. En d'autres termes, on ne peut définir aucune longueur ou espacement caractéristiques dans les "linear kinematic features" observées. Par conséquent, dans une démarche d'étude de la rhéologie de la banquise, il n'est pas possible, à cette échelle de temps, de définir un volume élémentaire représentatif (VER) à partir duquel des opérations de moyennage ou homogéneisation nous permettraient d'évaluer les comportements mécaniques de la banquise à

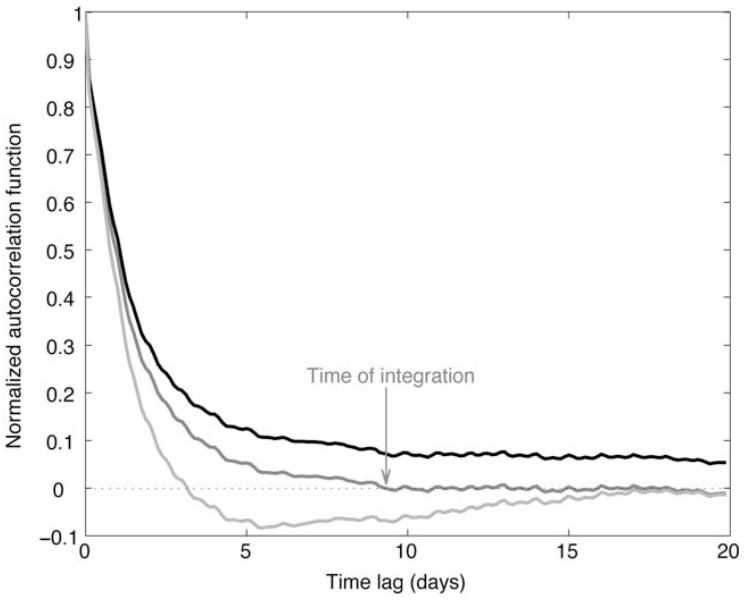

FIGURE 1.11 – Fonctions normalisées d'autocorrélation des fluctuations de vitesses (*Rampal et al.*, 2009b). Les vitesses fluctuantes sont calculées après la soustraction du champ moyen estimé au champ de vitesse totale. Le champ moyen est estimé en réalisant différentes echelles de moyennisation spatiale et temporelle : pas de soustraction de champ moyen (en noir), soustraction du champ moyen calculé à l'échelle d'espace $L = 50$ km et temporelle $T = 40$ jours (en gris clair), et pour $L = 400$ km et $T = 160$ jours (en gris foncé). On peut définir un temps de corrélation pour les 2 derniers cas comme le temps où l'on rencontre la valeur zéro pour la première fois.

l'échelle du bassin Arctique. Ainsi, pour décrire en moyenne de manière simple et analytique la rhéologie de la banquise, il convient de regarder si cette invariance d'échelles spatiale est conservée lorsque l'on considère un temps d'intégration des déplacements plus important.

L'analyse des propriétés cinématiques de la banquise réalisée par *Rampal et al.* (2009b) permet de répondre à cette question. Ces travaux ont consisté en l'analyse, à partir des données de bouées IABP, des champs de déplacements moyens et fluctuants de la banquise. Au même titre que dans les milieux granulaires (*Radjai and Roux*, 2002), la banquise Arctique présente certaines des caractéristiques d'un fluide turbulent : même régime de diffusion et propriétés multi-fractales des vitesses. La Figure 1.11 montre l'autocorrélation temporelle des fluctuations de vitesses hivernales de la banquise, ces dernières ayant été calculées en soustrayant différents champs moyens, i.e. calculées à différentes échelles de moyennisation spatiale et temporelle, au champ de vitesse échantillonné par les bouées. Il apparait clairement, sur cette figure, que l'on peut définir un temps de corrélation dans le champ de déplacement fluctuant uniquement lorsque l'on soustrait un champ moyen calculé à l'échelle de $L_{win} = 400$ km et $T_{win} = 160$ jours, donc approximativement toute la saison d'hiver dans les régions polaires. En effet, lorsque

l'on considère des échelles spatio-temporelles plus faibles pour construire ce champ moyen, on observe une autocorrélation négative du champ fluctuant, provenant du fait qu'une variabilité spatiale et temporelle est inclue dans le champ moyen, biaisant donc de cette manière la fonction d'autocorrelation. En été, les échelles appropriées de moyennage sont $L_{sum} = 200$ km et $T_{sum} = 80$ jours, donc approximativement toute la saison d'été dans les régions polaires.

Ainsi, pour des échelles de temps de l'ordre de la saison et d'espace supérieures à 400 km en hiver et 200 km en été, la rhéologie de la banquise peut être caractérisée en moyenne. C'est ce que nous nous proposons de faire par la suite.

1.5 Comment caractériser, de 1979 à aujourd'hui et à l'échelle du bassin, la rhéologie de la couverture de glace Arctique ?

La résistance mécanique globale de la banquise à un forçage extérieur va donc être fonction d'une part de son épaisseur et sa concentration, et d'autre part de ce que l'on va nommer, dans le reste de cette étude banquise, sa friction effective. Cette friction effective correspond à "une friction macroscopique équivalente", i.e. une friction mécanique aux grandes échelles de temps et d'espace. Ce sont les changements potentiels dans la valeur de cette friction effective que l'on souhaite caractériser dans cette étude, de manière à répondre aux questions suivantes : les variations d'épaisseur et de concentration ainsi que les changements potentiels dans les forçages extérieurs suffisent ils à expliquer les changements dynamiques intervenant dans la banquise ? Ou bien des effets indirects induits par des variations de concentration et d'épaisseur discutés précédemment, comme des changements dans l'arrangement spatial des réseaux de fractures, des floes, etc..., jouent un rôle prépondérant ? Si oui, comment peut-on intégrer ces modifications dans un modèle simple pour reproduire la complexité rhéologique de la banquise ?

Pour répondre à ces questions, il convient d'analyser la réponse mécanique de la banquise à une perturbation locale connue, donc à un forçage extérieur bien identifié. Opérant à une fréquence caractéristique f_0 de l'ordre de 2 cycles par jour dans l'Arctique, le forçage de Coriolis apparait comme pertinent. Ainsi, l'idée de notre étude de la rhéologie de la banquise consiste à analyser la réponse dynamique de la banquise au forçage spécifique de Coriolis de manière à caractériser les processus de friction interne opérant dans la couverture de glace.

Dans une première partie, nous examinerons, à partir d'une analyse fréquencielle appliquée aux trajectoires de bouées IABP, la réponse mécanique de la banquise au forçage inertiel. Nous proposons dans cette partie une mesure adimensionnée de l'amplitude des oscillations inertielles, afin de quantifier leurs variations spatio-temporelles.

Dans une seconde partie, nous établirons un modèle analytique couplé océan-glace, modélisant les processus de friction à grande échelle comme de la friction fluide. Nous verrons que ce modèle

permet de reproduire le contenu fréquenciel de la dérive des bouées IABP, et donc d'apporter des informations sur les changements dans les processus de friction intervenant dans la banquise.

Chapitre 2

Les oscillations inertielles de banquise dans le bassin Arctique

Sea ice inertial oscillations in the Arctic basin

D'après :

Gimbert, F., D. Marsan, J. Weiss, N.C. Jourdain, and B. Barnier (2012), Sea ice inertial oscillations in the Arctic basin, *The Cryosph.*, *6*, 1187-1201, doi :10.5194/tc-6-1187-2012, 2012.

Abstract

An original method to quantify the amplitude of inertial motion of oceanic and ice drifters, through the introduction of a non-dimensional parameter M defined from a spectral analysis, is presented. A strong seasonal dependence of the magnitude of sea ice inertial oscillations is revealed, in agreement with the corresponding annual cycles of sea ice extent, concentration, thickness, advection velocity, and deformation rates. The spatial pattern of the magnitude of the sea ice inertial oscillations over the Arctic basin is also in agreement with the sea ice thickness and concentration patterns. This argues for a strong link between the magnitude of inertial motion on one hand, the dissipation of energy through mechanical processes, and the cohesiveness of the cover on the other hand. Finally, a significant multi-annual evolution towards greater magnitudes of inertial oscillations in recent years, in both summer and winter, is reported, thus concomitant with reduced sea ice thickness, concentration and spatial extent.

2.1 Introduction

The spectacular evolution of the Arctic sea ice cover over the last few decades is not restricted to the shrinking of the ice extent (*Comiso et al.*, 2008; *Stroeve et al.*, 2008), its thinning (*Rothrock et al.*, 2008; *Kwok and Rothrock*, 2009), or, consequently, a continued decline of the ice volume (*Lindsay et al.*, 2009). Kinematics is affected as well, and its evolution plays a central role in the changes currently taking place in the Arctic Ocean. As observed from buoy drift data, the sea ice mean speed over the Arctic increased at a rate of 9 % per decade from 1979 to 2007, whereas the mean deformation rate increased by more than 50 % per decade over the same period (*Rampal et al.*, 2009a). These two aspects of recent sea ice evolution, i.e. strong decline in terms of ice extent and thickness, and accelerated kinematics, are strongly coupled within the albedo feedback loop. Increasing deformation means increasing fracturing, hence more lead opening and a decreasing albedo (*Zhang et al.*, 2000). As a result, ocean warming, in turn, favours sea ice thinning in summer and delays refreezing in early winter, i.e. strengthens sea ice decline. This thinning should decrease the mechanical strength, therefore allowing even more fracturing, hence larger speed and deformation. A consequence is the acceleration of the export of sea ice through Fram Strait, with a significant impact on sea ice mass balance (*Rampal et al.*, 2009a, 2011; *Haas et al.*, 2008), and ice age (*Nghiem et al.*, 2007). Moreover, sea ice mechanical weakening decreases the likelihood of arch formation along Nares Strait, therefore allowing old, thick ice to be exported through this strait (*Kwok et al.*, 2010).

The principle of a strong interaction between the ice state (concentration, thickness), on one hand, and the mechanical behaviour of the cover and its strength on the other hand, although rather intuitive, needs however to be quantified more precisely. Beyond the trivial reduction of strength in proportion to the thinning of an ice plate, one can expect a more complex effect of the compactness of the ice cover on its average strength, e.g. as in granular media (*Rajchenbach*, 2000; *Aranson and Tsimring*, 2006). This is the combination of these two effects that we aim to explore here. Ideally, one would like to check whether the sea-ice cover responds differently from year to year to the same mechanical forcing. We here propose to tackle this problem by analysing its response, as deduced from ice drifter trajectories, to the specific inertial forcing. The effect of the Coriolis force on geophysical fluids dynamics has been studied for more than a century. Interestingly, the first studies of oceanic inertial oscillations (*Ekman*, 1905) were prompted by the observations of Nansen, made during the Fram's journey along the Transpolar drift, that sea ice was moving with a 20°–40° angle to the right of the wind direction (*Nansen*, 1902). Indeed, as the Coriolis force acts perpendicularly to the particle velocity, it induces a deviation of the trajectory to the right in the Northern Hemisphere. This deviation generates inertial oscillations, characterized by a frequency of

$$f_0 = 2\sin\phi \quad \text{cycles} \quad \text{day}^{-1} \tag{2.1}$$

where ϕ is the latitude, i.e. close to a semi-diurnal frequency ($2\,\text{cycles}\,\text{day}^{-1}$) in the Arctic.

Within the ice-free ocean, these oscillations are triggered by wind forcing events such as storms or moving fronts (*Price*, 1983; *Gill*, 1984; *D'Asaro et al.*, 1995a). These events generate inertial oscillations within a few hours, which then decrease progressively with a characteristic time scale of a few days (*Park et al.*, 2009). This damping is essentially due to the internal friction within the Ekman ocean layer, as well as to the radiation of inertial waves toward the thermocline.

On ice-covered oceans, we expect other processes to strengthen the damping of these oscillations, such as friction at the ice/ocean interface or, more importantly, the internal ice stresses resulting from solid mechanical interactions within the ice cover such as fracturing, friction between adjacent floes and shearing of leads, or crushing during convergent deformation and ridge formation, i.e. the "ice internal friction" (*Lepparanta*, 2004; *Colony and Thorndike*, 1980). These terms are apparent in the momentum balance of sea ice dynamics :

$$\frac{D\vec{U}_\mathrm{i}}{Dt} + (f_0 \Omega \vec{k} \times \vec{U}_\mathrm{i}) = \frac{1}{\rho_\mathrm{i} h_\mathrm{i}} \left(\vec{\nabla} \cdot \vec{\sigma} + \vec{\tau}_\mathrm{a} + \vec{\tau}_\mathrm{w} \right) \tag{2.2}$$

where $D/Dt = \partial/\partial t + \vec{U}_\mathrm{i}$, Δ is the Lagrangian time derivative, ρ_i the ice density, h_i the ice thickness, $\vec{U}_\mathrm{i}$ the ice velocity vector expressed in Cartesian coordinates, $\vec{\sigma}$ the internal stress tensor, $\vec{\tau}_\mathrm{a}$ and $\vec{\tau}_\mathrm{w}$ respectively the wind and oceanic "stresses" (forces per unit ice area). The last term on the left hand side of Eq. (2.2) is the Coriolis force, with f_0 the inertial oscillation frequency, expressed in cycles day^{-1}, $\Omega = 2\pi \,/\, 24\,\mathrm{rad\,h^{-1}} = 7 \times 10^{-5}\,\mathrm{rad\,s^{-1}}$ the Earth rotation velocity and $\vec{k}$ a unit vector aligned along the South to North Pole axis.

Here, we neglect the contribution of the sea surface tilt to the momentum balance, which is small compared to the other contributions (*Steele et al.*, 1997). In Eq. (2.2), the wind forcing $\vec{\tau}_\mathrm{a}$ excites the oscillations, whereas the oceanic drag $\vec{\tau}_\mathrm{w}$ and the internal stress term $\vec{\nabla} \cdot \vec{\sigma}$ damp those oscillations (*Colony and Thorndike*, 1980).

We expect the response of sea ice to the Coriolis force in the frequency domain to be within two following extremes. A buoy moving in free drift, i.e. fixed on an ice floe that drifts according to wind and ocean currents without any mechanical interaction with other ice floes (the term $\vec{\nabla} \cdot \vec{\sigma}$ is then negligible compared to the others), is expected, in first order approximation, to follow the oceanic fluid parcel and thus to oscillate in a similar way, although another source of damping of the oscillations might come from the friction between the ice bottom and the ocean surface (*Lepparanta et al.*, 2012). In contrast, on a compact ice cover experiencing strong internal stresses, the corresponding contribution $\vec{\nabla} \cdot \vec{\sigma}$ will dominate the other terms in Eq. (2.2) so that the oscillations are immediately damped out and thus become undetectable.

To measure the amplitude of the inertial oscillations of the ice drifters is therefore to estimate the level of mechanical dissipation within the ice cover, and therefore its degree of cohesiveness. As such, its evolution and its spatial pattern can highlight the changes in ice conditions and ice cover mechanical behaviour. Internal ice stress measurements have been performed directly from in situ sensors (*Richter-Menge and Elder*, 1998; *Richter-Menge et al.*, 2002). The seasonal variations of these local stress measurements have shown an increase of ice-motion induced stresses as the winter season progresses and the cohesiveness/compactness of the ice cover develops (*Richter-Menge and Elder*, 1998). While of major importance to analyze sea ice mechanical behaviour and rheology (*Weiss et al.*, 2007), these measurements are however limited to the local scale and do not carry any information about a possible large-scale, long-term trend of the mechanical state of the cover. Our approach is thus complementary, as it allows a much better sampling, both in time and space.

The idea to relate the amplitude of the inertial oscillations to the degree of consolidation of the ice cover was already formulated by *McPhee* (1978) as well as *Colony and Thorndike* (1980). The latter studied the role of the mechanical behaviour of the ice on the coherency of inertial motion between different buoys, an approach different from what is described below as we analyze trajectories individually. More recently, from buoys trajectories near the Antarctic Peninsula, *Geiger and Perovich* (2008) observed an increase of inertial motion related to the degradation of the ice pack during the spring breakup. *Hutchings et al.* (2012) also discussed the link between the degree of fragmentation of the ice cover, the mechanical dissipation of energy, and the amplitude of inertial motion. These last authors based their discussion on the analysis of strain-rate records obtained from a dense array of buoys in the Weddell Sea, i.e. they did not analyze individual trajectories. However, although sea ice inertial oscillations have been studied by several others authors (*Colony and Thorndike*, 1980; *McPhee*, 1978; *Hunkins*, 1967; *Lammert et al.*, 2009), including recently on ice strain-rate records (*Kwok et al.*, 2003), this is the first time that a systematic analysis is performed at the Arctic Basin and multidecadal scales.

In this paper, we propose a method to quantify the magnitude of inertial oscillations from Lagrangian (buoys) trajectories (Sect. 2.3). We then apply this methodology to the International Arctic Buoy Program (IABP) dataset covering 30 yr of data in the Arctic Ocean (Sect. 2.4). As shown below, this analysis is in full agreement with the above expectations : inertial oscillations are very weak or absent in a highly cohesive ice cover, such as in winter within the central

Arctic, but are well developed in summer at the periphery of the basin, i.e. in regions of less concentrated, loose ice. In addition, a significant strengthening (on average) of these oscillations is observed, suggesting a mechanical weakening of the Arctic sea ice cover. This is confirmed in *Gimbert et al.* (2012b), where a simple ocean-sea ice coupled dynamical model explains these seasonal, geographical and multi-annual variations of inertial oscillation magnitude in term of changes within sea ice internal mechanical properties, through an associating decrease of sea ice internal friction in recent years.

2.2 Dataset

2.2.1 IABP buoy dataset

The sea ice drifting buoy dataset, provided by the International Arctic Buoy Program (IABP), consists of approximately 650 buoy tracks recorded from January 1979 to December 2008. These ice drifters are dropped every year at the end of winter, mostly in April, and drift according to the ice motion. Their positions are tracked by GPS receivers or Argos transmitters with a position uncertainty of the order of 100 m and 300 m, respectively. The raw buoy positions are irregularly sampled through time. Thus, in order to get a regular sampling, the buoy positions provided by the IABP result from a cubic interpolation of the raw positions with a 3 h time re-sampling (see the IABP documentation at *http ://iabp.apl.washington.edu/data.html* for further details). This interpolation procedure acts as a low-pass filter, thus most likely reducing the position error around 100 m or below (*Lindsay and Stern*, 2003). Figure 2.1 shows all the buoy tracks on a polar stereographic map, where buoy locations are defined as $x\vec{e_1} + y\vec{e_2}$, where $\vec{e_1}$ and $\vec{e_2}$ are two orthogonal unit vectors with $\vec{e_1}$ being along the Greenwich meridian and $(x, y) = (0, 0)$ at North Pole.

2.2.2 Oceanic buoy dataset

In order to get an example of the amplitude of inertial oscillations in the absence of sea ice, i.e. when the damping of oscillations is mainly due to the internal friction of the Ekman layer without contribution from internal ice stresses, we consider trajectories of buoys drifting in the North Atlantic, along the northern Spanish coast (Figure 2.2). Of course, in this region, the winds and ocean currents are expected to significantly differ from the ones of Arctic regions. However, this dataset will allow us to evidence similar observations than the one obtained considering the IABP buoys dataset and to show that our computations we perform in the Arctic basin in the presence of ice are, at least qualitatively, in agreement with a reference case of an ice free ocean surface.

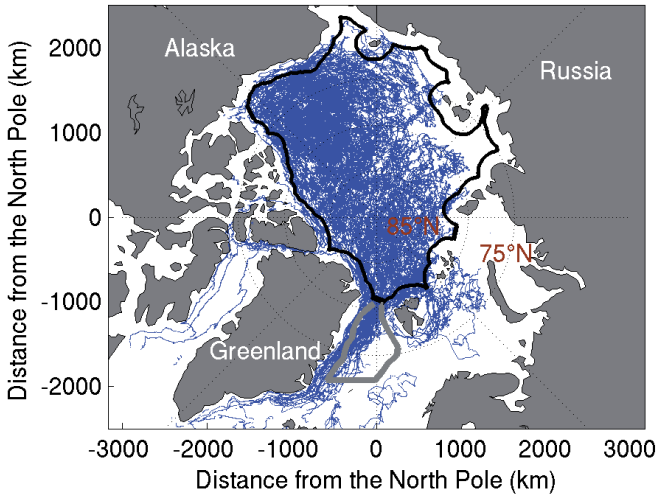

FIGURE 2.1 – Map of the Arctic Basin showing the buoy trajectories of the IABP dataset. The positions are sampled every 3 h from January 1979 to December 2008 and plotted following a stereographic projection centered on the North Pole. The Laptev Sea is poorly covered by this dataset. The thick solid black and grey lines define the central Arctic Basin and the Fram Strait region, respectively.

This oceanic buoy dataset, provided by the SHOM (Service Hydrographique et Oceanographique de la Marine), consists of 4 buoy tracks (B239, B241, B242, B245). These buoys were deployed between 6 and 11 December 2006 in the framework of the CONtinental GAScogne (CONGAS) project (*Le Cann and Serpette*, 2009). The buoy positions were tracked by GPS receivers with a position uncertainty of the order of several tens of meters. The temporal sampling was regular, equal to 1 h. Thus, the buoy positions do not result from any re-sampling or re-interpolation. Buoys B239 and B245 operated during 1 yr, whereas buoys B241 and B242 operated only 1 month. For each latitude (ϕ)–longitude (φ) buoy position, we define the orthogonal base ($\vec{e_1'}$, $\vec{e_2'}$) of this coordinate system as $\vec{x}_{(\phi,\varphi)} = x\vec{e_1'} + y\vec{e_2'}$ using a Lambert projection centered in the coordinates $\phi = 43°$ and $\varphi = 6°$.

2.3 Quantifying the magnitude of inertial oscillations

2.3.1 Observations

We analyze here several cases of inertial oscillations observed over an ice-free ocean or over sea ice.

Figure 2.3a shows 1 month of the trajectory of the oceanic buoy B245. Inertial oscillations are noticeable during this time period : being in the Northern Hemisphere, the buoy drift trajectory exhibits cycloids in the clockwise direction. The intermittent character of inertial oscillations is also clearly visible. Periods of strong inertial oscillations, marked by cycloidal loops (red boxes in Figure 2.3a), might have been triggered by storms. Following these periods, the oscillations are

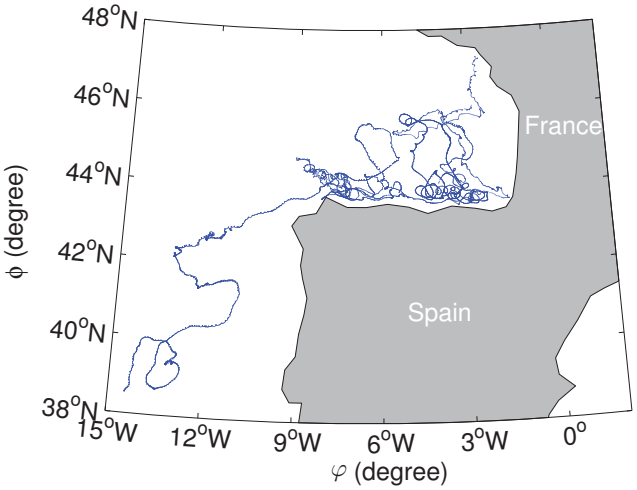

FIGURE 2.2 – Map of the Atlantic Ocean showing the oceanic buoy trajectories deployed during the Congas project. The positions are sampled every 1 h and plotted following a Lambert projection.

progressively damped out and the loops nearly disappear (green boxes in Figure 2.3a), before a new storm or moving front can trigger new inertial oscillations.

We compute the $u_x(\tilde{x},\tilde{y},\tilde{t})$ (along the x-axis) and $u_y(\tilde{x},\tilde{y},\tilde{t})$ (along the y-axis) speeds as follows :

$$\begin{aligned} u_x(\tilde{x},\tilde{y},\tilde{t}) &= (x(t+\Delta t)-x(t))/\Delta t \\ u_y(\tilde{x},\tilde{y},\tilde{t}) &= (y(t+\Delta t)-y(t))/\Delta t \end{aligned} \tag{2.3}$$

with $\Delta t = 1\,\mathrm{h}$ and where the mid-points $\tilde{x}$, $\tilde{y}$ and $\tilde{t}$ are defined as $\tilde{x} = (x(t+\Delta t)+x(t))/2$, $\tilde{y} = (y(t+\Delta t)+y(t))/2$ and $\tilde{t} = ((t+\Delta t)+t)/2$. The Fourier transform $\hat{U}_\mathrm{b}(\omega)$ of the buoy velocities u_x and u_y for a selected buoy trajectory, which starts at time t_0 and ends at time t_end, is defined as

$$\hat{U}_\mathrm{b}(\omega) = \frac{1}{N}\sum_{t=t_0}^{t_\mathrm{end}-\Delta t} e^{-i\omega t}(u_x(\tilde{x},\tilde{t}) + iu_y(\tilde{y},\tilde{t})) \tag{2.4}$$

where N is the number of velocity samples along the trajectory and $\omega = 2\pi f$. This vectorial Fourier transform distinguishes negative and positive frequencies : peaks at $f<0$ and $f>0$ are associated with clockwise and counter-clockwise displacements, respectively.

Figure 2.3b shows the Fourier spectrum $|\hat{U}_\mathrm{b}(\omega)|$ of the buoy velocities associated with the trajectory plotted in Figure 2.3a. The Fourier transform reveals a peak of magnitude $5.2\,\mathrm{km\,day^{-1}}$ at the inertial oscillation frequency ($f_0 \approx -1.35\,\mathrm{cycles\,day^{-1}}$ using the average latitude $\phi = 1/N\sum_t \phi(t) \approx 42°$ in Eq. 2.1). This peak corresponds to the component of the buoy motion associated with the Coriolis force. The peak at $f=0$ represents the advective component of the buoy motion. Finally, the two peaks observed at $f = -2\,\mathrm{cycles\,day^{-1}}$ and $f = 2\,\mathrm{cycles\,day^{-1}}$ are associated with a semi-diurnal tidal oscillation. Unlike the inertial oscillation, the tidal oscillation does not rotate and the associated peak is therefore observed at

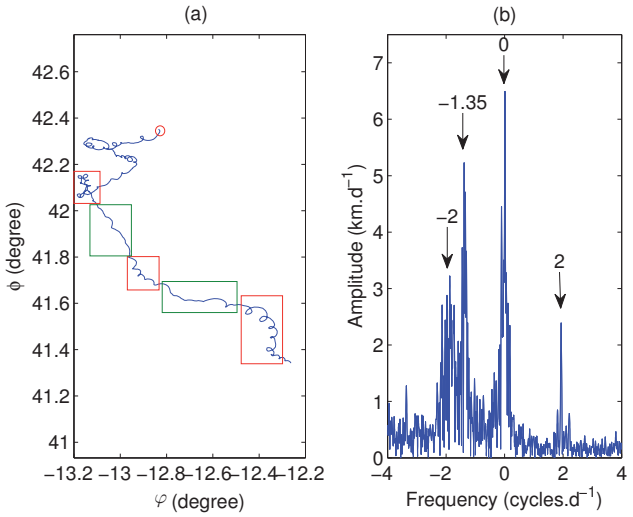

FIGURE 2.3 – **(a)** 1 month sample of the trajectory of buoy B245 (25 May to 25 June 2007). The trajectory is plotted in latitude-longitude coordinates. Its beginning is marked by the red circle. The red and green boxes outline periods with strong and low cycloidal loop activity, respectively. **(b)** Fourier spectrum of the buoy velocity. The velocity is computed following Eq. (2.3) with $\Delta t = 1\,\mathrm{h}$.

positive and negative frequencies.

We now consider IABP ice drifters. A buoy moving in free drift, i.e. fixed on an ice floe that drifts according to wind and ocean currents alone, hence without any mechanical interaction with other ice floes, is expected to oscillate in a way similar to e.g. the oceanic B245 buoy of Figure 2.3 when subjected to similar forcing conditions, although another source of damping of the oscillations might come from the friction between the ice bottom and the ocean surface.

Figure 2.4a shows an IABP buoy trajectory within the Fram Strait during the summer period, where ice is highly fragmented and loosely packed. The clockwise-cycloids are clearly visible. We observe bursts in the inertial oscillation intensity (red rectangles) followed by a period of decaying intensity (green rectangle).

The velocity of the buoy is computed using Eq. (2.3), with stereographic coordinates x and y and with $\Delta t = 3\,\mathrm{h}$. The inertial oscillations are evidenced by a strong peak observed on the velocity Fourier spectrum (Figure 2.4b), at the inertial frequency $f_0 \approx -1.97\,\mathrm{cycles\,day^{-1}}$ (calculated using $\phi = 80°$ in Eq. 2.1). As the Arctic Basin lies between 70° and 90° of latitude, the inertial oscillation frequency varies from -1.88 to $-2\,\mathrm{cycles\,day^{-1}}$ at these latitudes and is thus merged with the semi-diurnal tidal oscillation frequency. The differentiation of these two types of oscillations can be done by looking at the amplitude of the Fourier spectrum with respect to signed frequencies : we assume the spectral peaks associated with the semi-diurnal tidal oscillation to be roughly symmetric at positive and negative frequencies (as a first order approximation, as bathymetry or ocean currents can regionally affect this symmetry), and consider that the excess within the amplitude of the peak at the inertial frequency f_0 is likely

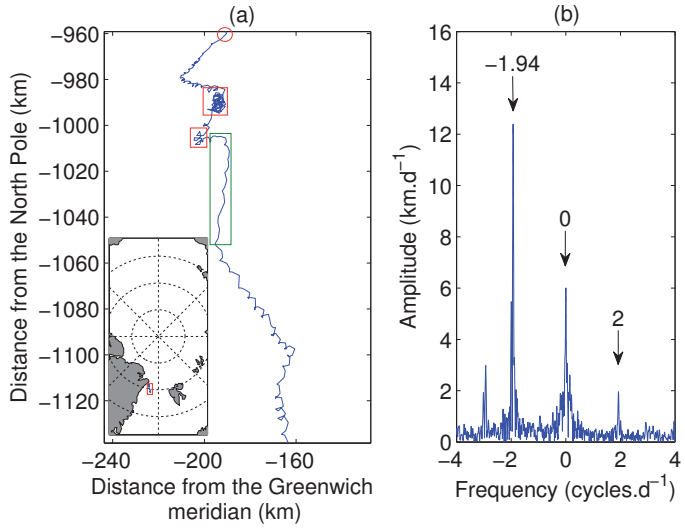

FIGURE 2.4 – **(a)** 1 month sample of the trajectory of IABP buoy 1897 (30 August to 30 September 1987). The location of the buoy is indicated by the red box in the inset of Figure 2.4a. The red boxes show periods when cycloidal loops are best observed, whereas the amplitude of the loops is much lower in the green boxes. **(b)** Fourier spectrum of the buoy velocity. The velocity is computed following Eq. (2.3) with $\Delta t = 3\,\mathrm{h}$.

to represent the inertial component of the buoy motion. For example, in Figure 2.4b, the tidal oscillation generates a small peak at $f = 2\,\mathrm{cycles\,day}^{-1}$, which means that most of the amplitude of the peak observed at f_0 comes from the inertial oscillation of the buoy.

We now consider a buoy tethered to a strongly cohesive multi-year ice pack : the internal stress term of the momentum equation (Eq. 2.2) is then expected to dominate over any external forcing, including the Coriolis force. Consequently, the inertial oscillations that might be generated by storms or moving fronts are immediately damped and thus not visible. Figure 2.5a shows an example of such a trajectory within the multi-year ice pack at the end of winter. The cycloids seen in Figure 2.4a do not appear anymore and the Fourier spectrum plotted in Figure 2.5b does not show any peak at the inertial frequency f_0. Conversely, we can notice that *Kwok et al.* (2003) found significant oscillations in the same region but in a different time period. This points out the temporal variability in the strength of inertial oscillations, which may depend on both the storm activity and the sea ice state. In the following, a simple method is proposed to quantify the strength of inertial oscillations. Then, performing statistics on this quantity will allow us to interpret space and time variabilities in terms of dissipation of energy through mechanical processes that takes place within sea ice.

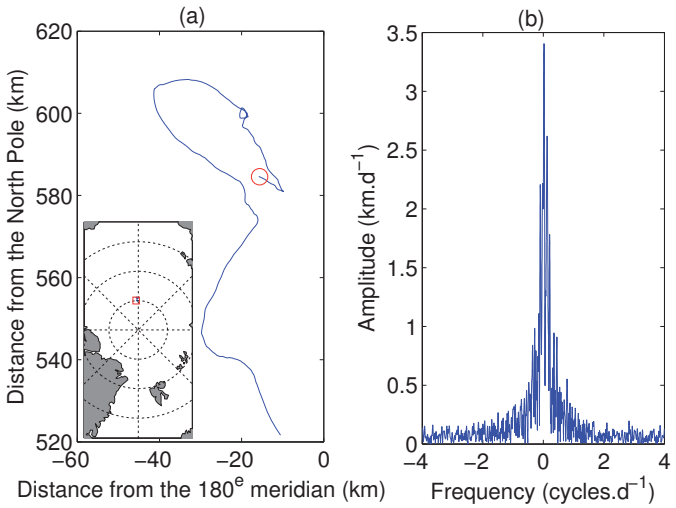

FIGURE 2.5 – **(a)** 1 month sample of the trajectory of buoy 12825 (20 April to 21 May 1992). The location of the buoy within the Arctic Basin is indicated by the red box in the inset of Figure 2.5a. **(b)** Fourier spectrum of the buoy velocity. The velocity is computed following Eq. (2.3) with $\Delta t = 3\,\mathrm{h}$.

2.3.2 Methodology

We now define a parameter M that quantitatively accounts for the time-dependent inertial oscillation magnitude.

The cycloids observed in the trajectories (Sect. 2.3.1) result from the superposition of an advection ($f = 0$) and a rotation at the inertial frequency ($f = f_0$). In Figs. 2.3 and 2.4, the red boxes show parts of the trajectories characterized by cycloidal loops : these loops indicate that the rotation velocity is larger than the advection velocity. In contrast, no full loops are observed within the green boxes, showing that the rotation velocity is lower than the advection velocity. *Lepparanta* (2004, p. 157) proposed a simple ratio of cycloidal rotation velocity over the advection velocity to qualitatively estimate the strength of inertial oscillations.

We here propose to evaluate in a quantitative way the time-dependent oscillation magnitude using the Fourier spectrum at the inertial frequency f_0. Since inertial oscillations are best quantified by means of a spectral analysis, we here perform such an analysis on a sliding time window. This will enable us to define a time-varying quantity M that measures how inertial oscillations evolve with time as a buoy drifts. For a given buoy location defined by the coordinates (x_{pst}, y_{pst}, t_{pst}), where "pst" stands for "present", we define a Gaussian window function $g_{\mathrm{pst}}(t)$ centered on t_{pst} with a characteristic duration of the order of several inertial time periods :

$$g_{\mathrm{pst}}(t) = \exp\left(\frac{-(t - t_{\mathrm{pst}})^2}{2(nT_{\mathrm{o}})^2}\right) \tag{2.5}$$

where $T_o = -1/f_0$ is the inertial time period and n controls the width of the window. In this analysis, we set $n = 1$, i.e. a time interval around t_{pst} that is long enough to really probe the

inertial time scale, since it corresponds to 3 days, and short enough to properly measure rapid time variations in the inertial oscillation magnitude. Thus, 24 data points within which about half the points carry significant weight are used to compute Fourier transform calculations.

Gaps (missing data) are present in the IABP buoy records. Their duration varies from one sample every few hours (i.e. a time interval of 6 h between successive positions) to several weeks. Therefore, we introduce in our calculations a selection condition such that no gap of data is allowed for values of t that verify $g_{\rm pst}(t) > P$, where we set $P = 0.01$. No M value is thus computed at time $t_{\rm pst}$ if one or more sampling time t verifying this later condition is lacking. Moreover, since missing data even occurring far from $t_{\rm pst}$ (i.e. at values of t such that $g_{\rm pst}(t) < P$) can play a non-negligible role on the Fourier transforms, the Gaussian of Eq. (2.5) is truncated at ± 1.5 days from $t_{\rm pst}$.

Under these conditions, we can compute 1.3×10^6 M values from the IABP dataset, which represents 83 % of the total number of observations available.

We then compute the velocity $\vec{W}_{\rm pst}(t)$ as follows :

$$\vec{W}_{\rm pst}(t) = \vec{U}_{\rm b}(t) g_{\rm pst}(t) \tag{2.6}$$

where $\vec{U}_{\rm b}(t) = u_x(t)\vec{e_1} + u_y(t)\vec{e_2}$.

We compute the normalized Fourier spectrum at time $t_{\rm pst}$ of the velocity time series $\vec{W}_{\rm pst}(t)$ at the inertial frequency f_0, where f_0 is made to vary according to the buoy latitude (Eq. 2.1), as

$$\hat{W}_{\rm pst}(f_0) = \Delta t \sum_{t=t_0}^{t_{\rm end}} (u_x(t) + i u_y(t)) g_{\rm pst}(t) e^{-i\omega_0 t} \tag{2.7}$$

where $\omega_0 = 2\pi f_0$ and t_0 and $t_{\rm end}$ are the starting and ending times of the trajectory. This value is likely to represent the amplitude of the inertial oscillations. We further normalize it in order to define a non-dimensional parameter M that measures the magnitude (still at $t_{\rm pst}$) of the inertial oscillation :

$$M = \frac{|\hat{W}_{\rm pst}(f_0)|}{1.27} \times \frac{4}{\pi \overline{W}_{\rm pst}} \tag{2.8}$$

where

$$\overline{W}_{\rm pst} = \frac{1}{1.27} \sum_{t_0}^{t_{\rm end}} {\rm d}t |\vec{W}_{\rm pst}(t)|. \tag{2.9}$$

is the (current, at time $t_{\rm pst}$) mean magnitude of the drift velocity, and the value 1.27 is equal to $\int_{t_0}^{t_{\rm end}} g_{\rm pst}(t){\rm d}t$.

2.3.3 Application to the buoy trajectories

Figure 2.6 shows the values of M computed using the different trajectories plotted in Sect. 2.3.1. Large M values are obtained for the oceanic buoy trajectory plotted in Figure 2.3, with an average of 0.56. For the ice drifter of Figure 2.4, we also get large M values with an

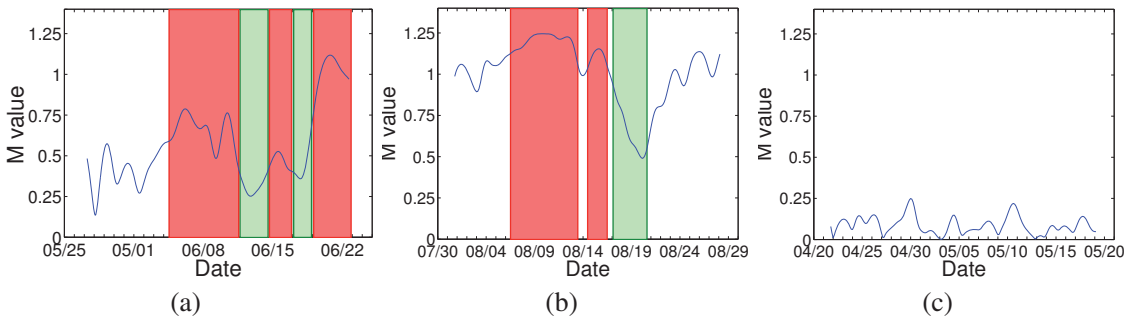

FIGURE 2.6 – M values for **(a)** the trajectory of the oceanic buoy 255 plotted in Figure 2.3a, **(b)** the trajectory of the ice-tethered buoy 1897 plotted in Figure 2.4a and **(c)** the trajectory of the buoy 12825 plotted in Figure 2.5a. The red and green rectangles respectively correspond to those shown in Figs. 2.3 and 2.4.

average of 0.8 : the $M > 1$ values are all associated with cycloidal loops observed in Figure 2.4a (red rectangles), followed by their decay as characterized by a decrease of M (green rectangles). In contrast, for the ice drifter of Figure 2.6c, the M values are much lower : the mean M value over the time period is only equal to 0.13, illustrating the relative absence of inertial loops.

As the raw buoy positions of the IABP ice drifters dataset are irregularly sampled through time, then interpolated (cubic interpolation) and re-sampled at a regular 3 h interval, we investigated the effect of this procedure on the values of M computed for the IABP dataset. To do so, we artificially degraded the oceanic buoy dataset, which samples buoys positions every hour, by randomly removing a given % of raw positions. A cubic interpolation followed by a re-sampling at 3 h is then performed on the degraded dataset, as done for IABP data, and the associated M values (noted M_{D}) are re-computed (Figure 2.7). The cubic interpolation alone, i.e. without degrading the raw data, has almost no influence on M (Figure 2.7a). In Figure 2.7b, we can see that the deviation of the M_{D} time series from the M time series becomes visible only when more than 50 % of the raw buoy positions are missing. For 50 % of missing data, the error on individual M values is lower than 5 %. More importantly, as we focus in the following on M values averaged over trajectories, the departure of averaged M_{D} values from the average M value for increasing missing data ratios is shown in Figure 2.7c. Average M_{D} values do not deviate significantly from the average M value for missing data ratios up to 60 %, which corresponds to an average time sampling of about 02 :50 h and a time sampling maximum gap of about 6 h. Thus, for sampling times lower than these threshold values, we can consider that the computed M values are not affected by an irregular sampling through time. While not shown here, similar results have been obtained by considering ice drifters initially regularly sampled at 1 h during the TARA field campaign (*Gascard et al.*, 2008). This indicates the robustness of IABP interpolation procedure coupled to our estimation of the amplitude of inertial oscillations.

These examples demonstrate that the parameter M is appropriate to quantify the inertial oscillation magnitude. Small average values of M (say lower than 0.2) correspond to buoy trajectories within a strongly cohesive ice pack, while large values of M (say greater than 0.6)

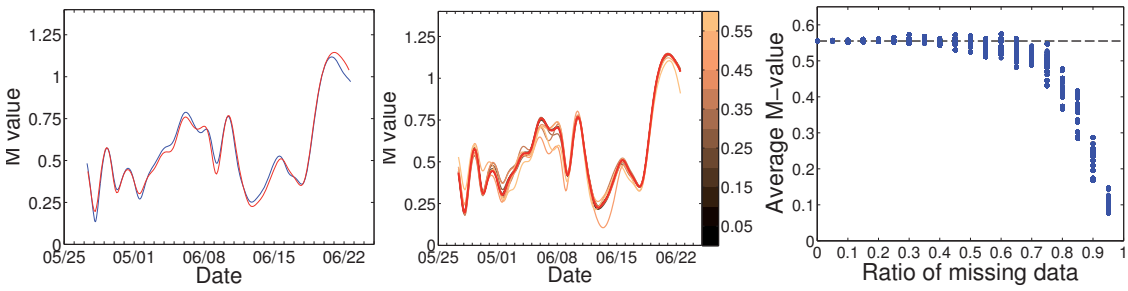

(a) (b) (c)

FIGURE 2.7 – **(a)** M values for the trajectory of the oceanic buoy 255 plotted in Figure 2.3 (raw data : blue line, same as Figure 2.6a) and the trajectory obtained after a cubic interpolation and a 3 h resampling of the raw positions (red line). **(b)** M_D time series computed from the degraded datasets of missing data ratio varying between 0 and 60 % (the red line is the same as in **a**). **(c)** M_D values averaged over the whole trajectory (1 month) as a function of the missing data ratio. 20 realisations have been done at each given value of missing data ratio. The grey dashed line shows the average raw M value, equal to 0.56.

correspond to buoy trajectories that we can consider to be nearly in free drift condition.

2.4 Analysis of 30 yr of IABP data

In this section, we analyse the spatial and temporal patterns of the inertial oscillation magnitude M, and check whether a significant trend can be observed over the Arctic Basin during the 30 yr of the IABP dataset, which would reveal a significant change in ice conditions. As previously explained in Sect. 2.3.1, inertial oscillations are caused by sudden changes in external forces (strong wind), which then decay due to kinetic energy dissipation within the Ekman layer or friction that takes place at the ice/water interface, or due to internal ice stresses. Therefore, more frequent and stronger storms over the years should imply larger M values on average. Cyclonic activity over the Arctic Ocean shows a maximum during summer that could partly explain an annual cycle of the inertial oscillation magnitude (*Serreze and Barrett*, 2008) (see below). On the other hand, no significant trend in cyclonic activity has been found over the last 50 yr (*Serreze and Barrett*, 2008). Similarly, the average wind speed over the Arctic Basin, as estimated from the ERA-40 reanalysis dataset, does not show any significant trend over the period 1979–1999 (*Rampal et al.*, 2009a).

2.4.1 Seasonal variation

In this section, we compute M for buoys located within the central Arctic Basin, as delimited by the thick black line in Figure 2.1, and then investigate intra-annual (monthly) variations by grouping M values into monthly periods, i.e. one average monthly value $\vec{M}$ for all the M values occurring in January, whatever the calendar year, etc. The central Arctic is here delimited by all buoy positions lying further than 150 km away from the coasts and the Fram Strait. This

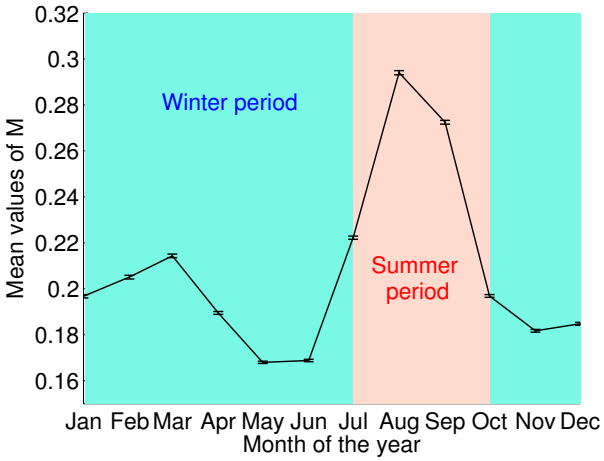

FIGURE 2.8 – Average annual cycle in the M values. The average is performed considering the central Arctic Basin buoy dataset. The error bars show the deviation $\Delta\vec{M}$ from the average $\vec{M}$ value estimated using the central limit theorem and computed as $\Delta\vec{M} = \frac{\vec{M}}{\sqrt{N_M}}$, where N_M is the number of M values used to calculate the monthly mean $\vec{M}$. Here, N_M ranges from a minimum of 6.4×10^4 in February to a maximum of 1.1×10^5 in May.

way, we skip from the analysis buoys possibly stuck on fast ice.

Figure 2.8 shows the monthly $\vec{M}$ value averaged over the 30 yr of record. To estimate the associated error bars, we checked using a bootstrap method (*Rampal et al.*, 2009a) that the standard deviation $\Delta\vec{M}$ indeed varies as $\frac{\vec{M}}{\sqrt{N_M}}$, where N_M is the number of M values used to calculate the monthly mean $\vec{M}$. Here, N_M ranges from a minimum of 6.4×10^4 in February to a maximum of 1.1×10^5 in May. The monthly mean $\vec{M}$ value reaches a minimum of 0.168 in May and a maximum of 0.294 in September, and exhibits an obvious annual cycle. We define the summer season by the three months of July, August and September and the winter period by the rest of the year. These results are consistent with other observations : sea ice concentration, sea ice thickness and sea ice deformation also describe an annual cycle (*Rampal et al.*, 2009a; *Rothrock et al.*, 2008). The annual cycle of ice thickness within the Arctic Basin has a maximum on 30 April (*Rothrock et al.*, 2008), in phase with our minimum $\vec{M}$ value in May. Being thinner and less concentrated in summer, sea ice is less cohesive and more deformable during this time period. This leads, on average, to a lower damping of the inertial oscillations, and therefore larger M values. However, we cannot exclude that a stronger cyclonic activity during summer (*Serreze and Barrett*, 2008) could reinforce the annual cycle described by the average M values by triggering more oscillations.

2.4.2 Spatial pattern

The question arises as to whether the seasonal changes in the M values evidenced in the previous section can be associated with a spatial pattern. In this section, we select values of M associated to buoys located within the central Arctic Basin and within the Fram Strait

(thick black and grey lines in Figure 2.1). From theses values, we build a seasonal M dataset by separating the M values computed in winter, i.e. all the M values recorded for all the 30 winter seasons, from the M values computed in summer. The seasonal spatial patterns of M for both seasons are plotted in Figure 2.9. The spatially averaged M value, denoted $\overline{M}(X_j, Y_j)$, is computed for each grid point j of coordinates (X_j,Y_j) as

$$\overline{M}(X_j, Y_j) = \frac{1}{\sum_i w_{ij}(x_i, y_i)} \sum_i w_{ij}(x_i, y_i) M_i(x_i, y_i) \tag{2.10}$$

where the summation is performed over all the buoy positions (x_i, y_i) contained in a circle of radius $L = 400\,\mathrm{km}$ centered on the coordinates (X_j,Y_j). The weight $w_{ij}(x_i, y_i)$ is defined as

$$w_{ij}(x_i, y_i) = e^{-\mathrm{d}^2/2L^2} \tag{2.11}$$

where $d = \sqrt{(x_i - X_j)^2 + (y_i - Y_j)^2}$ is the distance between the buoy position (x_i, y_i) and the grid point (X_j, Y_j).

The patterns observed in Figure 2.9 are, at least qualitatively, consistent with the observed distribution of the sea ice thickness (*Kwok and Rothrock*, 2009) and concentration (*http* : *//nsidc.org/data/seaice/index.html*) (*Comiso et al.*, 1990, updated 2012). In summer, large $\overline{M}$ values are observed at the edge of the basin in the Beaufort, Chukchi and Laptev seas, i.e. in regions where the multi-year ice cover has been progressively disappearing during the last decade (*Maslanik et al.*, 2011). On the contrary, small values of $\overline{M}$ can be observed along the Canadian coasts, where the average ice thickness is at its maximum (*Kwok and Rothrock*, 2009). Sea ice behaves more as a strongly cohesive plate in this region, unsensitive to the Coriolis force. This zone corresponds to the multi-year ice still remaining nowadays. Large values of $\overline{M}$ are also observed south of Fram Strait, which is consistent with the buoy trajectory plotted in Figure 2.4a, which we discussed in Sect. 2.3.1. In contrast, the winter pattern does not reveal any particular structure within the basin. The values of $\overline{M}$ are small over the whole basin, except relatively larger M values computed north of Canadian coasts. These larger M values could be attributed to buoys drifting along the "Circumpolar flaw lead" that consists of a sheared, thus highly fragmented, zone (*Lukovich et al.*, 2011).

To further test the link between the state of the sea ice cover and its cohesiveness, as expressed by the amplitude of the inertial oscillations, we perform a correlation analysis between the M values and the open water concentration $1 - \alpha$, where α is the sea ice concentration dataset collected by NSIDC (*http* : *//nsidc.org/data/seaice/index.html*) (*Comiso et al.*, 1990, updated 2012). This dataset has a spatial resolution of 25 km and consists of ice concentration values sampled every two days from 1979 to 1987 (SMMR), and every day since 1987 (SSM/I). For each value of M, we search for the corresponding value of open water concentration as the closest sample in time and space : a $1 - \alpha$ value is associated with a given M value if we can find, for the same day of record, within one day during the period 1979–1987, a sample that is closer than 25 km. The corresponding correlation coefficient R is equal to $0.245(\pm 0.002)$. This positive

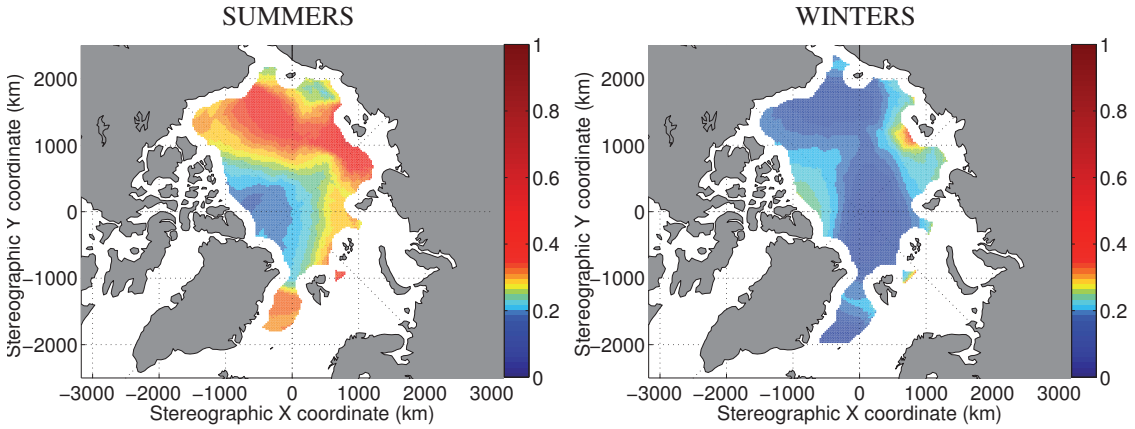

FIGURE 2.9 – Spatial pattern of inertial oscillation magnitude within the Arctic Basin in summer (left) and in winter (right). These two fields are computed from the seasonal M dataset. A spatially averaged value of M values, denoted $\overline{M}$, is computed following Eq. (2.10) for each point of a 25 km resolution grid. The graphic representation is a linear interpolation of the gridded $\overline{M}$ values. In order to not represent regions with little data, an $\overline{M}$ value at a given grid point is plotted only if its associated weight is greater than a minimum value we arbitrarily set to 1000.

correlation is statistically significant as R is more than 120 times greater than the standard deviation obtained in the null hypothesis at no correlation (numerically computed by randomly reshuffling the M and $1-\alpha$ values). This is consistent with stronger oscillations characteristic of a less compact sea ice cover.

In order to check whether this global correlation is, or not, only due to the fact that M and $1-\alpha$ both describe an annual cycle, we group together these values by months. We then compute the cross-correlation coefficient R separately for each month of the year, over the 30 yr of record. While not plotted here, the annual variation of the correlation coefficient is in phase with the annual cycle of M plotted in Figure 2.8 : the correlation is larger in summer. The correlation coefficient is equal to $0.350(\pm 0.005)$ in August, which means that the M values are spatially correlated with the associated open water concentration values. In winter, the correlation is much less significant, which can be understood by the fact that, during this period, the sea ice concentrations are equal to 1 almost everywhere within the basin and therefore show very little fluctuations. Moreover, in winter, we could expect that small departures of the ice concentration from unity would not be so significant to decreasing the ice strength provided that the floes are in continual contact.

Here, all the computed coefficients of correlation remain small. This suggests that other factors than the ice concentration control the M values : we expect both the variability in wind forcing materialized by storm activity and the ice thickness to significantly depress the correlation between M and $1-\alpha$. We will see in Sect. 2.4.3.2 that the correlation between M and $1-\alpha$ is much improved when setting free of the influence of wind forcing variability, i.e. by considering averaged $\overline{M}$ and $\overline{1-\alpha}$ values.

2.4.3 Multi-annual variation

We have shown so far that the M parameter is a useful proxy for the cohesiveness of the cover and, consequently, the level of internal stresses. We now analyze whether the M values have changed over the last three decades owing to a change in ice conditions.

2.4.3.1 M time series

In this section, we use the central Arctic buoy dataset. The temporal sampling of the IABP buoy dataset is heterogeneous, being characterized by variations of data density over the period. Most notably, a larger number of observations are available in the later years, as compared to the early 1980s or during the late 1990s. To circumvent this problem, the evaluation of the multi-annual variation of M is done by equally binning the M values in time. The summer and winter datasets are both separately split into 10 successive bins, all containing the same number of observations. For each bin, an average value of M, associated with an average value of time, is computed.

Figure 2.10 shows the time series $M(t)$ between January 1979 and December 2008 for the summer and winter seasons. The error in the average M value is computed using a bootstrap method as explained in *Rampal et al.* (2009a). The bootstrap method is performed individually for each bin, and the deviation from the mean ΔM is represented by the error bars. We see on both plots that the most prominent feature is a significant increase of the inertial oscillation amplitude through time. A linear fit gives a positive trend equal to $1.19\,(\pm 0.34) \times 10^{-5}\,\mathrm{yr}^{-1}$ (i.e. a 16.5 %

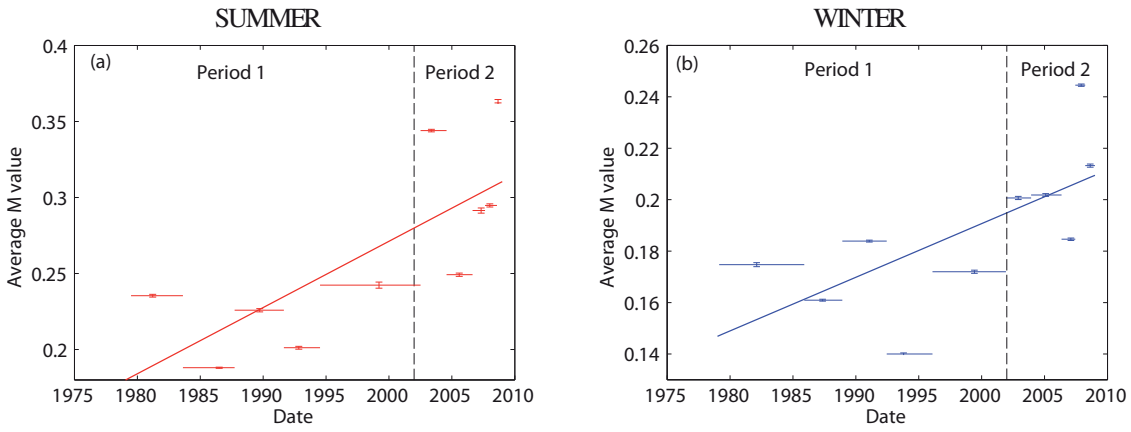

FIGURE 2.10 – Time series $M(t)$ from January 1979 to December 2008 computed using **(a)** the summer dataset and **(b)** the winter dataset. For each season, the dataset is equally split into 10 bins over which the average is computed. One bin corresponds to approximately 3.1×10^4 M values in summer and 8.0×10^4 M values in winter. The horizontal lines associated with each data point indicate the time period associated with each bin. Vertical lines are error bars computed from a bootstrap method. Bold lines are linear fits : the trends are $1.19\,(\pm 0.34) \times 10^{-5}\,\mathrm{yr}^{-1}$ (i.e. 16.5 % increase per decade) for summer and $5.7\,(\pm 1.9) \times 10^{-6}\,\mathrm{yr}^{-1}$ (i.e. 11 % increase per decade) for winter.

increase per decade) for summer and $5.7\,(\pm\,1.9)\times10^{-6}\,\mathrm{yr}^{-1}$ (i.e. a 11 % increase per decade) for winter. Thus, the increase of inertial oscillations is relatively more marked in summer than in winter.

The use of GPS as the buoy positioning system has become more common since the end of the last century. As noted in Sect. 2.2.1, this system is more accurate than ARGOS positioning. We thus check whether the observed trend on the mean time series $M(t)$ could be a spurious effect caused by reduced noise in recent years. To do so, noised mean time series $M_N(t)$ are built by computing M values on buoy trajectories over which Gaussian noise is added. Because the increase in the average $M(t)$ values is particularly marked from the beginning of the 21 century, Gaussian noise is only added to buoy trajectories recorded during the period 2002–2008. For each IABP position $(x_\mathrm{b},\,y_\mathrm{b})$ of buoy trajectories recorded from the year 2002 onwards, we define a noised buoy position $(\widetilde{x_\mathrm{b}},\,\widetilde{y_\mathrm{b}})$ as $\widetilde{x_\mathrm{b}}=x_\mathrm{b}+\delta x$ and $\widetilde{y_\mathrm{b}}=y_\mathrm{b}+\delta y$ where δx and δy are increments randomly picked from a centered Gaussian distribution with a standard deviation σ. Figure 2.11 shows realizations of mean time series $M_N(t)$ built using $\sigma=300\,\mathrm{m}$ and $\sigma=1000\,\mathrm{m}$, along with the IABP time series $M(t)$, as in Figure 2.10. From the year 2002, the mean time series $M_N(t)$ deviate from $M(t)$, showing that noise on the buoy positions has an influence on the parameter M. However, almost systematically, values of $M_N(t)$ are larger than $M(t)$, showing that noise most generally acts to increase the M values rather than to decrease them.

This can be explained as follows : noise increases the amplitude of the Fourier spectrum at high frequencies. This has two competing consequences : (i) the norm of the drift velocity $\overline{W}_\mathrm{pst}$ slightly increases, which tends to decrease M (see Eq. 2.9) ; and (ii) the amplitude at the inertial frequency $\hat{W}_\mathrm{pst}(f_0)$ is increased, which tends to increase M. The second effect is particularly marked when the inertial motion (so, M) is small, and, most of the time, dominates over the first effect, so that M is increased by noise. Consequently, the evolution observed in Figure 2.10 is not the consequence of possible reduced position noise in recent years, as the difference between the periods 1979–2001 and 2002–2008 would have been even larger if the level of noise had remained the same over the entire record. In other words, the observed trend in $M(t)$ is most likely an underestimation of the multi-annual evolution of the inertial oscillation magnitude.

The same is also true for the annual cycle (Figure 2.7) : as the effect of noise is stronger for low M values, winter M values are, in average, more overestimated than summer M values.

In addition, *Rampal et al.* (2009a) reported a significant (9 % per decade) increase of sea ice speeds in the Arctic Basin over the last three decades. Therefore, as increasing advection velocities act to decrease M (Sect. 2.3.2), the multi-annual positive trend on the M values reported here most likely underestimates the associated decrease of the mechanical energy dissipation within the ice cover in the later years.

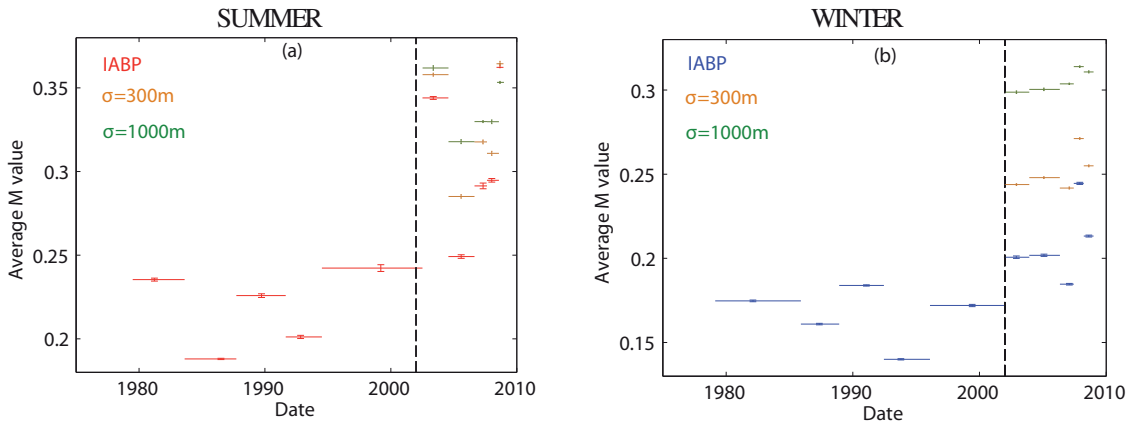

FIGURE 2.11 – Influence of noise, prescribed on the positions of buoys, on the monthly mean time series $M(t)$ for **(a)** the summer season and **(b)** the winter season. Gaussian noise, with a constant standard deviation σ, has been added to all buoy positions recorded since year 2002. Results for noised mean time series $M_N(t)$ (in yellow and green) for $\sigma = 300\,\mathrm{m}$ and $\sigma = 1000\,\mathrm{m}$ are compared with the IABP mean time series $M(t)$ as in Figure 2.10.

2.4.3.2 Evolution of spatial patterns

The previous section demonstrated a strong evolution of the average inertial oscillation amplitude, although it is more strongly marked in summer. We here analyze the spatial consequences of the observed multi-annual changes. To do so, we split the whole IABP buoy seasonal dataset into two periods. A Student t-test performed on the winter and the summer $M(t)$-time series in Figure 2.10 shows that the most significant changing point occurs in 5 averaged M values out of the 10. More precisely, splitting the winter time series $\{M_1, M_2, \ldots, M_{10}\}$ into two distributions $\{M_1, \ldots, M_5\}$ and $\{M_6, \ldots, M_{10}\}$, the probability that these two distributions have the same mean is only 0.92 %. We have verified that this probability is indeed the lowest when splitting the time series just after M_5. Similarly, we find the same optimal change-point in summer, with an associated probability that the two distributions share the same mean equal to 0.42 %. This leads to define two distinct periods, with period 1 from 1979 to 2001 and period 2 from 2002 to 2008 (see Figure 2.10). We can remark that, according to this periodic splitting, period 1 and period 2 contain the same number of observations, i.e. 5 bins each. As done in Sect. 2.4.2, the spatial patterns of the M values for the summer and winter seasons associated with each period are shown in Figure 2.12. As expected, the changes are stronger in summer. They affect most of the Arctic, but are more pronounced on the Siberian side : a drastic increase of the peripheral ice zone area is observed in the later years. Conversely, winter changes are milder north of Canada and Greenland, where the thickest multi-year ice can be found nowadays (*Kwok and Rothrock*, 2009).

To underline the link between the spatial repartition of M values and open water concentration values $1 - \alpha$, Figure 2.13 provides open water concentration maps obtained in summer for both periods. Winter concentration maps are not shown here, since they correspond to $1 - \alpha$

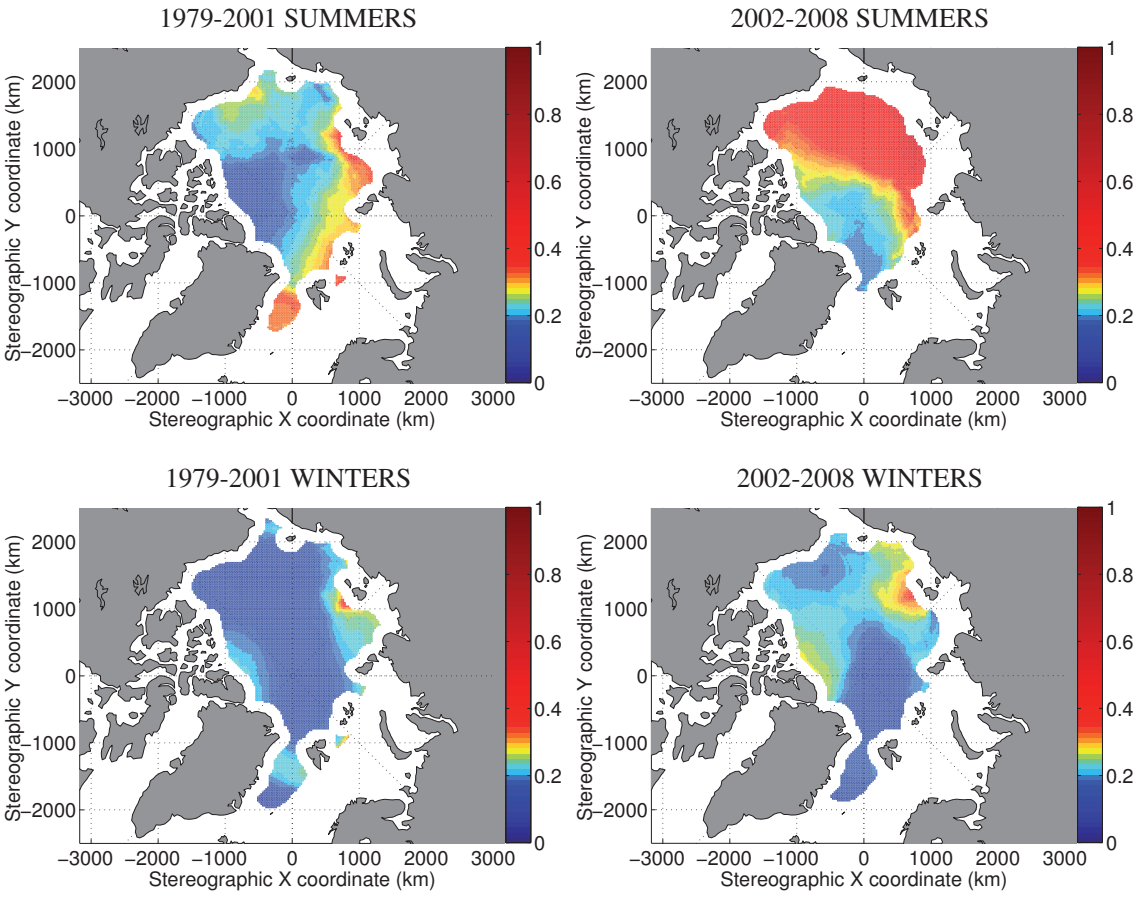

FIGURE 2.12 – Spatial repartition of M within the Arctic Basin in summer and winter computed using the seasonal dataset of the period 1979–2001 and the seasonal dataset of the period 2002–2008. An average mean value of M, denoted $\overline{M}$, is computed following Eq. (2.10) for each node of a 25 km resolution grid. The smoothing parameter L is equal to 400 km In order to not represent regions with little data, an M value at a given grid point is plotted only if its associated weight is greater than a minimum value we arbitrarily set to 1000.

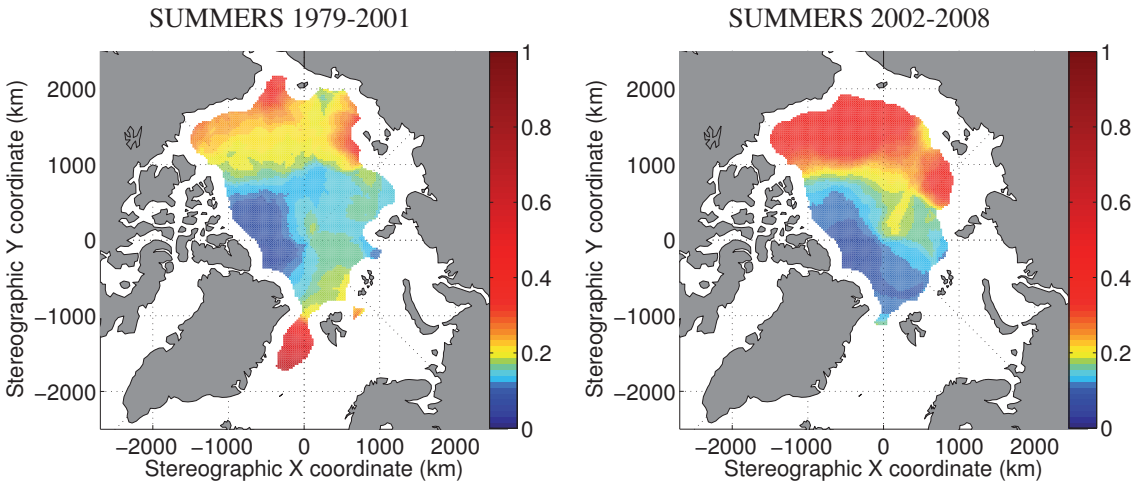

FIGURE 2.13 – Spatial repartition of open water concentration within the Arctic Basin in summer computed using the seasonal dataset of the period 1979–2001 and the seasonal dataset of the period 2002–2008. An average mean value of open water concentration, denoted $\overline{1-\alpha}$, is computed following Eq. (2.10) for each node of a 25 km resolution grid. The smoothing parameter L is equal to 400 km In order to not represent regions with little data, an open water concentration value at a given grid point is plotted only if its associated weight is greater than a minimum value we arbitrarily set to 1000.

values very close to 0 over the whole Arctic Basin. Sea ice concentration values are sampled at buoy positions, as done in section 2.4.2, and averaged similarly to M values, i.e. following Eq. 2.10. Common features evidenced by $\overline{M}$ in Figure 2.9 (left) and Figure 2.12 (top) can also be recognized in spatially averaged open water concentration values $\overline{1-\alpha}$. Low values of $\overline{1-\alpha}$ are observed along the Greenland and Canadian coasts, while large values are observed in the periphery of the basin, i.e. in the Beaufort, Chukchi and Laptev seas. Moreover, the evolution from period 1 to period 2 is also similar to the one observed on $\overline{M}$, materialized by a slight migration of the pack zone toward the south, and an increase of the peripheral zone area, materialized by larger open water concentration values. The correlation coefficient computed between $\overline{M}$ values shown in Figure 2.12 and values of $\overline{1-\alpha}$ is equal to 0.57 for period 1 and 0.80 for period 2. These correlation coefficients are much larger than the one obtained in section 2.4.2. This is explained by the fact that average M and $1-\alpha$ values are considered here prior to compute the correlation coefficient, removing like this the influence of wind forcing activity in the variability of M. Thus, we expect the discrepancies that still remain here between $\overline{M}$ and $\overline{1-\alpha}$ to be mostly due to changes in ice thickness and ice degree of fragmentation. The respective role of ice concentration, ice thickness and ice degree of fragmentation on the inertial oscillation amplitude is thoroughly examined in *Gimbert et al.* (2012b).

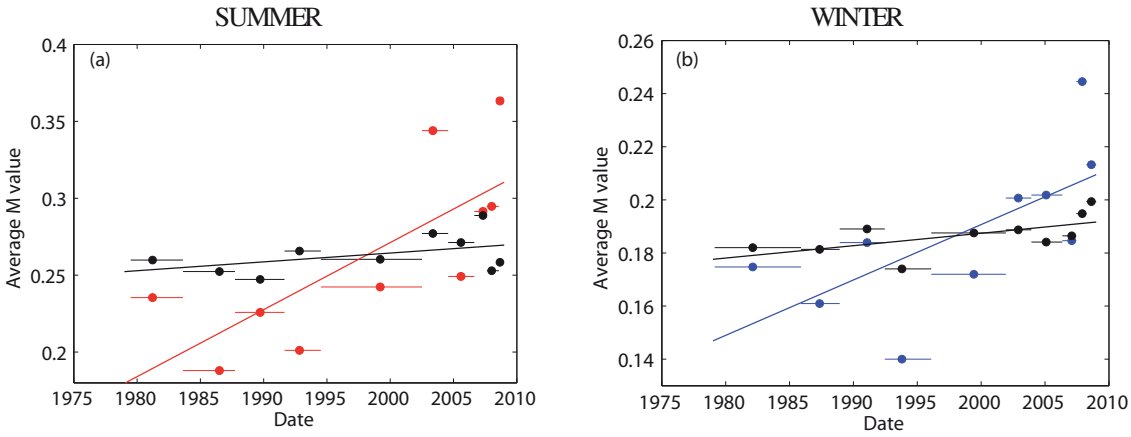

FIGURE 2.14 – Mean time series $M(t)$ **(a)** in summer (red) and **(b)** in winter (blue), as in Figure 2.10 and $M_0(t)$ (black lines), resulting from the null hypothesis. The best linear fits are also plotted, showing that changes in spatial sampling only account for a small fraction of the observed trend.

2.4.3.3 Is the observed evolution from the IABP buoy dataset representative of the whole Arctic Basin ?

In the two previous sections, care was taken to remove the effect of temporal heterogeneities in the IABP buoy dataset. However, the IABP buoy dataset is spatially heterogeneous : changes in the spatial sampling by the buoys could affect the overall trend. In order to check whether the results reported in Figure 2.10 truly indicate a significant increase of the M values, we investigate whether this trend could be an artefact of changes in spatial sampling.

Following the procedure described in *Rampal et al.* (2009a) for ice velocities, we formulate a null hypothesis : in this hypothesis, there exists no temporal changes in M-maps over the year, but the effect at spatially sampling these maps in different ways at different periods will cause the M-time series to evolve with time. To construct these M-maps, we consider any buoy position associated with a given M value and recorded at a given year and a given season. For such a position, we compute the mean M_0 value for summer, respectively winter, by considering all the M values recorded in summer, respectively winter, and whatever the year, contained within a circle of radius $L = 200\,\mathrm{km}$, using Eq. (2.10). This mean value is therefore year-independent, and corresponds to our null hypothesis of no inter-annual changes. Then, we calculate our null-hypothesis M_0 time series as the mean of the summer, respectively winter M values, using the same bins as in Figure 2.10. Any inter-annual variation observed in the time series $M_0(t)$ could only be explained by changes in the spatial sampling rather than by an actual, global trend : for example, a positive trend would be explained if IABP buoy had a tendency to sample regions associated with large M values more often in the later years as compared to earlier years.

Figure 2.14 shows the mean time series $M(t)$ and $M_0(t)$ over the whole time period 1979–2008. The trend associated with the null hypothesis is equal to $1.57\,(\pm 0.98) \times 10^{-6}\,\mathrm{yr}^{-1}$ in summer and $1.28\,(\pm 0.51) \times 10^{-6}\,\mathrm{yr}^{-1}$ in winter. This means that changes in spatial sampling are

responsible for approximately 10 % of the observed trend in summer and 20 % of the observed trend in winter. We thus conclude that the trend observed in the average M values cannot only be explained by an irregular sampling of the buoys. This increase in M is not an artefact and reveals a genuine increase of the inertial oscillations magnitude over the whole Arctic Basin.

2.5 Conclusions

From the IABP ice drifter trajectories recorded between 1979 and 2008, we analyzed the average amplitude of inertial oscillations over the Arctic sea ice cover. To do so, we defined a non-dimensional parameter M that quantifies the magnitude of inertial oscillations relative to advection motion along the trajectories. For a sea ice cover of low concentration, constituted from a loose floe field moving nearly in free drift, inertial motions and M values are large. On the reverse, a highly cohesive sea ice pack, characterized by strong internal stresses, is expected to be associated with low M values. From appropriate averaging of this 30-yr dataset at different space or time scales, we have shown the following :

(i) The M values describe an annual cycle with a minimum reached in May and a maximum in September, in a qualitative agreement with the corresponding annual cycles of sea ice extent (*Comiso et al.*, 2008), concentration, thickness (*Rothrock et al.*, 2008; *Kwok and Rothrock*, 2009), advection velocity and deformation rates (*Rampal et al.*, 2009a).

(ii) The spatial pattern of M over the Arctic Basin is in agreement with the sea ice thickness and concentration patterns. Low M values are observed in western Arctic, whereas large values are observed within a peripheral zone (Beaufort Sea, eastern Arctic) and south of Fram Strait.

(iii) A significant increase of average values of M is observed from 1979 to 2008. This increase, although more marked in summer, is observed in both seasons and is associated with the reduction of the thick, multi-year ice zone in recent years.

From the expected link between the magnitude of the oscillations and the degree of consolidation of the ice cover (*McPhee*, 1978; *Colony and Thorndike*, 1980; *Geiger and Perovich*, 2008), we believe that point (iii) is a signature of the mechanical weakening of the Arctic sea ice cover in recent years. However, one may argue from the momentum balance of sea ice (see Eq. (2.2)), that this strengthening of inertial motion might simply and more directly result from the observed thinning of the cover, i.e. a reduction of ice mass per unit area. In addition, this evolution could, to some extent, be the result of a modification of vertical penetration of turbulent momentum within the ocean boundary layer. In *Gimbert et al.* (2012b), we have shown, from a simple ocean-sea ice coupled dynamical model, that these two explanations cannot fully account for the evolution of inertial motion in the Arctic, which actually reveals a genuine mechanical weakening, through an associate decrease of the sea ice internal friction magnitude, of the cover at the basin scale. Such mechanical weakening has (will have) strong consequences in terms of ice drifting speeds, deformation rates, export (*Rampal et al.*, 2009a) and therefore on mass balance (*Rampal et al.*, 2011).

Chapitre 3

Affaiblissement mécanique récent de la couverture de glace Arctique révélé par l'augmentation des oscillations inertielles de banquise

Recent mechanical weakening of the Arctic sea ice cover as revealed by larger sea ice inertial oscillations

---

D'après :

Gimbert, F., N.C. Jourdain, D. Marsan, J. Weiss, and B. Barnier (2012), Recent mechanical weakening of the Arctic sea ice cover as revealed by larger sea ice inertial oscillations, *J. Geophys. Res.*, *117*(C00J12), 10.1029/2011JC007633.

Abstract

We present a simple and analytical ocean boundary layer - sea ice coupled dynamical model that we apply to the modelling of Arctic sea ice motion in the frequency domain, and particularly in the inertial range. This study further complement our related work *Gimbert et al.* (2012a) where the sea ice cover response to the Coriolis forcing has been studied. This analytical model allows interpretation of the spatial, seasonal and pluri-annual dependence of the magnitude of the inertial oscillations detailed in *Gimbert et al.* (2012a) in terms of mechanical behavior of the ice cover. In this model, the sea ice mechanical response is simplified through the introduction of a linear internal friction term K. A dependence of K allows to explain the associated dependence of the seasonal and regional Arctic sea ice inertial motion. In addition, a significant decrease of K, i.e. a mechanical weakening of the sea ice cover, is observed for the period 2002-2008 compared to 1979-2001, for the entire Arctic in both seasons. These results confirm the statistical analysis of inertial oscillations magnitude detailed in *Gimbert et al.* (2012a), and show that the regional, seasonal and pluri-annual variations of sea ice inertial motion are not only the trivial consequence of simultaneous variations of thickness and concentration (and so of ice mass per unit area). Instead, the shrinking and thinning of the Arctic sea ice cover over the last few decades has induced a mechanical weakening, which in turns has favoured sea ice fracturing and deformation.

3.1 Introduction

In recent decades, Arctic sea ice underwent a spectacular decline in terms of concentration, extent (*Comiso et al.*, 2008; *Stroeve et al.*, 2008), and average thickness (*Rothrock et al.*, 2008; *Kwok and Rothrock*, 2009). From this evolution of the sea ice state, that is, of the degree of consolidation of the ice cover, a simultaneous evolution of the magnitude of internal stresses and of the mechanical behavior is expected. In turns, such expected evolution of the sea ice mechanical response should enhance sea ice fracturing, deformation, and drift, as actually observed (*Rampal et al.*, 2009a). To measure such possible mechanical weakening is however difficult. Internal ice stress measurements (*Richter-Menge and Elder*, 1998; *Richter-Menge et al.*, 2002), of great interest to analyze mechanical processes and sea ice rheology at the local scale (*Weiss et al.*, 2007), are limited to local spatial and short time scales. Our approach, performed at the basin- and multidecadal scales from the International Arctic Buoy Dataset (IABP), consists in the analysis of the response of sea ice to the well-defined Coriolis force. As the Coriolis acceleration is constant over time, an evolution of the ice response, i.e. of ice motion around the inertial frequency $f_0 \approx 2$ cycles.day^{-1} within the arctic basin, would be a signature of a change in the mechanical behavior of the ice cover.

In *Gimbert et al.* (2012a), we performed from the same dataset a statistical analysis of the magnitude of inertial motion, relative to advection motion, and revealed spatial and seasonal patterns in agreement with the corresponding ice concentration and thickness patterns, i.e. inertial motion is more pronounced in regions (Beaufort Sea, eastern Arctic) and seasons (summers) where ice is thinner and less concentrated. This analysis also revealed a significant strengthening of ice inertial motion at the basin scale, in both summer and winter, in recent years. This evolution, we suggested, is likely to be the signature of a mechanical weakening of the ice cover and a decrease of the magnitude of internal stresses. This analysis, however, did not allow to differentiate precisely the direct effect of ice thinning, the effect of a possible modification of vertical penetration of turbulent momentum within the ocean boundary layer, or that of an actual mechanical weakening, onto this strengthening of inertial motion.

In the present paper, we present a simple ice-ocean boundary layer coupled dynamical model. As shown below, although crude, this model describes well sea ice motion in the inertial range, its seasonal as well as regional variations, and allows to account for the role of the different factors listed above. A genuine mechanical weakening of the Arctic sea ice cover in recent years is revealed by the model, as changes within the sea ice rheological term are required to explain the observations.

In another hand, this simple ice-ocean boundary layer coupled dynamical model allows to investigate the link between the sea ice properties and the propagation of inertial oscillations within the ocean. Indeed, the Arctic ocean is characterized by a shallow mixed-layer depth at near freezing-point temperatures. The mixed-layer depth is generally small and controlled by the pronounced underlying cold halocline that limits the depth of winter convection. The mixed-layer freshwater results from ice melting, rivers runoff, and from the transport of low salinity

Pacific waters. The vertical mixing rate is of high importance, because mixing of warmer deeper layers can heat the mixed layer and affect surface fluxes and the sea ice variability. The observed mixing rate has been found to be small as compared to lower latitudes (*Gregg*, 1989; *Rainville and Winsor*, 2008; *Fer*, 2009). Relatively high vertical mixing rate are nonetheless found over bottom topographic features, which highlights the role of internal waves in the Arctic basin (*D'Asaro and Morison*, 1992). These internal waves can be generated by tides (*D'Asaro and Morison*, 1992) or by sea ice motions that generate near inertial currents (*McPhee and Kantha*, 1989; *Pinkel*, 2005; *Lenn et al.*, 2011). Thus, understanding the variability of the energy transfer from the atmosphere to the ocean, through sea ice, in the inertial range is a major concern. Typical values of the thickness of the mixed layer and the turbulent kinetic energy produced within the ocean mixed layer can be inferred from the model.

3.2 A simple ocean - sea ice coupled dynamical model

For about 40 years, many works have focused on the modelling of oceanic inertial currents induced by moving storms and fronts because they significantly contribute to the vertical mixing of the global ocean (*Pollard and Millard*, 1970; *Watanabe and Hibiya*, 2002; *Alford*, 2003; *Elipot and Gille*, 2009). A full description of the propagation of inertial waves requires taking topography, eddies, and the entire momentum equation into account (*D'Asaro et al.*, 1995a; *Young and Ben Jelloul*, 1997; *Garrett*, 2001). However, a focus on the few first inertial periods after the storm passage (*i.e.* before the propagation of inertial waves towards the thermocline) allows a simplified description of the energy transfer from winds to inertial currents. Thus, a slab model of the oceanic surface boundary layer is suitable for the description of inertial oscillations (*Pollard and Millard*, 1970; *Plueddemann and Farrar*, 2006). The horizontal pressure gradients may be dropped from the momentum equation if the storm translation speed is greater than the internal wave group velocity (1 to 3 $\mathrm{m.s^{-1}}$), which is the case for most of the storms (*Greatbatch*, 1984). Finally, the non-linear advection terms may also be dropped from the momentum equation because of their little effect in the ocean response to a moving storm (*Greatbatch*, 1983).

The damping of inertial motions is related to a downward radiation of near-inertial waves excited by inertial pumping, and to the vertical penetration of turbulent momentum related to the shear induced by near-inertial motions ((*Park et al.*, 2009) and references therein). As we need an analytical solution of the ocean mixed-layer response, we choose a very idealized description of the damping term : the deep ocean is assumed to be at rest, and the damping term is written as a friction at the base of the ocean surface boundary layer that is proportional to the surface ocean velocity (as, *e.g.*, in (*Pollard and Millard*, 1970; *Gent et al.*, 1983; *Plueddemann and Farrar*, 2006)). The friction velocity that takes place within the ocean surface layer is referred to as γ (unit $\mathrm{m.s^{-1}}$), so that the induced stress corresponds to $\rho_w \gamma U_w$ (unit $\mathrm{N.m^{-2}}$), where U_w and ρ_w are the norm of the ocean surface velocity and the density of the ocean surface layer, respectively.

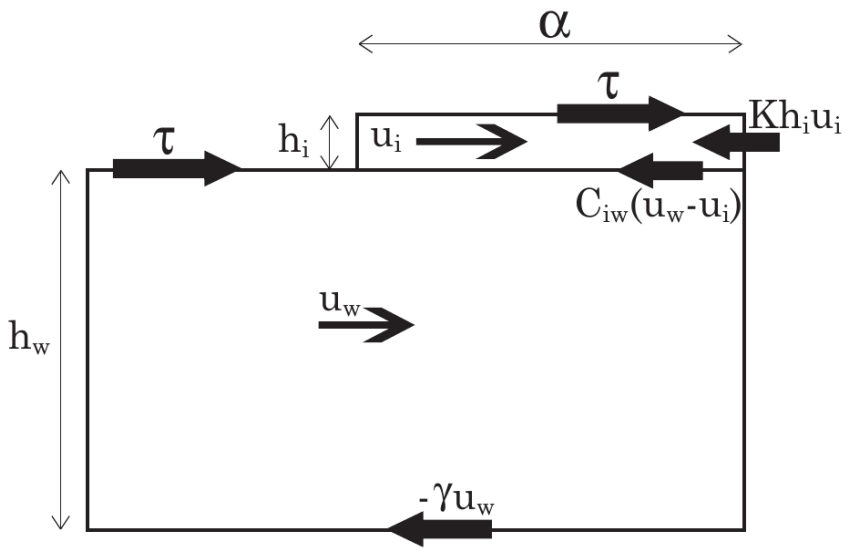

FIGURE 3.1 – Sketch of the sea ice slab model coupled to the ocean slab model following hypotheses discussed in section 3.2 : a sea ice slab (indices i) of thickness h_i is coupled to an ocean layer (indices w) of with h_w. Wind stress forcing τ is applied to both the ice and the water column, with relative weights α and $1-\alpha$, respectively, where α represents the ice concentration. Friction is present within the ice (Kh_iu_i), at the ice-water interface ($C_{iw}(u_w - u_i)$) and at the bottom of the ocean layer (γu_w).

The simplifications mentioned above are assumed to be suitable for the sea ice response to a moving storm, and the resulting sea ice slab model is coupled to the ocean slab model as outlined on Figure 3.1. The resulting set of coupled momentum equations is :

$$\begin{cases} \frac{du_i}{dt} &= \omega_0 v_i - \frac{C_{iw}}{h_i}(u_i - u_w) - K u_i + \frac{\tau_x}{\rho_i h_i} \\ \frac{dv_i}{dt} &= -\omega_0 u_i - \frac{C_{iw}}{h_i}(v_i - v_w) - K v_i + \frac{\tau_y}{\rho_i h_i} \\ \frac{du_w}{dt} &= \omega_0 v_w - \frac{\gamma}{h_w} u_w - \frac{\alpha C_{iw}}{h_w}(u_w - u_i) + \frac{(1-\alpha)}{\rho_w h_w}\tau_x \\ \frac{dv_w}{dt} &= -\omega_0 u_w - \frac{\gamma}{h_w} v_w - \frac{\alpha C_{iw}}{h_w}(v_w - v_i) + \frac{(1-\alpha)}{\rho_w h_w}\tau_y \end{cases} \tag{3.1}$$

where (u, v) are the horizontal velocity components of sea ice (index i) and the ocean surface layer (index w), h_i and h_w are the thickness of sea ice and the ocean surface layer respectively. The densities of each layer are referred to as ρ_i and ρ_w, α is the sea ice surface fraction, and $\omega_0 = 2\pi f_0$ is the Coriolis frequency. The stress at the interface between sea ice and the underlying water is taken as $\rho_w C_{iw}(U_i - U_w)$ (in N.m^{-2}), where U_i and U_w are the speed norm of sea ice and ocean surface layer, and C_{iw} is the ice-ocean drag coefficient. Here, we consider that C_{iw} is independent of the velocities U_i and U_w. Such a linear form is more suitable for the ocean-ice friction than for the air-ice friction because the air kinematic viscosity is about 10 times smaller

than the sea water viscosity, and because currents are slower than winds. The quadratic form would nonetheless be a better approximation because the Reynolds number remains greater than unity, and because the form drag associated with sea ice protuberances is usually defined using a quadratic form (*McPhee and Kantha*, 1989). However, we use a linear form (as *Heil and Hibler III* (2002) and *Weatherly et al.* (1998)) since it allows an analytical solution of (3.1). For the sake of simplicity, the wind stress (τ_x, τ_y) is choosen to be the same on sea ice as on open water (according to *Lepparanta* (2004) the factor between both is typically 1.2).

In this crude model, the internal sea ice friction is taken as a stress equal to $\rho_i K h_i U_i$ (unit N.m^{-2}), where K (unit s^{-1}) is a friction coefficient that represents the inverse of a temporal scale of dissipation. The introduction of such a linear friction term might appear as a strong simplification with regard to the elasto-brittle, i.e. strongly non-linear, character of sea ice rheology (*Girard et al.*, 2011; *Weiss et al.*, 2007). However, as shown below, a simple model such as this describes reasonably well the ice behavior in the frequency domain when properly averaged over large spatial and time scales, especially during summer. Instead of performing a mechanical modelling at the fine scale, we here use this model for a comparative study of the sea ice average mechanical behavior between winter and summer, in different regions of the Arctic, or between different periods. This model takes into account the effect of ice thickness (e.g. ice thinning in recent years) and concentration in the momentum balance

3.3 Solution of the model equations

It is convenient to use the complex velocities and stress :

$$\left\{ \begin{array}{lcl} \tilde{U}_i &=& u_i + iv_i \\ \tilde{U}_w &=& u_w + iv_w \\ \tilde{\tau} &=& \tau_x + i\tau_y \end{array} \right. \tag{3.2}$$

Hence, equations (3.1) become :

$$\left\{ \begin{array}{lcl} \frac{d\tilde{U}_i}{dt} &=& -i\omega_0\tilde{U}_i - \frac{C_{iw}}{h_i}\tilde{U}_i + \frac{C_{iw}}{h_i}\tilde{U}_w - K\tilde{U}_i + \frac{\tilde{\tau}}{\rho_i h_i} \\ \\ \frac{d\tilde{U}_w}{dt} &=& -i\omega_0\tilde{U}_w - \frac{\alpha C_{iw}}{h_w}\tilde{U}_w + \frac{\alpha C_{iw}}{h_w}\tilde{U}_i - \frac{\gamma}{h_w}\tilde{U}_w + \frac{(1-\alpha)}{\rho_w h_w}\tilde{\tau} \end{array} \right. \tag{3.3}$$

Taking the derivative of the first equation of (3.3) with respect to time, and combining to the second equation yields :

$$\left\{ \begin{array}{lcl} \frac{d^2\tilde{U}_i}{dt^2} &+& \left(2i\omega_0 + \frac{\alpha C_{iw}}{h_w} + \frac{C_{iw}}{h_i} + \frac{\gamma}{h_w} + K\right)\frac{d\tilde{U}_i}{dt} \\ &+& \left[\left(i\omega_0 + \frac{\gamma}{h_w} + \frac{\alpha C_{iw}}{h_w}\right)\left(i\omega_0 + \frac{C_{iw}}{h_i} + K\right) - \frac{\alpha C_{iw}^2}{h_i h_w}\right]\tilde{U}_i \\ &=& \frac{1}{\rho_i h_i}\frac{d\tilde{\tau}}{dt} + \left[(1-\alpha)\frac{C_{iw}}{\rho_w h_w h_i} + \frac{1}{\rho_i h_i}(i\omega_0 + \frac{\gamma}{h_w} + \frac{\alpha C_{iw}}{h_w})\right]\tilde{\tau} \end{array} \right. \tag{3.4}$$

which can be solved in the Fourier's domain to write the transfer function :

$$\begin{cases} \hat{G}(\omega) = \frac{\hat{U}_i(\omega)}{\hat{\tau}(\omega)} \\ = \frac{1}{\rho} \dfrac{\frac{1}{h_i h_w}(C_{iw}+\gamma)+i(\omega+\omega_0)\frac{1}{h_i}}{\left[\left(-(\omega+\omega_0)^2+\frac{1}{h_w}(\alpha C_{iw}+\gamma)(K+\frac{C_{iw}}{h_i})-\frac{\alpha C_{iw}^2}{h_i h_w}\right)+i(\omega+\omega_0)\left(\frac{C_{iw}}{h_i}+\frac{\alpha C_{iw}}{h_w}+\frac{\gamma}{h_w}+K\right)\right]} \end{cases} \tag{3.5}$$

where $\omega = 2\pi f$ and $\rho_i = \rho_w = \rho$ is assumed. Equation 3.5 shows a resonance when $\omega + \omega_0 = 0$, hence at the negative frequency of $-f_0 \approx -2$ cycles per day.

This transfer function allows linking between ice velocities and wind stresses, i.e. to express the frequency response of sea ice to a given external forcing as a function of oceanic and sea ice internal parameters. In this analysis, no oceanic data (*e.g.* velocity) are needed. This is the strength of our method since such data do not exist or are very rare. Aside from the present study, equation (3.5) could be used to infer angles between the average wind stress and ice motion by looking to its imaginary part at $\omega = 0$ cycle.day^{-1}. We here briefly checked that angles predicted by our model were consistent with common observations : by setting values of parameters inferred from section 3.5.2 and summed up in table 3.1, we find average angles varying from -29° to -37°, the minus sign indicating an angle in the clockwise direction, i.e. an ice drift deviated toward the right with respect to the wind direction, which is consistent in the northern hemisphere.

3.4 Computation of the transfer functions from the data

We consider 8 different ice-tethered buoy datasets, built from the International Arctic Buoy Program (IABP) buoys dataset (described in more details in *Gimbert et al.* (2012a)) in the following way. First, two datasets related to 10-day buoy trajectories are constructed : the "central pack" and the "peripheral zone" dataset contains buoy positions recorded within the regions delimited on Figure 3.2 by the blue and red lines, respectively. The central pack consists of thick, highly cohesive perennial sea ice, i.e. is characterized by small inertial oscillations and small M values, where M is defined in *Gimbert et al.* (2012a) : M is a non dimensional parameter that evaluate the magnitude of the sea ice velocity at the inertial frequency with respect to the norm of the velocity. This way, the parameter M quantitatively accounts for the sea ice time-dependant inertial oscillation magnitude. In contrast, the peripheral zone is nowadays essentially covered by seasonal sea ice, hence a poorly cohesive cover during the summer months, and so is associated with strong oscillations and large M-values. Secondly, each of these 2 datasets are splitted following the winter and summer seasons, defined in *Gimbert et al.* (2012a) from the annual cycle described by the monthly M-values (the summer period goes from July to September and the winter period is the rest of the year). Finally, from these 4 datasets, we define 8 datasets by separating the two periods defined from the pluri-annual analysis of M in *Gimbert et al.* (2012a) : period 1 extending from 1979 to 2001, and period 2 from 2002 to

			Dataset Number	Fixed parameters h_i (m)	α	Tunning parameters K (d^{-1})	h_w (m)	$\mathcal{T}$ (d)	M
Period 1	Pack Zone	Winter	1	4	0.98	12	45	52	0.151
		Summer	2	3	0.9	7	35	40	0.172
	Periph. Zone	Winter	3	3	0.96	11.5	45	52	0.156
		Summer	4	2	0.82	7	25	29	0.244
Period 2	Pack Zone	Winter	5	3.5	0.96	7.5	30	35	0.182
		Summer	6	2.5	0.84	5.5	25	29	0.220
	Periph. Zone	Winter	7	2.5	0.95	8.5	20	23	0.202
		Summer	8	1.5	0.62	4.5	10	12	0.371

TABLE 3.1 – Model parameters used to compute the simulations plotted on Figure 3.6. We here set $C_{iw} = 5.10^{-4}\ m.s^{-1}$ and $\gamma = 10^{-5}\ m.s^{-1}$. The values of C_{iw}, γ and h_i are typical values taken from the literature. The concentration α is computed from the NSIDC sea ice concentration dataset. The modeled transfer functions are adjusted compared to the data by tuning K and h_w, since these two parameters play an independent role : K controls the amplitude of the inertial peak while h_w only controls its width.

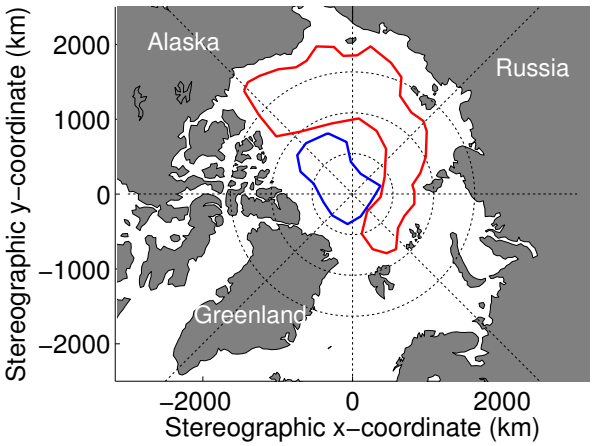

FIGURE 3.2 – Spatial sampling of the 10 days buoy trajectories : peripheral zone (red) and central pack (blue).

2008. Each dataset are numbered from 1 to 8 as recapitulated in table 3.1.

3.4.1 Sea ice data

For each 10-day buoy trajectory in any one of the 8 datasets, the Fourier transform $\hat{U}_b$ of the buoy velocities is computed following equation 4 of *Gimbert et al.* (2012a). This equation leads to a signed fourier transform of the buoys velocities, in which the inertial frequency is negative and corresponds to $f = -f_0$, since inertial oscillations are associated to a rotation in the clockwise direction in the northern hemisphere. These Fourier transforms thus obtained are then averaged over all trajectories of a given dataset. The results, shown in Figure 3.3(a), confirm :

- the existence of seasonal and spatial variations of the inertial oscillation amplitude
- the increase of the inertial oscillation amplitude in recent years, more or less marked depending on the dataset. For example : the maximum increase is observed in summer and within the peripheral zone, where the inertial oscillation amplitude varies from 1.16 km.d^{-1} in period 1 to 2.12 km.d^{-1} in period 2, i.e. a 86% increase, and the minimum increase is observed in summer and in the central pack, where the inertial oscillation amplitude varies from 0.59 km.d^{-1} in period 1 to 0.87 km.d^{-1} in period 2, i.e. a 40% increase.

3.4.2 Wind data (forcing)

Estimates of the surface winds for each buoy position are obtained from the ERAinterim data set provided by the ECMWF ($http://data-portal.ecmwf.int/data/d/interimdaily/$). This dataset is a model simulation at a T255 horizontal resolution, including 12 hours 4D-VAR assimilation of observations. The 12 h time window for data assimilation introduces an artificial peak in the wind velocity spectrum undifferently present at $f = -2$ and $f = 2$ cycles.day^{-1} ; in the following, this peak is deleted using a linear interpolation in log-log space between the

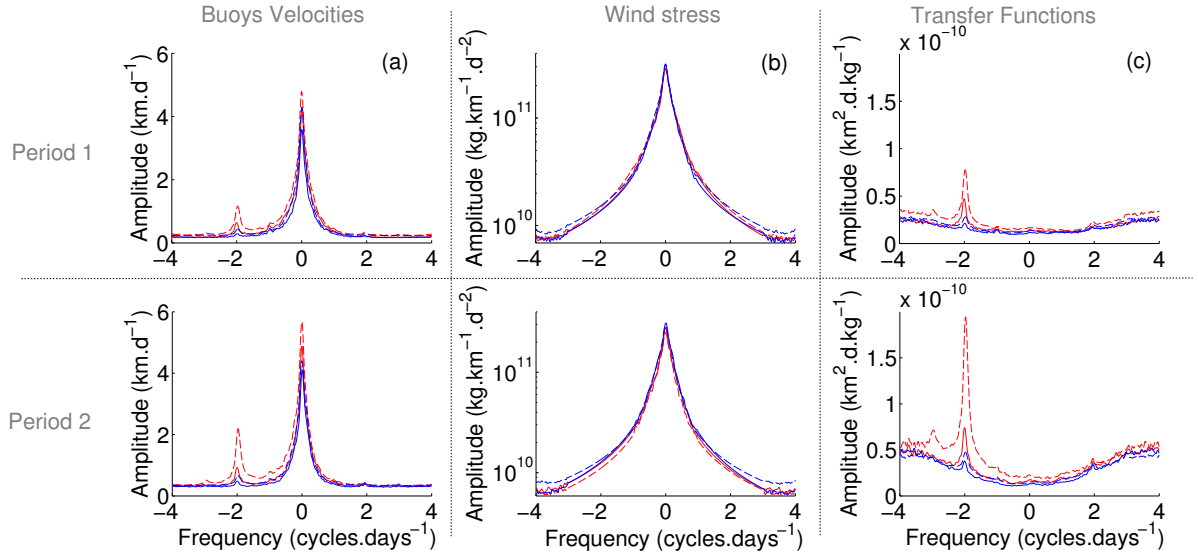

FIGURE 3.3 – Fourier transform of the buoy velocities (column (a)), of the wind stress (column (b)) and associated transfer functions (column (c)) for period 1979-2001 (top row) and period 2002-2008 (bottom row). The red and blue curves correspond respectively to summer and winter. The thick and dashed lines correspond to the pack zone and peripheral zone, respectively.

frequencies -2.5 and -1.5 cycles.day^{-1} and 1.5 and 2.5 cycles.day^{-1}. The outputs used here are 3-hourly, on a regular grid of 0.625° by 0.625°.

For each buoy position (x_i, y_i), we associate the wind velocity components u_a and v_a by looking for the closest value that Figures within the ERAinterim dataset. Then for each buoy trajectory of the 8 datasets, the Fourier transform $\hat{\tau}_b$ of the wind stress at the buoys locations is computed using a quadratic dependence to the wind speed with a constant drag coefficient $C_a = 0.0012$ (*Hibler*, 1979). Finally, the Fourier transfroms are averaged over all the trajectories, for each dataset.

Remarkably, no significant change in the spectrum of the wind forcing with neither the region, the season, nor the period, is obtained from the ERA-interim dataset (Figure 3.3(b)).

This is in strong contrast with what is observed for ice velocities in section 3.4.1, which shows much changes with respect to the season and the period. This underlines the purpose of this study, showing that changes within sea ice (weither they are about changes in sea ice concentration, sea ice thickness or sea ice internal mechanical properties) are necessary to explain these discrepencies. The purpose of this paper is to evaluate the relative contribution of these sea ice properties in the observed overall change, by evaluating changes of sea ice motion relatively to wind forcing from the use of transfer functions.

3.4.3 Transfer functions

The transfer function amplitudes $|\hat{G}_b|$ computed using $\hat{U}_b$ and $\hat{\tau}_b$ (Figure 3.3(a) and Figure 3.3(b)) are plotted on Figure 3.3(c). They are roughly symmetric with respect to $f = 0$,

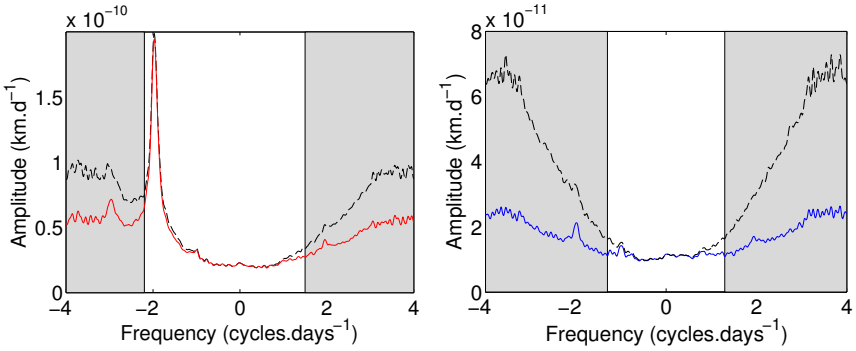

(a) (b)

FIGURE 3.4 – Illustration of the effect of the buoy position uncertainty on the transfer function using datasets (a) number 8 and (b) number 1. The red and blue bold curves are the transfer functions computed from the raw buoy positions. The black dashed curves are associated transfer functions computed using the respective dataset, but after adding noise to the buoy positions (300 m standard deviation). We outline in gray the frequencies affected by the uncertainty on the buoy positions.

except at $f = -f_0$ for which we recognize the inertial oscillation peak with varying amplitude. A plateau characterizes low frequencies, whereas $|\hat{G}_b|$ slightly increases above f_0. As there is a significant uncertainty on the buoys' locations (100 to 300 m, depending on the positioning system), we first analyze the effect of such an uncertainty on the transfer function : from a given dataset, we add noise on the raw buoys positions (x_b, y_b) by defining ($\widetilde{x_b}$,$\widetilde{y_b}$) as $\widetilde{x_b} = x_b + \delta x$ and $\widetilde{y_b} = y_b + \delta y$, where δx and δy are (small) increments randomly picked from a centered gaussian distribution with 300 meters standard deviation. Then, a synthetic transfer function is computed from the noisy buoy positions ($\widetilde{x_b}$, $\widetilde{y_b}$), see Figure 3.4 : the color curves are the transfer function computed from the raw data (here dataset n°8 and dataset n°1) while the black dashed curve are the respective transfer function computed from the noisy buoy positions.

For both of these plots, a good agreement between the two transfer functions is obtained at low frequencies while, at larger frequencies, the two transfer functions disagree. Regions where a strong disagreement is observed are highlighted in gray. We thus explain the high frequency increase of the transfer functions in Figure 3.6 by measurement error of the ARGOS and GPS positioning systems of the buoys. Moreover, on Figure 3.4(a), which considers a dataset showing a large peak at the inertial frequency, we observe an apparent dissymetry on the discrepency between negative and positive part of the spectrum : this is explained by the fact that addition of noise can be neglected at frequencies where its amplitude is much less than the amplitude of the signal itself. For the same reason, on Figure 3.4(b), where almost no peak is observed at the inertial frequency, such dissymetry is not observed anymore and, because velocities are in average smaller for this dataset, the mismatch between the two transfer functions starts earlier (at about 1.5 cycles.days^{-1}) and thus affects the value of the peak at the inertial frequency.

As a consequence, it is important to note that, for transfer functions where a clear peak is observed at the inertial frequency, i.e. for most datasets, values of $|\hat{G}_b|$ are not affected in

between -2.2 and +1.5 cycles.day^{-1} while, for transfer functions exhibiting no peak at the inertial frequency (mostly datasets 1, 3 and 5), the values of $|\hat{G}_b|$ at the inertial frequency may have been artifially increased by noise on the buoys positions, leading to an associated underestimation of K in these cases (see paragraph (iii) of section 3.5.2).

3.5 Modelled transfer functions and results

In *Gimbert et al.* (2012a), we argue that the sea ice inertial oscillation magnitude might be a proxy of the degree of cohesiveness of the sea ice cover. In this study, in order to quantitatively investigate this consideration, the respective contributions of the ocean boundary layer and sea ice cover mechanical properties on the spatial, seasonal and pluri-annual dependance of the inertial oscillations magnitude pointed out in *Gimbert et al.* (2012a) are evaluated through our analytical model presented in section 3.2. To do so, we split the model parameters into two categories :

- The parameters we consider to be fixed or known : C_{iw}, γ, h_i and α. Appropriate values to consider for each dataset are discussed in section 3.5.1. Values for h_i and α are obtained from observations and thus vary from one dataset to another, while, as the absence of direct observations induces large uncertainties on C_{iw} and γ, their respective values are kept the same for all the 8 datasets. A sensitivity analysis will be performed in section 3.6.1 on the values of C_{iw} and γ.
- The tuning parameters h_w and K, on which we discuss the physics. As shown in paragraph (iii) of section 3.5.2, these parameters h_w and K behave separately, allowing the determination of h_w independantly of the K value considered.

Under these considerations, we answer, in a first instance (section 3.5.2), the following questions :

- Is the crude analytical model presented in section 3.2 able to reproduce the main features of sea ice motion in the frequency domain ?
- Is it needed, in addition to already accounted variations in the sea ice thickness h_i and the sea ice concentration α, to consider changes within the Ekman layer thickness h_w and the internal sea ice friction coefficient K in order to reproduce the transfer functions computed for the 8 datasets ? If yes, how h_w and K vary from one dataset to another ?

Secondly, a sensitivity analysis (section 3.6.2) is performed in order to answer to the reciprocal question asked in the second point : can we explain the observations by varying only C_{iw} and γ, instead of K ?

3.5.1 Fixed parameters

The average values of sea ice thickness h_i for each dataset are listed in table 3.1. They are obtained from *Rothrock et al.* (2008). The sea ice concentration is computed at each buoy position from the sea ice concentration dataset collected by the National Snow and Ice Data Center (http ://nsidc.org/data/seaice/index.html), using the same procedure as the one described in

section 4.2 of *Gimbert et al.* (2012a). Then, an average concentration value α is associated to each dataset by averaging all the concentration values associated to each buoy position.

In contrast to α and h_i, direct observations of C_{iw} and γ are missing. The drag C_{iw} related to the linear friction is taken as 5.10^{-4} m.s^{-1}, following previous studies (*Weatherly et al.*, 1998; *Heil and Hibler III*, 2002). This value might be affected by changes in basal ice roughness, for instance if sea ice is more or less fractured. Nonetheless, we will see in section 3.6 that C_{iw} is unlikely to have varied substantially.

Estimating a value of γ suitable for the Arctic basin is more difficult. Indeed, such estimates are absent from the literature. The parameter γ is related to the decay timescale $\mathcal{T} = h_w/\gamma$ that corresponds to the e-folding time of ocean-only free inertial oscillations (see solution of equation 3.3 if $\alpha = 0$ and $\tilde{U}_i = 0$). Equatorward of the polar circle, $\mathcal{T}$ is usually found between 2 and 20 days (*D'Asaro*, 1985), which, for a typical $h_w = 50$ m, corresponds to γ between 3.10^{-4} and 3.10^{-5} m.s^{-1}. However, $\mathcal{T}$ is usually used as a tuning parameter rather than being physically based. The decay timescale $\mathcal{T}$ is related to 2 distinct processes : the turbulence production by vertical current shear, and the radiation of internal waves toward the thermocline (through the so called inertial pumping (*Price*, 1983)). Wave propagation plays the dominant role when rapid decay occurs, the case for which *Park et al.* (2009) have managed to link $\mathcal{T}$ to the ocean characteristics :

$$\mathcal{T} \quad \sim \quad \left(\frac{\omega_0}{\beta^2 h_w^2 N^2} \right)^{1/3} \tag{3.6}$$

The right hand side (RHS) of (3.6) can be estimated from the ocean reanalysis GLORYS1 (Global Eddy permitting Ocean Reanalysis and Simulation (*Ferry et al.*, 2010)), which has been used in the Arctic basin by *Lique et al.* (2010). To estimate h_w in equation (3.6), we use a density criteria rather than the temperature criteria used by *Park et al.* (2009), because the mixed-layer depth is strongly controlled by salinity in the Arctic (*Rudels et al.*, 1996). Hence, the depth h_w is taken as the depth over which the potential density σ_0 does not vary by more than 0.01 kg.m^{-3} as compared to the surface. Typical winter and summer temperature and salinity profiles from GLORYS1 are shown in Figure 3.5(b) with the related mixed layer-depths.

Climatological values of h_w are shown in Figure 3.5(a), together with the RHS of (3.6). Figure 3.5(a) shows that if the theory of *Park et al.* (2009) is extended northward of the Arctic circle, the decay timescale $\mathcal{T}$ is expected to be much longer than the maximum of 20 days that they found near 60°N. Hence, $\mathcal{T}$ is probably controlled by the vertical current shear and observations show very small vertical mixing rates in the Arctic as compared to lower latitudes (*Gregg*, 1989; *Rainville and Winsor*, 2008; *Fer*, 2009). Hence, we have to choose a value of γ that gives decay timescales $\mathcal{T}$ longer than 20 days. With a maximum h_w of 50 m (Figure 3.5(a)), it can be estimated that $\gamma < 3.10^{-5}$ m.s^{-1} in the Arctic basin. In the following, we first use an order of magnitude for γ of 10^{-5} m.s^{-1}. The sensitivity of our model's results to a varying γ will be discussed in section 3.6.1.

The mixed-layer term of equation (3.3) with no wind forcing ($\tilde{\tau} = 0$) shows that the decay timescale of ocean currents (in the absence of forcing) depends on γ and C_{iw}. The values that

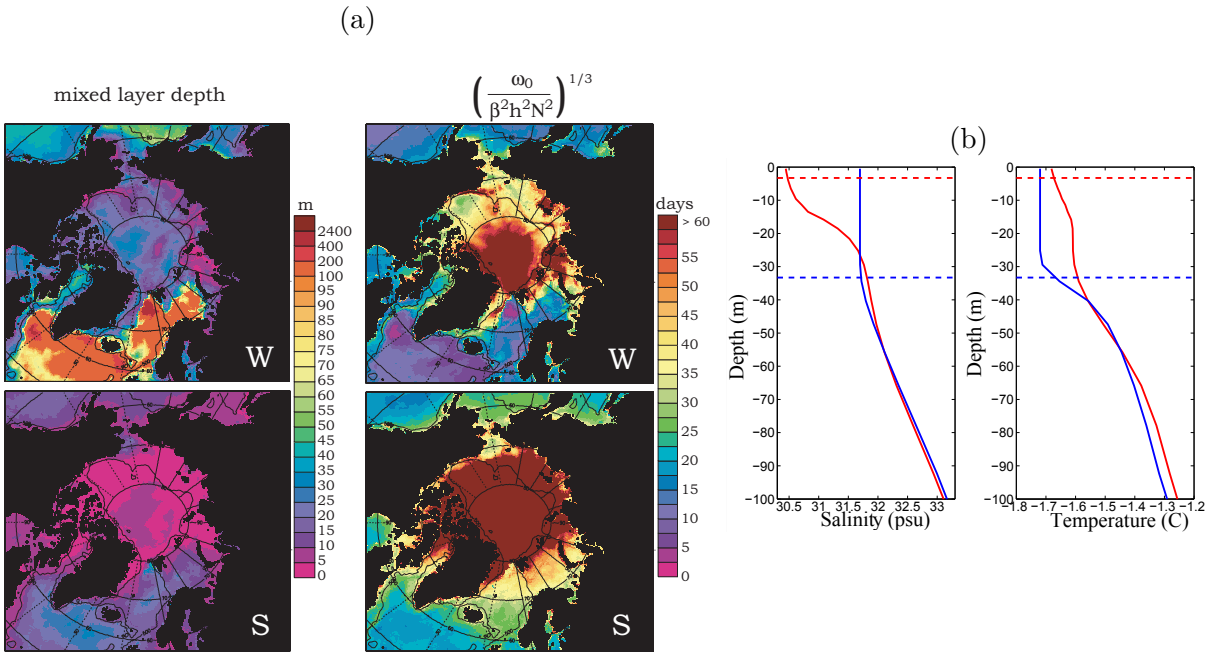

FIGURE 3.5 – Oceanic parameters evaluated using GLORYS1. (a) Mixed-layer depth in meters defined using a density criteria (left) and right hand side of equation (3.6), in days (right). Top row corresponds to the winter (W) season and bottom row to the summer (S) season. Summer stands for July-August-September, a winter for the other months of the climatology. The climatology is computed using monthly means of the 2002-2008 ocean - sea ice reanalysis GLORYS1 (*Ferry et al.*, 2010) and a density criteria of 0.01 kg.m^{-3}. The buoyancy frequency N^2 in equation 3.6 is computed using the maximum stratification in the whole water-column. (b) Salinity and temperature profiles at North Pole, from monthly climatological fields from GLORYS1 in August (summer, in red) and February (winter, in blue). The mixed-layer depth calculated using the density criteria of 0.01 kg.m^{-3} is indicated by the dashed lines.

have been taken for these parameters ensure that the decay of ocean currents is controled by C_{iw}, since $C_{iw} \gg \gamma$. This is in good agreement with the results found by *Pinkel* (2005) using a linear model of near-inertial wave propagation and observations in the Arctic.

3.5.2 Results and interpretation

Figure 3.6 shows the modulus of the transfer functions computed from the data, as well as the one modelled by using the tuning parameter values K and h_w that give the best fit (in the mean least square sense) for frequencies ranging from -2.2 cycles.days^{-1} to 1 cycles.days^{-1}. The parameters used to reproduce the transfer functions for each of the 8 datasets are detailed in table 3.1. We can see that :

(i) In general, for all 8 datasets, the model of equation 3.5 accounts well for the observed transfer function within the frequency range of -2.2 cycles.days^{-1} to 1 cycles.days^{-1}. This is not the case outside this window, due to the result of noise on the buoys' positions (see section 3.4.3).

(ii) This simple linear model works better for summer datasets, when sea ice is closer to a free drift configuration, i.e. when sea ice remains closer to a fluid-like linear behaviour. However, the

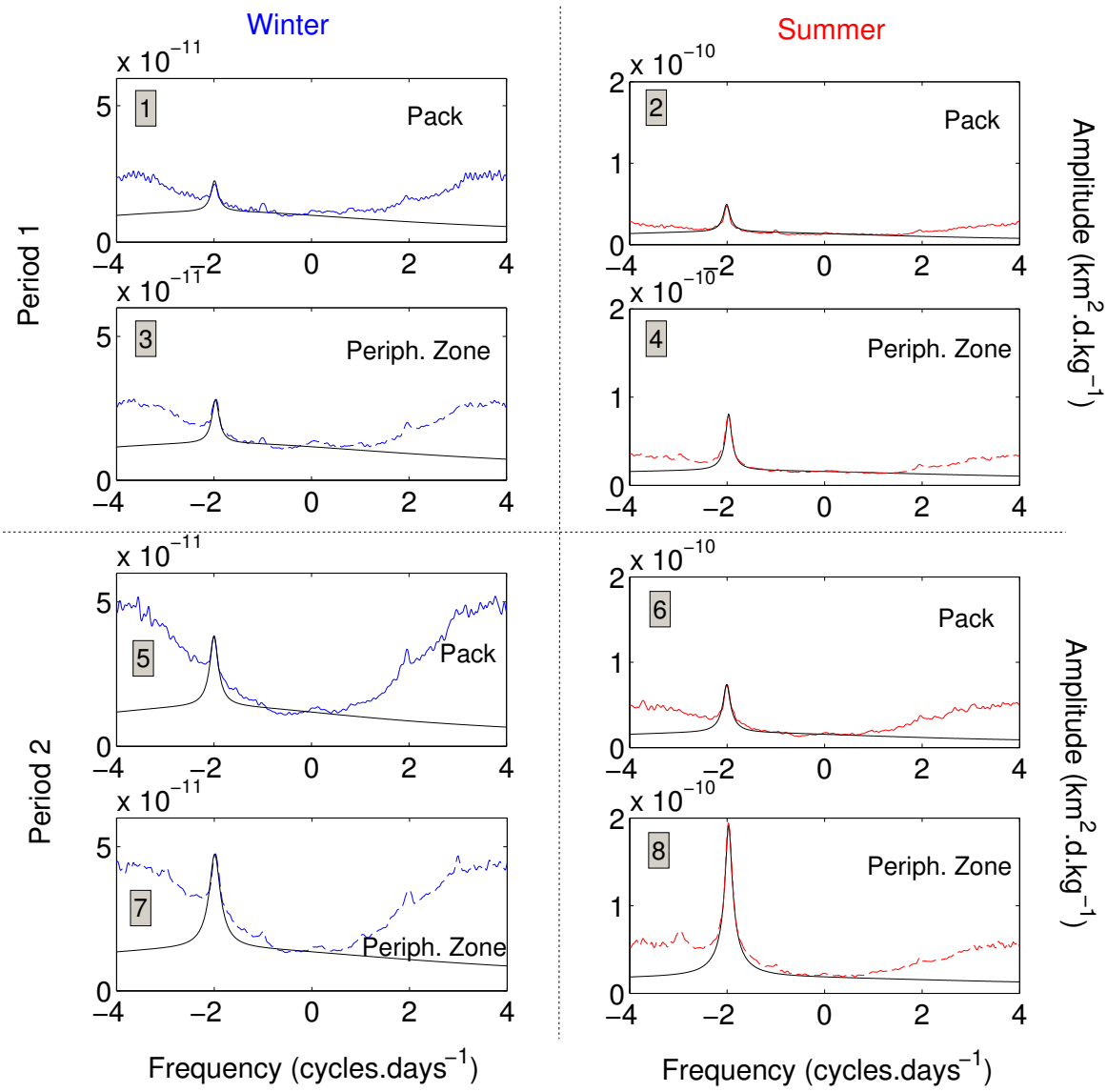

FIGURE 3.6 – Modulus of the transfer functions of the buoy trajectories for the 8 datasets. The bold and dashed lines indicate the transfer functions computed using buoy trajectories selected within the central pack zone and within the peripheral zone, respectively. Top and bottom rows plot the transfer functions computed for period 1 and period 2, respectively. Left column and right column plot the transfer functions computed from the winter datasets (blue curves) and from the summer datasets (red curves), respectively. The modelled transfer functions computed using equation 3.4 and parameters of table 3.1 are plotted in black.

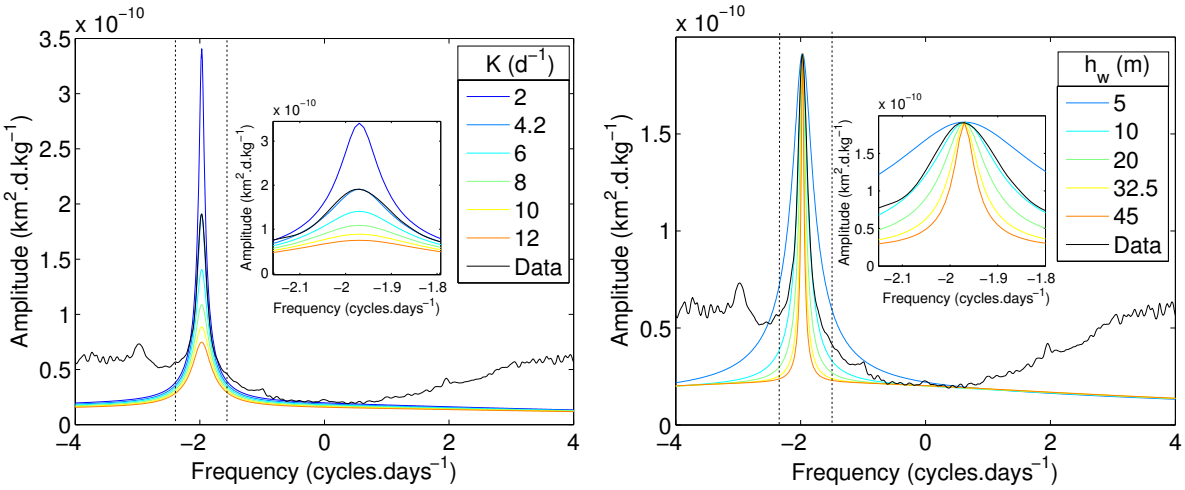

(a) (b)

FIGURE 3.7 – Influence of the tuning parameters on the shape of the transfer function for dataset number 8. (a) Influence of the sea ice cover internal friction K fixing $h_w = 12.5$ meters and (b) influence of the Ekman layer thickness h_w fixing $K = 1.2$ days^{-1}. For both plots, the data transfer functions are plotted in black. A zoom around the inertial frequency $-f_0$ is done for each plot. The known parameters used are those considered for dataset number 8 in table 3.1.

agreement is still good for the winter datasets, at least for datasets 3, 5 and 7. This means that a simple linear formulation of the internal sea ice friction is able to reproduce the main features of the sea ice cover average mechanical response in the frequency domain. For the winter ice pack of period 1 (dataset number 1), the agreement is less convincing. This sets, in this present analysis, the limit of the present linear model to describe the elasto-brittle rheology of sea ice (*Weiss et al.*, 2007; *Girard et al.*, 2011), even after averaging at large spatial and time scales.

(iii) Setting typical values for C_{iw}, γ, h_i and α, both K and h_w need to vary from one dataset to the other to best fit. To highlight this point, Figure 3.7 plots the data transfer function of dataset number 8 along with the modelled one by fixing h_w and varying the values of K (Figure 3.7(a)) and by fixing K and varying the values of h_w (Figure 3.7(b)). From these two plots, it is obvious that the two parameters K and h_w work separately : K controls the amplitude of the transfer function peak at the frequency $f = -f_0$ and, to a lesser extent, the level of the plateau at low frequency, while h_w only affects the width of the peak at $f = -f_0$, without affecting its amplitude nor the plateau at low frequencies. Thus, for a value of K that leads to a good estimate of the data transfer function at $f = -f_0$ and $f = 0$, the tuning of h_w further allows to get a good agreement in the surroundings of $-f_0$.

Because noise on the buoy positions may have increased the amplitude of the peak at the inertial frequency for datasets 1,3 and 5, it is important to notice that the associated values of K are likely to be underestimated in these cases.

(iv) Changes within sea ice dynamic reported by *Rampal et al.* (2009a) with respect to time and space are associated not only to changes in the sea ice thickness h_i and the sea ice

concentration α, which are parameters already taken into account in the momentum balance of our model, but also to changes in the sea ice internal friction K and the ocean Ekman layer thickness h_w.

The friction coefficient K is strongly decreased from winter to summer, in the central ice pack as well as in the peripheral zone. This means that the sea ice mechanical behaviour varies drastically with the season, independently of the region considered. This is in agreement with the annual cycle described by the M values in *Gimbert et al.* (2012a).

Wether it is for period 1 or period 2 and in summer or in winter, K seems to be independent of the region considered. This suggests that the large inertial oscillation amplitudes observed in summer in the peripheral zone (see *Gimbert et al.* (2012a)) essentially result from a direct effect of ice thinning and decreasing concentration on the momentum balance, and shows that there is no contrast of mechanical behavior between multiyear and first-year sea ice.

Finally, whatever the season or the region considered, K decreased by a factor of 1.5 from period 1 to period 2. As an example, the mechanical behavior of winter sea ice in recent years is comparable to that of summer sea ice in previous years.

For all that, considering the 8 datasets, we obtain an anticorrelation of $\xi = -0.75$ between the M and K values. The probability to find a lower correlation coefficient is estimated to 0.25% by randomly reshuffling the values, proving that this correlation is significant. This means that the previously defined M parameter (*Gimbert et al.*, 2012a) is a simple and reasonably accurate proxy of the level of internal friction.

We can thus conclude that the sea ice decline already pointed out by several authors (*Lindsay and Zhang*, 2005; *Comiso et al.*, 2008; *Kwok and Rothrock*, 2009; *Rampal et al.*, 2009a) is not restricted to a decrease of sea ice concentration and sea ice thickness, but is accompanied by a mechanical weakening of the ice cover. As the direct effect of ice thinning and declining concentrations on the momentum balance is already taken into account in our model, this evolution is, we believe, an indirect effect of the ice state onto the ice internal friction through the degree of fragmentation of the ice cover.

Concerning the oceanic boundary layer h_w, the order of magnitude as well as the seasonal and regional dependence obtained from our model within the second period are in good agreement with those obtained from GLORYS, shown on Figure 3.5, for the period 2002-2008 : h_w is of the order of 10 meters within the peripheral zone in summer and of the order of several tens of meters (approximately 30-40 meters) in winter within the central pack. Values of h_w considerably decreased from period 1 to period 2, since it is almost divided by two whatever the season and the region. Thus, seasonal and decadal variations of the ocean mixed-layer depth h_w are observed. These variations are consistent with previous studies showing an enhanced stratification in the upper halocline when sea ice melts or when river runoffs are intense (*Rudels et al.*, 1996). The stronger stratification may alter h_w either because the criteria used to define h_w ($\Delta\sigma_0 < 0.01$ kg.m^{-3}) is reached closer to the surface, or because the stronger stratification limits vertical mixing (*Stull*, 1988). In these 2 cases, h_w is decreased when ice melting and river runoff are increased, as found in GLORYS and in our parameter estimation. Such an explanation

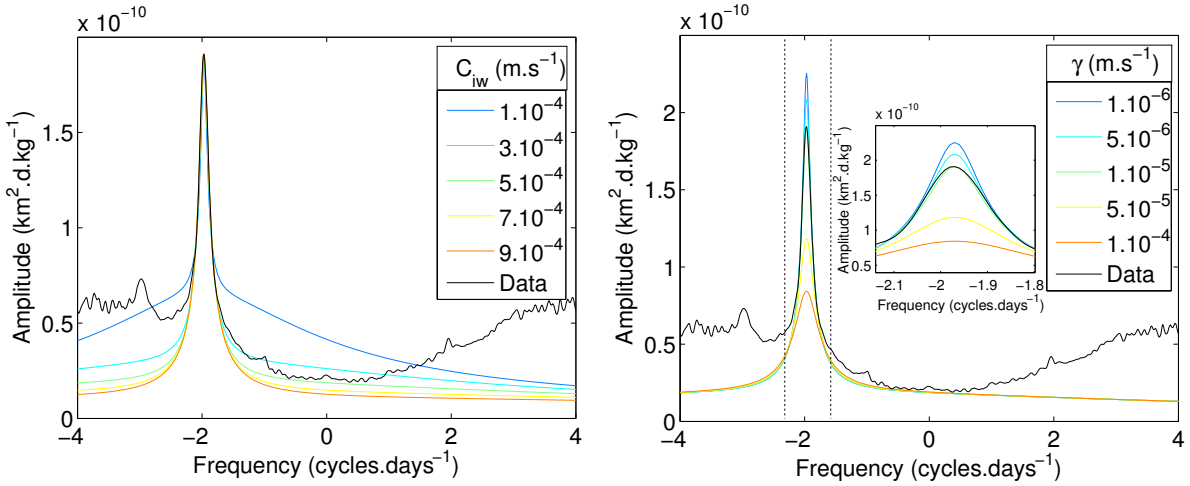

(a) (b)

FIGURE 3.8 – (a) Influence of the drag coefficient C_{iw} and (b) influence of the turbulent viscosity γ on the shape of the transfer function for dataset number 8. For both plots, the data transfer functions are plotted in black. A zoom around the inertial frequency $-f_0$ is done on graph 3.7(b). The other known and tuning parameters used are those considered for dataset number 8 in table 3.1.

relates the evolution of h_w to the evolution of the salinity barrier. A more complete picture of the evolution of h_w would include evolution of the mechanical forcing of h_w, through the estimation of the production of turbulent kinetic energy $\gamma|\tilde{U}_w|$ within the ocean surface layer. Such an estimation can be done using our model and, since this study is out of the scope of this paper, these computations are presented in Appendix 3.8.

3.6 Sensitivity analysis

We showed above that assuming typical values for C_{iw} and γ, changes observed within the sea ice dynamical response to the inertial forcing are explained by tuning K and h_w. However, since large uncertainties lie on C_{iw} and γ, it is important to ask the following questions :

- 1- To what extent K and h_w vary when considering different values for γ and C_{iw} ? Is the hierarchy in the K values obtained for the different datasets conserved in these cases ?
- 2- Can the observations be explained by changing γ and C_{iw}, while keeping K constant over all datasets ?

3.6.1 Sensitivity on γ and C_{iw}

Figure 3.8(a) shows the influence of C_{iw} on the shape of the transfer function. When varying the values of C_{iw} of one order of magnitude around the typical value of 5.10^{-4} m.s^{-1}, this shape is largely affected, at all frequencies. This implies that the value of C_{iw} is robust and well constrained. This is confirmed when trying to fit all 8 datasets by allowing K, h_w and C_{iw}

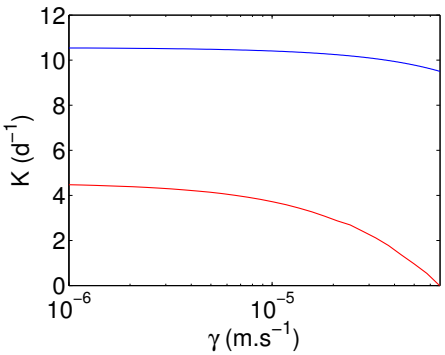

FIGURE 3.9 – K vs γ for dataset number 1 (blue line) and 8 (red line), for γ ranging between 1.10^{-6} m.s^{-1} and $6.7.10^{-5}$ m.s^{-1} and taking $C_{iw} = 5.10^{-4}$ m.s^{-1}. The best fit of the data transfer functions for each γ value is obtained by only tuning the internal sea ice cover friction K, with h_w as in table 3.1.

to vary : in that case, the values of C_{iw} giving the best fits only vary from $3.5.10^{-4}$ m.s^{-1} to $4.6.10^{-4}$ m.s^{-1}. Figure 3.8(b) shows the influence of γ on the transfer function : in addition to K, γ controls the amplitude of the peak at $f = -f_0$ as well. We thus consider $C_{iw} = 5.10^{-4}$ m.s^{-1} to be a robust value and limit, in this section, our sensitivity analysis to the study of the parameter γ, since it qualitatively plays the same role as K on the transfer function.

We start by defining a lower and upper bounds for γ. The lower bound is arbitrarily chosen to be equal to 1.10^{-6} m.s^{-1}, which is one order of magnitude lower than the value taken into account in section 3.5.2. The upper bound is set from the observations : indeed, the amplitude of the peak at the inertial frequency $-f_0$ for dataset number 8 cannot be reproduced when considering a value of γ greater than $6.7.10^{-5}$ m.s^{-1}. We thus consider $\gamma = 6.7.10^{-5}$ m.s^{-1} as an upper bound. Such a value gives $K = 0$ d^{-1} for dataset number 8, which means that, in this case, sea ice exactly behaves in free drift within the peripheral zone during the second period. We thus assume that γ can vary between 1.10^{-6} m.s^{-1} and $6.7.10^{-5}$ m.s^{-1}.

Figure 3.9 shows the variation of K with respect to γ for datasets number 1 and number 8. For dataset number 1, we can see that the value of K does not vary considerably with γ : the internal friction that takes place within the sea ice cover dominates compared to the damping that takes place within the oceanic Ekman layer. On the contrary, for dataset number 8, the turbulent viscosity γ strongly influences the value of K. K ranges from about 4 d^{-1} to 0 d^{-1} as γ increases from 1.10^{-6} m.s^{-1} to $6.7.10^{-5}$ m.s^{-1}. It is also clear from Figure 3.9 that K-values would not significantly change when considering γ values below 1.10^{-6} m.s^{-1}, whatever the dataset considered. The K-values obtained for the 8 datasets when considering $\gamma = 6.7.10^{-5}$ m.s^{-1} are given in table 2.

The hierarchy between the different datasets, and therefore the associated interpretation, is conserved compared to that of table 1 and section 3.5.2. We note however that with such large value of γ the associated decay timescales $\mathcal{T} = h_w/\gamma$ vary between 2 to 8 days, i.e. are small compared to expected values in the Arctic (see section 3.5.1).

			Dataset Number	Fixed parameters h_i (m)	α	Tunning parameters K (d^{-1})	h_w (m)	$\mathcal{T}$ (d)	M
Period 1	Pack Zone	Winter	1	4	0.98	10.5	45	8	0.1514
		Summer	2	3	0.9	6	35	6	0.172
	Periph. Zone	Winter	3	3	0.96	10.5	45	8	0.156
		Summer	4	2	0.82	5	25	6	0.244
Period 2	Pack Zone	Winter	5	3.5	0.96	6	30	5	0.182
		Summer	6	2.5	0.84	3.5	25	4	0.220
	Periph. Zone	Winter	7	2.5	0.95	7	20	3	0.202
		Summer	8	1.5	0.62	0	10	2	0.371

TABLE 3.2 – K-values computed from the model by considering $C_{iw} = 5.10^{-4}\ m.s^{-1}$, as on table 3.1, and $\gamma = 6.7.10^{-5}$ m.s^{-1}. This value for γ is the upper bound when considering $C_{iw} = 5.10^{-4}$ m.s^{-1}. The fixed model parameters considered as well as the Ekman boundary layer thickness h_w obtained from the model are the same as those summed up in table 3.1. The modeled transfer functions are adjusted compared to the data by tuning K and h_w. Such a large value for γ lead to decay timescales lower than 10 days for all datasets and corresponds to $K = 0$ d^{-1} for dataset number 8.

3.6.2 Can K be constant ?

Choosing a fixed value for K, we now try to explain the 8 datasets by allowing C_{iw} and γ to vary simultaneously.

- Assuming $K = 1$ day^{-1}, C_{iw} has to vary between $4.2.10^{-4}$ m.s^{-1} (dataset number 8) and $8.8.10^{-4}$ m.s^{-1} (dataset number 1), and γ between $1.9.10^{-3}$ m.s^{-1} (dataset number 1) to $5.4.10^{-5}$ m.s^{-1} (dataset number 8). The values of C_{iw} are reasonable, since they vary within a factor of two around the typical value $C_{iw} = 5.10^{-4}$ m.s^{-1}. However, considering the values of h_w of table 3.1, such variations for γ lead to variations of the decay timescale $\mathcal{T} = h_w/\gamma$ between 0.3 day (dataset number 1) and 2 days (dataset number 8), which we cannot accept for two reasons : first, changes in the decay timescale of one order of magnitude at similar latitudes are difficult to explain and, secondly, these values are very small i.e. one to two orders of magnitude lower than the lower bound value of 20 days discussed previously (section 3.5.1) from the observations of *Park et al.* (2009) near 60°N (see section 3.5.1 ; such values for $\mathcal{T}$ are even smaller than typical values found for tropical regions (*Park et al.*, 2009)).
- By assuming $K = 10$ days^{-1}, negative values of γ are required to explain dataset number 8, which is non sense.

Consequently, changes in the sea ice internal friction with the hierarchy discussed above are required to explain the observations from our ocean boundary layer - sea ice dynamical model.

3.7 Conclusion

In *Gimbert et al.* (2012a), we analyzed the magnitude of inertial oscillations over the Arctic sea ice cover from the IABP buoy trajectories dataset covering three decades (1979-2008). A seasonal and regional dependence of this magnitude of inertial oscillation was observed : larger oscillations are associated to thinner, less cohesive sea ice, such as in summer and/or in the peripheral zone of the Arctic basin. We therefore proposed that the sea ice response to the constant inertial forcing could be used to investigate its average mechanical behavior ; a weak, poorly cohesive cover being characterized by strong inertial motion. We also observed a remarkable strengthening of inertial motion in recent years (since 2002), especially in the peripheral zone of the Arctic basin where sea ice decline has been particularly marked, which we therefore interpreted as a mechanical weakening of the sea ice cover.

In the present paper, we proposed a simple ocean boundary layer - sea ice coupled dynamical model that we apply to the modelling of Arctic sea ice motion in the frequency domain, and particularly in the inertial range. In this model, the sea ice mechanical response is simplified through the introduction of a linear friction term K. This model allows particularly to discriminate the direct effect of ice thinning and decreasing concentration onto the momentum balance of the ice cover, and the effect of the ice internal friction that we aim to analyze. The main conclusions of this work are : (i) The proposed coupled dynamical model well describes sea ice motion in

the frequency domain from inertial motion to advection motion, when averaged over large time (season) and spatial (1000 km) scales from IABP buoy trajectories. The accuracy is less good for the central pack in winter, for which the non-linear brittle rheology of sea ice is not very well described by a linear friction term, even after averaging. (ii) This model allows to explain the seasonal and regional dependence of Arctic sea ice inertial motion through an associated dependence of the internal friction K. K is maximal for the thick multiyear ice pack in winter, and minimal in summer over a peripheral zone covered mainly nowadays by 1st year ice. (iii) A significant decrease of K, i.e. a genuine mechanical weakening of the sea ice cover, is observed for the period 2002-2008 compared to 1979-2001. Most notably, the mechanical behavior of winter sea ice in recent years is comparable to that of summer sea ice in previous years. (iv) The observed IABP average spectra of ice motion cannot be correctly modeled by varying parameters such as the ocean-ice friction coefficient (C_{iw}) or the damping term within the ocean boundary layer (γ), while keeping K constant. In other words, an annual and interannual dependence of the ice internal friction is the only way to explain the observations. (v) This coupled dynamical model can also be used to estimate the thickness of the oceanic boundary layer h_w, independently of the determination of K. We obtained thicknesses of the order of 10 meters within the peripheral zone in summer, and of several tens of meters in winter within the central pack. Values of h_w also considerably decreased from the period 1979-2001 to recent years (2002-2008), by a factor of about 2. These variations are consistent with an enhanced stratification in the upper halocline when sea ice melts or when river runoffs are intense.

In conclusion, the evolution of Arctic sea ice in recent years in terms of extent, concentration or thickness, is accompanied by a mechanical weakening of the cover at the basin scale. These two aspects are coupled, as a weaker ice deforms and drifts more easily, thus enhancing sea ice export out of the basin as well as lead opening that strengthen the positive albedo feedback in summer. This, in turn, has a negative impact on sea ice balance, ice thickness, and concentration (*Rampal et al.*, 2011), so weakens the ice cover. This mechanical feedback most likely reinforces the sea ice decline.

3.8 Estimating the production of turbulent kinetic energy within the ocean

A more complete picture of the evolution of h_w (described in section 3.5.2) must include evolution of the mechanical forcing of h_w. Though little is known about the Arctic, it has been shown that the erosion of a salt barrier at lower latitudes require strong mixing events rather than a slow mixing resulting from average winds (*e.g.* (*McPhaden et al.*, 1992; *Zhang and McPhaden*, 2000)). Thus, the storm-induced inertial currents described by our model might be suitable to represent a part of the evolution of the mechanical forcing of h_w (even though h_w is constant in our model). Then, the term $\rho_w \gamma |\tilde{U}_w|^2$ (in W.m^{-2}) is likely to represent, by meter square, the rate of production of turbulent kinetic energy in our model, *i.e.* the mechanical forcing of h_w if

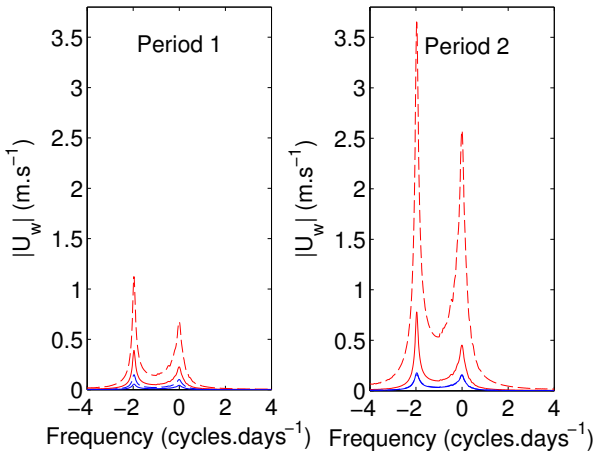

FIGURE 3.10 – Amplitude of the Fourier transform of U_w computed for the 8 datasets from the model by using the parameter values summed up in table 3.1 and the wind stress Fourier transforms presented in section 3.4.2. The bold and dashed lines indicate the Fourier transforms computed using buoy trajectories selected within the central pack zone and within the peripheral zone, respectively. The blue and red lines indicate the Fourier transforms computed using buoy trajectories selected in winter and in summer, respectively.

the latter were to vary. In this Appendix, the variation of production of turbulent kinetic energy in the ocean is estimated by determining $|U_w|$ using the coupled model described in this paper.

Similar calculations as in section 3.3 allow to express $|U_w|$ as

$$\hat{U}_w(\omega) = \frac{\tau}{\rho h_w} \frac{\frac{C_{iw}}{h_i} + (1-\alpha)K + i(1-\alpha)(\omega+\omega_0)}{\left[\left(-(\omega+\omega_0)^2 + \frac{1}{h_w}(\alpha C_{iw}+\gamma)(K+\frac{C_{iw}}{h_i}) - \frac{\alpha C_{iw}^2}{h_i h_w}\right) + i(\omega+\omega_0)\left(\frac{C_{iw}}{h_i} + \frac{\alpha C_{iw}}{h_w} + \frac{\gamma}{h_w} + K\right)\right]} \tag{3.7}$$

where $\omega = 2\pi f$ and $\rho_i = \rho_w = \rho$ is assumed.

The respective values of $|U_w|$ for the 8 datasets are plotted on Figure 3.10, using the wind stress Fourier spectrum computed in section 3.4.2 and the parameters summed up in table 3.1. As stated in section 3.4.2, the atmospheric forcing does not vary much among the 8 data sets. By contrast, $|\tilde{U}_w|$ shows substantial variations :

- in the peripheral zone and in summer, the magnitude of $|\tilde{U}_w|$ increased by a factor of 2 from period 1 to period 2 ; the value of $|\tilde{U}_w|$ at the inertial frequency goes from 1.5 m.s^{-1} to 3 m.s^{-1}.
- on the contrary, for the other datasets, i.e. in the central pack or in the peripheral zone in winter, the magnitude of $|\tilde{U}_w|$ is very small compared to the values computed in the peripheral zone and in summer and does not vary that much between the different datasets.

This shows that the production of inertial currents at the ocean surface is mainly controlled by the concentration of open water. The production of stronger inertial currents are modelled for larger values of open water concentration. This effect would have increased the mixed-layer depth from period 1 to period 2 if the surface freshwater flux had not changed. However, both

our estimates and GLORYS show a decrease of the mixed-layer depth from period 1 to period 2. This means that the effect of increased inertial currents is smaller than the inhibition effect on mixing caused by an increase in sea-ice melt and river runoff. Nonetheless, the increase of $|\tilde{U}_w|$ from period 1 to period 2 means that the energy radiated towards the deep ocean through inertial waves is likely to have increased. As the interaction between these waves and the bottom topography is important for the properties of water masses in the Arctic (see Introduction), the increase of $|\tilde{U}_w|$ could be of climatic importance. However, more realistic studies would need to be carried out if this work were to be made more accurate.

Chapitre 4

Conclusions et perspectives

Nous avons vu, dans cette première partie de thèse, que la banquise est un matériau modèle exceptionnel pour étudier le comportement mécanique des milieux géophysiques complexes sous contraintes. En effet, un panel très large d'observables quantifient les propriétés physiques pértinentes pour étudier le comportement mécanique de ce matériau géophysique. Notamment, nous disposons actuellement d'informations sur les propriétés statiques (épaisseur, concentration) et cinématiques (champ de vitesse, de déformation) de la banquise avec une très grande couverture et résolution tant spatiales que temporelles. Ces types d'observables construisent ainsi un catalogue de données très riche permettant d'étudier la physique des processus intervenant dans la réponse mécanique de la banquise.

Cependant, aujourd'hui, peu d'observables sont disponibles concernant le comportement rhéologique global de la banquise Arctique. En effet, les mesures in-situ permettant d'accéder aux états de contraintes résidant à l'intérieur de la couverture de glace, bien que très utiles car apportant une information tensorielle, présentent la limitation forte d'être très localisées en temps et en espace. Les données résultant de ce type de capteurs ne sont en effet acquises que depuis le début des années 2000, et se restreignent à quelques zones ponctuelles. D'autre part, très peu d'études spécifiques concernant l'étude du comportement mécanique de la banquise ont été jusqu'alors menées en laboratoire. En effet, au regard de la complexité dans la géométrie du chargement appliqué ainsi que dans les propriétés statiques changeantes de la banquise (degré de fracturation, valeur de concentration, d'épaisseur, etc...), estimer et quantifier la résistance mécanique de ce matériau fait appel à des dispositifs et outils expérimentaux spécifiques. Des études récentes progressent dans cette direction, telles que celle de *Lishman et al.* (2011) ou encore le travail de thèse de Vincent Pellissier démarré en Septembre 2009 au Laboratoire de Glaciologie de Grenoble, au cours duquel des données expérimentales considérant une pellicule de glace flottant sur une couche d'eau, soumise à un chargement mécanique de type 'Couette', ont pu être acquises.

Ainsi, de par la mise en place d'un cadre d'analyse original permettant de quantifier in-situ la résistance mécanique de la banquise, ce travail de thèse a permis d'apporter un nouveau type d'observable, s'ajoutant aux autres évoqués précèdemment. Celui-ci quantifie la résistance mécanique de la banquise aux grandes échelles de temps et d'espace. Nous avons proposé une méthode permettant d'extraire, à partir de données lagrangiennes de déplacement présentant une forte résolution temporelle, des informations concernant les changements d'ordre rhéologiques

intervenant dans la couverture de glace à travers les saisons ainsi qu'au fil des années, et ceci de 1980 à nos jours. Nous avons pu montrer que le paramètre M, défini dans le Chapitre 2 à partir d'une analyse spectrale des trajectoires individuelles de bouées enchâssées dans la glace, est un quantificateur simple de la résistance mécanique globale de la couverture de glace. Celui-ci présente l'avantage d'être sensible à un paramètre supplémentaire à l'épaisseur et la concentration intervenant dans la résistance mécanique de la couverture de glace, qui est ce que l'on a nommé le 'degré de fragmentation' de la couverture de glace. De plus, il apparait dans le Chapitre 3 que des variations dans ce 'degré de fragmentation' représentées par des variations du paramètre rhéologique K, qui contrairement aux épaisseurs et concentrations rend compte de la rigidité effective du milieu, sont nécessaires pour expliquer les modifications observées ces dernières années dans la cinématique globale du système banquise. Les résultats obtenus dans le Chapitre 3 mettent en évidence un affaiblissement mécanique intrinsèque à la couverture de glace, résultant d'un effet indirect des modifications d'épaisseur et de concentration de glace jusqu'alors caractérisées (*Kwok and Rothrock*, 2009; *Rothrock et al.*, 2008). En effet, les modifications d'épaisseur, de concentration ainsi que les potentielles modifications dans les processus de friction jouant un rôle dans la dissipation d'énergie par le ≪système banquise≫, telles que des modifications dans la stratification des océans et le frottement à l'interface océan-glace, ne suffisent pas à expliquer le déclin de la banquise actuellement observé dans sa cinématique.

Ce travail souligne donc que la composante rhéologique de la banquise est l'élément essentiel à la source des modifications observées dans la cinématique globale du système banquise. C'est très certainement la mauvaise représentation de cette composante dans les modèles qui est à la source de l'écart entre les changements observés dans la dynamique de la banquise et ceux reproduits dans les modèles climatiques globaux (*Rampal et al.*, 2011). Dans cette direction, les perspectives sont multiples :

– d'une part, la méthode présentée dans cette partie présente la limitation forte de n'être valable qu'aux grandes échelles de temps et d'espace. En effet, le processus génèrant les oscillations inertielles de banquise, à savoir les contrastes dans les amplitudes de vent de surface, rend l'interprétation du paramètre M comme rhéomètre uniquement valable lorsque celui-ci est moyenné sur des périodes pour lesquelles les perturbations atmosphériques (périodes de tempête) sont statistiquement inchangées. Ainsi, le développement d'autres outils de mesure et concepts permettant d'accèder aux propriétés mécaniques intrinsèques de la banquise s'avère nécessaire pour caractériser les changements rhéologiques intervenant aux plus petites échelles de temps et d'espace. Le travail initié récemment par *Tsai and McNamara* (2011) s'inscrit à mon avis pleinement dans cette perspective. Ces auteurs proposent la caractérisation de la résistance mécanique de la banquise à partir de l'analyse de l'atténuation du bruit de fond sismique par cette dernière. Ils montrent notamment, comme pour le paramètre M, que l'atténuation du bruit de fond sismique est fortement corrélée à la concentration de glace et qu'une information supplémentaire concernant le degré de fragmentation peut être extraite de l'attenuation du bruit de fond. Cette

méthode présenterait donc l'avantage, par rapport à M, d'obtenir une information locale en temps (de l'ordre de la journée) et en espace (de l'ordre de la centaine de kilomètres), et ouvre en cela des perspectives très interessantes concernant l'instrumentation en continu, telle qu'elle est aujourd'hui réalisée par satellites pour la concentration de glace, de la résistance mécanique de la couverture de glace. On peut ensuite envisager que cette information puisse soit permettre de faire de la prévision à court terme soit être incluse par assimilation dans des modèles plus globaux comme le modèle d'endommagement proposé par *Girard et al.* (2011).

– d'autre part, le modèle proposé dans le Chapitre 3 s'avère être un modèle permettant de rendre compte simplement et en moyenne de la dynamique grande échelle de la banquise. Ainsi, celui-ci pourrait être utilisé pour reproduire la dynamique de la banquise dans des modèles globaux, en assimilant, en plus des valeurs de concentration et d'épaisseur, les valeurs de la résistance mécanique K déduites des données IABP et des ré-analyses de vent.

Bibliographie

Agnolin, I., and J-N. Roux (2007), Internal states of model istorpic granular packings. III. Elastic properties., *Phys. Rev. E*, *76*, 061304.

Alford, M. H. (2003), Improved global maps and 54-year history of wind-work on ocean inertial motions, *Geophys. Res. Lett*, *30*(8), 1424.

Aranson, I., and L. Tsimring (2006), Patterns and collective behavior in granular media : Theoretical concepts, *Rev. Mod. Phys.*, *78*(2), 641–692.

Colony, R., and A. Thorndike (1980), The horizontal coherency of the motion of summer arctic sea ice, *J. Phys. Oceanography*, *10*(8), 1281–1289, doi :10.1175/1520-0485.

Comiso, J. C., C. L. Parkinson, R. Gersten, and L. Stock (1990, updated 2012), Bootstrap sea ice concentrations from nimbus-7 SMMR and DMSP SSM/I, *Edited by J. Maslanik and J. Stroeve, Boulder, Colorado, USA :NSIDC. Digital media.*

Comiso, J. C., C. L. Parkinson, R. Gersten, and L. Stock (2008), Accelerated decline in the Arctic sea ice cover, *Geophys. Res. Lett.*, *35*, L01,703, doi :200810.1029/2007GL031972.

D'Asaro, E. A. (1985), The energy flux from the wind to near-inertial motions in the surface mixed layer, *J. Phys. Oceano.*, *15*(8), 1043–1059.

D'Asaro, E. A., and J. H. Morison (1992), Internal waves and mixing in the Arctic ocean, *Deep Sea Research Part A*, *39*(2), S459–S484.

D'Asaro, E. A., C. C. Eriksen, M. D. Levine, P. Niiler, C. A. Paulson, and P. V. Meurs (1995a), Upper-ocean inertial currents forced by a strong storm. Part I : Data and comparisons with linear theory, *J. Phys. Oceanography*, *25*(11), 2909–2936, doi :10.1175/1520-0485.

Ekman, W. (1905), On the influence of the earth's rotation on ocean-currents, *Arkiv for matematik, Astronomi ocho Fysik*, *2*, 1–52.

Elipot, S., and S. T. Gille (2009), Estimates of wind energy input to the Ekman layer in the Southern Ocean from surface drifter data, *J. Geophys. Res*, *114*.

Fer, I. (2009), Weak vertical diffusion allows maintenance of cold halocline in the central Arctic, *Atmos. Oceanic Sci. Lett*, *2*(3), 148–152.

Ferry, N., L. Parent, G. Garric, B. Barnier, N. C. Jourdain, and the Mercator Ocean team (2010), Mercator Global Eddy Permitting Ocean Reanalysis GLORYS1V1 : Description and Results, *Mercator Quarterly Newsletter*, *36*, 15–27.

Garrett, C. (2001), What is the "Near-Inertial" Band and Why Is It Different from the Rest of the Internal Wave Spectrum ?, *J. Phys. Oceano.*, *31*(4).

Gascard, J., J. Festy, H. le Goff, M. W. B. Bruemmer, M. Offermann, M. Doble, P. Wadhams, R. Forsberg, S. Hanson, H. Skourup, S. Gerland, M. Nicolaus, J. Metaxian, J. Grangeon, J. Haapala, E. Rinne, C. Haas, G. Heygster, E. Jakobson, T. Erko, J. Wilkinson, L. Kaleschke, K. Claffey, B. Elder, and J. Bottenheim (2008), Exploring Arctic transpolar drift during dramatic sea ice retreat, *EOS*, *89*(3), 21–22.

Geiger, C., and D. Perovich (2008), Springtime ice motion in the western Antarctic peninsula region, *Deep-Sea Res. II*, *55*, 338–350.

Gent, P., K. O'Neill, and M. Cane (1983), A model of the semiannual oscillation in the equatorial Indian Ocean, *J. Phys. Oceano.*, *13*(12), 2148–2160.

Gill, A. E. (1984), On the behavior of inertial waves in the wakes of storms, *J. Phys. Oceano.*, *14*, 1129–1151.

Gimbert, F., D. Marsan, J. Weiss, N. Jourdain, and B. Barnier (2012a), Sea ice inertial oscillations in the Arctic basin., *The Cryosph. Discuss.*

Gimbert, F., N. Jourdain, D. Marsan, J. Weiss, and B. Barnier (2012a), Recent mechanical weakening of the Arctic sea ice cover as revealed from larger inertial oscillations., *J. Geophys. Res.*, *117*(C00J12), doi :10.1029/2011JC007633.

Girard, L., S. Bouillon, J. Weiss, D. Amitrano, T. Fichefet, and V. Legat (2011), A new modelling framework for sea-ice mechanics based on elasto-brittle rheology, *Annals Glaciol.*, *52*(57), 123–132.

Greatbatch, R. (1984), On the response of the ocean to a moving storm : Parameters and scales, *J. Phys. Oceano.*, *14*(1), 59–78.

Greatbatch, R. J. (1983), On the response of the ocean to a moving storm : The nonlinear dynamics, *J. Phys. Oceano.*, *13*, 357–367.

Gregg, M. C. (1989), Scaling turbulent dissipation in the thermocline, *J. Geophys. Res.*, *94*(C7), 9686–9698.

Haas, C., A. Pfaffling, S. Hendricks, L. Rabenstein, J. Etienne, and I. Rigor (2008), Reduced ice thickness in Arctic transpolar drift favors rapid ice retreat, *Geophys. Res. Lett.*, *35*, L17,501, doi :200810.1029/2008GL034457.

Heil, P., and W. Hibler III (2002), Modeling the High-Frequency Component of Arctic Sea Ice Drift and Deformation, *J. Phys. Oceano.*, *32*(11), 3039–3057.

Hibler, W. D. (1979), A dynamic thermodynamic sea-ice model., *J. Phys. Oceano.*, *9*, 815–846.

Hunkins, K. (1967), Inertial oscillations of fletcher's ice island (T-3), *J. Geophys. Res.*, *72*(4), 1165–1174, doi :196710.1029/JZ072i004p01165.

Hutchings, J., P. Heil, A. Steer, and W. D. H. III (2012), Sub-synoptic scale spatial variability of sea ice deformation in the western Weddell sea during early summer, *Journal of Geophysical Research*, *117*(C01002), doi :10.1029/2011JC006961.

Kwok, R., and D. A. Rothrock (2009), Decline in arctic sea ice thickness from submarine and icesat records : 1958-2008, *Geophys. Res. Lett.*, *36*(15), L15,501, doi :10.1029/2009GL039035.

Kwok, R., G. F. Cunningham, and W. D. H. III (2003), Sub-daily sea ice motion and deformation from RADARSAT observations, *Geophys. Res. Lett.*, *30*, 2218, doi : 200310.1029/2003GL018723.

Kwok, R., L. T. Pedersen, P. Gudmandsen, and S. S. Pang (2010), Large sea ice outflow into the nares strait in 2007, *Geophy. Res. Lett.*, *37*, L03,502, doi :201010.1029/2009GL041872.

Lammert, A., B. Brummer, and L. Kaleschke (2009), Observation of cyclone-induced inertial sea-ice oscillation in fram strait, *Geophys. Res. Lett.*, *36*(10), L10,503, doi : 10.1029/2009GL037197.

Le Cann, B., and A. Serpette (2009), Intense warm and saline upper ocean inflow in the southern bay of biscay in autumn-winter 2006-2007, *Cont. Shelf Res.*, *29*(8), 1014–1025, doi : 10.1016/j.csr.2008.11.015.

Lenn, Y., T. Rippeth, C. Old, S. Bacon, I. Polyakov, V. Ivanov, and J. H
olemann (2011), Intermittent intense turbulent mixing under ice in the laptev sea continental shelf, *J. Phys. Oceano.*, *41*(3), 531–547.

Lepparanta, M. (2004), *The drift of sea ice*, Springer.

Lepparanta, M., A. Oikkonen, K. Shirasawa, and Y. Fukamachi (2012), A treatise on frequency spectrum of drift ice velocity, *Cold Reg. Sci. Tech.*, *76* - *77*(0), 83 – 91, doi : 10.1016/j.coldregions.2011.12.005.

Lindsay, R., and H. Stern (2003), The radarsat geophysical processor system : Quality of sea ice trajectory and deformation estimates, *J. Atmos. and Ocean Tech.*, *20*(9), 1333–1347.

Lindsay, R. W., and J. Zhang (2005), The thinning of Arctic sea ice, 1988-2003 : Have we passed a tipping point ?, *J. Climate*, *18*(22), 4879–4894, doi :10.1175/JCLI3587.1.

Lindsay, R. W., J. Zhang, A. Schweiger, M. Steele, and H. Stern (2009), Arctic sea ice retreat in 2007 follows thinning trend, *J. Climate*, *22*, 165–175.

Lique, C., A. M. Treguier, G. Garric, B. Barnier, F. Girard-Ardhuin, N. Ferry, and C. E. Testut (2010), Evolution of the Arctic Ocean salinity, 2007-2008 : Contrast between the Canadian and the Eurasian basins, *J. Climate*, doi :10.1175/2010JCLI3762.1.

Lishman, B., P. Sammonds, and D. Feltham (2011), A rate and state friction law for saline ice *J. Geophys. Res.*, *116*(C05011), doi :10.1029/2010JC006334.

Lukovich, J.V., D.G. Babb, and D.G. Barber (2011), On the scaling laws derived from ice beacon trajectories in the southern Beaufort Sea during the International Polar Year - Circumpolar Flaw Lead study, 2007–2008, *J. Geophys. Res.*, *116*(C00G07), doi :10.1029/2011JC007049.

Marsan, D., H. Stern, R. Lindsay, and J. Weiss (2004), Scale dependence and localization of the deformation of Arctic sea ice, *Phys. Rev. Lett.*, *93*(17), 178,501, doi : 10.1103/PhysRevLett.93.178501.

Maslanik, J., J. Stroeve, C. Fowler, and W. Emery (2011), Distribution and trends in Arctic sea ice age through spring 2011, *Geophys. Res. Lett.*, *38*(L13502), doi :10.1029/2011GL047735.

McPhaden, M., F. Bahr, Y. Du Penhoat, E. Firing, S. Hayes, P. Niiler, P. Richardson, and J. Toole (1992), The response of the western equatorial pacific ocean to westerly wind bursts during november 1989 to january 1990, *J. Geophys. Res*, *97*, 14,289–14,303.

McPhee, M. (1978), A simulation of inertial oscillation in drifting pack ice, *Dyn. Atmos. Oceans*, *2*(2), 107–122, doi :10.1016/0377-0265(78)90005-2.

McPhee, M., and L. Kantha (1989), Generation of internal waves by sea ice, *J. Geophys. Res.*, *94*(C3), 3287–3302.

Nansen, F. (1902), Oceanography of the north polar basin : The norwegian north polar expedition 1893-96, *Scientific Results*, *3*.

Nghiem, S., I. Rigor, D. Perovich, P. Clemente-Colón, J. Weatherly, and G. Neumann (2007), Rapid reduction of Arctic perennial sea ice, *Geophys. Res. Lett.*, *34*, L19,504, doi : 10.1029/2007GL031138.

Park, J. J., K. Kim, and R. W. Schmitt (2009), Global distribution of the decay timescale of mixed layer inertial motions observed by satellite-tracked drifters, *J. Geophys. Res.*, *114*, C11,010, doi :200910.1029/2008JC005216.

Pinkel, R. (2005), Near-inertial wave propagation in the western Arctic, *J. Phys. Oceano.*, *35*(5), 645–665.

Plueddemann, A. J., and J. T. Farrar (2006), Observations and models of the energy flux from the wind to mixed-layer inertial currents, *Deep-Sea Res. II*, *53*(1-2), 5–30.

Pollard, R. T., and J. R. C. Millard (1970), Comparison between observed and simulated wind-generated inertial oscillations, in *Deep-Sea Res. Oceano. Abs.*, vol. 17, pp. 813–816, Elsevier.

Price, J. F. (1983), Internal wave wake of a moving storm. Part I. scales, energy budget and observations, *J. of Phys. Oceano.*, *13*(6), 949–965, doi :10.1175/1520-0485.

Radjai, F., and S. Roux (2002), Turbulentlike fluctuations in quasistatic flow of granular media, *Phys. Rev. Lett.*, *89*, 064,302, doi :10.1103/PhysRevLett.89.064302.

Rainville, L., and P. Winsor (2008), Mixing across the Arctic ocean : Microstructure observations during the Beringia 2005 expedition, *Geophys. Res. Lett.*, *35*(8).

Rajchenbach, J. (2000), Granular flows, *Adv. Phys.*, *49*, 229–256.

Rampal, P. (2009), Analyses of the Arctic sea ice drift and deformation properties from lagrangian trajectories analyses. *Thèse de Doctorat*, Université Joseph Fourier.

Rampal, P., J. Weiss, and D. Marsan (2009a), Positive trend in the mean speed and deformation rate of Arctic sea ice, 1979-2007, *J. Geophys. Res.*, *114*, doi :200910.1029/2008JC005066.

Rampal, P., J. Weiss, D. Marsan, and M. Bourgoin (2009b), Arctic sea ice velocity field : general circulation and turbulent-like fluctuations, *J. Geophys. Res.*, *114*(C10014), 17 PP., doi : 10.1029/2008JC005227.

Rampal, P., J. Weiss, C. Dubois, and J.-M. Campin (2011), IPCC climate models do not capture Arctic sea ice drift acceleration : Consequences in terms of projected sea ice thinning and decline, *J. Geophys. Res.*, *116*(C00D07), doi :10.1029/2011JC007110.

Richter-Menge, J. A., and B. C. Elder (1998), Characteristics of pack ice stress in the Alaskan Beaufort sea, *J. Geophys. Res.*, *103*(C10), 21,817–21,829, doi :199810.1029/98JC01261.

Richter-Menge, J. A., S. L. McNutt, J. E. Overland, and R. Kwok (2002), Relating Arctic pack ice stress and deformation under winter conditions, *J. Geophys. Res.*, *107*, 8040, doi : 200210.1029/2000JC000477.

Rothrock, D. A., D. B. Percival, and M. Wensnahan (2008), The decline in Arctic sea-ice thickness : Separating the spatial, annual, and interannual variability in a quarter century of submarine data, *J. Geophys. Res.*, *113*, C05,003, doi :200810.1029/2007JC004252.

Rudels, B., L. G. Anderson, and E. P. Jones (1996), Formation and evolution of the surface mixed layer and halocline of the Arctic ocean, *J. Geophys. Res.*, *101*(C4), 8807–8821.

Serreze, M. C., and A. P. Barrett (2008), The summer cyclone maximum over the central Arctic ocean, *J. Climate*, *21*, 1048–1065.

Steele, M., J. Zhang, D. Rothrock, and H. Stern (1997), The force balance of sea ice in a numerical model of the Arctic ocean, *J. Geophys. Res.*, *102*(C9), 21,061–21,079, doi : 199710.1029/97JC01454.

Stroeve, J., M. Holland, S. T. Meier, W., and M. Serreze (2007), Arctic sea ice decline : Faster than forecast, *Geophys. Res. Lett.*, *34*, doi :10.1029/2007GL029703.

Stroeve, J., M. Serreze, S. Drobot, S. Gearheard, M. Holland, J. Maslanik, W. Meier, and T. Scambos (2008), Arctic sea ice extent plummets in 2007, *Eos Trans. AGU*, *89*(2), 13, doi :200810.1029/2008EO020001.

Stull, R. B. (1988), *An Introduction to Boundary Layer Meteorology*, Kluwer Academic Publisher.

Tsai, V.C., and D.E. McNamara (2011), Quantifying the influence of sea ice on ocean microseism using observations from the Bering Sea, Alaska, *Geophys. Res. Lett.*, *38*(L22502), doi :10.1029/2011GL049791.

Watanabe, M., and T. Hibiya (2002), Global estimates of the wind-induced energy flux to inertial motions in the surface mixed layer, *Geophys. Res. Lett.*, *29*(8), 1239.

Weatherly, J. W., B. P. Briegleb, W. G. Large, and J. A. Maslanik (1998), Sea ice and polar climate in the NCAR CSM, *J. Climate*, *11*(6).

Weiss, J., and D. Marsan (2004), Scale properties of sea ice deformation and fracturing, *C. R. Physique*, *5*(7), 735–751, doi :10.1016/j.crhy.2004.09.005.

Weiss, J., E. M. Schulson, and H. L. Stern (2007), Sea ice rheology from in-situ, satellite and laboratory observations : Fracture and friction, *EPSL*, *255*(1-2), 1–8, doi : 10.1016/j.epsl.2006.11.033.

Young, W. R., and M. Ben Jelloul (1997), Propagation of near-inertial oscillations through a geostrophic flow, *Journal of Marine Research*, *55*, 735–766.

Zhang, C., and M. J. McPhaden (2000), Intraseasonal surface cooling in the equatorial western pacific, *J. Climate*, *13*(13), 2261–2276.

Zhang, J., D. Rothrock, and M. Steele (2000), Recent changes in Arctic sea ice : the interplay between ice dynamics and thermodynamics, *J. Climate*, *13*(6), 3099–3114.

Deuxième partie

Comportement mécanique multi-échelles des milieux granulaires frottants sous compression

Multi-scale mechanical behaviour of frictional granular materials submitted to compressional loading

Chapitre 1

Introduction

Dans le Chapitre 3 de la première partie, nous avons développé un formalisme analytique simple dans le but d'analyser les changements rhéologiques intervenant dans la banquise aux grandes échelles de temps et d'espace. Nous nous sommes ainsi placés dans un cadre d'étude visant à caractériser un comportement moyen par l'intermédiaire d'une loi de comportement simple. Nous avons notamment vu que ce comportement moyen, par définition, ne peut être défini uniquement à des échelles caractéristiques en temps et en espace au delà desquelles les fluctuations associées au comportement mécanique deviennent négligeables.

De manière générale, dans l'étude d'une rhéologie, au même titre que ce que nous avons vu précèdemment pour la banquise, l'identification des échelles caractéristiques de temps et d'espace est cruciale. En effet, elle permet la description, par l'intermédiaire d'une loi de comportement, de la réponse mécanique macroscopique d'un matériau quelconque soumis à un chargement. Cette description entre comportement microscopique et comportement macroscopique est souvent rendue possible par l'introduction d'une échelle caractéristique, communément dénommée VER (Volume Elémentaire Représentatif) par la communauté des mécaniciens, pour laquelle une loi de comportement peut être définie en fonction des variables internes du milieu. Ensuite, des opérations d'homogénéisation sont réalisées à partir du comportement à l'échelle du VER pour décrire le comportement macroscopique. L'hypothèse sous-jacente à cette étape d'homogénéisation est qu'à une échelle supérieure ou égale au VER, le comportement mécanique du matériau considéré est homogène.

Cependant, pour bon nombre de matériaux de la physique, les processus de déformation prenant place à l'échelle microscopique, se matérialisant par exemple par de l'endommagement par fracturation dans les roches (*Amitrano*, 2003), par des dislocations dans les métaux ou la glace (*Weiss and Marsan*, 2003; *Richeton et al.*, 2005), ou par des rearrangements dans les milieux granulaires (*Radjai and Roux*, 2002; *Richefeu et al.*, 2012), se caractérisent par un comportement très fluctuant en temps et en espace. En effet, une dynamique collective résultant des interactions entre ces éléments constituants le matériau engendre une signature intermittente dans la réponse mécanique de l'échantillon. Celle-ci est caractérisée par l'appartition d'évènements discrets dans l'espace et dans le temps couvrant une large gamme d'échelles. Cette signature est communément dénommée "Crackling noise" (*Sethna et al.*, 2001) par la communauté physique statistique.

Ainsi, pour comprendre et décrire de manière appropriée les caractéristiques de la réponse mécanique macroscopique des matériaux présentant ce type de comportement, il convient d'analyser et identifier le rôle des fluctuations résultantes du comportement collectif des éléments

constituants le matériau sur son comportement global.

Dans cette deuxième partie de thèse, nous nous proposons d'étudier et de caractériser les échelles de temps et d'espace des fluctuations observées dans le comportement mécanique des milieux granulaires frottants, secs et non cohésifs lorsque ces derniers sont soumis à un chargement en compression.

L'objectif est donc d'une certaine façon de réaliser un travail amont de celui présenté dans la partie I, c'est à dire non pas de travailler sur l'élaboration d'une rhéologie pour décrire le comportement mécanique des milieux granulaires mais d'identifier, en utilisant des outils de la physique statistique, les processus physiques à l'origine de la dynamique des hétérogénéités ainsi que le rôle de ces dernières dans la réponse mécanique macroscopique de ce matériau.

Nous focaliserons ici notre étude dans un premier temps (Chapitre 3) sur l'instabilité macroscopique, ou "rupture", qui se caractérise par la transition d'un comportement quasi-statique où le matériau résiste à la contrainte appliquée, à un comportement d'écoulement dense où, lorsque la contrainte devient supérieure à une contrainte seuil, le matériau se déstabilise et s'écoule. On définit le régime quasi-statique d'un matériau granulaire, par opposition aux deux autres types d'écoulements que sont l'écoulement dense et l'écoulement gazeux, lorsque les effets inertiels prenant place dans l'échantillon sont négligeables dans le comportement mécanique global de celui-ci (*Roux and Combe*, 2002). Un écoulement dense, quant à lui, se différencie d'un écoulement gazeux par le fait qu'un réseau de contact percolant réside dans l'échantillon (*Midi*, 2004; *Pouliquen and Chevoir*, 2002). En pratique, nous nous attacherons à caractériser le rôle des fluctuations observées dans les champs de déformation et de contrainte à l'approche de ce comportement caractéristique. Ces analyses seront réalisées à partir de résultats obtenus d'une part à l'aide de la simulation numérique, en utilisant un code aux éléments discrets de dynamique moléculaire (DEM), et d'autre part à l'aide d'essais expérimentaux, réalisés au laboratoire 3S-R sur un matériau analogue composé de cylindres de PVC.

Cependant, nous verrons que les observations et caractérisations que nous réalisons dans cette première partie considèrent des échantillons granulaires aux propriétés spécifiques, dans le sens où ces derniers présentent initialement une forte densité d'assemblage ainsi qu'une forte coordination, i.e. un fort nombre de contacts par grain.

C'est pourquoi, dans un second temps (Chapitre 4), nous exposerons un travail en cours consistant à générer différents types d'assemblages granulaires caractérisés par des mécanismes de déformation différents dans la phase initiale du chargement sous compression. Nous focaliserons notamment la discussion sur la variation de volume de l'échantillon au cours du chargement, le maximum de contrainte ainsi que l'état critique, qui est l'état final stable atteint par l'échantillon, caractérisé par une déformation macroscopique opèrant sans changements de volume (*Rothenburg and Kruyt*, 2004).

Dans cette introduction, nous présentons dans un premier temps le type de chargement et de comportement que l'on souhaite caractériser à travers l'étude référence en géomécanique menée

sur le sable d'Hostun par *Desrues and Viggiani* (2004). Aussi, nous situons dans cette section notre approche en discutant des outils et concepts de la littérature pour la caractérisation de ce type de comportement. Dans un second temps, nous présentons des champs de déformation observés à grande résolution temporelle que nous avons obtenus avec le dispositif $1\gamma2\epsilon$ au 3S-R ainsi que ceux récemment obtenus par une équipe de l'Institut de Physique de Rennes.

1.1 Configuration de l'étude

1.1.1 Présentation du chargement biaxial et d'observations aux grands incréments de déformation macroscopique

L'essai en compression que nous réalisons dans cette étude est un essai biaxial. Cet essai consiste en une sollicitation mécanique traditionnellement utilisée dans le domaine de la géotechnique/géomécanique. Les travaux expérimentaux réalisés au cours de ces 20 dernières années sur le sable d'Hostun par Jacques Desrues et ses collègues du laboratoire 3S-R (*Desrues and Viggiani*, 2004) correspondent très certainement aux premières expériences ayant permis l'observation directe du champ de déformation au cours de ce type de sollicitation mécanique. Le dispositif expérimental (voir *Desrues and Viggiani* (2004) pour plus d'informations) consiste en un échantillon de sable placé entre deux murs rigides, imposant ainsi une déformation nulle dans une direction, et en l'application de 2 contraintes indépendantes dans les 2 autres directions de l'espace : une contrainte radiale de confinement σ_3 et une contrainte axiale $\sigma_1 \geq \sigma_3$, cette dernière induisant une composante déviatoire $\tau = \frac{\sigma_1 - \sigma_3}{2}$, i.e. cisaillante, dans la sollicitation. Les parois rigides en verre permettent de suivre, à l'aide de prises de vues et de la stéréophotogrammetrie, les champs de déformation plans associés au chargement mécanique. Ces essais sont réalisés à déformation imposée en appliquant au plateau supérieur une vitesse verticale, i.e. dans la direction de la contrainte majeure σ_1, et constante dans le temps V_1.

La Figure 1.1 montre un exemple de réponse mécanique obtenue en considérant un échantillon de sable. On peut voir que, dans cette étude, les configurations successives à partir desquelles les champs de déformation incrémentaux sont calculés sont espacées en déformation, car séparées d'environ 1% de déformation les unes des autres. A cette résolution, dans la phase initiale du chargement, les champs de déformation apparaissent comme assez homogène (images 1-2 et 3-4). On ne distingue en effet aucune structure particulière lorsque l'on examine visuellement ces champs. A l'inverse, aux alentours du maximum de contrainte, le champ de déformation devient hétérogène et se caractérise par une structure linéaire appelée bande de cisaillement à l'intérieur de laquelle la déformation cisaillante et divergente semble se concentrer. Cette bande de cisaillement s'initie à un endroit de l'échantillon et se propage jusqu'à traverser l'échantillon de bord en bord, bords sur lequels une réfléxion de bande peut être observée.

De manière générale, le phénomène de localisation de la déformation sous la forme d'une

(a)

Test	γ_0 (kN/m^3)	e_0	σ'_3 (kPa)	H_0/L_0
shf00	14.93	0.741	90	2.00

(b)

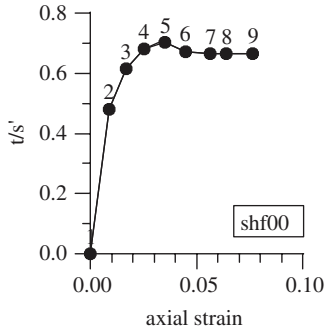

(c)

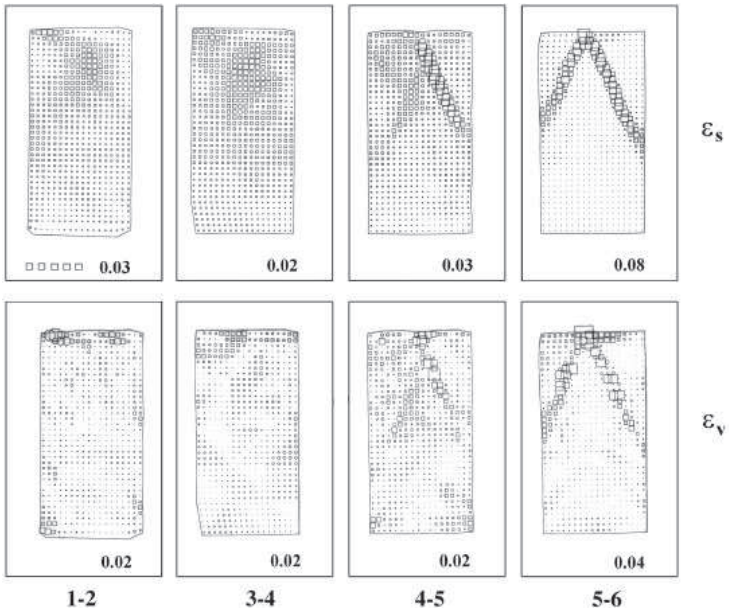

FIGURE 1.1 – Réponse mécanique du sable d'Hostun obtenue lors d'un essai biaxial réalisé à déformation imposée par *Desrues and Viggiani* (2004). (a) Caractéristiques de l'échantillon n° shf00 : γ_0 est le poids volumique, e_0 est l'indice des vides et H_0/L_0 est le rapport d'aspect de l'échantillon. σ'_3 désigne la pression de confinement latérale appliquée, constante au cours du test. (b) Courbe contrainte-déformation obtenue au cours du chargement biaxial : la contrainte déviatorique t est normalisée par la contrainte moyenne s'. Les points numérotés de 1 à 9 sur cette même courbe correspondent aux positions auxquelles les photos ont été acquises. Une image est réalisée environ tous les 1% de déformation. (c) Incréments de déformation cisaillants en haut et divergents en bas obtenus en utilisant la méthode de 'False Relief Stereophotogrammetry' à partir des couples d'images dénotés par les points numérotés en (b).

bande se développant à l'échelle macroscopique a été observé et caractérisé expérimentalement sur une multitude de géomatériaux différents (*Reches and Lockner*, 1994; *Haimson and Chang*, 2000; *Baud et al.*, 2006; *Stanchits et al.*, 2009).

L'étude théorique du processus physique associé à la localisation de la déformation sous la forme d'une bande au cours d'un chargement multi-axial représente un champ de recherche important depuis les travaux précurseurs de *Rudnicki and Rice* (1975). En effet, ces auteurs ont formulé, à travers la théorie de la bifurcation, une description mécanique permettant de prédire l'occurence de cette bande de cisaillement (i.e. sa position sur la courbe contrainte déformation) ainsi que l'angle que décrit cette dernière par rapport à la contrainte principale. L'hypothèse constituant les fondements de la théorie de la bifurcation de *Rudnicki and Rice* (1975) consiste à considérer qu'une discontinuité dans les gradients de déplacements prend place à l'interface entre l'intérieur et l'extérieur de la bande. Ainsi, lorsque la bande apparait, le milieu s'assimile en un assemblage de deux blocs rigides séparés par une bande, d'épaisseur donnée, accomodant toute la déformation préscrite aux limites. Sous ses hypothèses, la théorie de *Rudnicki and Rice* (1975) a permis avec succès d'apporter un cadre mathématique expliquant, dans les milieux continus, la localisation de la déformation par la formation d'une bande de déformation en rendant compte de leurs orientations observées expérimentalement. Ce cadre d'analyse a dans un premier temps été établi pour des roches denses (*Rudnicki and Rice*, 1975), où la bande s'associe à une déformation en cisaillement, comme dans les granites (*Haimson and Rudnicki*, 2010) et a ensuite été étendu au cas des roches très poreuses (*Olsson*, 1999; *Issen and Rudnicki*, 2001), où la bande s'associe à une bande de compaction, comme observé par exemple dans des grès (*Stanchits et al.*, 2009).

Cependant, ce formalisme définissant la bande de cisaillement, qui présente les propriétés telles qu'énoncées ici, est il encore valide dans les milieux granulaires tels que les sables ? si oui, la bande de cisaillement peut elle être considérée comme un précurseur à l'affaiblissement mécanique macroscopique observé dans la courbe de chargement ? si non, peut on trouver d'autres précurseurs ? On pourra notamment noter que dans la théorie de *Rudnicki and Rice* (1975), donc toujours dans les matériaux continus, la localisation de la déformation sous forme de bande de cisaillement est possible uniquement dans la phase de 'softening' ou d'adoucissement mécanique, i.e. dans la zone située après le pic de contrainte sur la courbe contrainte-déformation.

Lorsque l'on regarde les résultats obtenus sur le sable d'Hostun (Figure 1.1), toutes les caractéristiques de la bande de cisaillement évoquées précèdemment sont qualitativement observées : on distingue une bande d'épaisseur finie, caractérisée par une discontinuité entre l'intérieur et l'extérieur de la bande dans les valeurs de déformation. De plus, pas/peu de déformation est observée en dehors de la bande.

Toutefois, cette vision d'ensemble est nuancée par les auteurs, qui stipulent : "shear band formation in biaxial tests is progressive, that is, there is a period between the onset of non-homogeneous deformation and complete formation of a shear band during which the patterns

formation are not necessarily simple. Temporary modes of localized strain are often observed in different forms prior to the development of a final, persistent shear band". C'est précisemment le détail de ce comportement souligné par les auteurs que nous nous proposons d'analyser et de quantifier dans la suite de ce manuscrit pour répondre aux questions suivantes : à quel moment du chargement et à quelles échelles de déformation macroscopique et d'espace le champs de déformation présente t-il des tailles caractéristiques associées à la formation d'une bande de cisaillement ? Ces champs de déformation ne présentent-ils pas des hétérogénéités aux propriétés d'échelles particulières au maximum de contrainte ?

Pour répondre à ces questions, nous utilisons les outils de la physique statistique.

1.1.2 Utilisation des outils de la physique statistique

Pour le physicien, le test biaxial est un essai assez complexe : l'échantillon est en effet contrôlé en déformation dans une direction, celle des murs, en contraintes dans une autre direction, la direction de σ_3, et en contrainte ou en déformation dans la direction de σ_1, en fonction de la manière dont on souhaite augmenter la contrainte axiale au cours du test. Cependant, ce dernier présente l'avantage de simuler une sollicitation du type de celles rencontrées en géosciences, i.e. caractérisée par l'application d'une contrainte déviatorique ainsi que d'une pression de confinement, tout en simplifiant l'analyse de la réponse mécanique du matériau en une analyse plane, bidimensionnelle.

Les travaux numériques de *Radjai and Roux* (2002) et expérimentaux réalisés récemment par *Richefeu et al.* (2012) ont visé à caractériser les comportements collectifs des milieux granulaires frottants soumis à ce type de chargement. Ces travaux ont consisté en une analogie entre les caractéristiques de la dynamique des milieux granulaires sous chargement quasi-statique et celles de la turbulence dans les fluides. Les auteurs montrent notamment que, dans le domaine quasi-statique, la dynamique de déformation irréversible matérialisée par le réarrangement des grains se caractérise par un comportement très fluctuant associé à des corrélations longues distances dans l'espace et des distributions exponentielles, i.e. non gaussiennes, des fluctuations de vitesse. Cependant, dans ces études, les auteurs n'ont pas étudié le lien entre l'organisation spatiale de ces fluctuations et la déformation de l'assemblage granulaire à l'échelle macroscopique. On peut en effet reporter ici la conclusion de *Richefeu et al.* (2012) : 'The link between the velocity fluctuations (and their spatial organization) and the deformation of granular materials at the macro scale (including dilatancy, strain localization, critical state) remains still to be investigated'. C'est précisement dans cette direction que nous souhaitons apporter notre contribution en se focalisant non pas sur les déplacements mais sur les champs de contrainte et de déformation.

Ces dernières années, les outils de caractérisation et concepts pour la compréhension du développement des hétérogénéités dynamiques dans les milieux granulaires à l'approche d'un comportement macroscopique particulier ont notamment beaucoup progressé chez les physiciens

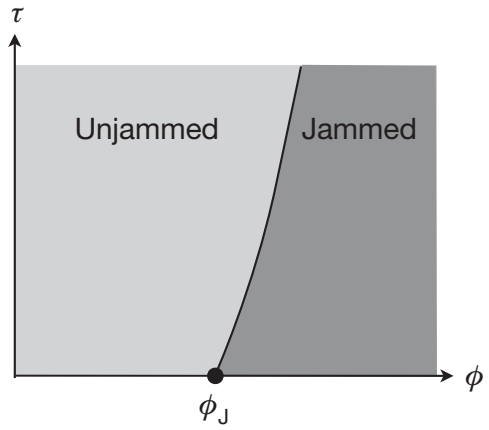

FIGURE 1.2 – Diagramme de phase du jamming proposé par *Liu and Nagel* (1998) pour un assemblage de grains non frottants et non soumis à une agitation thermique (extrait de *Bi et al.* (2011)).

dans l'étude de la transition de 'jamming' ou, en français, de la transition de blocage. Pour la petite histoire, les travaux precurseurs de *Liu and Nagel* (1998) ont fait apparaitre, pour un système de grains non frottant et non infiniment rigides, i.e. pouvant avoir un recouvrement non nul, l'existence d'une transition de phase se produisant à une densité critique ϕ_j. En dessous de cette valeur critique, l'assemblage granulaire s'apparente à un état fluide dans lequel dominent des empilements sans recouvrements et donc avec des modules de compression et de cisaillement nuls. A l'inverse, au dessus de cette valeur, il devient impossible de trouver de tels empilements et le système possède alors des modules de compression et de cisaillement non nuls. De plus, cette valeur de densité d'empilement critique ϕ_j varie si l'échantillon est soumis à une contrainte (voir Figure 1.2). Les 2 paramètres de contrôle associés à cette transition pour des grains non frottants et non soumis à une agitation thermique sont donc la densité d'empilement et la contrainte cisaillante.

Pour cette raison essentiellement, la configuration de chargement que l'on considère dans notre étude diffère des sollicitations considérées par les physiciens lorsqu'ils étudient la transition de 'jamming'. En effet, la densité étant un des paramètres de contrôle dans cette transition, les expériences développées considèrent des chargements mécaniques réalisés à volume constant, ce qui n'est pas le cas dans nos essais (cf Figure 1.4(a)). On pourra notamment citer, par exemple, les expériences du groupe de R.P. Berhinger (*Bi et al.*, 2011) à Duke University ou encore celles du groupe d'Olivier Dauchot (*Marty and Dauchot*, 2005; *Dauchot et al.*, 2005) au Service de Physique de l'Etat Condensé (SPEC). D'autres expériences telles que celles de *Keys et al.* (2007) considèrent une table à surface fixe sur laquelle les grains, directement soumis à une contrainte homogène par l'intermédiaire d'un flux d'air, sont déposés.

Ainsi, la particularité de notre travail par rapport à d'autres travaux d'étude de la transition de jamming réside donc dans le caractère frottant des particules et dans le type de chargement

considérés. En effet, lors d'un chargement biaxial, le volume de l'échantillon varie au cours de l'essai, ainsi que la pression moyenne $P = \frac{\sigma_1+\sigma_3}{2}$. De plus, dans cette étude, nous évaluons les échelles des hétérogénéités liées aux fluctuations sur les propriétés mécaniques de l'échantillon, telles que les contraintes et les déformations. Pour pousser l'analogie avec le concept de 'jamming' discuté précèdemment, notre démarche, lorsque l'on réalise un essai biaxial, consiste à approcher cette transition dans le sens inverse de celui habituellement traité par les physiciens, i.e. de dans le sens du 'unjamming', c'est à dire d'aller d'un état bloqué vers un état d'écoulement.

Dans la section suivante, nous présentons plus en détail, toujours dans le cadre d'essais biaxiaux, d'autres champs de déformation observés à une échelle temporelle beaucoup plus fine que celle considérée dans l'étude de *Desrues and Viggiani* (2004).

1.2 Observations aux petits incréments de déformation macroscopique

Si par exemple les expériences de R.P. Behringer (*Majmudar and Berhinger*, 2005; *Bi et al.*, 2011) permettent d'accèder au forces de contact par l'utilisation de la photoelasticité, la communauté scientifique de la géomécanique ne dispose pas, à ma connaissance, de ce type d'observations pour un milieu granulaire soumis à un chargement biaxial.

Dans cette section, nous présentons donc d'autres observations expérimentales permettant l'observation des champs de déformation opérant au cours d'un chargement biaxial. A l'inverse des essais réalisés par *Desrues and Viggiani* (2004), les essais présentés ici ne considèrent pas des matériaux naturels, mais des matériaux analogues constitués de particules cylindriques (en 2D) ou sphériques (en 3D) frottantes. L'apport de ces observations par rapport à celles de *Desrues and Viggiani* (2004) présentées dans la section 1.1.1 réside dans le fait qu'une analyse beaucoup plus fine au cours du chargement, considérant des incréments en déformation macroscopique inférieurs d'environ deux ordres de grandeurs, est considérée ici dans l'évaluation des champs de déformation.

Dans un premier temps, nous présentons qualitativement les données obtenues dans cette thèse suite à des essais réalisés avec le dispositif $1\gamma2\epsilon$ au laboratoire 3S-R à Grenoble. Ensuite, nous présentons des observations similaires plus récemment obtenues par une équipe de l'Institut de Physique de Rennes constituée d'Antoine Le Bouil, Axelle Amon et Jérôme Crassous, avec qui nous avons initié une collaboration.

1.2.1 Dans les essais $1\gamma2\epsilon$

1.2.1.1 Présentation du dispositif

Le dispositif expérimental $1\gamma2\epsilon$ consiste en un cadre formant un parallelogramme qui renferme un materiau analogue formé de la combinaison d'environ 45000 rouleaux de PVC de 3 diamètres différents (1.5, 3 et 3.5 mm), mesurant chacun 60 mm de long (voir la Figure 1.3). Pour

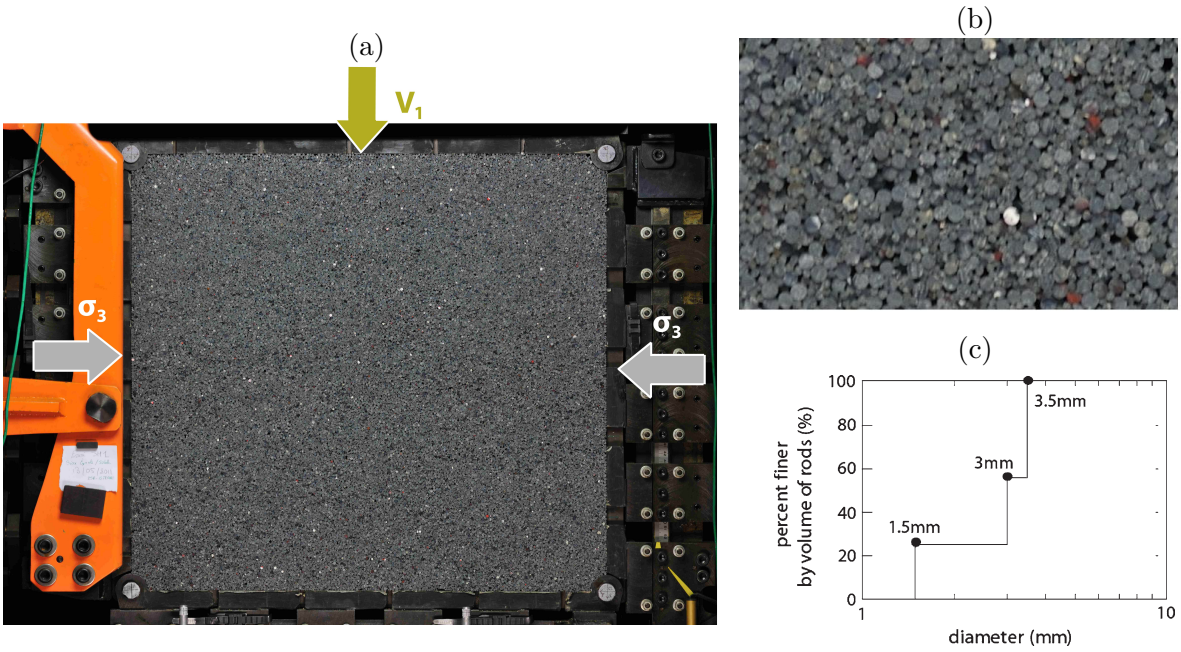

FIGURE 1.3 – Photos du dispositif expérimental $1\gamma 2\epsilon$. (a) Photo de l'ensemble. (b) Zoom sur une partie de l'échantillon. (c) Distribution de tailles de grains.

plus d'informations concernant ce dispositif, voir *Joer et al.* (1992) et *Calvetti et al.* (1997). La distribution des diamètres des cylindres, identique à celle considérée dans l'étude de *Hall et al.* (2010), correspond à celle présentée sur la Figure 1.3(c).

Pour fabriquer l'échantillon, les cylindres de PVC sont assemblés à la main, sous gravité. Ensuite, une compression isotrope est réalisée jusqu'à l'obtention d'une contrainte moyenne P de 50 kPa. A ce stade, la contrainte gravitaire devient ainsi négligeable devant la pression de confinement. Lors de l'essai biaxial, la contrainte de confinement σ_3 est conservée à 50 kPa et un taux de déformation est imposé en contrôlant la vitesse V_1 du plateau supérieur.

Dans cette configuration, il convient de définir le niveau de rigidité des grains $\kappa = k_N/P$ (*Roux and Chevoir*, 2005), où k_N est la rigidité élastique propre des grains. Ainsi, ce nombre adimensionel quantifie le 'niveau de déformabilité' ou déflexion normale des grains (en 2D). Dans ce dispositif, on a $\kappa = 60000$.

1.2.1.2 Comportement macroscopique

La Figure 1.4 montre la réponse macroscopique obtenue au cours d'un essai en fonction de la déformation axiale ϵ_1. On observe dans un premier temps une diminution du volume total de l'échantillon jusqu'à l'obtention d'une valeur de déformation pour laquelle le phénomène de dilatance apparait, matérialisé par une augmentation de volume. Ensuite, l'échantillon se dilate continuellement au cours de la déformation. D'autre part, la courbe contrainte-déformation est similaire à celle observée sur la Figure 1.1, i.e. montre une augmentation de contrainte jusqu'à atteindre un pic de contrainte à partir duquel le matériau s'adoucit. On remarque que, aux

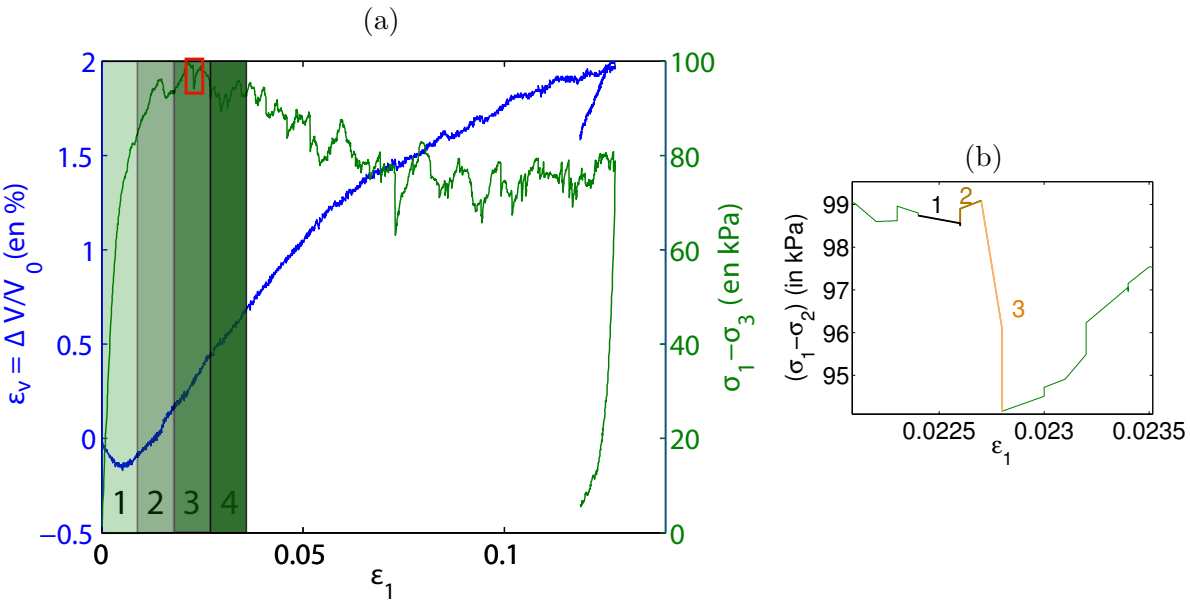

FIGURE 1.4 – Réponse macroscopique obtenue lors d'un essai biaxial réalisé avec $1\gamma 2\epsilon$. Les résultats sont exprimés en fonction de la déformation axiale ϵ_1. (a) Courbe de contrainte cisaillante $\tau = \sigma_1 - \sigma_3$, matérialisée en vert, et courbe de variation de volume $\Delta V/V_0$, matérialisée en bleu. Les rectangles délimitent des zones où la corrélation d'images a été réalisée. Les rectangles verts numérotés en dégradé de couleurs correspondent aux cartes de déformation cisaillante montrées sur la Figure 1.5. La taille des fenêtres considérées est de $2.3.10^{-3}$ en déformation. Le rectangle rouge matérialise la position où le zoom de la Figure (b) est réalisé. (b) Zoom sur une région particulière de la courbe contrainte déformation délimitée par le carré rouge en (a). La numérotation de 1 à 3 correspond aux corrélations d'images montrées sur la Figure 1.6. La taille en déformation de la fenêtre considérée pour ces corrélations d'images est de l'ordre de 5.10^{-5}.

alentours du pic de contrainte et après, la courbe contrainte déformation est assez irrégulière et se matérialise par des sauts de contrainte brutaux.

1.2.1.3 Les champs de déformation associés

Dans cette section, les champs de déformation incrémentaux associés à cette réponse macroscopique sont calculés par corrélation d'images. La corrélation d'image est réalisée à l'aide du logiciel 7D élaboré par Pierre Vacher du laboratoire SYMME d'Annecy et décrit dans *Vacher et al.* (1999). Celui-ci procède de la manière suivante. Une grille régulière de $n \times n$ pixels est générée sur l'échantillon et, pour chaque point, une fenêtre de corrélation de la taille de $p \times p$ pixels est définie. Pour chaque fenêtre de corrélation, l'interpolation des fonctions de gris dans l'espace permet l'estimation des déplacements avec une résolution subpixel d'idéalement 0.01 pixel (*Louche et al.*, 2008). Ici, une interpolation bilinéaire des niveaux de gris est utilisée pour calculer le champ de déplacement résultant à chaque point de grille. Celui-ci est ensuite différencié dans l'espace pour obtenir le champ de déformation.

Ainsi, la corrélation d'image réalisée ici est une analyse eulerienne : on impose une grille fixe et l'on regarde comment cette dernière se déforme. Une analyse lagrangienne, qui consisterait à suivre les grains, n'est pas réalisable dans cette configuration. En effet, la résolution, i.e. le nombre de pixels par grains, est trop faible pour permettre de les contourer. Ce contourage pourrait être rendu possible en considérant des tailles de grains supérieures. Cependant, étant donné que l'analyse des champs que nous réalisons par la suite est une analyse continue, il ne nous est pas nécessaire d'analyser les déplacements individuels des grains. De plus, l'utilisation de petits grains nous permet d'obtenir une plus grande dynamique d'échelles entre celle des grains et celle de l'échantillon, ce qui est un point important lorsque l'on s'attache à caractériser ces dernières.

De manière générale, la précision sur les déplacements issus de la corrélation d'image dépend principalement de 3 paramètres, à savoir (i) la texture de l'échantillon, correspondant ici essentiellement à la texture formée par le contour des grains, (ii) la configuration de l'optique et (iii) la procédure de corrélation. L'effet du bruit résultant sur le champ de déformation calculé peut être examiné en corrélant plusieurs images aquises successivement sans aucun changement dans l'échantillon, i.e. par exemple avant le démarrage de l'essai. Dans ce cas, au lieu d'un champ théorique caractérisé par aucune déformation, celui résultant de cette analyse provient uniquement d'une déviation artificielle dûe au dispositif. Dans notre configuration expérimentale présentée ici, ce test nous donne un écart type moyen de 8.10^{-4} mesuré sur la composante cisaillante du champ de déformation, et de 1.10^{-3} sur la composante divergente. Ainsi, dans cette section, nous pouvons considérer de manière qualitative que les zones où la déformation cisaillante excède 0.1% ne sont pas dûes à du bruit mais sont représentatives du comportement.

Nous considérons d'abord des configurations successives éloignées, correspondant à un espacement de $\delta\epsilon_w = 2.3.10^{-3}$ en déformation axiale macroscopique. La position des fenêtres

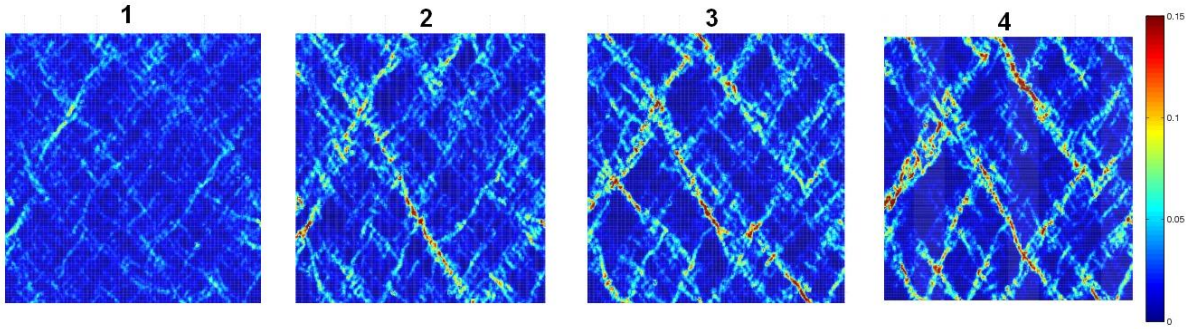

FIGURE 1.5 – Champs de déformation cisaillante calculés par corrélation d'images au cours d'un essai $1\gamma 2\epsilon$ en considérant des configurations successives éloignées. L'échelle d'observation en déformation est de $\delta\epsilon_w = 2.3.10^{-3}$. Les positions ainsi que la taille des fenêtres considérées pour la correlation d'images sont répertoriées sur la Figure 1.4(a). On considère ici $n = 10$ et $p = 50$ pixels.

considérées est matérialisée par les rectangles verts de la courbe macroscopique présentée sur la Figure 1.4.

Dans la suite de l'étude, on s'attache à caractériser les invariants de déformation divergente $\delta\epsilon_v$ et cisaillante $\delta\gamma$ définis de la manière suivante :

$$\begin{aligned} \delta\epsilon_v &= \delta\epsilon_I + \delta\epsilon_{II} \\ \delta\gamma &= \delta\epsilon_I - \delta\epsilon_{II} \end{aligned} \tag{1.1}$$

où $\delta\epsilon_I$ et $\delta\epsilon_{II}$ sont les composantes principales du tenseur incrémental de déformation.

La Figure 1.5 montre les champs incrémentaux de déformation cisaillante obtenus. Ce type de champs de déformation ont auparavant déjà été obtenus et caracterisés par *Hall et al.* (2010) en considérant le même dispositif expérimental. On peut voir, sur ces cartes, que la déformation cisaillante se localise sous forme de structures linéaires qui semblent s'installer avant le maximum de contrainte et se développer de manière continue et pérenne au cours du chargement. On peut par exemple suivre la croissance d'une de ces structures au cours du chargement, celle-ci apparaissant dès la phase initiale du chargement dans le coin supérieur gauche de l'échantillon. Ces structures linéaires semblent s'apparenter à la bande de cisaillement observée sur la Figure 1.1 : des précurseurs sont identifiables avant la matérialisation d'une bande finale, obtenue lorsque celle-ci traverse tout l'échantillon. Le phénomène de localisation de la déformation se caractérise donc ici par un effet de mémoire très marqué.

A l'inverse, la Figure 1.6 montre les champs de déformation obtenus en considérant un intervalle en déformation de plus d'un ordre de grandeur plus faible, ici égal à $\delta\epsilon_w \sim 1.10^{-4}$. Les configurations sont ici sélectionnées à l'intérieur du rectangle rouge de la Figure 1.4 et correspondent à une zone où l'on observe une chute de contrainte dans la courbe contrainte-déformation

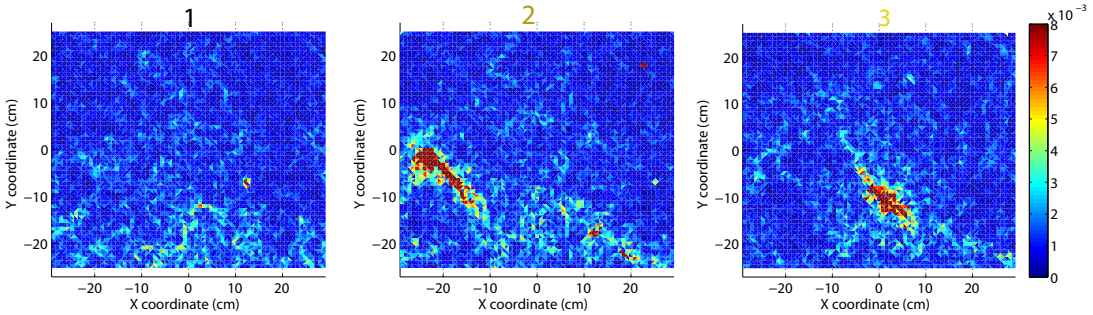

FIGURE 1.6 – Champs de déformation cisaillante calculés par corrélation d'images au cours d'un essai $1\gamma 2\epsilon$ en considérant des configurations successives rapprochées. L'échelle d'obervation en déformation est de $\delta\epsilon_w \sim 1.10^{-4}$. La résolution temporelle est donc ici plus d'un ordre de grandeur supérieure à celle considérée sur la Figure 1.5. Les positions ainsi que la taille des fenêtres considérées pour la correlation d'images sont répertoriées sur la Figure 1.4. On considère ici $n = p = 50$ pixels.

(Figure 1.4(b)). La position des cartes est matérialisée par les numéros correspondants sur cette même courbe. On s'aperçoit que, dans ce cas, les cartes de déformation cisaillante ne ressemblent aucunement à celles présentées sur la Figure 1.5.

Premièrement, la localisation de la déformation se matérialise ici par des amas à l'intérieur desquels la déformation se concentre. L'amplitude de la déformation cisaillante à l'intérieur de ces amas couvre une large gamme de valeurs, allant de $\delta\gamma = 1.10^{-3}$ à $\delta\gamma = 1.10^{-1}$. Au regard de la précision dont on dispose sur la déformation cisaillante dans cette expérience, qui est de l'ordre de 10^{-3}, on peut considérer que ces valeurs de déformation sont représentatives. Nous verrons de manière plus quantitative dans la section 3.5.1 que la structure particulière de ces champs que nous examinons dans la section 3.5 ne résulte aucunement du bruit dû au dispositif.

Deuxièmement, ces amas apparaissent très intermittents dans l'espace au cours du chargement. On observe sur la carte numéro 2 une zone de forte localisation de la déformation cisaillante dans le coin extrême gauche de l'échantillon. A l'instant d'après, i.e. sur la carte numéro 3, une autre zone de forte concentration de la déformation est observée à une position différente dans l'espace. Aussi, le précèdent amas de la carte numéro 2 a disparu. Ainsi, aucun effet de mémoire n'est visible à cet incrément de déformation macroscopique $\delta\epsilon_w \sim 1.10^{-4}$ et à cet endroit du chargement dans le champ de déformation.

Malheureusement, le dispositif expérimental $1\gamma 2\epsilon$ ne nous permet pas d'observer, aux petites échelles de déformation $\delta\epsilon_w \sim 1.10^{-4}$ telles que celles considérées précèdemment lors d'un saut de contrainte, comment les champs de déformation cisaillante se structurent dans la zone du chargement à laquelle nous nous interesserons dans le Chapitre 3, i.e. depuis l'initiation du chargement jusqu'au maximum de contrainte. En effet, la déformation étant majoritairement élastique dans cette partie du chargement, les déplacements des grains associés sont de très faibles amplitudes et donc indétectables avec le dispositif d'acquisition dont nous disposons.

Cependant, une équipe de l'Institut de Physique de Rennes constituée d'Antoine Le Bouil, Axelle Amon et Jérôme Crassous, avec qui nous avons initié une collaboration, a récemment obtenu de belles observations expérimentales dans cette zone particulière du chargement. Parce qu'elles illustrent très bien il me semble la démarche et l'étude que l'on a mené dans le Chapitre 3, Antoine Le Bouil nous a gracieusement permis de présenter leurs observations.

1.2.2 L'étude menée à l'Institut de Physique de Rennes

L'expérience de chargement biaxial élaborée dans le cadre de la thèse d'Antoine Le Bouil, initiée en 2011, considère un chargement similaire à celui de l'étude de *Desrues and Viggiani* (2004). Le matériau utilisé ici est un assemblage de billes de verre plus ou moins sphériques (voir Figure 1.7(b)) présentant une distribution de taille proche d'uniforme et une polydispersité de l'ordre de celle que l'on considèrera dans notre étude numérique, correspondant environ à un facteur 3 entre la plus grande et la plus petite particule (voir Figure 1.7(c)).

La mesure des micro-déformations est réalisée en utilisant les propriétés de diffusion multiple de la lumière du milieu granulaire. Un laser illumine la paroi de l'échantillon dans la direction où la déformation nulle est imposée et une caméra imageant la surface de la paroi permet de collecter la lumière rétro-diffusée. Les interférences entre les rayons rétro-diffusés par cette structure désordonnée donnent naissance à une figure dite de speckle. Lorsque la position des diffuseurs est modifiée, la différence de marche entre les rayons varie, ce qui entraine une modification de la figure de speckle. Le calcul des corrélations en intensité entre deux images de speckle correspondant à deux états différents du matériau donne alors une information sur la déformation de celui-ci. On obtient alors une valeur scalaire g_I caractérisant une perte de corrélation, proportionnelle à l'exponentielle d'une intensité de déformation. Cette déformation est donc, comme dans les cas pécèdents, incrémentale, car calculée entre 2 figures de speckle successives. Pour plus d'informations concernant cette méthode, consulter *Erpelding et al.* (2008); *Amon et al.* (2012).

L'originalité de cette expérience réside dans le fait que des images à très haute résolution, i.e. réalisées à une fenêtre de déformation de $\delta\epsilon_w = 1.10^{-5}$, sont disponibles dès la phase initiale du chargement. La Figure 1.7(a) montre la courbe contrainte-déplacement ainsi que les cartes d'intensité de déformation obtenues au cours du chargement. La longueur de l'échantillon dans la direction où la déformation est imposée est de 85 mm. Le maximum de contrainte est donc obtenu à une déformation axiale de l'ordre de 7%. Concernant les cartes de déformation, lorsque g_I est proche de 1, valeurs proches du jaune, la déformation est quasi nulle, de l'ordre de 1.10^{-6} et lorsque g_I est proche de 0, valeurs proches du rouge, la déformation est importante, de l'ordre de 1.10^{-4}. Au même titre qu'observé dans l'expérience $1\gamma 2\epsilon$ (Figure 1.6), la déformation se caractérise par des amas très localisés. Ces amas sont visibles dès l'initiation du chargement et leur taille semble croitre à l'approche du maximum de contrainte, où une bande de cisaillement apparait de manière pérenne dans la suite du chargement.

Pour illustrer l'intermittence temporelle et spatiale associée à ces amas de localisation de la

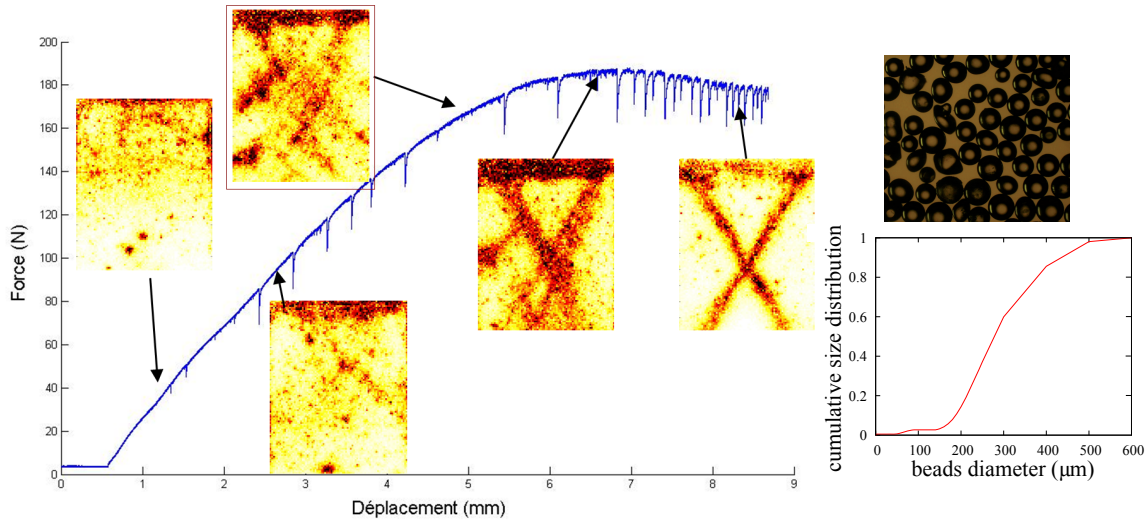

FIGURE 1.7 – Résultats expérimentaux obtenus au cours d'un chargement biaxial réalisé sur un assemblage de billes de verre par une équipe de l'Institut de Physique de Rennes en utilisant la technique de diffusion d'ondes lumineuses par spectroscopie (*Erpelding et al.*, 2008; *Amon et al.*, 2012). (a) Courbe contrainte-déplacement et cartes de l'indice de corrélation g_I, où g_I est proportionnel à l'exponentielle d'une intensité de déformation. (b) Image et (c) distribution des billes de verre constituant l'échantillon.

déformation, la Figure 1.8 montre les deux images qui précèdent à l'image encadrée en rouge sur la Figure 1.7. On voit très bien, d'une image à l'autre, que la répartition spatiale des amas d'intense déformation varie considérablement au cours du chargement, démontrant que le comportement à cette échelle de déformation macroscopique est très fluctuant et est associé à une mémoire très faible.

Enfin, la bande de cisaillement apparait très clairement au maximum de contrainte dans ces observations, même à cette échelle de déformation très faible de l'ordre de 1.10^5, ce que l'on ne voit pas dans $1\gamma 2\epsilon$ et dans le modèle aux éléments discrets que l'on considère.

1.2.3 Les objectifs de notre étude

Nous avons vu, à travers les différentes observations expérimentales présentées dans cette introduction, que les hétérogénéités des champs de déformation se matérialisent de manière diverses. On peut notamment qualitativement isoler deux types de comportement, l'un caractérisé par des amas d'intense déformation cisaillante, très fluctuants dans l'espace au cours du chargement, visibles uniquement aux petites échelles de déformation macroscopique et l'autre caractérisé par une ou plusieurs bandes de cisaillement établies, qui semblent présenter des tailles caractéristiques.

Dans la suite de cette partie portant sur les milieux granulaires, nous nous proposons de quantifier les propriétés de ces hétérogénéités de manière à évaluer dans quelle mesure et à quelles échelles de temps ou de déformation ces dernières présentent des caractéristiques particulières à l'approche de l'instabilité macroscopique.

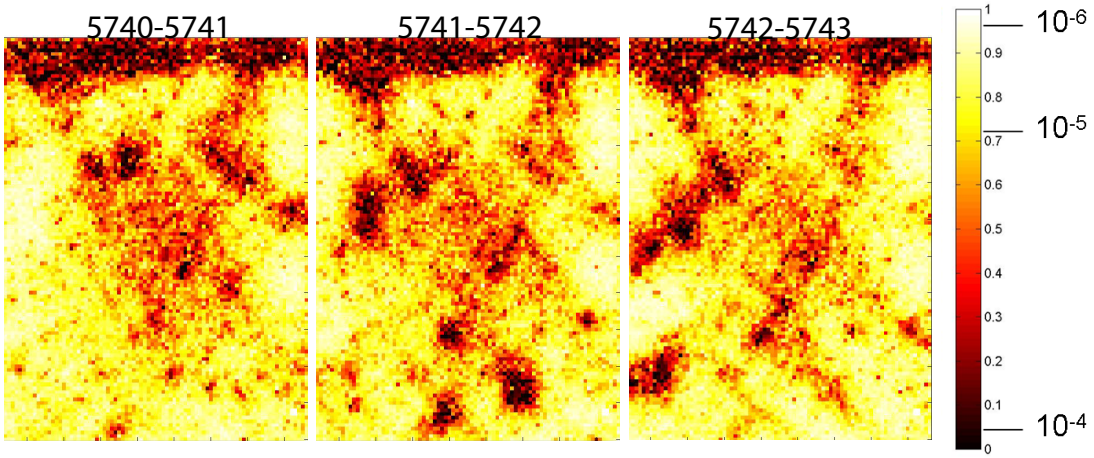

FIGURE 1.8 – Cartes du proxy de déformation g_I obtenues entre l'image 5740 et 5743, donc dans un intervalle de déformation macroscopique de 3.10^{-5}. L'échelle de couleur associée à l'amplitude de g_I est indiquée à droite et les tiretés sur cette échelle de couleur représentent un ordre de grandeur des intensités de déformation associées.

De manière à examiner spécifiquement le rôle des mécanismes microscopiques dans la structure de ces champs ainsi que d'effectuer des opérations de moyennage en considérant beaucoup d'essais mécaniques, nous utilisons principalement l'outil numérique, que nous présentons dans la section suivante.

Chapitre 2

Le modèle aux éléments discrets

The discrete element model

2.1 Model configuration

2.1.1 The molecular dynamics method

The molecular dynamics (MD) method is used in this study. This method considers the particles equations of motion that are time-discretized with a 3rd order predictor-corrector scheme. This model has been developped by Gaël Combe, from the 3S-R laboratory of Grenoble. Contrary to the contact dynamics (CD) method (*Radjai and Richefeu*, 2009; *Radjai and Dubois*, 2011), which considers perfectly rigid grains, the MD method takes into account the elastic deformation at the grain scale by treating elastic contacts. The grains are not deformable, i.e. the grain shapes do not change, but a contact overlap is considered.

Linear elastic contact laws are considered at grain contacts. A contact between two grains i and j is reached when the overlap $\delta = |x_i - x_j| - R_i - R_j$ is negative, x_i and x_j being the centers of the grains and R_i and R_j their radii.

When two grains are in contact, i.e. for $\delta < 0$, the contact laws are the following :

– the normal repulsive contact force f_n depends linearly on δ as follows :

$$f_n = -\delta k_n + v_n g_n \tag{2.1}$$

where k_n is the grain normal stiffness, v_n is the relative normal velocity between particles and g_n is a viscous damping coefficient. The last term of equation 2.1 corresponds to a damping force that opposes the relative velocity, allowing energy dissipation at contacts. Thus, the formulation for the normal force is linear with the interpenetration δ. More sophisticated laws can also be implemented by introducing a non linear formulation with interpenetration, for example considering Hertzian contacts (*Makse et al.*, 2004).

– the tangential force f_t is treated as proposed by *Cundall and Strack* (1979) : as for the normal force, f_t is proportional to the tangential elastic displacement with a tangential stiffness k_t, except that no viscous damping is considered in that case. Energy dissipation is accounted by contact sliding when the Coulomb criterion is reached. The Coulomb criterion $|f_t| \leq \mu f_n$, where μ is the friction coefficient, requires an incremental evaluation of f_t for each time step, which leads to some amount of slip each time the equality $|f_t| = \mu f_n$ is

verified. Thus, considering two grains in contact at time t_1, which remain in contact at least until time $t_2 = t_1 + \delta t$, and $f_t^{t_1}$ the tangential force lying in the contact at time t_1, the tangential force $f_t^{t_2}$ at time t_2 is defined as follows :

$$\begin{cases} f_t^{t_2} = f_t^{t_1} + \delta f_t & \textbf{where} \quad \delta f_t = -k_t v_t \delta_t \\ \textbf{if} \quad f_t^{t_2} > \mu f_n^{t_2} & \textbf{then} \quad f_t^{t_2} = -\mu f_n^{t_2} \frac{v_t}{|v_t|} \quad (v_t \neq 0) \end{cases} \tag{2.2}$$

where δf_t is a tangential force increment and v_t the relative tangential velocity.

The value of k_n is sized with respect to the nondimensional number $\kappa = \frac{k_n}{P}$ (*Roux and Chevoir*, 2005), where P is the average pressure at the isotropic state (see section 2.2), which quantifies the degree of rigidity of the grains. In this study, we set $\kappa = 1000$. This value for κ is small compared to most of real granular materials : for example, a value of $\kappa = 60000$ is associated to the $1\gamma 2\epsilon$ experiment (see section 1.2.1). As the discretisation time step scales with κ, such a choice for a low value of κ comes from a numerical necessity, as it allows to perform simulations that take little CPU times, of about one day for most of simulations performed in this study. The normal versus tangential stiffness ratio is $k_n/k_t = 1$. No rolling resistance is considered.

2.1.2 Periodic boundary conditions

Instead of considering a sample delimited by rigid walls on which force is applied, periodic boundary conditions are considered here (*Radjai and Dubois*, 2011). We consequently consider a periodic simulation cell (see section 6.3.3 of *Radjai and Dubois* (2011)), that is rectangular in our case. A linear operator $\mathbf{h}$, called the cell period and materialized in this particular geometry by a diagonal matrix, allows to map vector $\vec{s}$ as follows :

$$\vec{r} = \mathbf{h}.\vec{s} \tag{2.3}$$

where $\vec{r}$ is the grain position vector in the simulation cell and $\vec{s}$ the grain position vector in a unit square cell. The components h_{xx} and h_{yy} of matrix $\mathbf{h}$ define the size of the simulation cell in the horizontal and vertical direction. Accordingly, the particle velocities $\dot{\vec{r}}$ can be written as

$$\dot{\vec{r}} = \dot{\mathbf{h}}.\vec{s} + \mathbf{h}.\dot{\vec{s}}. \tag{2.4}$$

Thus, strain controlled simulations are performed by imposing constant deformation of the period, i.e. by controlling $\mathbf{h}$, while stress controlled simulations are performed writing the dynamic equations of motion of $\mathbf{h}$ as follows :

$$m_h \ddot{\mathbf{h}} = V \mathbf{h}^{-1} (\sigma^{int} + \sigma^{ext}) \tag{2.5}$$

where m_h is a fictive mass attributed to $\mathbf{h}$, which is set equal to the mass of the lightest grain in our simulations, V is the volume of the cell, σ^{int} is the internal stress resulting from internal

forces and σ^{ext} is the imposed external stress. In this formulation, σ^{int} and σ^{ext} have opposite signs.

2.2 Sample preparation

Sample preparation is performed using an assembling method. The goal of an assembling method is, once the shape and size distribution of grains are fixed, to put all particles together in order to reach a state of mechanical equilibrium of the whole granular assembly. Depending on the method considered, initial granular assemblies may differ in density (or packing fraction) ϕ, in average connectivity of particles or coordination number Z, in stress tensor fabric and in contact orientations (*Agnolin and Roux*, 2007; *Radjai and Dubois*, 2011). All these parameters are known to influence the subsequent mechanical properties of the samples under compression in the quasi-static regime.

The build of granular assemblies is here performed under static loading in the absence of body forces (such as gravity). Circular 2D grains of surfaces uniformly distributed are considered. All the samples built in this study consider the same polydispersity, setting the largest grain diameter D_{max} such that $D_{max} = 3D_{min}$. The particles are randomly placed on sites of a regular lattice, all spaced by D_{max} one from each other, before being mixed. This mixing procedure uses the contact dynamics (CD) method (*Radjai and Dubois*, 2011), so considers hard disks, and consists in setting grains in motion with random velocities, leaving them to interact in collisions that preserve kinetic energy, in order to produce a disordered configuration. At the end of this procedure, all grains velocities are set equal to 0 and an isotropic compression is performed using the molecular dynamics (MD) method.

A first category of samples, that show the largest value of initial packing density ϕ_{ini} and coordination number Z_{ini}, can be built by considering frictionless particles at this stage, i.e. setting the grains friction coefficient μ_{iso} equal to 0. The associate density ϕ_{ini} reached at mechanical equilibrium for those types of samples is about 0.845, i.e. is close to the jamming density $\phi_c \approx 0.84$ observed for 2D bidisperse samples (*O'Hern et al.*, 2003), while the associate coordination number Z_{ini} is about 3.95, i.e. is close to the isostatic number at jamming $Z_c = 2d$ (*O'Hern et al.*, 2003), where $d = 2$ is the dimensionality. This type of sample will be considered in Chapter 3.

Other types of samples with varying density ϕ_{ini} and coordination number Z_{ini} will be built in Chapter 4 by considering non-zero friction when performing the isotropic compression from the initial granular gas, or after having maintained strongly agitated granular gas states at high densities before isotropic compression. Details and results about samples properties obtained following these procedures are thoroughly examined in this last chapter.

2.3 Biaxial testing

The biaxial test is performed at constant confining pressure σ_3, applied in the horizontal direction, which is equal to the mean pressure reached at the end of the isotropic stage. This condition is satisfied by writing equation 2.5 along the horizontal direction, i.e. by adjusting h_{xx} to maintain $\sigma_3^{ext} = \sigma_3^{int}$ during biaxial testing. A deviatoric stress $\tau = \frac{\sigma_1 - \sigma_3}{2}$ is applied by increasing σ_1. This increase can either be imposed by controlling the axial strain rate $\dot{\epsilon}_1$ or the axial stress rate $\dot{\sigma}_1$:

- strain controlled simulations can be performed by setting $\dot{h}_{yy} = V_{imp}$, where V_{imp} is the imposed deformation rate of the period in the vertical direction. For strain controlled experiments performed in our study, the imposed velocity V_{imp} is chosen such that mechanical transformation can be assumed as quasi-static. To do so, we prescribe V_{imp} with respect to the non dimensional parameter I (*Roux and Chevoir*, 2005), called the inertial number, that quantifies the importance of dynamic effects in the macroscopic mechanical response of the granular assembly. I is defined in 2D as $I = \dot{\gamma}\sqrt{m/P}$, where m is the total mass and P the average pressure. In this study, we set $I = 5.10^{-5}$, that ensures quasi-static conditions (*Midi*, 2004; *Radjai and Dubois*, 2011). Compared to experimental mechanical testing performed in laboratory, for example the ones presented in section 1, this value for I is very large, approximately 3 to 4 orders of magnitude larger.
- stress controlled simulations can be performed by writing equation 2.5 along the vertical direction and setting $\sigma_1^{ext} = \sigma_1^{ext} + \delta\sigma_1^{t_r}$ at each time increment. The increment considered in our simulations is set to $t_r = \sqrt{\frac{m_{min}}{k_n}}/25$, where m_{min} is the mass of the lightest grain. As our goal in performing those types of simulations is to explore the transition from a quasi-static to a dense flow regime in chapter 3, the value of $\delta\sigma_1^{t_r}$ will there be made to vary, inducing variations of the inertial number I.

2.4 Mechanical behaviour of the granular assembly

An example of the mechanical behaviour obtained during a numerical multi-axial experiment performed on a 10000 grains sample is provided in Figure 2.1. Associated deformation fields computed at large deformation windows $\delta\epsilon_w = 3.10^{-3}$ are also shown. Here, the sample considered is built setting $\mu_{iso} = 0$ during the isotropic compression, i.e. on frictionless particles. The particle friction coefficient is set to $\mu = 1$ during multi-axial testing. A more detailed discussion on the variabilities in simulated macroscopic behaviors is provided in Chapter 4 but, from now, we can say that a similar macroscopic behaviour, characterized by a maximum of contraction and a maximum shear stress, than the one obtained experimentally in section 1 is reproduced in simulations. Moreover, in these simulations, strain localization materialized by linear features that accomodate most of the deformation is observed. At these large deformation windows of $\delta\epsilon_w = 3.10^{-3}$, these structures are perennial during mechanical loading and, in that regard, are associated to the shear band observed in *Desrues and Viggiani* (2004) and discussed in

Chapter 1. In the next chapter, we thoroughly examine these deformation structures and the associated stress field at the approach of the macroscopic instability.

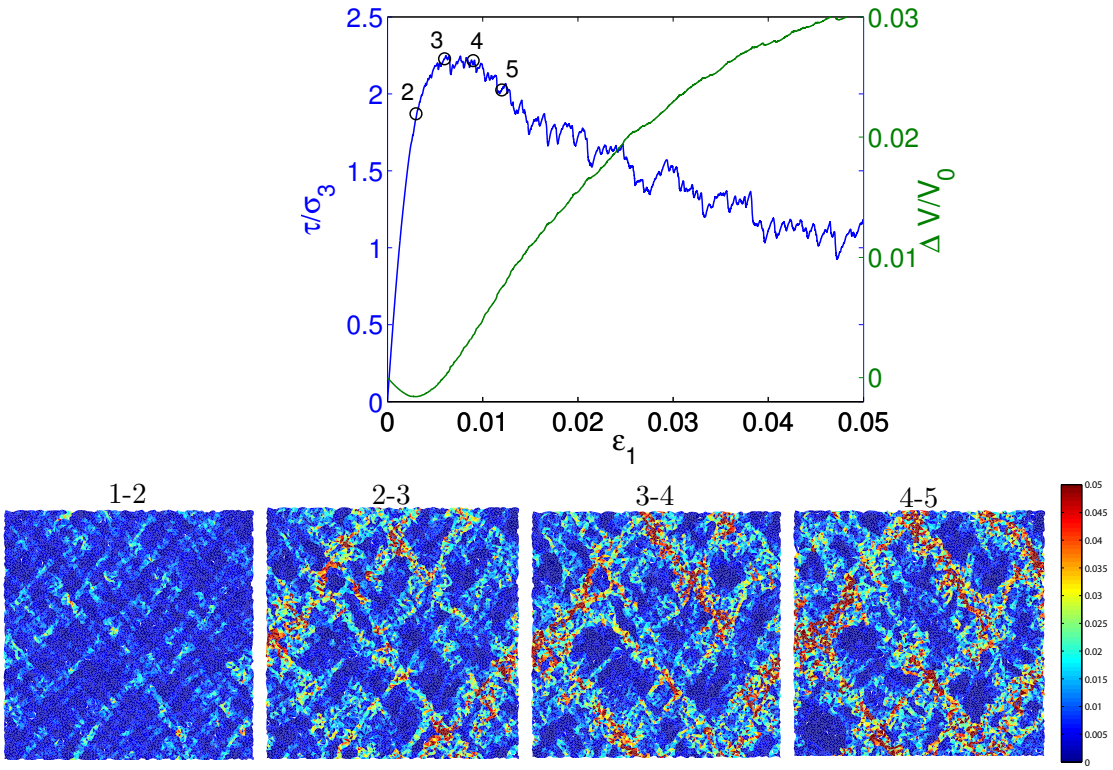

FIGURE 2.1 – Macroscopic behavior of a sample made of 10000 grains during compressional testing and associated shear deformation fields. (Top) Deviatoric stress $\tau/\sigma_3 = (\sigma_1 - \sigma_3)/\sigma_3$ (blue line) and macroscopic volume variation $\Delta V/V_0$ (green line) as a function of axial deformation. (Bottom) Shear deformation fields associated to the numbered deformation windows plotted on the stress verus strain curve. The incremental deformation window used here is $\delta\epsilon_w = 3.10^{-3}$.

Chapitre 3

Du quasi-statique à l'écoulement dense

Crossover from quasi-static to dense flow regime

3.1 Crossover from quasi-static to dense flow regime in compressed frictional granular media

D'après :

Gimbert, F., D. Amitrano, J. Weiss and G. Combe, Crossover from quasi-static to dense flow regime in compressed frictional granular media, *soumis à Phys. Rev. Lett.*, accessible sur *http* : *//arxiv.org/abs/*1208.1930.

Abstract

We investigate the evolution of multi-scale mechanical properties towards the macroscopic mechanical instability in frictional granular media under compressive loading. Spatial correlations of shear stress redistribution following nucleating contact sliding events and shear strain localization are investigated. We report growing correlation lengths associated to both shear stress and shear strain fields that diverge simultaneously as approaching the transition to a dense flow regime. This shows that the transition from quasi static to dense flow regime can be interpreted as a critical phase transition. Our analysis does not show any characteristic shear band thickness potentially formed at the onset of instability.

The mechanical behavior of granular materials is of wide concern, from natural hazard in geological context to engineering application. However, the evolution of properties towards the flowing instability is still partially understood. Within packings of spheres, heterogeneous distributions of contact forces on a scale much larger than the typical particle size (*Liu et al.*, 1995) may control the mechanical response of the granular assembly, characterized by long range correlations and collective motions (*Radjai and Roux*, 2002). The concept of jamming (*Liu and Nagel*, 1998) provides a framework to analyse the onset of granular flows. Large efforts have been done in this direction by considering assemblies of non frictional particles, which exibit jammed states resisting small stresses without irreversible deformation, whereas unjammed systems flow under any applied stresses (*Liu and Nagel*, 1998; *Combe and Roux*, 2000). As granular materials play a fundamental role in geophysical instabilities (e.g. granular gouges within fault zones, landslides), the concept of jamming might be a powerful tool to investigate these problems. However, two more ingredients are of primary importance in those cases. First, frictional granular materials have to be considered, leading to changes in the physics of jamming : the packing fraction is not a pertinent parameter anymore and the transition from an unjammed to a jammed state is rather controlled by the non-rattler fraction (*Bi et al.*, 2011). Secondly, the loading conditions drastically differ from the one commonly used to study jamming, since, rather than performed at constant volume, a confining pressure has to be considered. In that case, the non-rattler fraction is not allowed to evolve freely and a percolating strong force network remains in the flowing phase, called the dense flow regime (*Pouliquen and Chevoir*, 2002).

Here we consider compression tests under multi-axial loading : an increase of the axial stress σ_1 is prescribed whereas the 2D confining pressure σ_3 is kept constant. These multi-axial conditions correspond to the generic case encountered in the Earth and the stress control avoids stress relaxations and associated feedbacks, i.e. the stress and strain localization structures develop freely. Experiments (*Desrues and Viggiani*, 2004) and theoretical works (*Rudnicki and Rice*, 1975) have been conducted in this configuration on either continuous or discrete materials. In continuous materials, the macroscopic instability as been first tackled by the use of bifurcation theory, which considers a transition from an homogeneous to an heterogeneous deformation field materialized by the creation of a perennial macroscopic shear band spanning the whole sample (*Rudnicki and Rice*, 1975; *Haimson and Rudnicki*, 2010). Within granular materials, either in experiments or simulations, computing the deformation field over a large macroscopic strain window, those perennial shear bands appear and seem to show characteristic sizes (*Desrues and Viggiani*, 2004). However, this vision is counterbalanced by the heteregenous and long range correlated kinematics of quasi-static granular flow (*Radjai and Roux*, 2002) : at which temporal and spatial scales and at which stage of the loading can we consider the granular assembly to deform homogeneously ? What are the relevant key features of the deformation and stress fields associated to the onset of instability ?

We use the Molecular Dynamics discrete element method to perform our simulations (*Radjai and Dubois*, 2011). Two-dimensional granular assemblies made of frictional circular grains are considered. The grains surfaces are uniformly distributed, setting the largest grain diame-

ter D_{max} such that $D_{max} = 3D_{min}$. Periodic boundary conditions are used (*Radjai and Dubois*, 2011). Grains interact via linear elastic laws and Coulomb friction when they are in contact (*Cundall and Strack*, 1979). Dense and highly coordinated initial packings, characterized by a porosity $\eta_i \approx 0.15$ and a coordination number $z_i \approx 4$, are obtained by isotropic frictionless compression of dilute grains sets. We focus in this study on compression tests, setting the particle friction to $\mu_{micro} = 1$. The confining pressure σ_3 is sized by setting the contact stiffness $\kappa = k_n/\sigma_3$ equal to 1000 (*Radjai and Dubois*, 2011), where k_n is the normal contact stiffness coefficient. The vertical stress σ_1 is increased at constant rate. To characterize sample size effects (see section 3.2.2.2), we performed 320 simulations on 2500 grains samples, 80 simulations of 10000 grains and 20 simulations of 45000 grains. Most of the results presented here concern 10000 grains samples. Whatever the sample size, we used a stress increment $\delta\sigma_1^{t_r}$ equal to $1.10^{-6} \times \sigma_3$ at each discretisation time interval $t_r = \sqrt{\frac{m_{min}}{k_n}}/25$, where m_{min} is the mass of the lightest grain. This leads to an inertial number I (*Radjai and Dubois*, 2011) of the order of $10^{-6} - 10^{-5}$ at the initial stage of the test (Figure 3.1),which ensures quasi-static conditions.

Figure 3.1(a) shows a typical macroscopic stress-strain curve. An initial contracting phase is observed, only because of an elastic contact between particles (*Combe and Roux*, 2003), until a peak of contraction is reached, after which the sample dilates continuously. The deviatoric stress $\tau = \sigma_1 - \sigma_3$ reaches a plateau at values slightly larger than $2\sigma_3$, obtained for values of axial strain ϵ_1 of about 0.004. Before this specific point, while undergoing brutal increase during plastic avalanches, the inertial number I remains lower than 10^{-4} (Figure 3.1(b)), which is often considered as the upper bound for quasi-static conditions (*Radjai and Dubois*, 2011; *Midi*, 2004). This region corresponds to the quasi-static regime. On the reverse, at values of τ greater than $\tau_c = 2\sigma_3$, that corresponds to a macroscopic friction $\mu_{macro} \sim 0.5$, a brutal increase of I of several orders of magnitude is observed, reaching values of the order of 10^{-2}, which corresponds to a transition toward a dense flow regime, where inertia comes into play. At this transition, stress concentrations resulting from cooperative effects are expected, triggering preferential weak zones where flow is favoured. In the case of our samples made of circular grains, this leads to a softening of the whole granular assembly and thus to a macroscopic friction much smaller than μ_{micro}. According to this, studying the spatial structure of both stress and strain fields is a key point to understand the mechanisms that generate the macroscopic instability. We thus focus, in this study, on the "dynamics" of the granular assembly, i.e. on the response of the granular assembly to a small stress increment in terms of associated stress concentration and strain localization structures that form during mechanical loading.

We first characterize the spatial extent of stress concentrations within the granular sample by means of a coarse graining analysis (*Marsan et al.*, 2004; *Girard et al.*, 2010) : an averaged shear stress rate $< \dot{\tau} >$ is computed at different stages of mechanical testing (cf color dots on Figure 3.1) over a time window T and over a broad range of spatial scales L, from the microscale corresponding to the scale of the mesh element, to the macroscale corresponding to sample size (Figure 3.2). In the following, we define the invariant x, where x represents τ for the shear

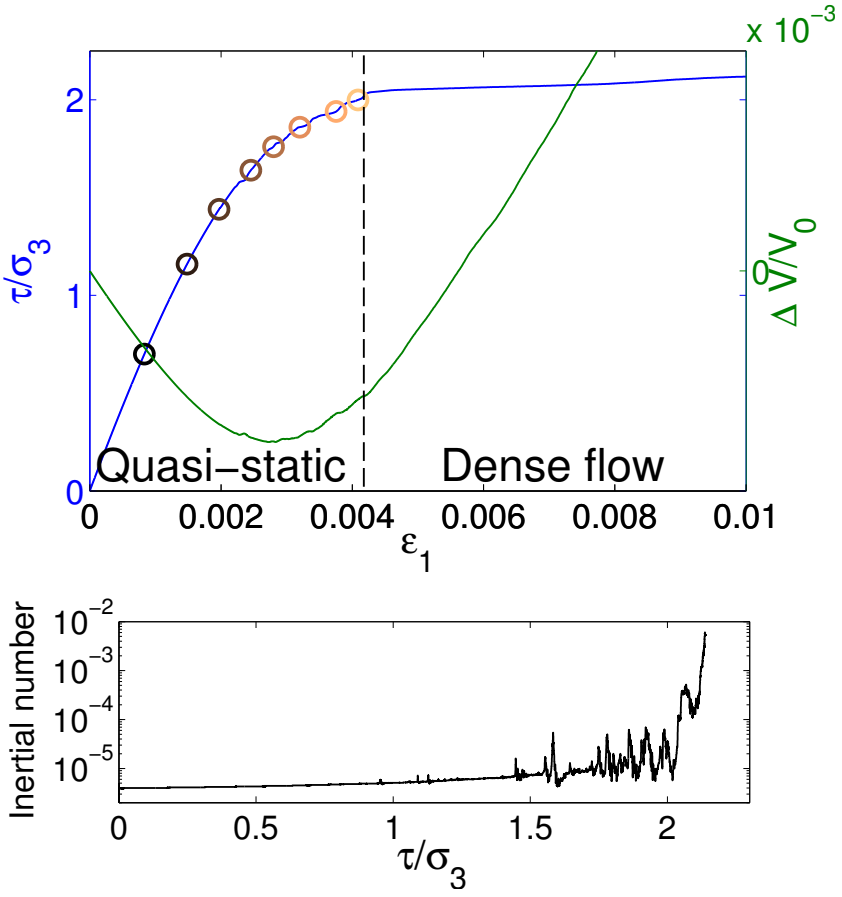

FIGURE 3.1 – Macroscopic behavior of a sample made of 10000 grains during compressional testing. Top : Deviatoric stress $\tau/\sigma_3 = (\sigma_1 - \sigma_3)/\sigma_3$ (blue line) and macroscopic volume variation $\Delta V/V_0$ (green line) as a function of axial deformation. Color dots correspond to locations where coarse-graining analyses of Figures 3.3(Top) and 3.4(Top) are performed. Bottom : Inertial number I as a function of the imposed deviatoric stress τ.

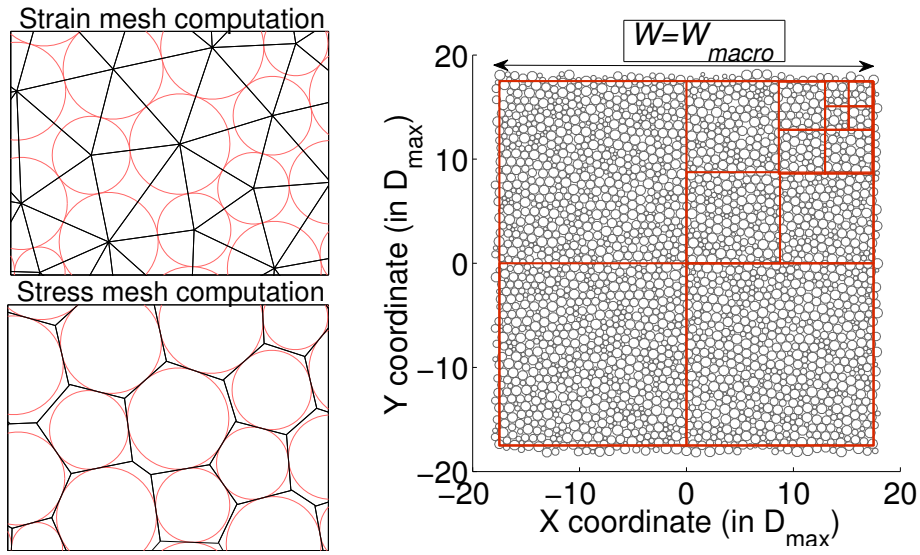

FIGURE 3.2 – Left : Delaunay (top) and modified Voronoi (bottom) tesselations for a polydisperse granular material. Right : Coarse graining analysis on a 2500 grains sample.

stress field or γ for the shear strain field, as $x = X_I - X_{II}$, where X_I and X_{II} are the principal components of the stress or strain tensor. For a given assembly of grains, the components of the stress tensor are computed as $\sigma_{ij} = \frac{1}{V}\sum_g \sum_c (r^c - r^g) f_g^c$ (*DeGiuli and McElwaine*, 2011), where V is the surface associated to the grain assembly, that corresponds to the sum of surfaces associated to each grain including the amount of porosity calculated using the modified Voronoi tesselation (Figure 3.2), f_g^c is the contact force exerted on grain g at contact c, r^c is the position of c, and r^g is the position of the center of g. Considering two successive configurations, the stress rate tensor is obtained by differentiating the respective stress tensor components in time. The time resolution used is $T = \sqrt{N_g} \times 100 \times t_r$, where N_g is the number of grains of the sample. This timescale corresponds to the travel time of elastic waves through the granular assembly (see section 3.2.1). Results are shown on Figure 3.3 (Top), from the early stages of biaxial testing up to $\tau_c = 2\sigma_3$. At the early stages of macroscopic deformation, a decrease of $< \dot{\tau} >$ with L is observed at small scales while for L-values larger than a crossover scale l_τ^* a plateau is observed. This means that shear stress rate fields are heterogeneous for $l << l_\tau^*$, and homogeneous for $l >> l_\tau^*$. Hence, l_τ^* is the associated correlation length (*Girard et al.*, 2010). As macroscopic deformation proceeds, l_τ^* grows until reaching the entire size of the system at τ_c where a power law scaling $< \dot{\tau} > \sim L^{-\rho_\tau}$ is observed, with $\rho_\tau = 0.38$. The cut-off remaining on the scaling at $\Delta \to 0$, where $\Delta = \frac{\tau_c - \tau}{\tau_c}$ is the control parameter, is a finite size effect (see section 3.2.2.2). These results suggest a progressive structuring of the stress field as approaching the transition to the dense flow regime, associated to the divergence of the correlation length l_τ^*. It can be verified from a collapse analysis (inset of Figure 3.3(Top)) that l_τ^* diverges as

$$l_\tau^* \sim \frac{L_s^\delta}{\Delta^{\nu_\tau} L_s^\delta + C}. \tag{3.1}$$

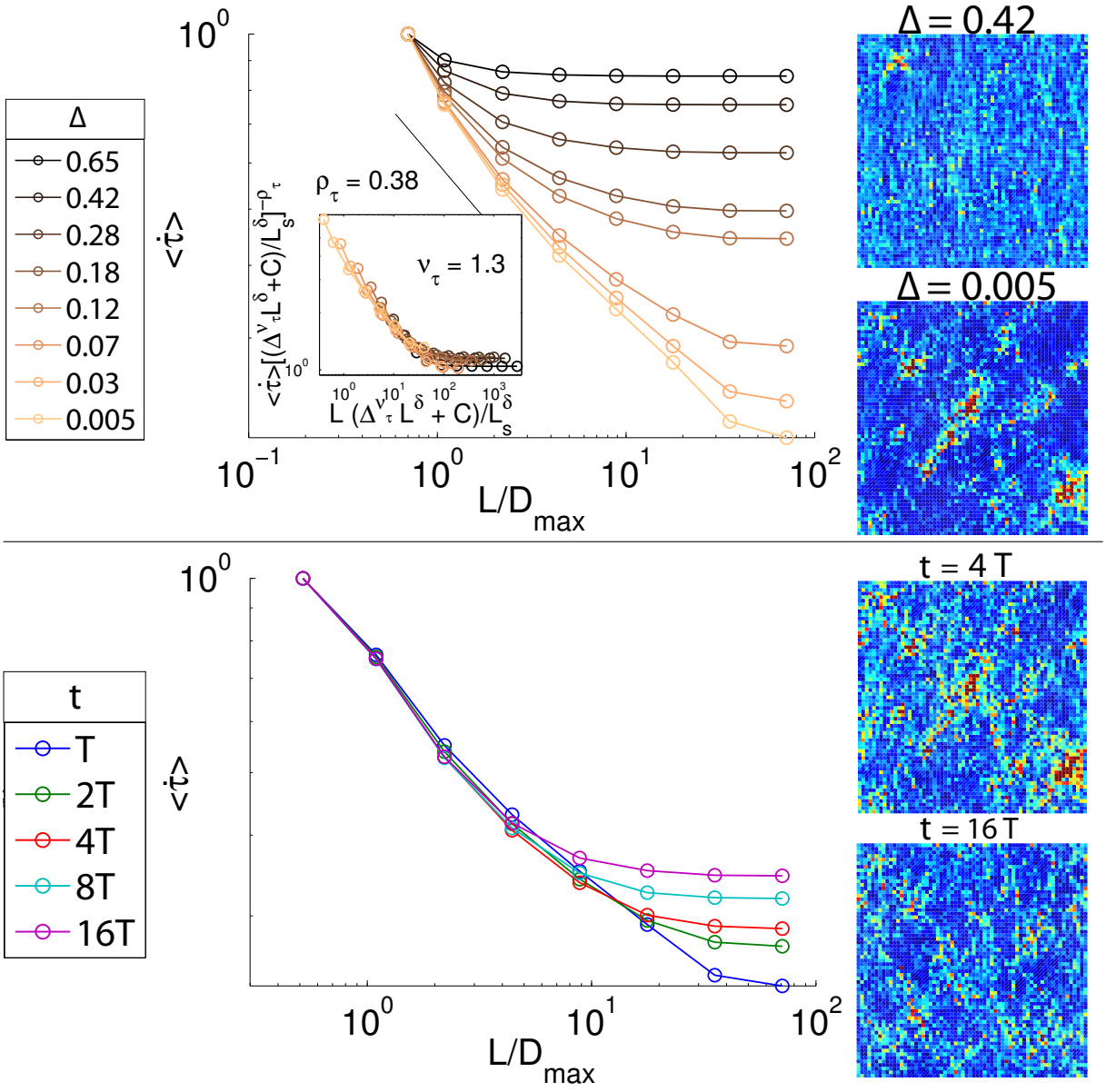

FIGURE 3.3 – Multi-scale analysis performed on the shear stress rate field $\dot{\tau}$. A selection of corresponding fields is shown on the right. Top : $< \dot{\tau} >$ versus L for decreasing values of Δ. Configuration locations on the stress-strain curve are shown on Figure 3.1. The timescale T is used to compute values of $< \dot{\tau} >$. The inset displays data collapse with respect to Δ (equation 3.1). We find $\nu_\tau = 1.3$, $C = 0.5$ and $\delta = 1$. Bottom : $< \dot{\tau} >$ versus L at $\Delta = 0.005$ when increasing the timescale t from $t = T$ to $t = 16T$. For graphical convenience, all computed values have been normalized by the ones computed at the microscale.

where $\nu_\tau = 1.3 \pm 0.1$ is the divergence exponent. Parameters δ and C characterize the finite size effect. A similar analysis performed on other moments $< \dot{\tau}^q >$ of the shear rate (see section 3.2.3) confirms the divergence of l^*_τ at $\Delta \rightarrow 0$, and reveals their multi-fractality at the critical point. As stated previously, these particular features of the shear stress field are observed at a specific timescale $t = T$ corresponding to the elastic waves travel time. This multi-scale behaviour is no longer observed at larger timescales (Figure 3.3(Bottom)), as a clear departure from power law is observed for $t > T$. Hence, the multi-scale properties of the shear stress rate field are only observed at the time of propagation of the elastic information throughout the sample. Beyond this time, a decorrelation is observed, explained by the superposition in time of several uncorrelated events, consistant with a correlated stress structure associated with little memory, limited to the elastic wave travel time.

To study whether similar observations can be reported on the shear strain field, we consider a Delaunay triangulation performed on the grain centers (Figure 3.2), after having removed the rattlers grains from the grain set, that allows to compute the partial derivatives at the mesh scale as $\epsilon_{ij} = 1/2(\partial u_i/\partial x_j + \partial u_j/\partial x_i)$, where (u_1, u_2) and (x_1, x_2) are respectively the incremental displacements and spatial coordinates of grain centers. Our coarse graining analysis is then performed by averaging partial derivatives at various scales, similarly to *Marsan et al.* (2004); *Girard et al.* (2010). An average shear strain rate is thus obtained as a function of L. While not shown here, if one uses the constant timescale T to compute incremental displacements, a divergence of the correlation length associated with the shear strain rate field is not observed. Thus, the structure of the total strain field does not form simulteanously to the stress field, by means of long-ranged elastic interactions. Intuitively, this would be the case if one would consider only the elastic component of the strain. Here, for $N_g = 10000$, $\sim 10^4$ stress increments are prescribed during the propagation time of an elastic wave throughout the sample. Hence, a multitude of contacts, in our case about 5% of the whole contact network, are then sliding, although elastic interactions didn't have time to travel across the entire sample, i.e. we are not in conditions of intinitly slow driving that could be obtained using event-driven algorithms (*Radjai and Dubois*, 2011). Despite this, a progressive structuring of the shear strain field is observed by considering constant macroscopic deformation windows $\delta\epsilon_1 = \delta\epsilon_p = 1.10^{-5}$ to compute the scaling of $< \delta\gamma >$ (Figure 3.4). A divergence of the correlation length l^*_γ similar to the one observed on the shear stress rate field is obtained as approaching the transition to the dense flow regime, as we find $\nu_\gamma = \nu_\tau = 1.3$ from a collapse analysis (equation 3.1). When considering larger macroscopic deformation windows, the multi-scale properties of the deformation field are no longer observed, pointing out that $\delta\epsilon_1 = \delta\epsilon_p$ is a characteristic value. As the material softens when τ increases, the corresponding time of integration decreases as the critical point is approached. This corresponding time can either be smaller or larger than the elastic wave traveling time T, depending on the imposed loading rate $\delta\sigma_1^{t_r}$. However, whatever the loading rate considered and the size of the system, $\delta\epsilon_1 = \delta\epsilon_p$ remains equal to 1.10^{-5}, pointing out that a given amount of plastic activity has to operate in order to observe mutli-scale properties within the incremental shear strain field. As the correlation lengths l^*_τ and l^*_γ diverge the same

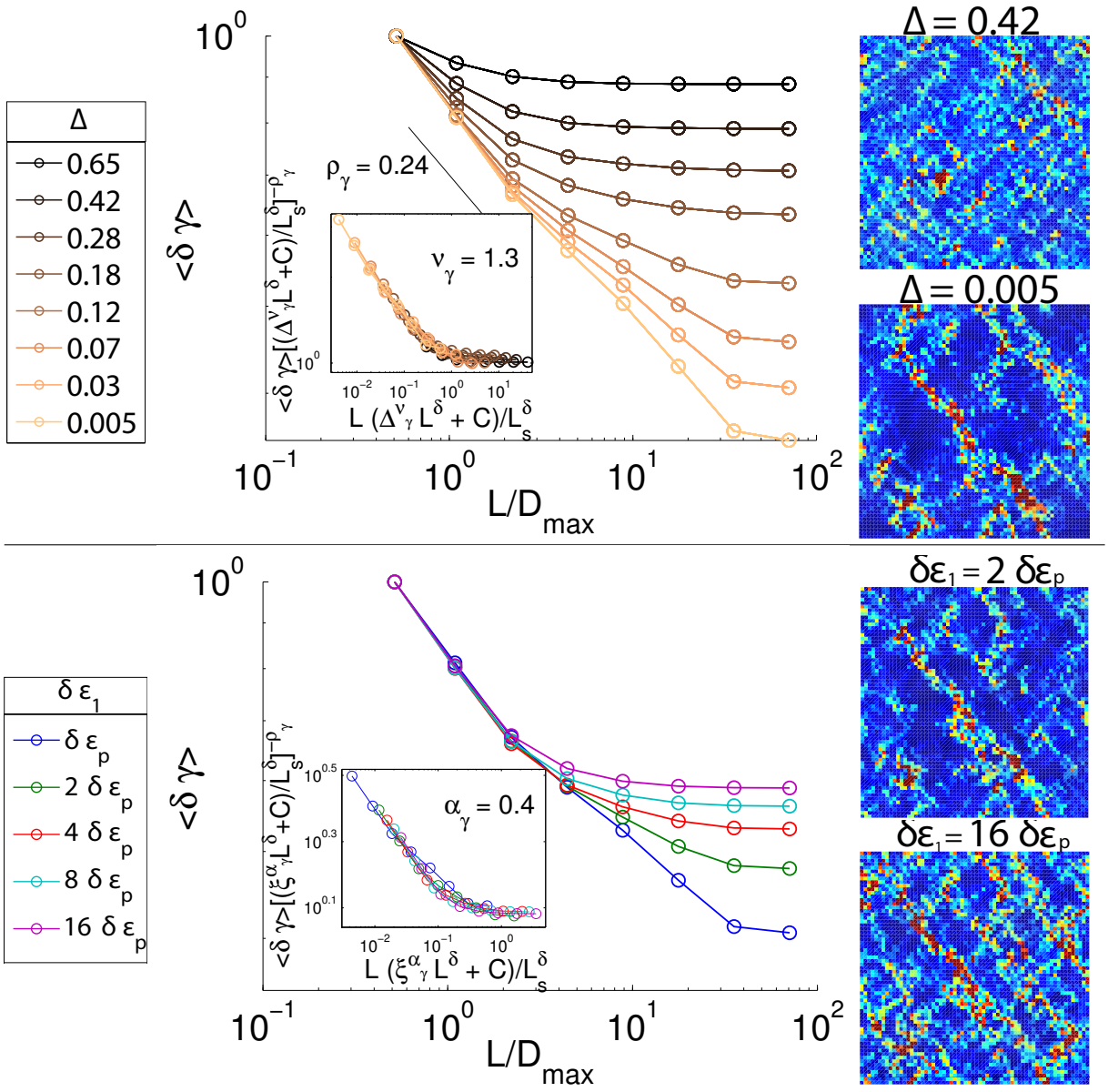

FIGURE 3.4 – Multi-scale analysis performed on the incremental shear strain field $\delta\gamma$. A selection of corresponding fields is shown on the right. Top : $<\delta\gamma>$ versus L for decreasing values of Δ towards the critical point. The deformation scale $\delta\epsilon_1 = \delta\epsilon_p = 1.10^{-5}$, consistant with the susceptibility analysis presented on Figure 3.5, is used to compute values of $<\delta\gamma>$. The inset displays data collapse with respect to Δ (equation 3.1). We find $\nu_\gamma = 1.3$, $C = 0.5$ and $\delta = 1$. Bottom : $<\delta\gamma>$ versus L at $\Delta = 0.005$ when increasing $\delta\epsilon_1$ from $\delta\epsilon_1 = \delta\epsilon_p$ to $\delta\epsilon_1 = 32\delta\epsilon_p$. The inset displays data collapse with respect to $\xi = \frac{\delta\epsilon_1 - \delta\epsilon_p}{\delta\epsilon_p}$. We find $\alpha_\gamma = 0.4$. For graphical convenience, all computed values have been normalized by the ones computed at the microscale.

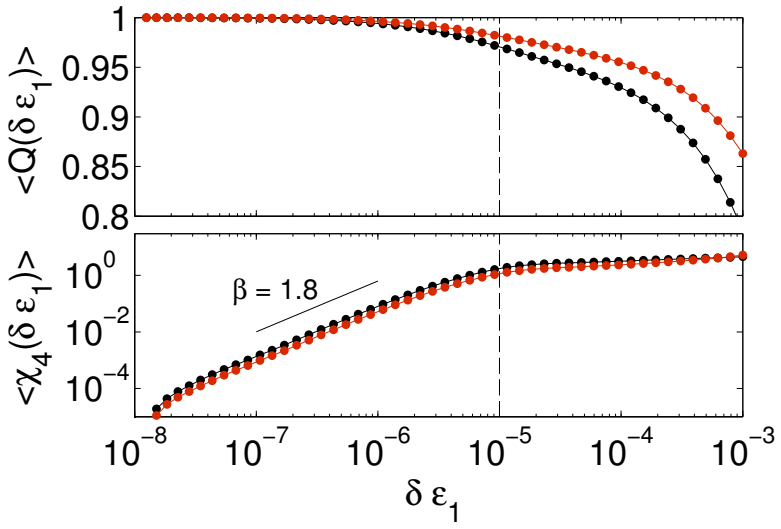

FIGURE 3.5 – Susceptibility analysis performed in the quasi-static phase on the sliding contacts taking part of the major (red curves) and minor (black curves) networks. Top : Averaged self-overlap order parameter $< Q(\delta\epsilon_1) >$. Bottom : Corresponding four-point average susceptibility $< \chi_4(\delta\epsilon_1) >$. The vertical dashed line indicates the deformation value $\delta\epsilon_p = 1.10^{-5}$, where a change of behavior is observed.

way, this plastic activity is probably the direct consequence of the progressive structuring of the stress field.

An understanding of the characteristic value $\delta\epsilon_p$ can be obtained from a four-point dynamic susceptibility χ_4 (*Abate and Durian*, 2007; *Keys et al.*, 2007) analysis performed on the inter-particles contact network. From a contact configuration that we refer as "initial", selected at a value of axial deformation denoted ϵ_1^{init}, we compute the self-overlap order parameter $Q_{\epsilon_1^{init}}(\delta\epsilon_1) = \frac{1}{N_c}\sum_{i=1}^{N_c} w_i$, where N_c is the number of contacts that are not sliding in the initial configuration and w_i is a step-function cutoff that equals 1 if no sliding event has been recorded on contact i over the whole deformation window $\epsilon_1^{init} \rightarrow \epsilon_1^{init} + \delta\epsilon_1$, and 0 otherwise. The first two moments $Q(\delta\epsilon_1) =< Q_{\epsilon_1^{init}}(\delta\epsilon_1) >$ and $\chi_4(\delta\epsilon_1) = N_c\big[< Q_{\epsilon_1^{init}}(\delta\epsilon_1)^2 > - < Q_{\epsilon_1^{init}}(\delta\epsilon_1) >^2 \big]$ of $Q_{\epsilon_1^{init}}(\delta\epsilon_1)$ (calculated from sample-to-sample fluctuations) are then computed in the quasi-static region ($\tau < \tau_c$). Like this, we evaluate from an initial configuration the number and the associated spatial heterogeneity of sliding events nucleation as axial deformation increases. Figure 3.5 shows $< Q(\delta\epsilon_1) >$ and $< \chi_4(\delta\epsilon_1) >$, where $< . >$ here means an average over all the values of Δ (since no significant variation of $Q(\delta\epsilon_1)$ and $\chi_4(\delta\epsilon_1)$ is observed in the quasi-static region) computed by considering separately the major and minor force networks. The major force network is defined by selecting contact force greater than the average. By construction, $< Q(\delta\epsilon_1) >$ is initially equal to 1. As $\delta\epsilon_1$ increases, $< Q(\delta\epsilon_1) >$ decreases but never reaches 0, meaning that a considerable amount of contacts never slides. When considering the whole test, about 35% (respectively 55%) of the contacts of the minor (respectively major) network didn't slide at the end of the test, meaning that the permanent deformation is extremely localized and

that rigid bodies remain throughout the whole test (*Szarf et al.*, 2011). The value of $< \chi_4(\delta\epsilon_1) >$ indicates, with respect to increasing axial deformation, the variability in the nucleation of new contact slidings. At low values of $\delta\epsilon_1$, it increases as $< \chi_4(\delta\epsilon_1) > \sim \delta\epsilon_1^{\beta}$ with $\beta = 1.8$, meaning that spatially correlated sites of contact sliding events are nucleating. As $\delta\epsilon_1$ exceeds the treshold value $\delta\epsilon_p = 1.10^{-5}$, $< \chi_4(\delta\epsilon_1) >$ saturates, as all the spatially correlated contacts located close to the coulomb criteria, i.e. susceptible to slide, have been destabilized. At this stage, only 4% (respectively 3%) of contacts have slided at least one time in the minor (respectively major) network.

To conclude, incremental stress and strain fields are both characterized by a growing correlation length that diverges at the onset of macroscopic instability, which can therefore be identified as a critical point. A similar behavior has been reported in compressive failure of continuous materials (*Girard et al.*, 2010, 2012). We interpret these stress and strain specific structures as resulting from dynamic stress redistributions induced by local dissipation of elastic energy materialized by contact slidings. At macroscopic instability, a local contact sliding event induces correlated elastic stress perturbations up to the scale of the whole granular assembly. These features can only be observed when carefully examining characteristic timescales for stresses, and macroscopic deformation for strains concentration processes. Thus, a long time memory, probably associated to a slow evolution of the topology, exists in the system, in relation with the growth of l_τ^* and l_γ^* during mechanical loading towards the macroscopic instability, while the spatial multi-scales structure of stress and strain fields have respectively a short time and deformation life.

The last question that arises is to whether a limit in decreasing correlation length l_γ^* on the shear strain field is reached at $\Delta \to 0$ for values of $\delta\epsilon_1$ much greater than $\delta\epsilon_p$, which would characterize the thickness of a perennial macroscopic shear band potentially formed at the onset of instability. To investigate this, we hypothesize that, close to the critical point ($\Delta \to 0$), l^* varies as $l_\gamma^* \sim \frac{L_s^\delta}{L_s^\delta \xi^{\alpha_\gamma} + C_\gamma}$ where $\xi = \frac{\delta\epsilon_1 - \delta\epsilon_p}{\delta\epsilon_p}$, L_s is the square root of the sample area and α_γ is an exponent. This hypothesis is checked from a collapse analysis (inset of Figure 3.4). We find $\alpha_\gamma = 0.7$. This shows that l_γ^* keeps decreasing as the considered deformation window size $\delta\epsilon_1$ is increased, showing that the correlation length only depends on the value of $\delta\epsilon_1$ and that no intrinsic scale of saturation, potentially associated to a shear band thickness, can be identified at the onset of macroscopic instability.

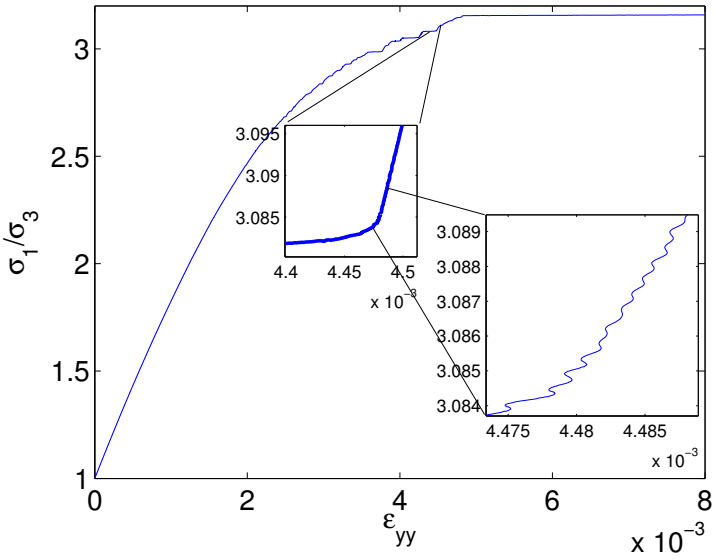

FIGURE 3.6 – Example of an oscillation on the stress-strain curve. The stress increment imposed at each time step is equal to $1.10^{-7} \times \sigma_3$.

3.2 Supplementary Informations

3.2.1 Determination of the travel time of an elastic wave through the granular sample

Figure 3.6 shows a typical macroscopic stress versus strain curve obtained when loading a granular sample made of 10000 grains extremely slowly, with an axial stress increment $\delta\sigma_1 = 1.10^{-7}\sigma_3$ prescribed here at each time step, i.e. a stress loading rate 10 times smaller than the one considered in section 3.1. In that case, local plastic instabilities associated to a local flatness of the stress-versus strain curve, are much more brutal. Looking more precisely immediately after these plastic instabilities, sample oscillations are observed. These oscillations, resulting from sudden stress redistributions that follow large plastic events, allow us to estimate elastic wave properties. They are only observed when applying a very slow loading on the sample, avoiding like this an immediate damping induced by stress increase at the boundaries.

Figure 3.7 shows typical horizontal displacements of selected grains along a vertical axis associated to the oscillation. Similar observations can be done on vertical displacements of radially selected grains. A stationary wave, that exhibits a spatial period $\lambda = L_s$, where L_s is the square root of the sample area, can easily be identified on these snapshots. As $c = \lambda/T$, where c is the wave velocity and T is the time period of oscillations, we can write :

$$T = L_s/c. \tag{3.2}$$

Thus, T corresponds to the travel time of the elastic wave through the granular assembly.

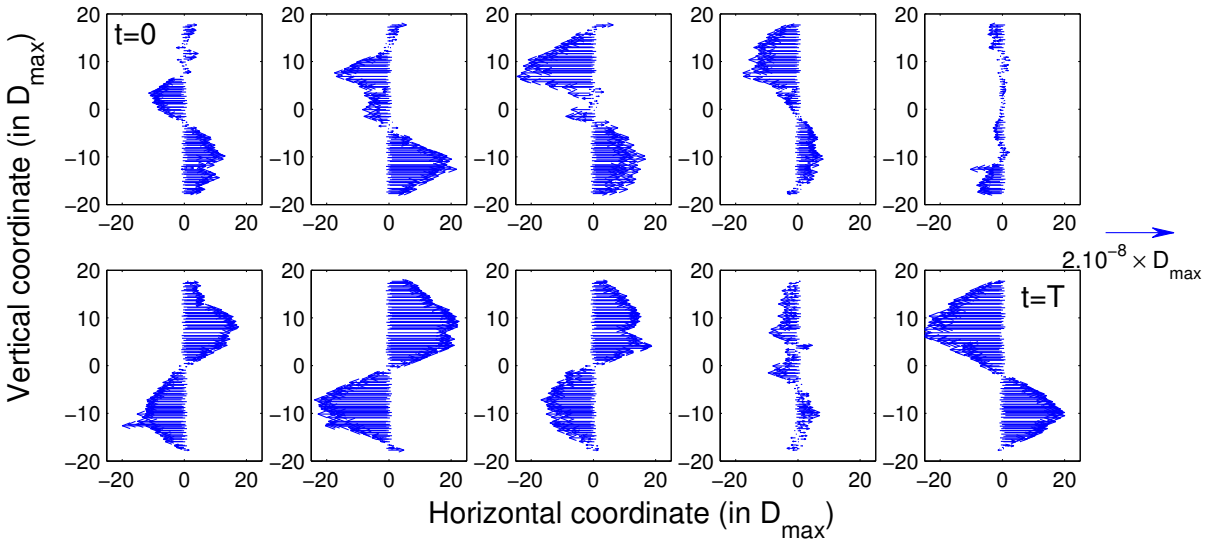

FIGURE 3.7 – Snapshots of selected grains displacement associated to an oscillation period T along the radial direction. Time increases from left to right and top to bottom. Similar observations can be done along the axial direction.

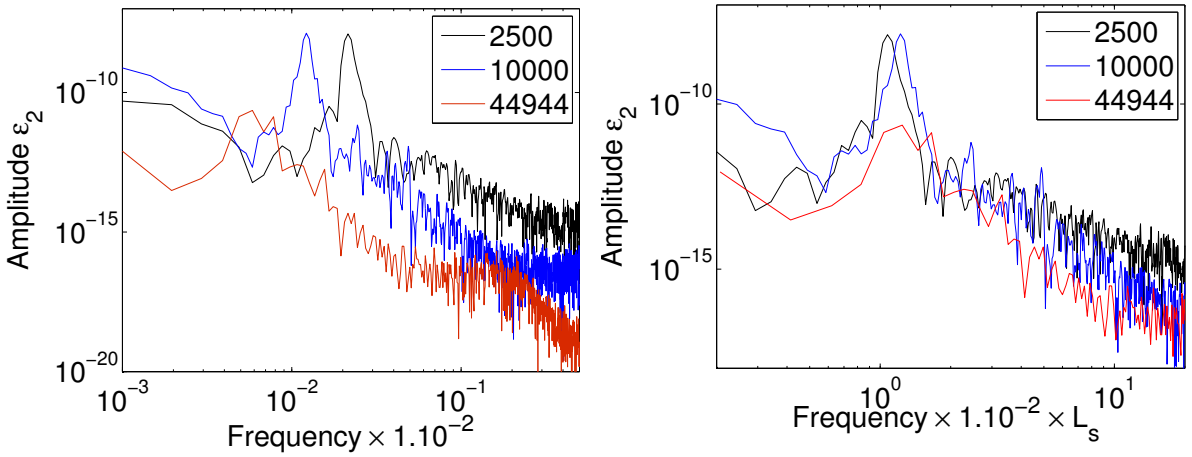

FIGURE 3.8 – (Left) Fourier spectra of the radial deformation rate $\dot{\epsilon}_2$ for various sample sizes indicated in the legend (number of grains). The respective peak indicates the frequency of oscillation, that is decreasing as the sample size is increasing. (Right) Collapse analysis performed by multiplying the frequencies by L_s.

The value of T can be accurately identified by performing the Fourier transform of the radial deformation rate $\dot{\epsilon}_2$ (Figure 3.8). At various sample sizes, i.e. for 2500, 10000 and 44944 grains samples, a clear peak is reported, that specifies the caracteristic frequency $f = 1/T$ of the oscillation mode. The collapse analysis shows that the frequency depends linearly on the sample size.

3.2.2 Collapse analyses on the shear stress rate and incremental shear strain

3.2.2.1 Analytical form hypothesis

The behaviour of $< x >$, where x characterizes whether the shear stress rate $\dot{\tau}$ or the incremental shear deformation $\delta\gamma$, can be expressed as

$$< x > (l, \Delta) \sim l^{-\rho_x} H(l/l_x^*) \tag{3.3}$$

where $H(l/l_x^*) \sim const$ for $l << l_x^*$ and $H(l/l_x^*) \sim l^{\rho_x}$ for $l >> l_x^*$.

We hypothesize that :

– for an infinite system, i.e. when $L_s \rightarrow +\infty : l_x^* \sim \Delta^{-\nu_x}$

– for L_s finite and $\Delta \rightarrow 0 : l_x^* \sim L^{\delta_x}$ where δ_x is a fractal exponent

– for L_s finite and $\Delta >> 0$, the finite size effect becomes negligible, as $l_x^* << L_s$.

A relation in agreement with these 3 points is

$$l_x^* \sim \frac{L_{sample}^{\delta_x}}{\Delta^{\nu_x} L_{sample}^{\delta_x} + C} \tag{3.4}$$

where C is a constant.

To check this hypothesis, the collapse analyses of insets of Figure 3 and 4 are performed by doing the following change of variable

$$\begin{cases} X = l \frac{\Delta^{\nu_x} L_{sample}^{\delta} + C}{L_{sample}^{\delta}} \\ Y = < x > \left[\frac{\Delta^{\nu_x} L_{sample}^{\delta} + C}{L_{sample}^{\delta}} \right]^{-\rho_x} \end{cases} \tag{3.5}$$

3.2.2.2 Finite size effects

To characterize finite size effects, we perform our scaling analysis procedure close to the critical point, here at $\Delta = 0.005$, considering sample sizes of 2500, 10000 and 44944 grains loaded at constant stress rates, setting $\delta\sigma_1^{t_r} = 1.10^{-6}\sigma_3$. Figure 3.9 shows scalings obtained on the shear stress rate and incremental shear strain fields. For the stress field, the temporal scale considered is the wave traveling time T defined in equation 3.2, that varies with sample size. For the strain field, $\delta\epsilon_p$ is observed to decrease slightly with increasing sample size. We here consider $\delta\epsilon_p = 5.10^{-6}$ for 44944 grains samples, $\delta\epsilon_p = 1.10^{-5}$ for 10000 grains samples and $\delta\epsilon_p = 2.10^{-5}$ for 2500 grains samples.

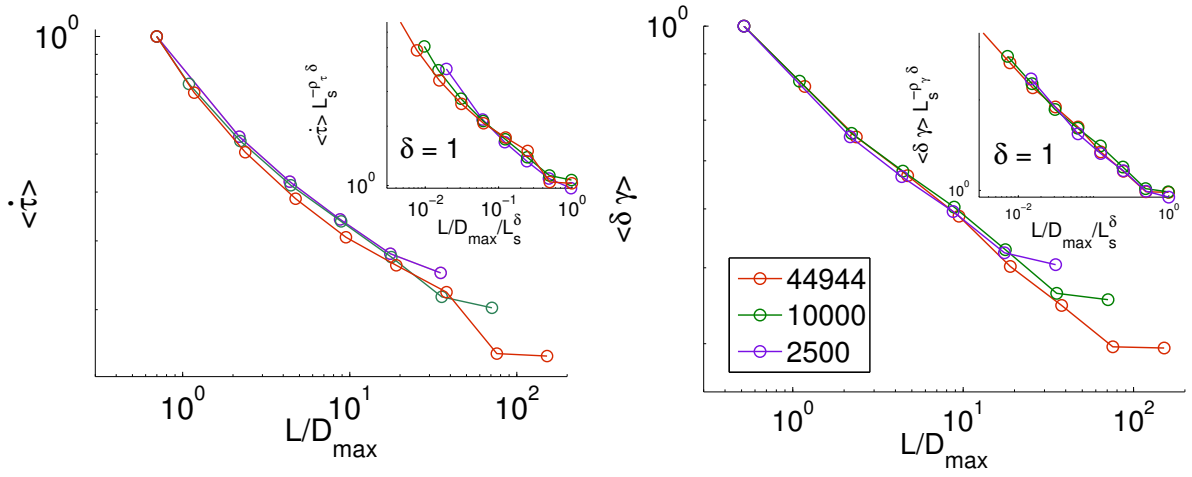

FIGURE 3.9 – Multi-scale analysis performed at $\Delta = 0.005$, i.e. close to the critical point, on the (Left) shear stress rate field and (Right) incremental shear strain field, for various sample sizes indicated in the legend (number of grains). We check that $l_x^* \sim L_s^{\delta_x}$ by data collapse, shown in the insets. We find $\delta = \delta_\tau = \delta_\gamma = 1$.

Close to the critical point, on both stresses and strains, the crossover scale directly depends on sample size L_s. We can check that $l_x^* \sim L_s^{\delta_x}$ from a collapse analysis, where $\delta_x = 1$.

3.2.3 Multi Fractal Analysis

The scale dependant heterogeneity of deformation is here examined more thoroughly by use of a multi-fractal analysis which characterizes the scaling of the moments $< x^q >$ for $0 \leq q \leq 3$. This moment analysis is a way to investigate the scale dependance of the entire distribution of x. Generalizing equation 3.4, we estimate the scaling exponents $\rho_x(q)$ and the critical exponents $\nu(q)$ by data collapse analysis for shear stresses and strains, respectively.

Examples for scalings of moments $< \dot{\tau}^q >$ are plotted on Figure 3.10, for $q = 0.5$ and $q = 2$. $\nu_\gamma = \nu_\tau = 1.3$ is found to be constant, independently of the moment order q, as one would expect for a correlation length, while $\rho_x(q)$ shows a curvature indicating multifractality (figure 3.11) for both the stress and strain fields. By performing a quadratic fit of the form $\rho_x = a_x q^2 + b_x q + c_x$, we find $a_\tau = 0.162$ and $a_\gamma = 0.184$.

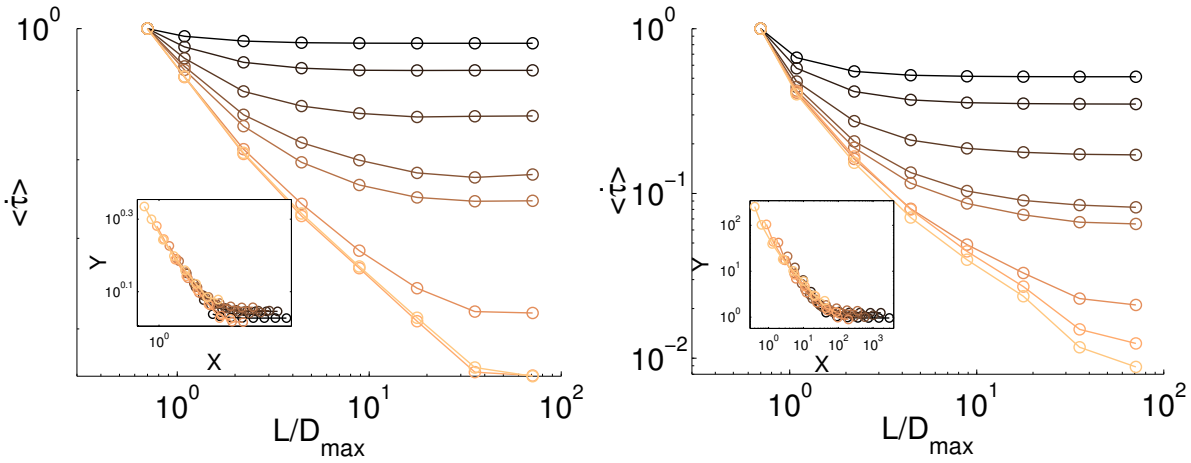

FIGURE 3.10 – Multi-scale analysis performed on the shear stress field for (left) $q = 0.5$ and (right) $q = 2$. Insets show data collapse, where X and Y are defined in equation 3.5.

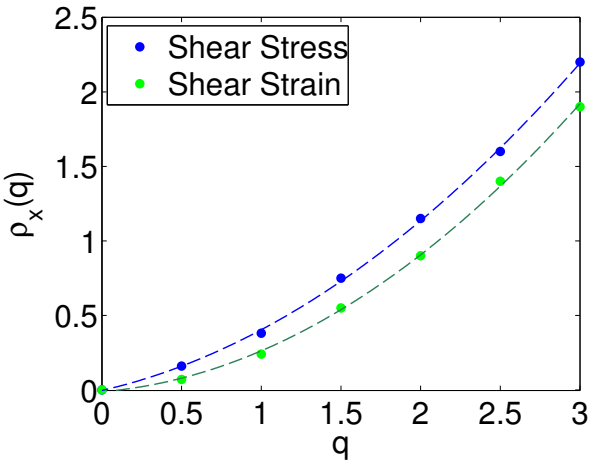

FIGURE 3.11 – Values of ρ_x as a function of q. Dashed lines display quadratic fits of the form $a_x q^2 + b_x q + c_x$. We find $a_\tau = 0.162$, $b_\tau = 0.245$ and $c_\tau = -0.0038$ for stresses and $a_\gamma = 0.184$, $b_\gamma = 0.09$ and $c_\gamma = -0.01$.

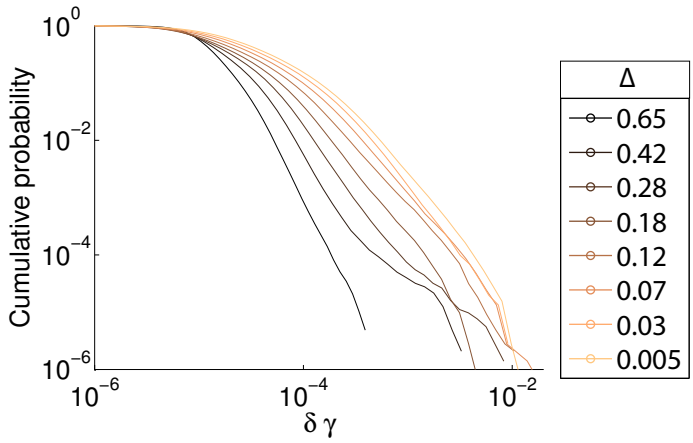

FIGURE 3.12 – Cumulative distributions of incremental shear deformation $\delta\gamma$ computed at the microscale as approaching the transition to dense flow regime. These distributions are computed by considering an incremental deformation window of $\delta\epsilon_w = \delta\epsilon_p$. The results are obtained by averaging over 80 simulations performed on 10000 grains samples.

3.3 Interpreting multifractal scalings

Multifractal scalings have been reported in section 3.1 at the transition from quasi-static to dense flow regime on both incremental shear strain and shear stress rate fields. Moreover, we have shown that these scalings were observed at specific time/deformation resolutions and argued that they result from correlated spatial structures.

In this section, focussing on the shear strain field, we provide the associated incremental shear strain distributions and examine, in a second time, the role of the spatial structure.

3.3.1 Cumulative distributions

Here, we examine the variations of the distributions of the incremental shear deformation $\delta\gamma$ with respect to the control parameter Δ, the considered deformation window $\delta\epsilon_w$ and the spatial scale L.

First, the effect of Δ is shown on Figure 3.12, on which the evolution of cumulative distributions of $\delta\gamma$ are computed at the microscale considering the incremental deformation window $\delta\epsilon_w = \delta\epsilon_p$. We can see that these distributions exhibit fater tails as Δ decreases, showing that $\delta\gamma$ spans a much larger range of values, consistent with a strengthening of shear strain localization as approaching the transition to the dense flow regime.

Secondly, the effect of increasing deformation window and spatial scale on the cumulative distributions is shown close to the critical point ($\Delta = 0.005$) on Figure 3.13. Two different deformation windows of $\delta\epsilon_w = 100 \times \delta\epsilon_p = 1.10^{-3}$ and $\delta\epsilon_w = \delta\epsilon_p = 1.10^{-5}$ are considered. Secondly, the effect of increasing deformation window and spatial scale on the cumulative distributions is shown close to the critical point ($\Delta = 0.005$) on Figure 3.13. Two different deformation windows of $\delta\epsilon_w = 100 \times \delta\epsilon_p = 1.10^{-3}$ and $\delta\epsilon_w = \delta\epsilon_p = 1.10^{-5}$ are considered. Whatever the spatial

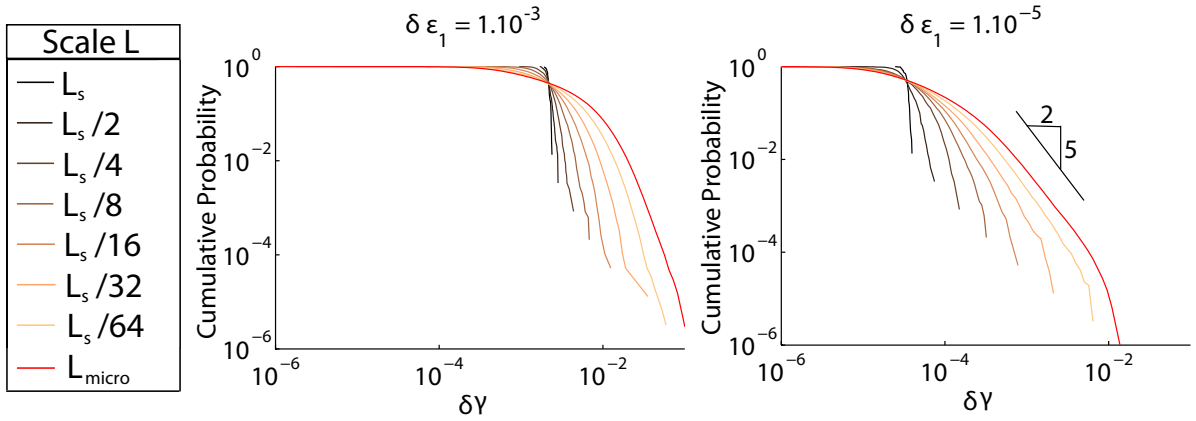

FIGURE 3.13 – Cumulative distributions of incremental shear deformation $\delta\gamma$ computed at spatial scales ranging from the microscale (red curves) to the scale of the sample W_{macro}. These distributions are computed by considering an incremental deformation window of (Left) $\delta\epsilon_w = 100\delta\epsilon_p = 1.10^{-3}$ and (Right) $\delta\epsilon_w = \delta\epsilon_p = 1.10^{-5}$. The results are obtained by averaging over 80 simulations performed on 10000 grains samples.

scale considered, we can see that the distribution is much more stretched when considering $\delta\epsilon_w = 1.10^{-3}$ than when considering $\delta\epsilon_w = \delta\epsilon_p$. Indeed, an enhancement of large deformation rates that amounts to the strengthening of shear strain localization can be observed at $\delta\epsilon_w = \delta\epsilon_p$. Moreover, for both deformation windows $\delta\epsilon_w = 1.10^{-3}$ and $\delta\epsilon_w = \delta\epsilon_p$, the whole distribution of $\delta\gamma$ (including the mean that we thoroughly evaluated in section 3.1) is shifted toward lower values when increasing the spatial scale L. This decrease of $\delta\gamma$ values with scale L directly results from the heterogeneous nature of the spatial structure associated to these fields. Illustrations and understandings on this behaviour are provided in the next section.

3.3.2 A power law scaling inherited from a correlated spatial structure

Figure 3.14 shows examples of incremental shear deformation fields associated to distributions shown on Figure 3.13. As considered previously, these deformation fields are computed at $\Delta \sim 0$ by considering both $\delta\epsilon_w = 1.10^{-5}$ and $\delta\epsilon_w = 1.10^{-3}$, and are shown at various spatial scales varying from the microscale to the scale of the sample.

When considering $\delta\epsilon_w = \delta\epsilon_p$, which corresponds to the incremental deformation window at which a power law scaling of $\delta\gamma$ versus L is reported in section 3.1, an heterogeneous structure remains in the deformation field whatever the spatial scale considered to compute the incremental shear deformation invariant $\delta\gamma$. In this case, at all scales, the entire range of shear deformation values is covered and localized structures that span the whole sample can be distinguished. On the opposite, when considering $\delta\epsilon_w = 100\delta\epsilon_p$, while the heterogeneous character of the strain field is still strongly marked at the microscale L_{micro}, the incremental shear strain field is homogenized at increasing spatial scales. Indeed, the linear features materialized by large values of shear strain can still be distinguished until $L = L_s/16$ but then disappear at larger scales at which the deformation fields appear homogeneous.

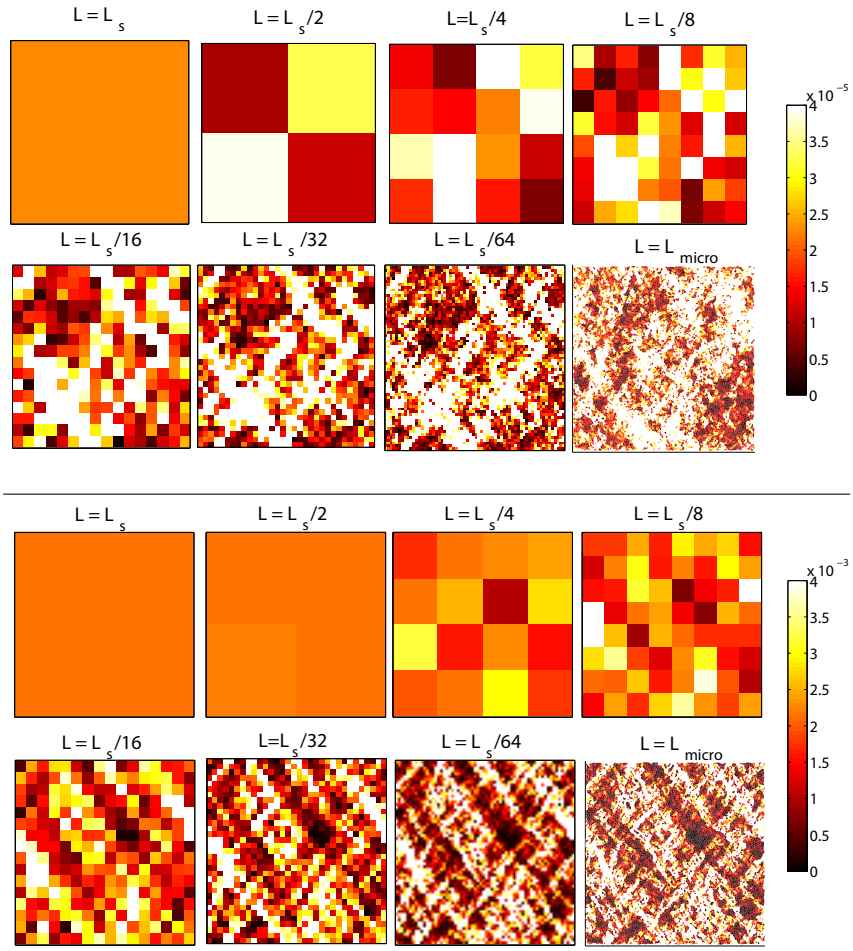

FIGURE 3.14 – Incremental shear deformation fields computed from the microscale to the scale of the sample considering an incremental deformation window (Top) $\delta\epsilon_w = \delta\epsilon_p = 1.10^{-5}$ and (Bottom) $\delta\epsilon_w = 100\delta\epsilon_p = 1.10^{-3}$. The colormap is linearly scaled between $\delta\gamma = 0$ and $\delta\gamma = 2\delta\gamma_M$, where $\delta\gamma_M$ is the computed macroscopic incremental shear deformation, and is kept constant with varying spatial scale.

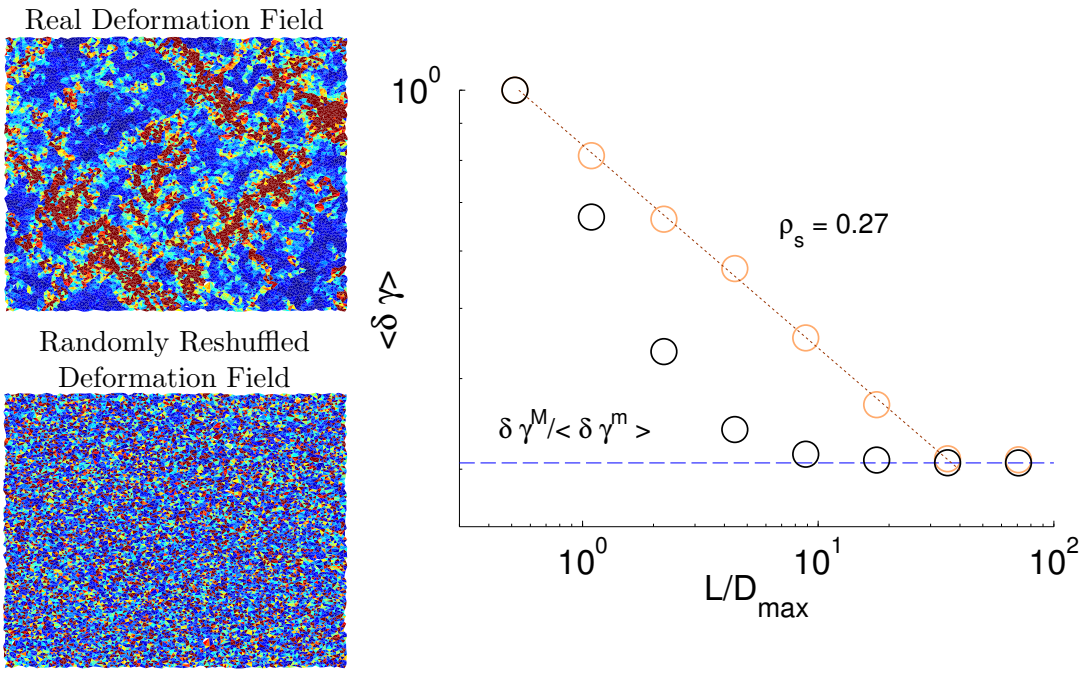

FIGURE 3.15 – Influence of randomly reshuffling (in position) the partial derivatives on the multi-scales properties of the shear deformation field. (Left) Real deformation field computed using $\delta\epsilon_w = \delta\epsilon_p$ at $\Delta \sim 0$ (same as Figure 3.14) and associated deformation field obtained after a random reshuffling of the partial derivatives in space. (Right) Associated multi-scale properties of the real deformation field (yellow dots) and reshuffled deformation field (black dots). The blue dashed line indicates the value of macroscopic shear deformation $\delta\gamma^M$ normalized by the average microscopic shear deformation $< \delta\gamma^m >$.

The power law decrease of $< \delta\gamma >$ with L associated to the deformation field plotted on Figure 3.14(Top) is materialized by the yellow dots plotted on Figure 3.15. In order to confirm that this power law decrease is the signature of spatial correlations in the deformation field, random reshuffling is performed on the partial derivatives while preserving the position and surface of the Delaunay grid. Consequently, the distribution of the incremental shear deformation values is conserved at the microscale, while the spatial structure is deleted. The scale dependance of $\delta\gamma$ versus L for the associated randomly reshuffled deformation field is materialized by the black dots on Figure 3.15. By construction, after reshuffling, the shear strain invariants are the same at both the micro and the macro-scale. However, a clear departure from power law is observed in the reshuffled case, pointing out that the power law behaviour results from the correlated spatial structure of the incremental shear deformation field. Thus, while distributions of $\delta\gamma$ evolve as approaching $\Delta \sim 0$ (see Figure 3.12), the critical behaviour much likely results from spatial organization.

The shape of the decay of the incremental shear deformation rate $< \delta\gamma >$ obtained in the random case can be understood by considering random values of partial derivatives $\partial u/\partial x ... \partial v/\partial y$ that exhibit gaussian distributions. In the case of centered variables $\partial u/\partial x ... \partial v/\partial y$, i.e. for a set of partial derivatives that do not show any average component at the macroscopic scale,

we get $< \delta\gamma > \sim L^{-1}$. Indeed, because $< \delta\gamma >$ scales as the absolute values of derivatives, the averaging at scale L implies summing $\sim L^2$ random variables, giving a $\sim L$ scaling. Then, dividing them by the number $\sim L^2$ of cells leads to a $\sim L^{-1}$ scaling for a 2D field. In our case, the strain components are not centered, so we need to correct this scaling by the incremental shear deformation obtained at the largest scale, which leads to the scaling observed in black dots in Figure 3.15, that follows the relation

$$< \delta\gamma > - \frac{\delta\gamma^M}{< \delta\gamma^m >} \sim L^{-1} \tag{3.6}$$

where $\delta\gamma^M$ is the macroscopic shear deformation and $< \delta\gamma^m >$ is the average microscopic shear deformation.

Thus, to summerize, a field characterized by random centered variables $\partial u/\partial x ... \partial v/\partial y$ leads to an exponent of the order of -1, while exponents lower than 1 mean that spatial correlations operate in the shear deformation field.

3.4 Sensitivity to the imposed macroscopic loading rate

The study conducted in section 3.1 shows that, using the coarse graining analysis illustrated in Figure 3.2 performed either on the stress or on the strain field, we are able to extract a correlation length that diverges as approaching the transition from quasi-static to dense flow regime. This interpretation means that the correlated spatial structure corresponding to the specific scalings observed in Figure 3.3 and 3.4 is likely to result from the particular nature of the quasi-static deformation regime. If this interpretation is consistent, these scaling properties should be independent of the loading rate as long as this rate ensures that the inertial number I remains small enough, whereas too rapid loadings might modify the picture.

We explore in this section whether the scalings depend on the imposed loading rate by making $\delta\sigma_1^{t_r}$ to vary between $1.10^{-7}\sigma_3$ and $5.10^{-6}\sigma_3$. Figure 3.16 shows the influence of loading rate on the scaling analysis performed on the shear deformation field at the critical point, i.e. at the control parameter value $\Delta = 0.005$, by averaging the behaviour over 30 simulations. The value of the inertial number I as a function of the control parameter τ is plotted on Figure 3.16(a). In our configuration, regarding the values of $\delta\sigma_1^{t_r}$, initial values of I range from 4.10^{-7} to 2.10^{-5}. Then, as biaxial loading proceeds, the value of I first slightly increases and then rises more drastically. As the result of averaging over many simulations, the increase of I as approaching the transition toward a dense flow regime reached at $\tau = 2\sigma_3$ is less brutal than the one observed on Figure 3.1 when considering one simulation. This smoothing effect around τ_c is the result of the variability in the position of the onset of instability with respect to deviatoric stress from one simulation to another.

When considering values of $\delta\sigma_1^{t_r}$ smaller than the one considered in section 3.1, i.e. for $\delta\sigma_1^{t_r} \leq 1.10^{-6}$, while values of I are very different far from the dense flow transition, they reach

a similar value at $\Delta \sim 0$, which is about $I_c = 3.10^{-5}$. This means that, as soon as the loading rate is small enough, the transition to a dense flow regime is observed at a constant inertial number value I_c. At that point, the granular assembly enters in the dense flow regime. We can see on Figure 3.16(b), which shows the variation of I as a function of ϵ_1, that beyond the dense flow transition, the sample flows the same way independently of the prescribed external loading. When considering a much larger loading rate $\delta\sigma_1^{tr} = 5.10^{-6}$ from the beginning of the test, the inertial number value at the dense flow transition is much larger than I_c. The respective scalings observed at $\Delta = 0.005$ on the shear deformation fields are shown on Figure 3.16(c). A similar scaling function materialized by a power law of slope $\rho_s = 0.24$, as obtained on Figure 3.4, is observed considering $\delta\sigma_1^{tr} = 1.10^{-6}$ and $\delta\sigma_1^{tr} = 1.10^{-7}$. The same correlation exponent $\nu_\gamma = 1.3$ is also found by doing a collapse analysis (not shown). However, when setting $\delta\sigma_1^{tr} = 5.10^{-6}$, a clear deviation from power law is observed at the critical point, showing that the correlation length does not diverge anymore at the approach of τ_c. We examined more thoroughly these simulations by changing both the hypothetic value of τ_c and $\delta\epsilon_w = 5.10^{-6}$ and found no way to observe a divergent correlation length, materialized by a power law behaviour at the critical point.

Thus, as soon as the value of $\delta\sigma_1^{tr}$ is sufficiently low, i.e. of the order or lower than the one considered in section 3.1, no scaling changes are observed with respect to the one obtained in section 3.1 with varying values of $\delta\sigma_1^{tr}$. On the opposite, when increasing the loading rate at values of I larger than about 3.10^{-5}, the multi-scale behaviour is no longer observed. Hence, it appears that this scaling emerges from quasi static deformation and is no longer observed when the mechanical behaviour is more related to a dense flow regime from the initial stages of

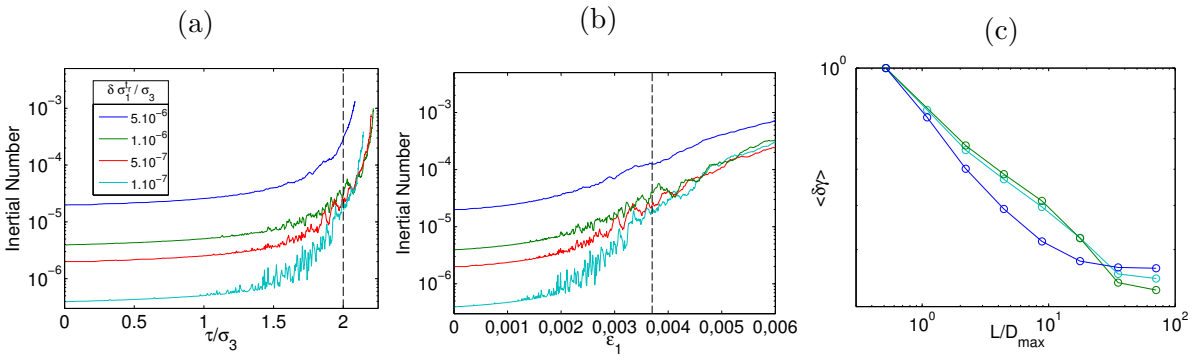

FIGURE 3.16 – Influence of the imposed macroscopic loading rate on the scaling performed on the incremental shear deformation close to the critical point, i.e. at $\Delta = 0.005$. (a) Evolution of the inertial number during biaxial testing as a function of τ for various values of loading rate $\delta\sigma_1^{tr}$. The value of $\tau_c = 2\sigma_3$, indicating the position of the dense flow transition, is materialized by the black dashed line. (b) Evolution of the inertial number during biaxial testing as a function of ϵ_1 for various values of loading rate $\delta\sigma_1^{tr}$. The value of ϵ_1 that corresponds to $\tau_c = 2\sigma_3$ is materialized by the black dashed line. (c) Associated values of $< \delta\gamma >$ versus L at $\Delta = 0.005$. A deformation window of $\delta\epsilon_w = 5.10^{-6}$ is considered here. Color correspond for all figures.

deformation. In that case, we expect inertial effects to overcome the structures that would be inherited from dynamic stress redistribution of elastic energy in case of a slow driving load.

This observation is consistent :

- with the growth of cooperative length scale with decreasing shear rate observed by *Tsamados* (2010) in glassy materials.
- with the decrease of velocity fluctuations with increasing values of inertial number I reported in *Midi* (2004) for frictional granular materials submitted to various loading configurations.

3.5 Experimental observations in $1\gamma 2\epsilon$

From the numerical study performed in section 3.1, we have seen that we were able to define caracteristic time and deformation scales at which, respectively, the incremental stress and strain fields show specific multi-scale properties related to the onset of macroscopic instability.

Because stress controlled experiments and observations of the force network cannot be obtained experimentally with the $1\gamma 2\epsilon$ apparatus, a study similar to the one performed in section 3.1 cannot be conducted with this device. Moreover, the resolution used in simulations (see section 3.1) to observe specific scalings in the shear deformation field, corresponding to $\delta\epsilon_p = 1.10^{-5}$, is difficult to obtain in the experiments when analysing the early stages of macroscopic deformation. Indeed, in regions associated to the green rectangles number 1 and 2 on Figure 1.4, the shear deformation fields computed considering $\delta\epsilon_w \sim \delta\epsilon_p$ are strongly affected by noise, since deformation in that particular region of the stress versus strain curve is mostly elastic and thus associated to very small displacements at the grain scale. Thus, the growth of the correlation length observed in simulations during this phase of the loading cannot be investigated experimentally.

However, we have seen in section 1.2.1 that representative incremental shear deformation fields can be obtained when considering macroscopic stress relaxation, i.e. transient instabilities (see Figure 1.6). Indeed, in this case, large grains displacements, expected to be associated to permanent grains rearrangements, are observed. We qualitatively discussed in section 1.2.1 about the intermittent and heterogeneous character of these deformation fields and their differences with the ones observed when considering larger deformation windows (see Figure 1.5). We here investigate whether these patterns obtained experimentally share similar multi-scale properties than the ones pointed out numerically in section 3.1.

3.5.1 At small deformation windows during stress relaxation

Figure 3.17 shows the multi-scale analysis performed when considering the incremental shear deformation fields presented in Figure 1.6, i.e. obtained near the stress relaxation phase using a deformation window of the order of $\delta\epsilon_w = 1.10^{-4}$ (see Figure 1.4(b)). This phase can be considered as a transient macroscopic instability.

We can see that, far from the stress relaxation (curve number 1), the average value of $< \delta\gamma >$ versus L decreases at small scales until reaching a crossover scale that we interpret, from the analysis of section 3.1, as a correlation length. We clearly see that, as approaching the destabilization of the whole granular assembly materialized by stress relaxation, this crossover scale increases, until a full power law in $< \delta\gamma >$ versus L is observed. We verified that this power law scaling observed at stress relaxation reflects the spatial structure of the deformation field by randomly reshuffling the partial derivatives, similarly to what has been done in section 3.3.2. Moreover, by applying the coarse graining analysis on a deformation field that results from the correlation of two successive photos taken without any specimen motion nor setup change, we checked that this scaling is not likely to result from an image analysis artefact. Indeed, in this

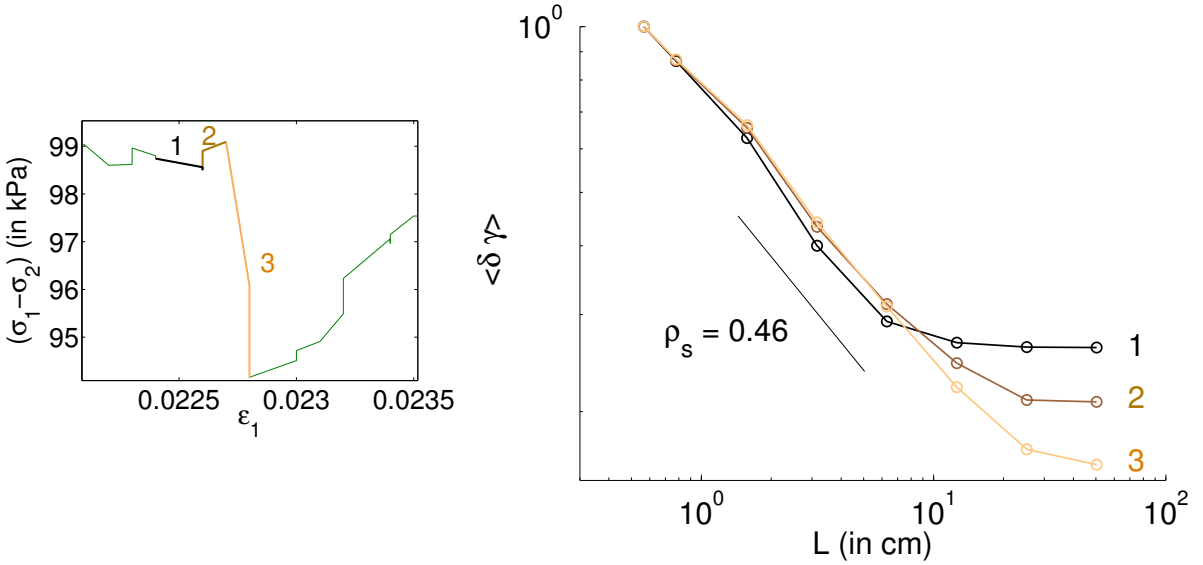

FIGURE 3.17 – (Left) Deformation windows for which incremental shear deformation fields are computed superimposed on the stress versus strain curve in a stress drop phase (same as Figure 1.4(b)). (Right) Multi-scale analysis performed on the incremental shear strain fields obtained in $1\gamma 2\epsilon$ at stress relaxation and plotted on Figure 1.6, comptued considering deformation windows shown in (a). Color numbers correspond. A deformation window $\delta\epsilon_w \sim 1.10^{-4}$ is considered here.

case, a similar power law than the one obtained in the case random noise is observed. Thus, as already noted numerically, similar multi-scale properties are observed experimentally at the onset of a macroscopic instability.

However, due to the strain controlled loading of this experiment, this power law behaviour remains transient. Indeed, as the critical transition is approached, the stress drop allows the sample to relax, moving it away from the transition towards an enduring dense flow regime. For this reason, i.e. to avoid feedback effects, numerical simulations perfomed in section 3.1 are done under stress control conditions.

Several numerical studies such that the ones of *Walker and Tordesillas* (2010) and *Griffa et al.* (2011) reported the growth of heterogeneities in the deformation field at the approach of stress relaxation during strain-controlled biaxial tests by evaluating the magnitude of the non-affine component of deformation (*Tordesillas et al.*, 2008). This is basically what we report here experimentally with our method. While not shown here, we obtain similar results numerically. However, contrary to their methods, we here do not introduce any spatial internal length to evaluate the heterogeneity of deformation. Instead, we show that, because a full power law is observed in $< \delta\gamma >$ versus L, the heterogeneity observed in the deformation field at stress relaxation spans the whole sample.

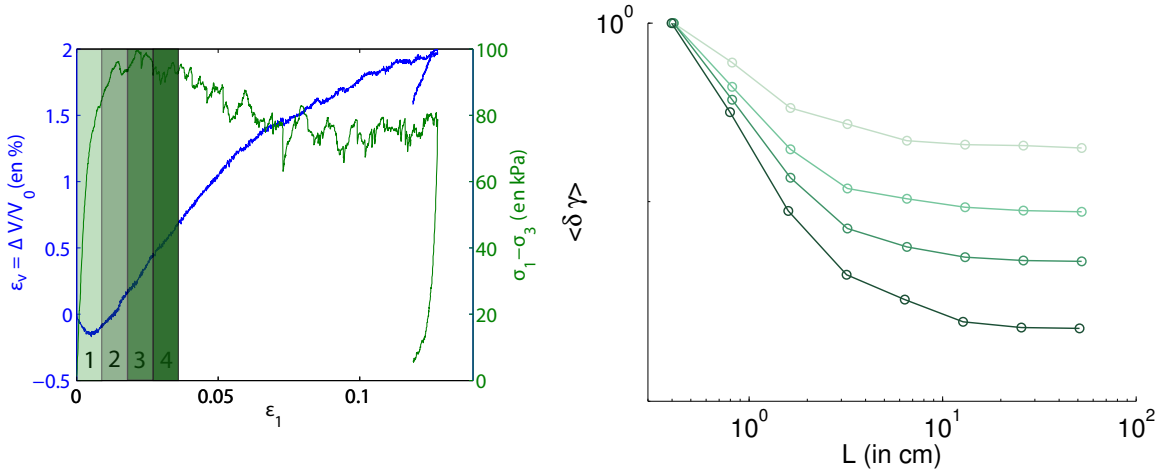

FIGURE 3.18 – (Left) Deformation windows for which incremental shear deformation fields are computed superimposed on the stress versus strain curve in the early stages of macroscopic loading (same as Figure 1.4(a)). (Right) Multi-scale analysis performed on the incremental shear strain fields obtained in $1\gamma 2\epsilon$ for strain fields plotted on Figure 1.5, comptued considering deformation windows shown in (a). Colors correspond. A large deformation window $\delta\epsilon_w = 2.3.10^{-3}$ is considered here.

3.5.2 At large deformation windows

Figure 3.18 shows the results obtained by performing the coarse graining analysis on the incremental shear deformation fields plotted on Figure 1.5 obtained in the early stage of biaxial testing by considering large deformation windows of $\delta\epsilon_w = 2.3.10^{-3}$. As expected from the numerical study, no specific scaling is oberved in that case for all deformation fields considered. A crossover scale of about 3 to 5 centimeters, that corresponds to the apparent shear band thickness at that stage, remains during the loading. Like this, our coarse graining method allows to characterize the shear band thickness, that, as seen in section 3.1, is likely to be function of the deformation window we consider to compute the incremental shear deformation fields.

3.6 Discussion

In this chapter, we thoroughly analyzed the intermittent stress and strain concentrations structures that form at small time/deformation scales and that develop in space during mechanical loading. Because a specific behaviour of these fields materialized by multi-scale properties is observed at the onset of macroscopic instability, we report that those types of heterogeneities play a significant role in the macroscopic flowing process. Indeed, intermittent stress concentration structures are observed synchroneously with dynamic stress redistributions by means of wave propagation through the granular assembly. These stress concentration structures are associated to intense shear strain localization zones under which flow is favoured, inducing strong consequences in terms of the granular assembly stability at the macroscopic scale.

All these observations have been characterized in deep by considering specific granular as-

semblies, associated to an initially large packing fraction ϕ_{ini}, of the order of the critical packing fraction $\phi_c = 0.845$ that characterizes the jamming transition for frictionless granular assemblies (*O'Hern et al.*, 2003), and coordination numbers $Z_{ini} \approx 4$. For such specific samples, strains of type I, i.e. mostly due to material strain in intergranular contact regions, are observed in the early stages of macroscopic loading (*Radjai and Dubois*, 2011). This configuration ideally incorporates the ingredients, discussed above, expected to be at the origin of the macroscopic instability : a remaining contact network that mainly deforms through contact slidings or contact loss events is expected to favor stress redistributions following microscopic instabilities toward larger scales. Moreover, in that case, we understand that these perturbations can have strong consequences at the macroscopic scale since the instability cannot be damped localy by contact network reorganization.

Thus, the question that arises is whether similar observations could be done considering initial granular assemblies exhibiting other properties in term of coordination numbers and packing densities. First evidences on this have been provided considering experimental observations, for which the granular assembly is not expected to emphasize specific properties similar to the one of samples considered in this chapter, as the assembling procedure drastically differs here, because performed under gravity and with frictional grains. However, the exploration of various physics of deformation, such as for example the case of granular assemblies undergoing exclusively type II strains, characterized by a continuously rearranging contact network (*Radjai and Dubois*, 2011), has to be done. Indeed, one could ask whether elastic stress perturbations would induce similar consequences in that case, since elastic parameters prescribed at the grain scale, as for example the value of κ, do not play a significant role on the macroscopic behaviour of the granular assembly (*Radjai and Dubois*, 2011).

Motivated by investigating such an open question in a near future, we present in the next chapter an ongoing work, that aims in generating various granular assemblies and in characterizing the relevant parameters that control characteristic macroscopic behaviours such as dilatancy, maximum shear stress and the so called "critical state" (*Casagrande*, 1936).

Chapitre 4

Vers l'étude d'autres types d'échantillons numériques

Towards the study of other numerical sample types

As mentioned in the discussion section of the previous chapter, the study performed there corresponds to a particular case, since the considered initial granular sample configurations are characterized by high packing density and coordination number. When prescribing a given set of elastic parameters at the grain scale for this type of samples, we have seen (see Figure 2.1) that an initial macroscopic contraction phase is observed, followed by macroscopic dilation. Then, a clear maximum value of stress is reached, at which we characterized in section 3.1 the associated macroscopic instability that occurs under stress controlled simulations. Of course, this picture is not always that simple, and may strongly depends on the initial properties of the granular assembly considered.

Notably, it is known that there exists a 'critical' state (*Casagrande*, 1936) characterized by a given value of packing density that any granular material tends to reach after a given amount of deformation. This critical state has nothing in common with the critical behaviour in the sense of statistical physics that we characterized in the previous chapter. Indeed, the critical state in the sense of *Casagrande* (1936) rather expresses that initially dense samples are likely to reach a steady state as a result of macroscopic dilation, while loose samples may reach the same state after volumetric contraction. As mentioned in *Rothenburg and Kruyt* (2004), a similar reasoning can be done on the coordination number, that would reach, rather by increasing or decreasing, a critical value after a given amount of deformation.

Thus, all the micromechanical mechanisms related to different variations in ϕ and Z in the early stages of macroscopic loading are expected to lead to distinct behaviours in terms of associated macroscopic volume variation and stress-strain curves. Consequently, the approach we performed as well as characterizations and interpretations we made in Chapter 3 need to be revisited in these cases.

Following this route, we propose in this chapter an assembling method framework based on the study of *Agnolin and Roux* (2007), that aims in approaching the critical state (*Casagrande*,

1936) from various initial conditions, thus exhibiting distinct behaviours in term of ϕ and Z variations from the early stages of macroscopic loading. An attempt to explore the relevant parameters that control the physics at the macroscopic scale will be done in order, in a future work, to investigate the associated role of mechanical heterogeneities.

Here, in order to examine the behaviour toward the critical state, we perform strain controlled multi-axial simulations.

4.1 Sample preparation

In this section, we explain in details the different assembling methods used to build various initial granular assemblies that differ in packing fraction ϕ_{ini} and coordination number Z_{ini}.

4.1.1 Initially Highly Coordinated (HC) samples

From the disordered granular gas configuration obtained as explained in section 2.2, highly coordinated (HC) samples are obtained from an isotropic compression, setting particle friction values between $\mu_{iso} = 0$ and $\mu_{iso} = 0.3$.

Samples built considering $\mu_{iso} = 0$ during this compression stage correspond to the ones considered in Chapter 3, for which samples are at their density maxima in configuration space, characterized by a packing fraction $\phi_{ini} = 0.847$ (see Table 4.1), i.e. close to the critical packing fraction $\phi_c = 0.845$ of the jamming transition for frictionless granular assemblies (*O'Hern et al.*, 2003). These samples also show very high coordinate numbers Z_{ini}, close to 4.

Considering non zero particle friction μ_{iso} during this isotropic compression stage induces both ϕ_{ini} and Z_{ini} to decrease with μ_{iso} (see Table 4.1). Moreover, Figure 4.1 shows that the decrease of Z_{ini} with ϕ_{ini} is proportional, since a relation $Z_{ini} = 22.6\phi_{ini} - 15$ is observed. As μ_{iso} is inscreased from 0.05 to 0.3, density ϕ_{ini} is decreased from 0.836 to 0.808 and coordination number Z_{ini} is decreased from 3.69 to 3.06.

4.1.2 Initially Low Coordinated (LC) samples

In order to separate the effect of initial density ϕ_{ini} and of the coordination number Z_{ini}, we here build samples that show various packing densities at approximately constant values of coordination numbers. To do so, Low Coordinated (LC) samples, characterized by $Z_{ini} < 3$, are obtained following the method of *Agnolin and Roux* (2007), i.e. by maintaining strongly agitated granular gas states at high densities before isotropically compressing with a final value of friction coefficient. Contrary to *Agnolin and Roux* (2007), shaking is here performed at various distances from the maximum packing fraction, by tunning the expansion parameter α.

Details of the procedure, starting from a disordered granular gas, are the following :

– first, an isotropic compression is perfomed on frictionless particles until reaching an equilibrium state of maximum packing fraction, as done in 4.1.1.

Sample type	Sample number	Tunning parameter	Density ϕ_{ini}	Coordination number Z_{ini}
HC	HC1	$\mu_{iso} = 0$	0.847	3.95
	HC2	$\mu_{iso} = 0.05$	0.836	3.69
	HC3	$\mu_{iso} = 0.1$	0.827	3.52
	HC4	$\mu_{iso} = 0.15$	0.821	3.37
	HC5	$\mu_{iso} = 0.2$	0.815	3.24
	HC6	$\mu_{iso} = 0.25$	0.811	3.13
	HC7	$\mu_{iso} = 0.3$	0.808	3.06
LC	LC1	$\alpha = 1.01$	0.848	2.68
	LC2	$\alpha = 1.02$	0.845	2.65
	LC3	$\alpha = 1.04$	0.839	2.65
	LC4	$\alpha = 1.06$	0.832	2.69
	LC5	$\alpha = 1.08$	0.823	2.71
	LC6	$\alpha = 1.12$	0.811	2.77
	LC7	$\alpha = 1.16$	0.805	2.79

TABLE 4.1 – Model parameters and sample properties in term of density ϕ_{ini} and coordination number Z_{ini} for all the samples considered in this study. Corresponding assembling methods are described in section 4.1.

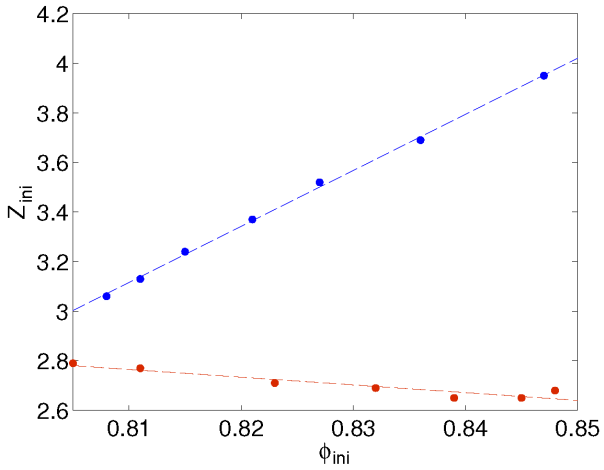

FIGURE 4.1 – Coordination number Z_{ini} versus density ϕ_{ini} along mechanical loading. Blue dots correspond to HC samples and red dots to LC samples. The associated color dashed lines are linear fits. All potential configurations lying in between these two lines can be reached by tunning α and μ_{iso} from the assembling method described in section 4.1.2.

– secondly, an homogeneous expansion, multiplying all coordinates by a constant factor α slightly larger than 1, is performed. Various values of α (see Table 4.1), that all lead to an expansion greater than the maximum grain interpenetration, are taken into account in this study.
– thirdly, a shaking procedure, that uses the same DEM code than the one used during the preparation of the granular gas, is performed. The number of iterations n_{it} is imposed to be constant for all samples generated. Here, we set $n_{it} = 5.10^5$, which corresponds to the lower bound value over which no changes in ϕ_{ini} and Z_{ini} are observed.
– finally, an isotropic compression with a particle friction $\mu_{iso} = \mu_{biax} = 0.5$ is performed, where $\mu_{biax} = 0.5$ is the particle friction considered during the multi-axial testing performed in section 4.2.

This leads to samples that span approximately the same range of density values than the one obtained for HC samples, i.e. varying from $\phi_{ini} = 0.80$ to $\phi_{ini} = 0.85$, but characterized by a much lower coordination number Z_{ini} that remains approximately constant with ϕ_{ini}, around 2.7 (see Table 4.1 and Figure 4.1).

4.1.3 Discussion on initial sample properties

We have seen that, depending on the assembling method considered, initial samples exhibit various properties in term of packing density and coordination number. Here, HC samples correspond to configurations for which, at a given density, the value of the coordination number Z_{ini} is maximized. On the reverse, the LC samples, while exhibiting various densities ϕ_{ini} when tuning the expansion parameter α, are characterized by a coordination number which is independently controlled by the chosen microscopic friction μ_{iso}. Hence, using the procedure described in section 4.1.2 at a chosen density ϕ_{ini}, imposed by α, lower values of Z_{ini} could be obtained from increasing values of μ_{iso}, i.e. considering $\mu_{iso} \geq \mu_{biax}$. However, this procedure is not consistent in our quasi-static study, since dynamical collapse phases associated to strong local reduction of porosity take place in that case in the initial stages of multi-axial deformation, inducing significant inertial effects. Thus, $\mu_{iso} = \mu_{biax}$ corresponds to an upper bound. Consequently, the two sample types HC and LC are likely to correspond to limit cases. By tunning α, as done here, and μ_{iso} to any values lower than μ_{biax}, any configuration lying in between the two lines plotted on Figure 4.1 can be reached from the assembling method described in section 4.1.2. Here, we limit our study by focusing on these two limit cases, in order to span as various mechanisms as possible.

4.2 Multi-axial testing

In order to allow comparisons between the mechanical behaviour of those different types of initial numerical samples, the multi-axial loading set up remains similar whatever the initial sample considered. The contact stiffness $\kappa = k_n/\sigma_3$ is equal to 1000. The particle friction is set

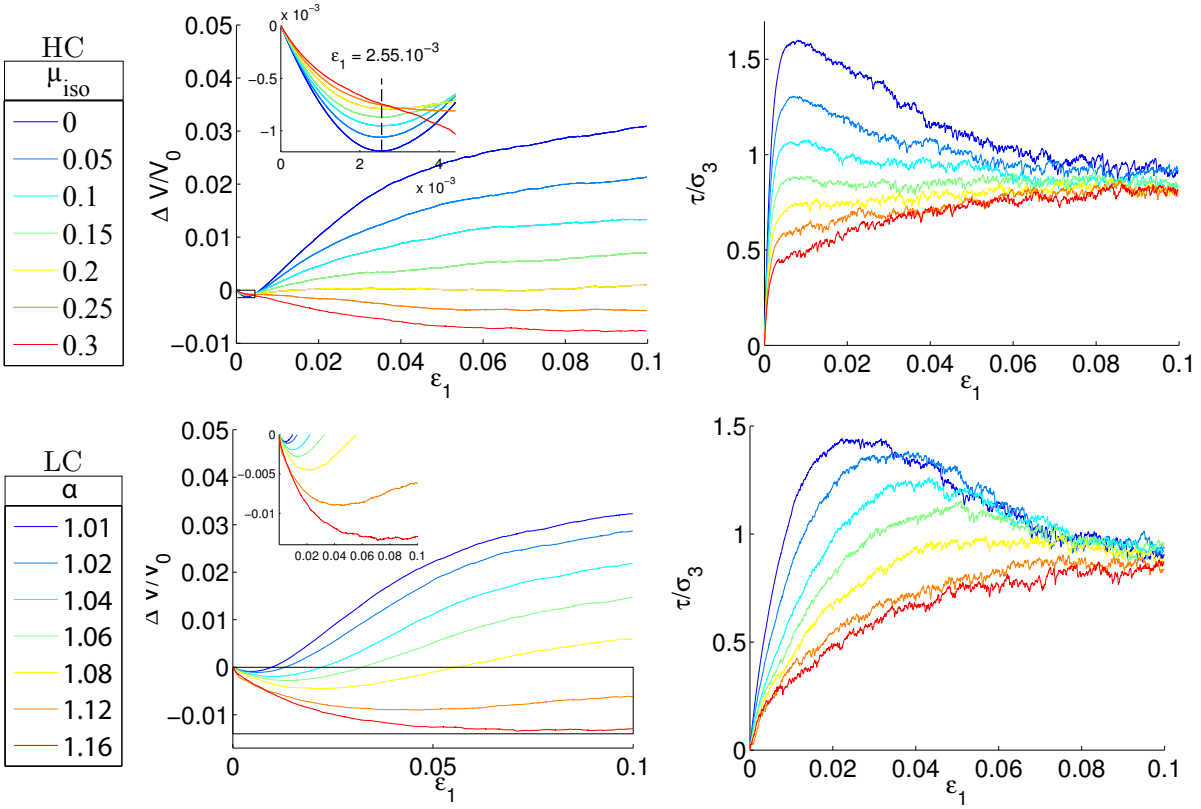

FIGURE 4.2 – Evolution of macroscopic (Left) volumetric strain $\Delta V/V_0$ and (Right) deviatoric stress τ as a function of axial deformation ϵ_1 during multi-axial testing considering (Top) Highly Coordinated (HC) samples and (Bottom) Low Coordinated (LC) samples. Insets of volumetric strain plots show zooms in the contracting region, delimited by the black rectangles. When dilation is observed, its onset is reached at constant value of $\epsilon_1^c = 2.55.10^{-3}$ for HC samples it varies over about one order of magnitude for LC samples, i.e. between $\epsilon_1^c = 3.10^{-3}$ and $\epsilon_1^c = 4.10^{-2}$, for the range of α considered in this study.

to $\mu_{biax} = 0.5$. The vertical deformation ϵ_1 is increased at constant rate by fixing the inertial parameter I equals to 5.10^{-5}, which ensures quasi-static conditions. All the simulations shown in this study consider 10000 grains samples. For each samples type, e.g. sample HC1, 5 simulations are done and average results are shown.

Figure 4.2 shows the macroscopic response of all samples types during multi-axial testing. Dilation is observed for the majority of samples considered. However, samples HC6 and HC7 are clearly always contractant, indicating that, for HC samples, there exists a critical value of density $\phi \approx 0.815$ under which those types of samples do not dilate anymore. The existence of such a critical value for LC samples also seems to exist, since for the LC7 sample that presents an initial porosity $\phi_{ini} = 0.805$, a continuously contracting behaviour is observed. One can also remark that, in the case for which no dilation is observed, strain softening is not observed on the stress versus strain curve.

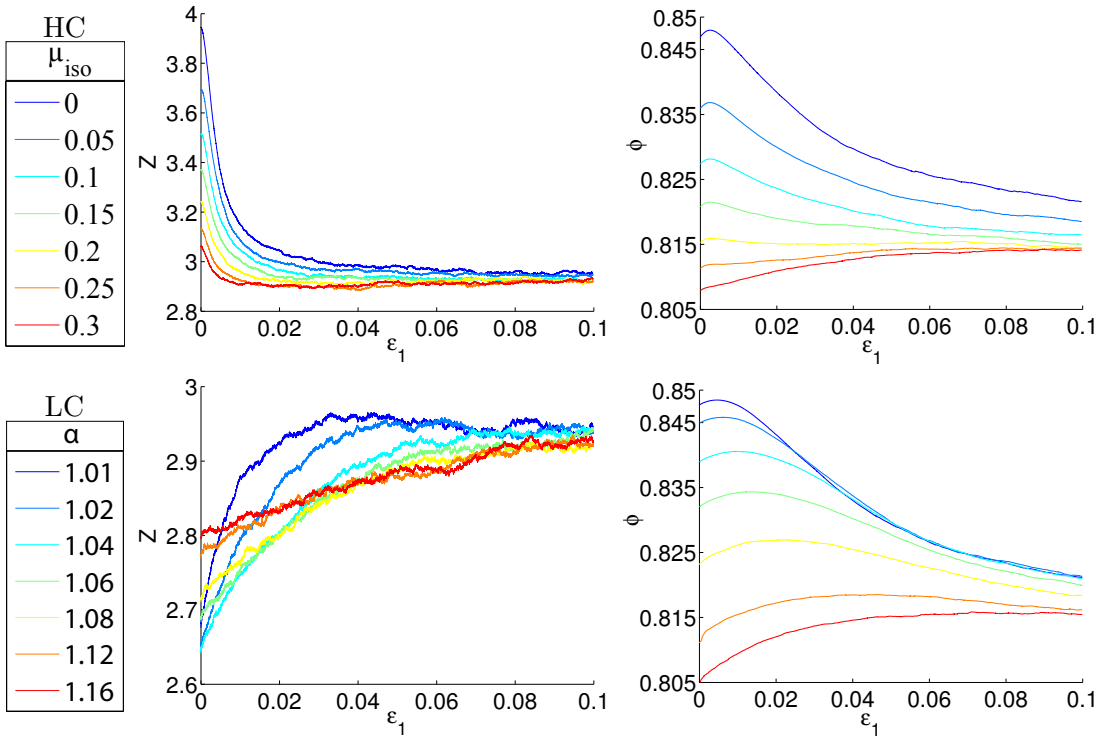

FIGURE 4.3 – Evolution of macroscopic average (Left) coordination number Z and (Right) packing density ϕ as a function of axial deformation ϵ_1. The microscopic friction is $\mu_{biax} = 0.5$, while multi-axial loading is performed on various samples prepared using the two modes of preparation detailed in section 4.1, i.e. on initially (Top) Highly Coordinated (HC) samples and (Bottom) Low Coordinated (LC) samples. Z continuously decreases with ϵ_1 for HC samples, while it continuously increases with ϵ_1 for LC samples. The parameters Z and η are not the parameter underlying the physics of dilation, since their values of Z_c and η_c reached at the onset of dilation differ depending on the samples considered.

The fundamental difference between HC and LC samples lies in the axial deformation ϵ_1 at which the onset of dilation and the maximum stress, when they exist, are observed. Indeed, for HC samples, dilation and maximum stress occur at a constant value of axial deformation of respectively $\epsilon_1 = 2.55.10^{-3}$ and $\epsilon_1 = 5.10^{-3}$ whatever the values of ϕ_{ini} and Z_{ini} considered for the initial sample (section 4.1.1). On the opposite, the onset of dilation and maximum stress for LC samples occur at increasing values of ϵ_1 as ϕ_{ini} decreases.

Consequently, whatever the value of μ_{iso} considered to build HC samples, the micromechanical origin of strains does not seem to be modified. While the values of ϕ_{ini} and Z_{ini} vary, they vary simultaneously in such a way that macroscopic strains appear to remain of type I, i.e. strains that are mostly related to particle interpenetration at contact, as when considering $\mu_{iso} = 0$ (*Radjai and Dubois*, 2011). Indeed, when considering HC samples made using non zero values of μ_{iso}, axial deformation is still accompanied by contact loss, as observed on Figure 4.3(Top). Moreover, the observed decrease of the macroscopic contraction amplitude (see inset of figure 4.2) for these samples may only be induced by the restricted number of contracting

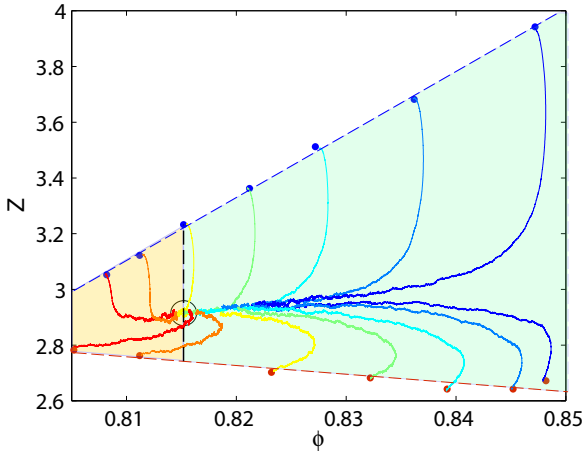

FIGURE 4.4 – Coordination number Z versus density ϕ paths obtained during multi-axial loading considering all samples built in this study. Blue dots correspond to initial HC samples and red dots to initial LC samples. The associated color dashed lines are linear fits. The colored curves display the associated loading path obtained under multi-axial loading. Color corresponds with Figures 4.2 and 4.3. The black circle points out the critical state (*Casagrande*, 1936).

contacts involved, since the coordination number is proportionately decreased.

On the contrary, for LC samples, rearrangements associated to contact gains are observed from the beginning of the test, materialized by the increase of Z (see Figure 4.3) during the contracting phase. In that case, contraction is associated with permanent deformation, characterized by a continuously rearranging contact network, in which grains move one with respect to others in order to fill pores. While further tests are needed to confirm this point, we expect the macroscopic behaviour of this type of samples, observed on figure 4.2(Right), not to be much sensitive to the prescribed contact stiffness, as this deformation type would corresponds to type II strains, i.e. strains that are associated to continuously rearranging force networks following microscopic instabilities (*Radjai and Dubois*, 2011).

To summarize, we have seen that we are able to build samples that show macroscopic contraction followed by macroscopic dilation but are associated to distinct behaviours in term of coordination number evolution, that decreases in the case of HC samples while it increases for LC samples. These two limit cases of mechanical behaviour are summed up on Figure 4.4, that shows all the presented macroscopic response superimposed on the coordination number Z versus density ϕ diagram already presented on Figure 4.1. The critical state point, materialized by the black circle at $\phi_c = 0.815$, is clearly evidenced on this plot. Loading paths that are observed for ϕ above ϕ_c (blue zone) are likely to exhibit, at some point, a dilating behaviour. On the opposite, HC samples located for ϕ below ϕ_c reach the critical state by continuously contracting. However, this is not the case for LC samples, at least for sample LC6, that starts on the left hand side of the critical state point but still exhibits a dilating behaviour. As stated

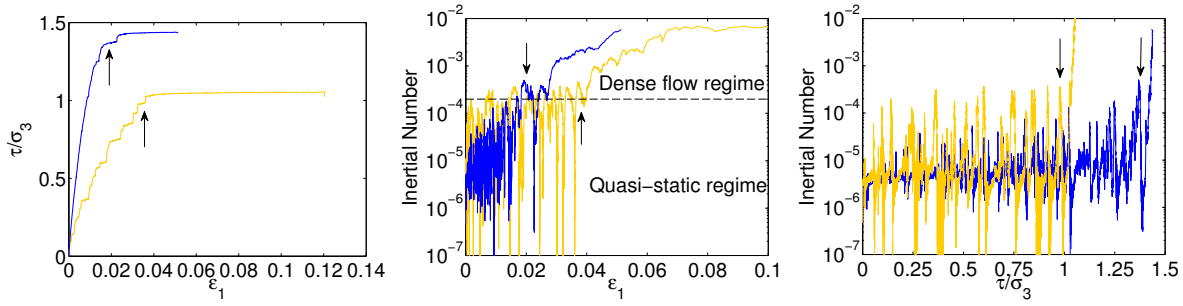

FIGURE 4.5 – Macroscopic behaviour of LC1 (blue) and LC5 (yellow) samples observed under stress controlled experiments.(Left) Deviatoric stress τ/σ_3 and (Middle) inertial number as a function of axial strain ϵ_1. (Right) Inertial number I as a function of deviatoric stress τ/σ_3. Arrows indicate the onset of dense flow regime.

by *Rothenburg and Kruyt* (2004), this picture would be drastically modified by changing the microscopic friction μ_{biax}, that would change the position of the critical state.

4.3 Discussion

From the multi-axial tests performed previously, we have seen that we were able to observe various physical processes of deformation in the early stages of mechanical loading. Thus, the next step is to test the analyses we performed in Chapter 3 considering these different configurations, in order to answer whether similar behaviours in term of correlation lengths growth or characteristic time/deformation scales can be extracted.

Firstly, Figure 4.5 shows the mechanical behaviour of samples LC1 and LC5 obtained when submitted to a stress controlled multi-axial loading similar to that of Chapter 3, considering $\delta\sigma_1^{tr} = 2.10^{-7}$. We can see that, compared to Figure 3.1, fluctuations of the inertial number I are much more pronounced. This implies that the position of the quasi-static to dense flow transition, approximately underlined by vertical arrows, considerably varies from one sample to another. Therefore to extract the type of behaviour obtained in Chapter 3, a significantly larger amount of simulations might be needed. Moreover, as the micro-mechanisms involved in stress or strain concentration processes may change for these samples, the relevant characteristic time or deformation windows may also differ from the study performed in Chapter 3. For all these reasons, studying the multiscale properties and their connection with macroscopic behaviour for those sample types requires further work.

Secondly, we could focus specifically on the transition between macroscopic contraction and macroscopic dilation. Indeed, looking at Figure 4.6, the transitional character of the onset of dilation is intriguing. First, for both HC and LC samples, the macroscopic dilation phenomenon only occurs for initial packing fraction greater than a treshold value $\phi_c = 0.815$. At lower values, macroscopic dilation does not seem to be possible. Second, at $\phi \geq \phi_c$, relevant control parameters can be extracted :

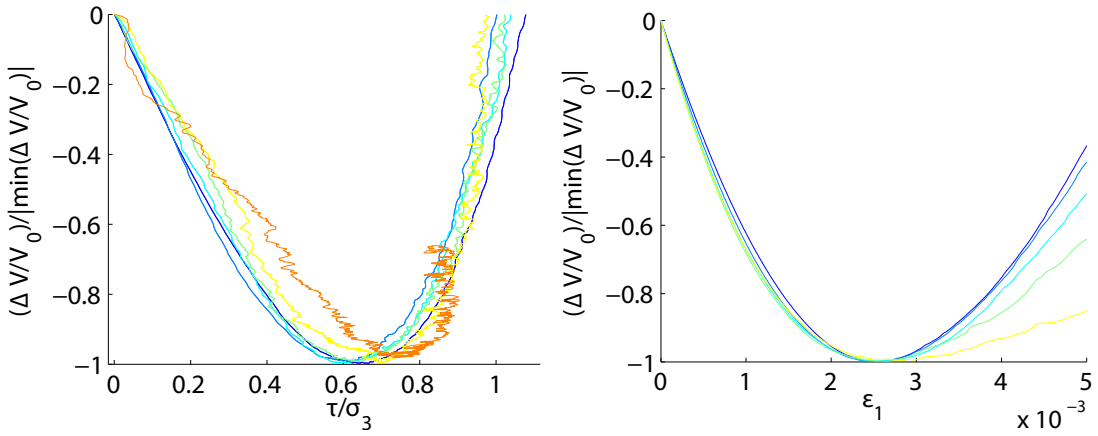

FIGURE 4.6 – Normalized macroscopic volume variation $(\Delta V/V_0)/|min(\Delta V/V_0)|$ for (Left) LC samples as a function of normalized deviatoric stress τ/σ_3 and (Right) HC samples as a function of axial deformation ϵ_1, where $|min(\Delta V/V_0)|$ is the minimum volume reached through mechanical testing.

- for HC samples, ϵ_1 appears to control the onset of dilation. Indeed, at the specific point $\epsilon_1 = 2.55.10^{-3}$, a sample that starts to dilate is likely to infinitely dilate during mechanical testing, while a sample that contracts is likely to infinitely contract during mechanical testing.
- for LC samples, an unintuitive result is that dilation is not observed at a constant value of density ϕ for all samples (see Figure 4.3), as one would expect in the case of a maximum filling of pores configuration reached by grains rearrangement. Instead, the control parameter appears to be the deviatoric stress τ. Indeed, when looking at $\Delta V/V_0$ normalized by maximum contraction as a function of τ (figure 4.6), almost all volumetric curves collapse, despite a slight gap for the LC6 sample, showing that τ might be the relevant parameter that controls the physics of dilation for LC samples, i.e. in the case of strains of type II (*Radjai and Dubois*, 2011).

Following this, an interesting perspective would be to examine whether heterogeneities presenting specific properties can be seen in the divergent deformation field at the transition from macroscopic contraction to macroscopic dilation. Figure 4.7 shows a divergent deformation field computed considering the LC1 sample at the onset of dilation. The volume variation seems heterogeneous at that point : does this heterogeneity only result from heterogeneities induced by shear deformation, or is there a pure divergent component that would present specific properties at the onset of macroscopic dilation ? The coarse graining analysis we performed in Chapter 3 is not appropriated to investigate this. Indeed :

- Firstly, primary tests show that computed power law scalings on the absolute values of divergent deformation are associated to slopes close to 1 at the onset of dilation. Consequently, as spatial correlations can only be extracted for lower slopes in the power law scaling (see section 3.3.2), this analysis cannot allow us to discriminate about the contri-

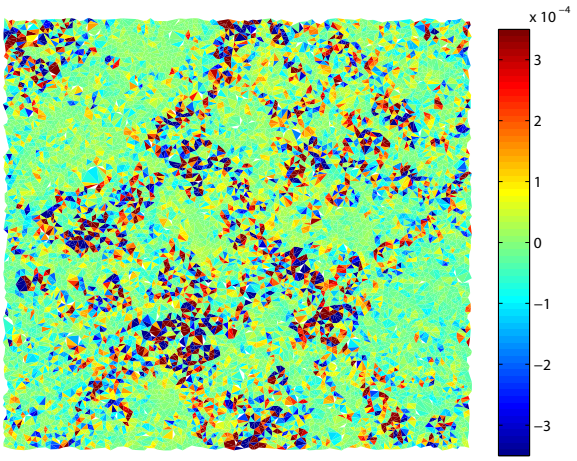

FIGURE 4.7 – Divergent deformation field observed at the onset of dilation considering the sample number LC1 and an incremental deformation window of $\delta\epsilon_w = 5.10^{-5}$.

bution of spatial correlations.

– Secondly, the incremental divergent deformation obtained at the largest scale, i.e. the second term on the left hand side of equation 3.6, decreases until reaching 0 at the onset of dilation, inducing artefacts in scaling crossovers.

Thus, other statistical tools such as for example susceptibility analyses performed on grains displacements or 2D correlograms performed on the shear deformation field have to be used to investigate this.

Chapitre 5

Conclusions et perspectives

Dans la seconde partie de ce travail de thèse, nous avons examiné les propriétés statistiques des hétérogénéités se développant dans les champs de contrainte et de déformation d'un milieu granulaire frottant soumis à un chargement biaxial. Expérimentalement, dans cette configuration de chargement très répandue en géotechnique/géophysique, l'observation du champ de déformation est généralement effectuée sur des incréments de déformation macroscopique importants (*Desrues and Viggiani*, 2004; *Hall et al.*, 2010). Le champ de contrainte, quant à lui, est difficile d'accès (*Majmudar and Berhinger*, 2005) et donc peu documenté dans cette configuration. Dans cette thèse, nous avons réalisé un travail essentiellement numérique de manière à accéder au champ de contrainte et aux glissements intergrains, et à une grande précision dans les déplacements des grains au cours du chargement. Ainsi, la caractérisation des champs à haute résolution temporelle a pu être effectuée. En complément, un travail expérimental basé sur l'analyse des champs de déformation à haute résolution temporelle a été réalisé avec le dispositif $1\gamma2\epsilon$, afin d'illustrer et confirmer les résultats numériques.

Pour des incréments de déformation macroscopique importants, nous avons vu que, dans la partie introductive, dans les simulations numériques et dans les essais $1\gamma2\epsilon$ des bandes de cisaillement s'installent de manière pérenne aux alentours du maximum de contrainte. L'analyse de champ que l'on a réalisée nous a permis de conclure que ces dernières ne sont pas associées à des propriétés multi-échelles, c'est à dire qu'elles présentent des tailles caractéristiques qui peuvent être quantifiées par l'analyse de décimation réalisée dans le Chapitre 3. Cependant, la définition de ces tailles caractéristiques n'est pas évidente. En effet, elle dépend de la taille de la fenêtre en déformation considérée pour évaluer le champ de déformation, du moins à l'instabilité macroscopique. Une analyse plus approfondie pourrait être réalisée dans cette direction en se placeant après le maximum de contrainte macroscopique lors d'essais à déformation imposée : il s'agirait alors d'analyser l'évolution de l'échelle de coupure obervée dans la dépendance d'échelle de la déformation cisaillante en fonction de la taille de la fenêtre considérée.

Par opposition, l'analyse détaillée des champs de déformation aux faibles incréments de déformation macroscopique nous a permis d'extraire un autre type de comportement, pour lequel les propriétés de la bande de cisaillement au sens de la théorie de *Rudnicki and Rice* (1975) ne sont plus vérifiées. En effet, les champs de déformation à ces échelles s'apparentent à un ensemble complexe d'amas qui concentrent la déformation, et dont la disposition spatiale est très fluctuante au cours du chargement. Ce type de comportement fluctuant avait déjà été caractérisé au cours d'un chargement biaxial dans le champ de déplacement, que ce soit numériquement (*Radjai and*

Roux, 2002) ou plus récemment expérimentalement (*Richefeu et al.*, 2012). Les observations expérimentales de l'équipe du laboratoire de Physique de Rennes, présentées dans la partie introductive, confirment l'observation de ces fluctuations dans le champ de déformation. Ici, nous montrons dans le modèle numérique et dans $1\gamma 2\epsilon$ que ces champs de déformation sont associés à des comportements multi-échelles spécifiques à l'instabilité macroscopique.

Ainsi, deux composantes caractéristiques, à savoir la bande de cisaillement et les amas intermittents de déformation, semblent coexister aux différentes échelles de déformation macroscopique dans l'échantillon granulaire au cours du chargement. De plus, ces deux composantes caractéristiques apparaissent toutes deux associées à l'instabilité macroscopique. Toutefois, dans cette thèse, nous n'avons pas pu identifier la relation entre ces deux composantes. Une première perspective serait donc d'analyser comment les amas de déformation diffusent dans l'espace au cours du chargement afin de voir de quelle manière ces derniers construisent, en cumulé, une bande de cisaillement qui perdure. Pour celà, des analyses de corrélation spatio-temporelle seraient à réaliser.

D'autre part, l'observation de propriétés multi-échelles sur le champ de contrainte au temps de propagation de l'onde élastique à travers l'échantillon nous a permis de conclure que le comportement spécifique des amas de déformation intermittents est directement associé aux redistributions de contrainte induites par l'énergie elastique libérée lors des glissements inter grains. Cependant cette interprétation se limite pour l'instant aux types d'échantillons considérés numériquement dans cette étude. En effet, nous avons vu que ces derniers présentent des propriétés d'assemblage (forte densité d'empilement et forte coordination entre les grains) telles que l'un des processus majeurs de déformation des assemblages granulaires, matérialisé par le réarrangement permanent du réseau de contacts, est très limité dans ce cas dans la phase initiale de chargement.

Ainsi, la seconde perspective de ce travail serait de réaliser le même type d'analyse en considérant le panel d'échantillons présenté dans le Chapitre 4. Dans ces derniers cas, d'autres mécanismes que ceux évoqués précèdemment peuvent être associés à l'instabilité macroscopique. Par conséquent, les échelles incrémentales caractéristiques de temps pour le champ de contrainte, correspondant à la propagation d'une onde élastique à travers l'échantillon, et de déformation axiale $\delta\epsilon_p$ pour laquelle un comportement similaire est observé dans le champ de déformation, seront probablement à redéfinir. De plus, nous pourrions envisager de quantifier d'autres paramètres caractérisant l'arrangement granulaire, tel que par exemple le tenseur de texture.

Enfin, une troisième perspective consisterait à rajouter dans le modèle granulaire de la cohésion dans les contacts. L'objectif serait ici double. D'une part, on s'attend à ce que les effets de mémoire soient drastiquement modifiés. Ainsi, la connexion avec les bandes de cisaillement pourrait être modifiée. D'autre part, il a été observé dans la banquise Arctique (*Stern and Lindsay*, 2009) qu'en hiver, lorsque la couverture de glace s'apparente à un milieu continu qui se fracture, les lois d'échelles observées sur le champ de déformation présentent les mêmes

propriétés que celles reportées par *Girard et al.* (2010) dans un modèle d'endommagement d'un milieu continu cohésif. A l'inverse, en été, lorsque la banquise se comporte plutôt comme un milieu granulaire (*Feltham*, 2005), les lois d'échelles observées sur le champ de déformation s'apparentent à celles obtenues dans cette partie sur les milieux granulaires avec, en particulier, un exposant plus élevé de la loi de puissance $< \delta\gamma > \sim L^{-\rho_s}$. Ainsi, la prise en compte d'une cohésion dans les contacts dans le modèle granulaire pourrait permettre d'explorer cette gamme de comportement dans les lois d'échelles, en allant d'un milieu granulaire purement frottant vers un milieu très cohésif.

Bibliographie

Abate, A. R., and D. J. Durian (2007), Topological persistence and dynamical heterogeneities near jamming, *Phys. Rev. E*, *76*, 021,306, doi :10.1103/PhysRevE.76.021306.

Agnolin, I., and J-N. Roux (2007), Internal states of model isotropic granular packings. I. assembling process, geometry, and contact networks, *Phys. Rev. E*, *76*, 061,302, doi : 10.1103/PhysRevE.76.061302.

Amitrano, D. (2003), Brittle-ductile transition and associated seismicity : Experimental and numerical studies and relationship with the b value, *J. Geophys. Res.*, *108*, 2044, doi : 10.1029/2001JB000680.

Amon, A., V. Nguyen, A. Bruand, J. Crassous, and E. Clément (2012), Hots spots in an athermal system, *Phys. Rev. Lett.*, *108*, 135,502.

Baud, P., V. Vajdova, and T. Wong (2006), Shear-enhanced compaction and strain localization : Inelastic deformation and constitutive modeling of four porous sandstones, *J. Geophys. Res.*, *111*, doi :10.1029/2005JB004101.

Bi, D., J. Zhang, B. Chakraborty, and R. Berhinger (2011), Jamming by shear, *Nature*, *480*, 355–358.

Calvetti, F., G. Combe, and J. Lanier (1997), Experimental micromechanical analysis of a 2D granular material : relation between structure evolution and loading path, *Mechanics of Cohesive Frictional Materials*, *2*, 121–163.

Casagrande, A. (1936), Characteristics of cohesionless soils affecting the stability of slopes and earth fills, *Journal of the Boston Society of Civil Engineers*, *23*(1), 257–276.

Combe, G., and J-N. Roux (2000), Strain versus stress in a model granular material : a devil's staircase, *Phys. Rev. Lett.*, *85*, 3628–3631.

Combe, G., and J-N. Roux (2003), Discrete numerical simulation, quasi-static deformation and the origins of strain in granular materials, *Deformation Charactersitics of Geomaterials, 3ème Symposium sur le Comportement des sols et des roches tendres, Lyon, 22-24 Septembre 2003, In di Benedetto et al.*, pp. 1071–1078.

Cundall, P., and O. Strack (1979), A discrete numerical model for granular assemblies, *Géotechnique*, *29*, 47–65.

Dauchot, O., G. Marty, and G. Biroli (2005), Dynamical heterogeneity close to the jamming transition in a sheared granular material, *Phys. Rev. Lett.*, *95*, 265,701, doi : 10.1103/PhysRevLett.95.265701.

DeGiuli, E., and J. McElwaine (2011), Laws of granular solids : Geometry and topology, *Phys. Rev. E*, *84*, 041,310, doi :10.1103/PhysRevE.84.041310.

Desrues, J., and G. Viggiani (2004), Strain localization in sand : an overview of the experimental results obtained in grenoble using stereophotogrammetry, *Int. J. Numer. Anal. Meth. Geomech.*, *28*, 279–321.

Erpelding, M., A. Amon, and J. Crassous (2008), Diffusive wave spectroscopy applied to the spatially resolved deformation of a solid, *Phys. Rev. E*, *78*, 046,104, doi : 10.1103/PhysRevE.78.046104.

Feltham, D. L. (2005), Granular flow in the marginal ice zone, *Phil. Trans. R. Soc. A*, *12*(1832), 1677–1700, doi :10.1098/rsta.2005.1601.

Girard, L., D. Amitrano, and J. Weiss (2010), Failure as a critical phenomenon in a progressive damage model, *J. Stat. Mech.*, *2010*(01), P01,013.

Girard, L., J. Weiss, and D. Amitrano (2012), Damage-cluster distibutions and size effect on strength in compressive failure, *Phys. Rev. Lett.*, *108*, 225,502, doi : 10.1103/PhysRevLett.108.225502.

Griffa, M., E. G. Daub, R. A. Guyer, P. A. Johnson, C. Marone, and J. Carmeliet (2011), Vibration-induced slip in sheared granular layers and the micromechanics of dynamic earthquake triggering, *Europhys. Lett.*, *96*(1), 129–137, doi :http ://dx.doi.org/10.1209/0295-5075/96/14001.

Haimson, B., and C. Chang (2000), A new true triaxial cell for testing mechanical properties of rock, and its use to determine rock strength and deformability of westerly granite, *International Journal of Rock Mechanics and Mining Sciences*, *37*(1–2), 285 – 296, doi :10.1016/S1365-1609(99)00106-9.

Haimson, B., and J. Rudnicki (2010), The effect of the intermediate principal stress on fault formation and fault angle in siltstone, *J. Struct. Geol.*, *32*, 1701–1711.

Hall, S., D. Wood, E. Ibraim, and G. Viggiani (2010), Localised deformation patterning in 2D granular materials revealed by digital image correlation, *Granular Matter*, *12*, 1–14, doi : 10.1007/s10035-009-0155-1.

Issen, K., and J. Rudnicki (2001), Theory of compaction bands in porous rock, *Phys. and Chem. Earth*, *26*, 95–100.

Joer, H., J. Lanier, J. Desrues, and E. Flavigny (1992), "1γ2ϵ" : A new shear apparatus to study the behaviour of granular materials, *Geotechnical Testing Journal*, *15*, 129–137, doi : 10.1520/GTJ10235J.

Keys, A. S., A. R. Abate, S. C. Glotzer, and D. J. Durian (2007), Measurement of growing dynamical length scales and prediction of the jamming transition in a granular material, *Nature Phys.*, *3*, 260–264, doi :10.1038/nphys572.

Liu, A. J., and S. R. Nagel (1998), Jamming is not just cool any more, *Nature*, *396*, 21–22.

Liu, C.-h., S. R. Nagel, D. A. Schecter, S. N. Coppersmith, S. Majumdar, O. Narayan, and T. A. Witten (1995), Force flucuations in bead packs, *Science*, *269*(5223), 513–515, doi : 10.1126/science.269.5223.513.

Louche, H., K. Bouabdallah, P. Vacher, T. Coudert, and P. Balland (2008), Kinematic fields and acoustic emission observations associated with the portevin le châtelier effect on an al–mg alloy, *Experimental Mechanics*, *48*, 741–751, 10.1007/s11340-008-9125-5.

Majmudar, T., and R. Berhinger (2005), Contact force measurements and stress-induced anisotropy in granular materials, *Nature*, *435*, 1079–1082, doi :10.1038/nature03805.

Makse, H. A., N. Gland, D. L. Johnson, and L. Schwartz (2004), Granular packings : Nonlinear elasticity, sound propagation, and collective relaxation dynamics, *Phys. Rev. E*, *70*, 061,302, doi :10.1103/PhysRevE.70.061302.

Marsan, D., H. Stern, R. Lindsay, and J. Weiss (2004), Scale dependence and localization of the deformation of Arctic sea ice, *Phys. Rev. Lett.*, *93*(17), 178,501, doi : 10.1103/PhysRevLett.93.178501.

Marty, G., and O. Dauchot (2005), Subdiffusion and cage effect in a sheared granular material, *Phys. Rev. Lett.*, *94*, 015,701, doi :10.1103/PhysRevLett.94.015701.

Midi, G. (2004), On dense granular flows, *Eur. Phys. J. E.*, *14*(4), 341–365, doi : 10.1140/epje/i2003-10153-0.

O'Hern, C. S., L. E. Silbert, A. J. Liu, and S. R. Nagel (2003), Jamming at zero temperature and zero applied stress : The epitome of disorder, *Phys. Rev. E*, *68*, 011,306, doi : 10.1103/PhysRevE.68.011306.

Olsson, W. (1999), Theoretical and experimental investigation of compaction bands in porous rock, *J. Geophys. Res.*, *104*(B4), 7219–7228, doi :10.1029/1998JB900120.

Pouliquen, O., and F. Chevoir (2002), Dense flows of dry granular material., *C.R. Physique*, *3*, 163–175.

Radjai, F., and F. Dubois (2011), *Discrete Numerical Modeling of Granular Materials*, Wiley-ISTE.

Radjai, F., and V. Richefeu (2009), Contact dynamics as a nonsmooth discrete element method, *Mechanics of Materials*, *41*(6), 715 – 728, doi :10.1016/j.mechmat.2009.01.028.

Radjai, F., and S. Roux (2002), Turbulentlike fluctuations in quasistatic flow of granular media, *Phys. Rev. Lett.*, *89*, 064,302, doi :10.1103/PhysRevLett.89.064302.

Reches, Z., and D. Lockner (1994), Nucleation and growth of faults in brittle rocks, *J. Geophys. Res.*, *99*, doi :10.1029/94JB00115.

Richefeu, V., G. Combe, and G. Viggiani (2012), An experimental assessment of displacement fluctuations in a 2D granular material subjected to shear, *arXiv :1208.0485v1 [cond-mat.soft]*.

Richeton, T., J. Weiss, and F. Louchet (2005), Breakdown of avalanche critical behaviour in polycrystalline plasticity, *Nature Materials*, *4*, 465–469, doi :10.1038/nmat1393.

Rothenburg, L., and N. Kruyt (2004), Critical state and evolution of coordination number in simulated granular materials, *Int. J. Sol. Struct.*, *41*, 5763–5774, doi : 10.1016/j.ijsolstr.2004.06.001.

Roux, J-N., and F. Chevoir (2005), Simulation numérique discrète et comportement mécanique des matériaux granulaires, *Bulletin des Laboratoires des Ponts et Chaussées*, *254*, 109–138.

Roux, J-N., and G. Combe (2002), Quasistatic rheology and the origins of strain, *Comptes Rendus de l'Académie des Sciences, Série IV - Physics-Astrophysics*, *3*, 131–140.

Rudnicki, J., and J. Rice (1975), Conditions for the localization of deformation in pressure-sensitive dilatant materials, *J. Mech. Phys. Solids*, *23*, 371–394.

Sethna, J., K. Dahmen, and C. Myers (2001), Crackling noise, *Nature*, *410*, 242–250, doi : doi :10.1038/35065675.

Stanchits, S., J. Fortin, G. Dresen, and Y. Gueguen (2009), Initiation and propagation of compaction bands in dry and wet bentheim sandstone, *Pure and Appl. Geophys.*, *104*, doi : 10.1007/s00024-009-0478-1.

Stern, H., and R. Lindsay (2009), Spatial scaling of Arctic sea ice deformation, *J. Geophys. Res.*, *114*(17), 178,501, doi :10.1029/2009JC005380.

Szarf, K., G. Combe, and P. Villard (2011), Polygons vs. clumps of discs : a numerical study of the influence of grain shape on the mechanical behaviour of granular materials, *Powder Tech.*, *2008*, 279–288.

Tordesillas, A., M. Muthuswamy, and S. Walsh (2008), Mesoscale measures of nonaffine deformation in dense granular assemblies, *J. Eng. Mech.*, *134*(12), 1095–1113.

Tsamados, M. (2010), Plasticity and dynamical heterogeneity in driven glassy materials, *Eur. Phys. J. E*, *32*(2), 165–181, doi :http ://dx.doi.org/10.1140/epje/i2010-10609-0.

Vacher, P., S. Dumoulin, F. Morestin, and S. Mguil-Touchal (1999), Bidimensional strain measurement using digital images, *J. Mech. Eng. Sci. C*, *213*, 811–817.

Walker, D. M., and A. Tordesillas (2010), Topological evolution in dense granular materials : A complex networks perspective, *International Journal of Solids and Structures*, *47*(5), 624 – 639, doi :10.1016/j.ijsolstr.2009.10.025.

Weiss, J., and D. Marsan (2003), Three-dimensional mapping of dislocation avalanches : Clustering and space/time coupling, *Science*, *299*(5603), 89–92, doi :10.1126/science.1079312.